Label-free Plasmonic Detection using Nanogratings Fabricated by Laser Interference Lithography

by

Koh Yiin Hong
B.Sc., University of Technology Malaysia, 2006
M.Sc., University Malaya, 2008

A Dissertation Submitted in Partial Fulfillment
of the Requirements for the Degree of

DOCTOR OF PHILOSOPHY

in the Department of Chemistry

© Koh Yiin Hong, 2017
University of Victoria

All rights reserved. This dissertation may not be reproduced in whole or in part, by photocopy or other means, without the permission of the author.

Supervisory Committee

Label-free Plasmonic Detection using Nanogratings Fabricated by Laser Interference Lithography

by

Koh Yiin Hong
B.Sc., University of Technology Malaysia, 2006
M.Sc., University Malaya, 2008

Supervisory Committee

Dr. Alexandre G. Brolo (Department of Chemistry)
Supervisor

Dr. Cornelia Bohne (Department of Chemistry)
Departmental Member

Dr. Fraser Hof (Department of Chemistry)
Departmental Member

Dr. Peter Wild (Department of Mechanical Engineering)
Outside Member

Abstract

Supervisory Committee
Dr. Alexandre G. Brolo (Department of Chemistry)
Supervisor
Dr. Cornelia Bohne (Department of Chemistry)
Departmental Member
Dr. Fraser Hof (Department of Chemistry)
Departmental Member
Dr. Peter Wild (Department of Mechanical Engineering)
Outside Member

Plasmonics techniques, such as surface plasmon resonance (SPR) and surface-enhanced Raman scattering (SERS), have been widely used for chemical and biochemical sensing applications. One approach to excite surface plasmons is through the coupling of light into metallic grating nanostructures. Those grating nanostructures can be fabricated using state-of-the-art nanofabrication methods. Laser interference lithography (LIL) is one of those methods that allow the rapid fabrication of nanostructures with a high-throughput. In this thesis, LIL was combined with other microfabrication techniques, such as photolithography and template stripping, to fabricate different types of plasmonic sensors. Firstly, template stripping was applied to transfer LIL-fabricated patterns of one-dimensional nanogratings onto planar supports (e.g., glass slides and plane-cut optical fiber tips). A thin adhesive layer of epoxy resin was used to facilitate the transfer. The UV-Vis spectroscopic response of the nanogratings supported on glass slides demonstrated a strong dependency on the polarization of the incident light. The bulk refractive index sensitivities of the glass-supported nanogratings were dependent on the type of metal (Ag or Au) and the thickness of the metal film. The described methodology provided an efficient low-cost fabrication alternative to produce metallic nanostructures for plasmonic chemical sensing applications. Secondly, we demonstrated a versatile procedure (LIL either alone or combined with traditional laser photolithography) to prepare both large area (i.e. one $inch^2$) and microarrays (μarrays) of metallic gratings structures capable of supporting SPR excitation (and SERS). The fabrication procedure was simple, high-throughput, and reproducible, with less than 5 % array-to-array variations in geometrical properties. The nanostructured gold μarrays were integrated on a chip for SERS detection of ppm-level of

8-quinolinol, an emerging water-borne pharmaceutical contaminant. Lastly, the LIL-fabricated large area nanogratings have been applied for SERS detection of the mixtures of quinolone antibiotics, enrofloxacin, an approved veterinary antibiotic, and one of its active metabolite, ciprofloxacin. The quantification of these analytes (enrofloxacin and ciprofloxacin) in aqueous mixtures were achieved by employing chemometric analysis. The limit of quantification of the method described in this work is in the ppm-level, with <10 % SERS spatial variation. Isotope-edited internal calibration method was attempted to improve the accuracy and reproducibility of the SERS methodology.

Table of Contents

List of Tables

List of Figures

Acknowledgments

Finally, it comes to an end for my doctorate studies. I must admit that this was never an easy and smooth-sailing journey. Struggling, discouraging, depressing, procrastinating — these were the terms that I had heard about but never had to experience before I arrived in Canada, for my Ph.D. Even though it is a little of pain, I am still grateful that I took a daring decision to move out from the comfort zone and commit in an odyssey to explore science, as well as, to mould myself to be better. Starting with knowing no one in Canada and almost nothing about 'plasmonics', all these (especially my dissertation) would not have been possible without the help, encouragement and support from many people. I wish to take the opportunity to express my gratitude to:

- My supervisor, Dr. Alexandre Brolo for his encouragement and guidance throughout my work. From Dr. Brolo, besides his expertise in plasmonics field, I have learned that no one should give up without a fight but to stay resilient during the tough times.
- Dr. Alex Wlasenko for his help in optical measurement setups and also his informative feedbacks whenever I need one.
- Dr. Jacson Menezes for his expertise in interference lithography, which was utilized in many parts of my research.
- UVic machine shop (Chris Secord and Jeff Trafton) for making me various parts and pieces in my measurement setups.
- UVic glass shop (Sean Adams) for making me the glass slides with perforated holes for an attempt of on-chip measurements.
- UVic CAMTEC for the nanofabrication facilities that allow me to perform metal deposition and substrate characterizations.
- UVic Engineering laboratory for allowing me to use their high-density UV light source and some optical fiber cleaving tools.
- AXYS Analytical (Dr. Coreen Hamilton) for generously providing me isotope-edited ciprofloxacin for one of my experiments.

- UVic electronic shop (Shubha Hosalli and Andrew Macdonald) for their helps in resolving the computer- and UV/Vis/NIR spectrometer (Perkin Elmer Lambda 1050)-related issues.
- Samantha Harder and coworkers (Jirasek's Group) for generously letting me to use their Matlab algorithms for spectral baseline correction and averaging.
- My coworkers in UVic Chemistry and friends around Victoria for the laughs and jokes we shared during all kinds of gatherings, which indeed soothed the tension and stress at work.
- My ex-superior, Dr. Chitkay Chu who inspired me to come to Canada for my studies.
- My parents and my siblings for their unconditional love and support.
- And lastly, I would like to acknowledge NSERC and UVic for the funding, which made my research work and my life in Canada possible.

A big 'TERIMA KASIH' to all of you!!!

Dedication

To my parents –

who love me unconditionally,

who have raised me to be the person I am today

Chapter 1

Introduction

1.1 Research motivation

At the end of the 1950s, Dr. Richard Feynmann used the illustration ‘there’s plenty of room at the bottom’ to depict the potentials of ‘nanotechnology’ [1]. Since then, this innovative idea has been revolutionizing the natural sciences and engineering. The applications of nano-scaled materials have progressed and expanded into different areas of both fundamental and applied sciences. Nowadays, the power of nanotechnology is clearly displayed in the semiconductor industry (e.g., microelectronic manufacturing silicon (MEMS) technology). Nanoscale microprocessor elements have led the transformation of huge and bulky personal computers from the 1980s into the modern hand-held devices (e.g. smartphones, smart watches) of today [2].

Modern nanotechnology involves different types of materials, including carbon materials, semiconducting quantum dots, metallic nanostructures and others, with exciting new optical and electronic properties [3, 4]. Plasmonics is a branch of nanotechnology associated with optical field enhancements created when photons couple to free electrons in nanostructured metallic surfaces. The nanoscale elements at the metal interfaces break the surface symmetry of a smooth metal film, allowing photonic coupling events to take place [5, 6]. The advent of nanofabrication, as well as the development of new tools for nanostructure characterization, has then greatly benefited plasmonic research, both in terms of conceptual understandings of the phenomenon and by enabling plasmonic applications [7]. Figure 1.1 shows the evolution of scientific publications having ‘surface plasmon’ as a keyword obtained by the Web of Science® search engine in October 2016. An exponential increase of research activity initiated by the 1990s is evident in Figure 1.1. On par with the dramatic hike in the interest for plasmonic systems, the science research in the development of new nanofabrication methods, especially new approaches for metallic nanoparticle synthesis and the lithographic-based nanofabrication techniques [8], also demonstrates an

upward trend since the 1990s (information obtained by the Web of Science® search engine with ‘nanostructure fabrication’ keywords searched).

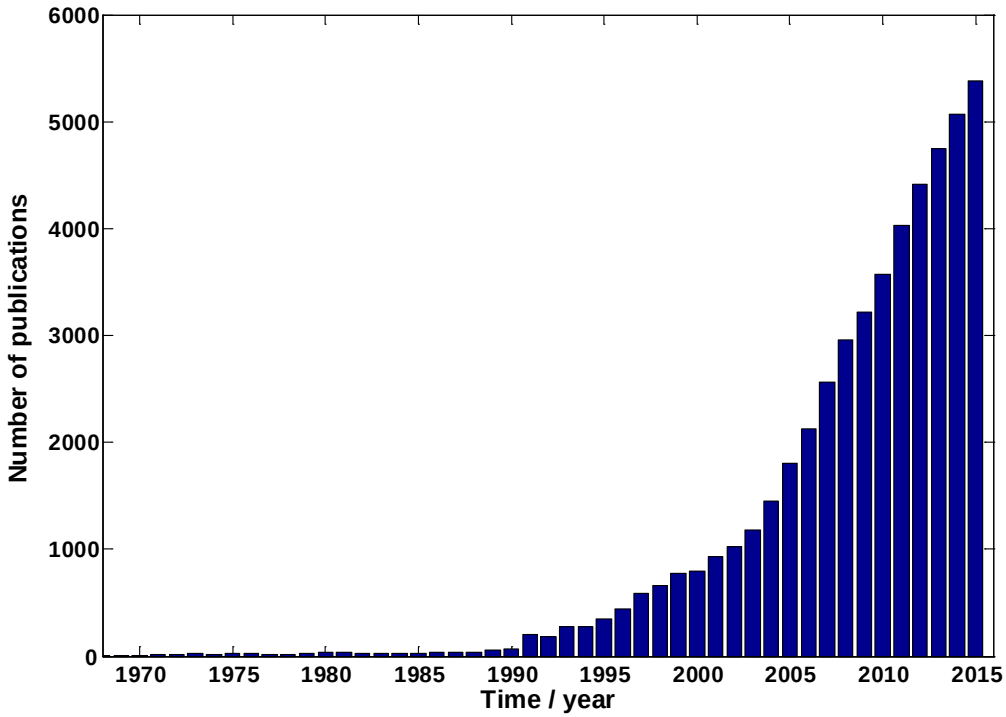

Figure 1.1 Number of publications with the keyword ‘surface plasmon’ in the period between 1968 and 2015. Source: Web of Science® search engine.

The type of plasmonic application that draws most attention from both academia and industries are related to surface plasmon-mediated chemical and biochemical sensing. These comprise both surface plasmon resonance (SPR) methods and a variety of plasmon-enhanced spectroscopic techniques, including surface enhanced Raman scattering (SERS). Both SPR and SERS are surface sensitive [9-11]. SPR is very useful to detect real-time molecular binding events [9]; while SERS is capable of not only quantitatively determine concentrations of analytes, but also qualitatively identify the molecular characteristics of unknowns [12-16].

As the world’s population continues to grow, different problems arise as consequences of increasing human activities. Health and environment are two of the most significant global problems that require ameliorative solutions, since they might directly

impact the safety and well-being of all living creatures [16, 17]. Appropriate chemical sensors are needed to monitor the level of risk in these two areas. Therefore, the development of plasmonic chemical sensors capable of performing adequate detection (i.e. high sensitivity and accuracy) is an important research area. Moreover, other requirements, such as the possibility of mass production at low-cost, simplicity in operation, rapid detection, and high throughput, can all be achieved through plasmonic nanostructures. These highlight the potential of plasmonics to benefit the world population. Within this spirit, the ultimate goal of this work is to develop both function- and cost-effective plasmonic sensors, which will fulfill the basic figure-of-merits (will be discussed in section 1.3.1) for biological and environmental detection.

1.2 Thesis organization

The thesis begins with a discussion of the fundamental aspects of SPR and SERS, including the coupling methods of electromagnetic field to the surface plasmon modes on the metal-dielectric interface (Chapter 1). At the end of Chapter 1, a section on chemometrics applications in spectroscopic analysis is discussed, as it is employed in the data analysis of the spectra of multi-component mixtures in Chapter 5.

After that, a literature review on the state-of-the-art of fabrication of plasmonic nanostructures will be presented in Chapter 2. The focus of the review will be set on solid-supported plasmonic substrates; encompassing both lithographic and non-lithographic fabrication methods. This chapter will also include reviews on microarray fabrication and on the setups of optofluidic plasmonic platforms capable of performing on-chip detections or multiplexed-detections. One of the main aspects of the thesis is the introduction of fabrication methods for mass fabrication of large area plasmonic structures. Therefore, the review in Chapter 2 will provide information on the state-of-the-art and help place our work within the broad context of nanofabrication.

Chapter 3 will be the first “results chapter” and it will focus on the fabrication of substrates by laser interference lithography (LIL). The fabrication of both large area and microarrays of nanogratings will be discussed in this chapter. Since the basic structure of

the substrates is an one-dimensional grating, the polarization anisotropy of the substrates will also be explored in Chapter 3. The chapter ends with a proof-of-concept on-chip environmental detection using the fabricated microarrays.

In Chapter 4, a template-stripping procedure to transfer the LIL-pattern to other planar substrates (i.e. glass slides and optical fiber tips) will be discussed. This effort is a starting point towards the fabrication of SPR refractive index sensors that can potentially be integrated to detect protein binding events (e.g. antigen-antibody binding).

In Chapter 5, a description of how the large area nanoplasmonic structure can be utilized to detect pharmaceutical contaminants (i.e. enrofloxacin and ciprofloxacin) in aqueous solutions using SERS will be presented. Chemometric data analysis have been employed to decouple the mixed vibrational spectra from the mixtures of the analytes. Isotopic internal calibration has also been attempted to improve the accuracy of the detection.

The thesis will end with the conclusion chapter (Chapter 6), which will also carry some discussion about potential improvements and next steps to advance this research further.

1.3 Background

In the beginning of the 1960's, R. Ritchie theoretically predicted the existence of surface plasmons in metals [18, 19]. This notable conjecture was then followed by two other independent groups of scientists (A. Otto, E. Kretschmann and his co-worker H. Raether), who successively demonstrated the attenuated total reflection (ATR)-prism coupling techniques to excite the surface plasmons (SPs) on metal-air interfaces [20, 21]. The SP excitation was found to be very sensitive to the changes in the dielectric properties (refractive index) of the air in contact to the metal surface.

The excitation of SP waves on metal interfaces can also be achieved by optical coupling using a metallic diffraction grating. This phenomenon was actually firstly observed by R.M. Wood, who documented the observation of optical anomalies from metal

diffraction gratings as early as the 1900s [22]. Those anomalous diffractions were later reproduced by U. Fano, who interpreted the effect as resonant absorption in 1935 [23, 24], and then more comprehensively in 1961 [25]. All these influential discoveries are precursors for the field of SPR sensing as we recognize it today.

Surface enhanced Raman scattering (SERS) is also a SP-mediated effect. The first SERS response was discovered when intense Raman scattering was observed for pyridine molecules adsorbed on a roughened silver electrode by M. Fleischmann et al. in 1974 [26]. The surprising enhancement from this extraordinary scattering phenomenon was later clarified to hinge on two inter-related mechanisms: the electromagnetic (by Van Duyne et al. [27] and M. Moskovits [28]) and the chemical (charge transfer) mechanisms (by Creighton et al. [29]).

The most classical substrates that support SERS are based on silver (Ag) and gold (Au) nanoparticles (NPs) colloids produced from the chemical reduction of aqueous metal salts [30, 31]. The sizes and geometries of the NPs are controlled during the reduction process [32-35]. Visually, the colloidal NPs of distinct sizes and shapes exhibit unique optical properties, including the formation of different stunning colors (e.g. Au NPs in 30-nm sizes are wine-red in color, while those of 90-nm sizes appear purple; Ag spheres in 50-nm diameter show greenish-grey, but Ag triangles in 50-nm edge length emerge blue). For instance, the SPR from these types of NPs had been utilized by artists as early as in 1400 AD to color artifacts (such as the Lycurgus Cup). The science behind, nonetheless, was not explored until the 20^{th} Century.

Gold and silver are the most commonly exploited plasmonic metals, mainly because their surface plasmon resonance frequencies reside in the visible/near-infrared range (~400 – 1000 nm) with relatively low optical losses. Based on a Drude model [36] description, Ag is expected to yield better plasmonic enhancements ($\varepsilon_{real} < 0$) in the visible, due to its lower (compared to Au) loss to the inter-band transitions (small $\varepsilon_{imaginary}$; with lower band-transition occurrences from d- to above Fermi level (i.e. s- or p-band)). Silver, however, has high tendency to be oxidized. As a result, Au is often the metal of choice in several types of applications.

The first demonstration of SPR sensing was presented by Liedberg et al. in 1983, where SPR was employed for gas detection. Some exploratory biosensing using an antigen-antibody system in a binding experiment was also presented [37]. In 1990, the very first commercial SPR-based biosensor equipment (BIACORE) was commercialized [38]. Typically, the instrument is reported (*www.biacore.com*) to achieve detection limits below 1 pg mm^{-2} and a resolution of ~ 10^{-7} refractive index units (RIU). On the other hand, SERS has been known for its single-molecule fingerprinting detection capabilities [39-41]. Commercial solid-supported SERS substrates (e.g. 'SERStrate' from *www.SILMECO.com*, 'RAM-SERS-AU/AG/SP' from *www.oceanoptics.com*) have been marketed starting in the 2000's and portable SERS analyzers (e.g. 'StellarCASE-Raman™ Applications from *www.stellarnet.us*, 'PSA' from Real Time Analyzer, Inc) have also been released in recent years for field detections.

Apart from the commercial plasmonic sensors mentioned earlier, the development of new plasmonic sensors is still an actively evolving research area with various contributions reported every year [13, 42-82]. To assess the performance of the new sensors as compared to the state-of-the-art, validation step is required to verify the analytical performance of the sensors. This can be done though the assessment of figure-of-merits (FoMs) [83-86]. In the following section, some fundamental figure-of-merits that are commonly used to assess the performances of analytical sensors are discussed.

1.3.1 Figure-of-merits (FoMs) of analytical sensors

Typical FoMs used to validate the performance of analytical sensors include those related to the analytes' responses to the sensors (e.g., sensitivity, selectivity, signal-to-noise ratio, limit of detection) [83-86]. Additionally, the stability of the sensing system (e.g. reproducibility, repeatability) is also important [83-85]. In the recent decade, portability (or the ease to be made portable) of the sensors has attracted more attention, as this feature allows on-site sampling and detection which is convenient for some applications (e.g. environmental detections) [46, 87-94]. In the following sections, some fundamental FoMs that are relevant to this work will be discussed.

1.3.1.1 Sensitivity

In general, the sensitivity of the detection of the analytes is given by the slope of the analytical calibration curve (i.e. calibration sensitivity, as illustrated in Figure 1.2). Typically, the calibration curve is a plot of the transducer unit response to the concentration of the analyte. The sensitivity performance of the sensors increases with the steepness (i.e. larger value) of the slope of the calibration curve. In other word, this indicates that a small change in concentration of analyte causes a large change in the response of the transducer.

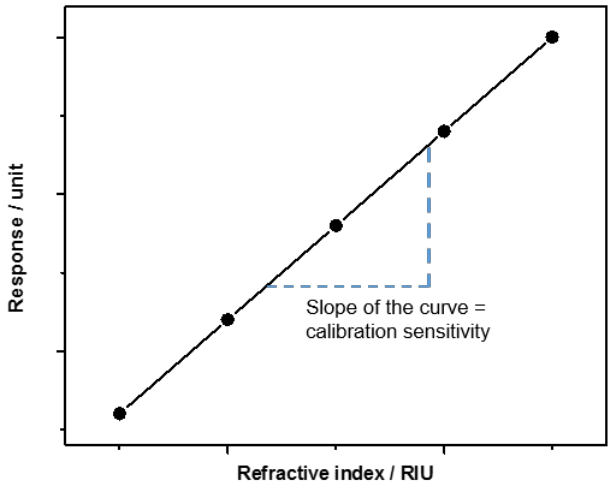

Figure 1.2 A typical calibration curve generated from SPR measurements. The slope of the curve corresponds to the calibration sensitivity of the detection.

For those SPR-based sensors, besides calibration sensitivity (also called bulk refractive index sensitivity (S_b) where calibration is done based on solution's refractive index, as seen in Figure 1.2), surface sensitivity (S_s) is also used to evaluate the sensors since most of the SPR sensors are employed in the detection of surface binding events (i.e. antigen-antibody binding) [86]. In S_s estimation, the effective refractive index (n_{eff}) on the metal-dielectric interface that takes into account the surface coverage, the adlayer (adsorbed layer) thickness and the extension of the SP-field from the surface, is employed in the calculations [86, 95].

1.3.1.2 Limit of detection (LOD)

Limit of detection (LOD) is the concentration with respect to the smallest detectable signals within a determined degree of certainty (i.e. clear distinction between signal and noise). Commonly, LOD is assessed through *n* times (e.g., IUPAC recommendation is that n=3) of the standard deviation (s) of repetitive measurements of the blank, as seen in Equation 1.1 [83]:

$$y_{LOD} = y_{blank} + 3s_{blank} \qquad (1.1)$$

where y_{LOD} is the instrument reading at LOD, y_{blank} is the mean reading of replicate blank measurements, and s_{blank} is the respective standard deviation from the blank measurements. This parameter is important as it describes the capability of the sensor in discriminating the signal of the analyte from the noise or background of the analytical output. The LODs achieved by reported SERS-based sensors in environmental detections are presented in section 1.6.

1.3.1.3 Reproducibility

The reproducibility of the analytical measurements implies the closeness of the agreement between successive measurements in different conditions (e.g., time intervals, changes of apparatus, change of operators). In practical, the degree of reproducibility is commonly presented in % relative standard deviation (%RSD).

1.3.1.4 Resolution

Resolution is another aspect that is important to validate SPR-based sensors. It is basically the smallest detectable change in refractive index unit (RIU). Equation 1.2 [86] is practically used to calculate the resolution of a sensing system:

$$Resolution = \frac{\sigma_{noise}}{S_b} \qquad (1.2)$$

where σ_{noise} is the standard deviation of repetitive measurements of the blank and S_b is the bulk sensitivity.

1.4 Surface plasmon resonance (SPR)

Technically, SP is the collective hybrid mode involving photons and the oscillation wave of the free electrons on the metallic interface. SPR leads to dramatic optical effects, such as extraordinarily large absorption or scattering responses, as the electromagnetic field of the light couples successfully to the oscillating electrons at the metallic interface [25, 96]. Specifically, there are two types of the SPs: (1) localized surface plasmon (LSP); and (2) propagating surface plasmon (PSP). Notably, both SP modes are surface-bound, but PSP has a longer decay length as compared to LSP [96].

Due to the mismatched momentum between the incident field and the free electron oscillation frequency in metals, direct coupling of light to the plasmon modes does not occur in normal conditions. This can be illustrated from the daily observation that these metals are genuinely good light reflectors (used as mirrors since the ancient times). The electromagnetic coupling conditions for SPR excitation will be discussed in the following sections. Another point to note is that the smooth metal films of Ag and Au, the two typical plasmonic metals (refer to Section 1.3), appear reflective in distinct colors. The explanation is related to the energy involved in their electrons' inter-band absorption. Since Ag absorbs in the ultraviolet region, so it reflects all visible spectrum and appears bright silvery. On the contrary, a smooth Au film shines in yellow because Au metal absorbs strongly in blue-green of the visible spectrum for the electronic transition from 3d band to the levels above Fermi level.

1.4.1 Localized surface plasmon resonance (LSPR)

The LSPR phenomenon can be illustrated using a tiny (nanometric) metallic sphere (e.g., NPs) [97]. Considering that the metallic NP has a relative small size compared to the visible wavelength (refer to Figure 1.3), the sphere experiences an uniform electric field. When a resonant electromagnetic field (i.e. matching to the oscillation frequency of the free electrons) illuminates the metallic sphere, the free electrons on the metal interface will be excited as if the external field is superimposed on the internal induced dipole of the metal sphere (charge oscillation of the electrons), as illustrated in Figure 1.3. Due to its small size,

in tenth of nanometers range, the intense charge confinement in the metal NP induces a highly localized field generated around the sphere.

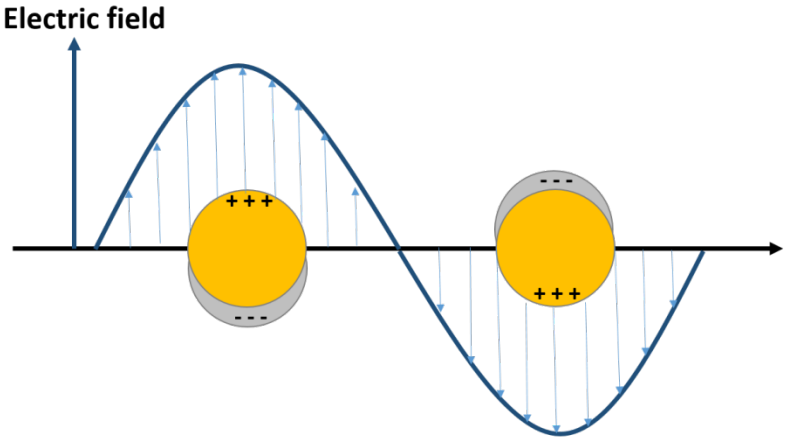

Figure 1.3 Schematic of the excitation of surface plasmon (SP) on metallic nanoparticles by free-space light (sphere diameter << light wavelength).

As discussed in section 1.3, the SPR phenomenon (more specifically LSPR) accounts for the assorted colors observed when metal nanoparticles exist in different sizes. The earliest analytical solution to explain the color extinction of gold nanoparticles (i.e. red color) was done by Gustav Mie in the early 1900s. In the Mie theory, the Maxwell's equation is solved using the spherical model. For nanospheres much smaller than the wavelength of light (sphere diameter << light wavelength), the extinction cross-section, σ_{ext} can be expressed by the following equations:

$$\sigma_{ext}(\omega) = 9\frac{\omega}{c}\varepsilon_d^{3/2} V \frac{\varepsilon_2(\omega)}{[\varepsilon_1(\omega)+2\varepsilon_d]^2+\varepsilon_2(\omega)^2} \qquad (1.3)$$

$$\sigma_{ext} = \sigma_{scatter} + \sigma_{abs} \qquad (1.4)$$

where ω is the angular frequency of the incidence, c is the speed of light, V is the volume of the particles, ε_d is the dielectric constant for the surrounding medium of the nanospheres, and lastly, ε_1 and ε_2 are the real and imaginary portions of the metal's dielectric constant and $\varepsilon_{metal}(\omega) = \varepsilon_1(\omega) + i\varepsilon_2(\omega)$. The notations, $\sigma_{scatter}$ and σ_{abs} are the scattering and absorption cross-sections of the nanospheres. From the equation 1.3, we can see that the resonance condition (LSPR) for the metal nanoparticles (i.e. large σ_{ext}) is fulfilled when

$\varepsilon_1(\omega) = -2\varepsilon_d$ and ε_2 is small (or weakly dependent on ω). These conditions are attained for Au, Ag and Cu in the visible and near IR.

In addition to that, the localized field will be even stronger when the metal nanosphere electromagnetically interacts with other nanospheres in its vicinity (nanometer range). Figure 1.4(a) shows an example of interaction when the inter-particles axis is parallel to the incidence polarization of the light field, allowing the coupling of the dipoles [98, 99]. The dipole coupling results in the generation of highly localized field inside the space between the particles (depicted by the highlighted red region in Figure 1.4(a)). These regions of highly localized electromagnetic fields are called 'hot-spots' [100, 101]. LSPR is thus a near-field effect that comes with very short decay length (10's of nm, depending on the wavelength). Figure 1.4(b) shows a scheme for the case where the incident field polarization is perpendicular to the inter-particle axis. In that case, the dipole coupling is not favoured and hot spot is not generated in the gap between the particles.

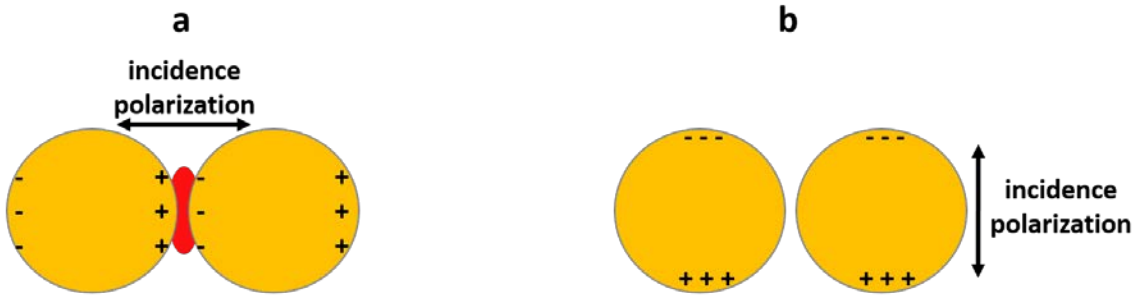

Figure 1.4 (a) The formation of hot spot in the cavity between two metal nanoparticles as the inter-particles' axis is parallel to the incidence polarization. **(b)** The lack of field in the cavity as the incidence polarization is perpendicular to the inter-particles' axis.

The LSPR effect is utilized in a variety of applications, and it is the main contribution to the amplification of the Raman signal observed in SERS [100, 102, 103]. Since LSPR frequency is very sensitive to dielectric changes on the interface of the NPs, it is useful for refractive index sensing [97, 104]. In addition, it is easier to tune the wavelength of LSPR by modulating the geometry of the metal nanoparticles (size and shape) [105, 106].

1.4.2 Propagating surface plasmon resonance (PSPR)

The typical PSP resonance is commonly known simply as 'SPR'. This is a very popular technique used in biomedical research to study biomolecular interactions. Similar to LSPR, the resonance energy of the SP is also very sensitive to dielectric changes (i.e. refractive index changes) on the metal interface [9, 37, 107]. Unlike LSPs, PSPs are non-radiative, and the energy transferred propagates along the interfaces of the planar substrates, as represented in Figure 1.5 (x-direction). The energy dissipates during propagation through optical absorption of the metal and scattering by surface roughness [108]. The energy loss is also portrayed through the decreasing of the PSP waves' amplitudes as the waves propagate along the metal interface in Figure 1.5.

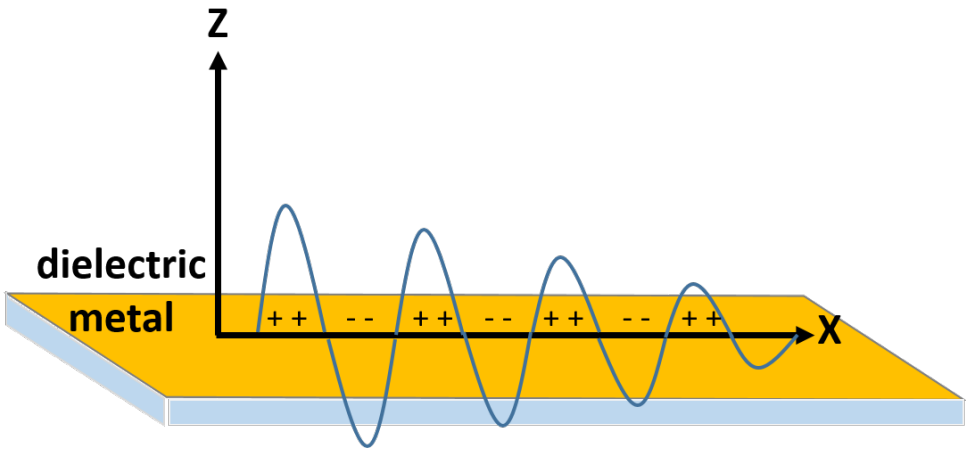

Figure 1.5 Schematic of a propagating surface plasmon (PSP) at the metal-dielectric interface.

For PSP waves, the typical propagation length for silver and gold is in the range of ~ 10 to 100 μm [109, 110]. Another SP related-length that is particularly important for SPR sensing, is the decay length of the PSP waves towards the dielectric materials (i.e. the penetration depth into the dielectric materials, along the z-direction in Figure 1.5). The decay lengths (penetration depths) into the dielectrics, $\delta_{dielectric}$, can be computed through equation 1.5 [110, 111]:

$$\delta_{dielectric} = \frac{1}{k_0}\left|\frac{\varepsilon_1 + \varepsilon_d}{\varepsilon_d^2}\right|^{\frac{1}{2}} \qquad (1.5)$$

where k_0 is the free space wavevector, ε_1 is the real portion of the metal's dielectric constant, and ε_d is the dielectric constant for dielectric materials. The $\delta_{dielectric}$ at the visible/infrared region for Ag is depicted in Figure 1.6. In general, PSPR is sharper compared to the classical LSPR (i.e. supported by metallic NPs), since the broadening of the PSPR mode is mainly contributed by propagation losses (e.g., from the random surface roughness, as seen in the imaginary portion of ε_m, metal's dielectric constant in equation 1.6).

$$k_{SP} = \left(\frac{\omega}{c}\right)\sqrt{\frac{\varepsilon_d \varepsilon_m}{\varepsilon_d + \varepsilon_m}} = \left(\frac{\omega}{c}\right)\sqrt{\varepsilon_{prism}}\sin\theta \qquad (1.6)$$

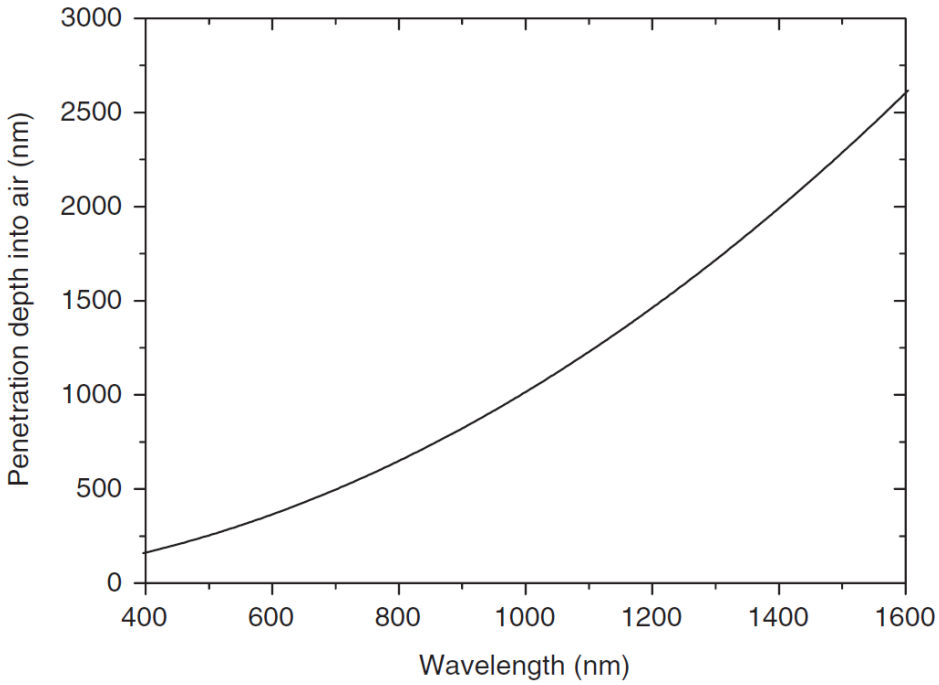

Figure 1.6 Penetration depth of surface plasmon of Ag into the dielectric (i.e. air) as a function of wavelengths. The data were computed using the Drude approximation. Reproduced with permission from [110].

1.4.2.1 PSPR prism coupling

There are two configurations to excite PSPR with prisms. These SPR excitation techniques are based on evanescent fields generated by the attenuated total internal reflection in prisms and they were developed by Otto [20] and Kretschmann [21] in the late 1960s. The

schematic of the Kretschmann setup is presented in Figure 1.7. The main difference between the Otto and the Kretschmann configurations is the position of the metal film relative to the prism. Kretschmann's directly coated the metal film on the prism, while Otto's allowed a space between the prism and the metal film [20, 21]. The Kretschmann configuration is more straightforward and easier to implement, since it does not require control of the space between the prism and metal film.

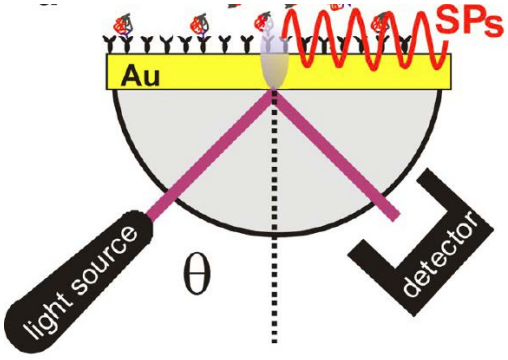

Figure 1.7 Kretschmann configuration is commonly used to couple the optical field to thin metal films in SPR biosensing experiments. Reproduced with permission from [90].

The SPR for both setups are detected in reflection mode (Figure 1.7), by measuring either a change of incidence angle or a change in the wavelength of the reflected light. The resonance conditions can be obtained by solving Maxwell equations [112, 113] and approximated as in equation 1.6 (also shown in Section 1.4.2):

$$k_{SP} = \left(\frac{\omega}{c}\right)\sqrt{\frac{\varepsilon_d \varepsilon_m}{\varepsilon_d + \varepsilon_m}} = \left(\frac{\omega}{c}\right)\sqrt{\varepsilon_{prism}}\sin\theta \qquad (1.6)$$

where k_{sp} is the SP wavevector, ε is the dielectric constant (for the dielectric materials, *d*, and metal, *m*), ω is the frequency of incident light, *c* is the speed of light in vacuum, and θ is the incident angle indicated in Figure 1.7. From the equation 1.6, the prism is needed to increase the momentum of the photons (more specifically the transverse magnetic (TM) mode (p-polarization) of the electromagnetic field [108, 114]), so that they can couple with the SP on the metal interfaces.

In practical terms, the PSP-prism coupling involves more stringent optical conditions (i.e. angular or incident wavelength), in order to fulfill the frequency and momentum requirements for SP excitation, as compared to the alternative coupling methods (e.g. extraordinary optical transmission (EOT), will be discussed in Section 1.4.2.2).

1.4.2.2 SPR grating coupling

Another way to couple photons to surface plasmons is through the incorporation of (periodic) surface roughness or gratings on the metal interface to break the symmetry on the planar metal interface [19]. Special-fabricated periodic metallic surface gratings (e.g. nanoholes [115-118], nanorods [119], and nanoslits [120-122]) permit direct optical coupling on zero-angle incidence [96, 123]. A schematic of experimental geometries for SPR grating coupling experiments is shown in Figure 1.8. The resonance conditions are achieved through the approximation as follows:

$$k_{SP} = \left(\frac{\omega}{c}\right)\sqrt{\frac{\varepsilon_d \varepsilon_m}{\varepsilon_d + \varepsilon_m}} = \left(\frac{\omega}{c}\right)\sin\theta \pm \frac{2\pi}{p}\, m \qquad (1.7)$$

where k_{sp} is the SP wavevector, ω is the frequency of incident light, c is speed of light in vacuum, ε is the dielectric constants (d for the dielectric materials, m for the metals), θ is the incident angle, p is the periodicity of nanostructures, and m is the mode defining the transmission order.

Extraordinary optical transmission (EOT) was discovered by Ebbesen et al. in 1998 [96]. In EOT, the grating coupling to produce PSPR occurs in transmission mode, rather than classical reflection (see Figure 1.7). The first observation related to EOT, as mentioned earlier in Section 1.3, was actually reported in the 1900s [22]. Even though the surface plasmon was already recognized in the 1960s, their relationship to EOT was not confirmed until Ebbesen et al. observed that the enhanced transmissions are actually affected by the periodicity of the gratings (nanohole arrays) on the metal interfaces [96, 109]. Since the EOT is normally generated by grating coupling at zero-angle incidence ($\theta = 0$), Equation 1.7 is simplified to:

$$\left(\frac{\omega}{c}\right)\sqrt{\frac{\varepsilon_d\varepsilon_m}{\varepsilon_d+\varepsilon_m}} = \frac{2\pi}{p}\,m \qquad (1.8)$$

The free photon wave-vector that is responsible in achieving SPR in equation 1.8 can then be substituted with angular frequency ($\omega = 2\pi f$; f is the ordinary frequency) and light equation ($c = f\lambda$) giving the Equation 1.9 and 1.10.

$$\left(\frac{2\pi}{\lambda_{SPR}}\right)\sqrt{\frac{\varepsilon_d\varepsilon_m}{\varepsilon_d+\varepsilon_m}} = \frac{2\pi}{p}\,m \qquad (1.9)$$

$$\lambda_{SPR} = \frac{p}{m}\sqrt{\frac{\varepsilon_d\varepsilon_m}{\varepsilon_d+\varepsilon_m}} \qquad (1.10)$$

where λ_{SPR} is the SPR wavelength. The rest of the notations are the same as equation 1.7.

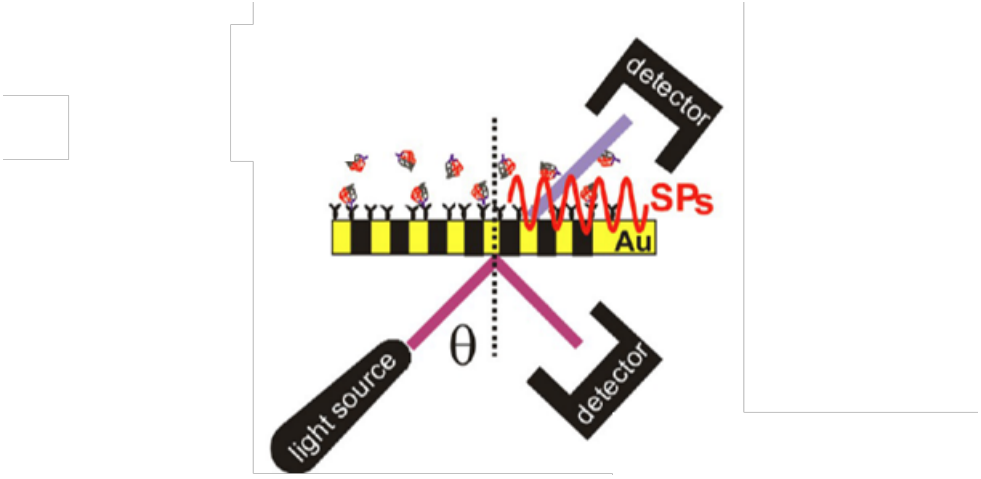

Figure 1.8 Schematic of grating coupling methods used to excite propagating surface plasmon on metal surfaces patterned with periodic nanostructures. Two experimental geometries are indicated: reflection and transmission. The transmission geometry is used in extraordinary optical transmission (EOT) measurements. Reproduced with permission from [86].

In optical physics, the incident light polarization can be decomposed in two components in the incident plan called transverse magnetic (TM) and transverse electric (TE) (also known as p-polarization and s-polarization, respectively). These two components are represented on a periodic slit structure shown in Figure 1.9. PSPR is only excited by the TM-mode of the incident field in one-dimensional or unsymmetrical metallic nanostructures

[124-126], as shown in Figure 1.9. This means that these kinds of nanostructures preserve polarization anisotropy. In contrast, when the polarization mode of the incidence is parallel to the long axis of the gratings (i.e. the structures are longer than the wavelengths in that direction), as illustrated in TE polarization in Figure 1.9, the SP excitation is less probable. This is because under this circumstance, the nanostructures are seen as a smooth metal film by the incident field, which reflects the incident light rather than absorb (transmit) it.

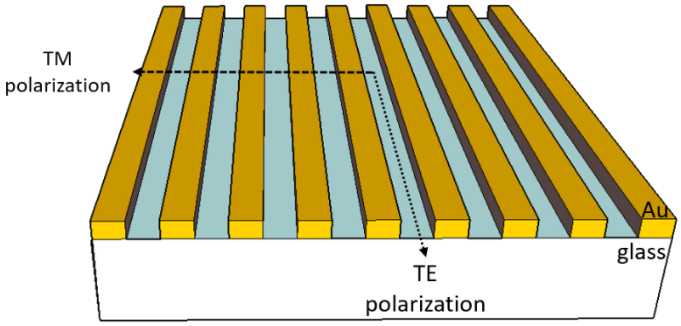

Figure 1.9 TM and TE-polarization directions with respect to the structure of an one-dimensional metallic nanogratings substrate**.**

1.5 Raman scattering

The phenomena of Raman scattering was discovered with very minimal optical setup (i.e. sunlight as excitation source and human eyes as detector) by an Indian scientist called Chandrasekhara Venkata Raman in 1921 [127]. The effect is observed when incident photons are inelastically scattered from molecules. Molecular vibrational energy is exchanged during the photon–molecule interaction. The resulted frequency shift of the scattered photon (relative to the incident light) is specific for different molecules, producing the characteristic molecular vibrational spectra. In addition to that, there are two types of Raman scattering, as shown in Figure 1.10: (a) Stokes scattering, where the energy of scattered photon is lower than the incoming photon; (b) anti-Stokes scattering, where the up-conversion of energy is observed from the scattered photons as a result of the interaction with an already excited vibrational state.

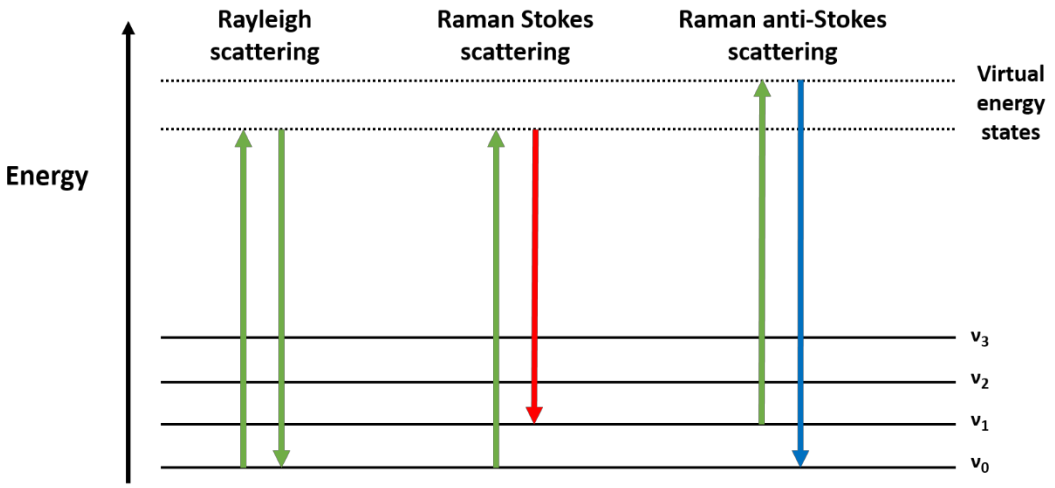

Figure 1.10 Jablonski diagram representing Rayleigh (green down-arrow), Raman Stokes (red down-arrow) and anti-Stokes scatterings (blue down-arrow). The vibrational states in different energy levels are shown by solid black lines with labels v_0 - v_3. The dotted black lines are the virtual excited states of scattering processes with transient life-time.

Even though the Raman effect led to the physics Nobel Prize in 1930 [128], the discovery did not progress into mainstream applications due to the weak nature of the effect. In fact, the Raman phenomenon has a very scarce occurrence, where only approximately one in 10 million molecules experiences Raman scattering when they interact with light. Moreover, the probability of occurrence of anti-Stokes scattering is even lower, because most molecules are at the ground vibrational state at standard conditions (298 K). The development of this vibrational spectroscopic technique accelerated significantly after the invention of the laser in the 1960s [129]. Since then, other innovations, such as notch filters, holographic gratings, high throughput spectrographs, microscope integration, multi-channel charge-coupled (CCD) detectors, have gradually led to the advent of the sophisticated Raman instrument of today [130].

In order to produce the Raman effect, the interaction with light must induce a change in molecular polarizability (which is associated with the induced dipole exhibited by the molecule when interacting with light) with respect to a vibrational coordinate. The magnitude of the induced dipole (i.e. changes of the charge distribution in the molecules)

generated as the electric field polarizes the molecules, can be obtained through Equation 1.11:

$$P = \alpha E \qquad (1.11)$$

where P is the induced dipole of the molecules under the applied electric field, E. α corresponds to the polarizability tensor of the molecules. The relationship between the magnitude of the associated Raman intensities, I_R, and the respective molecular induced dipole moment, P, is given by:

$$I_R = \frac{16\pi^4 f^4}{3c^3} N P^2 = \frac{16\pi^4 f^4}{3c^3} N E^2 |\alpha|^2 \qquad (1.12)$$

$$I_R \propto |\alpha|^2 \qquad (1.13)$$

Where f is the scattered frequency (s^{-1}), c is the speed of light (ms^{-1}) and N is the number density of the scattering molecules (number of the molecules in unit volume). The rest of the notations are the same as Equation 1.11.

One typical way to increase the efficiency of normal (spontaneous or non-resonant) Raman process is by careful selection of the excitation frequency to match with one of the electronic transitions (i.e. increase the contribution of the molecular Raman polarizability tensor). The relationship of the direct square-proportion of the Raman intensity, I_R and the polarizability tensor, α, is given in Equation 1.13. This technique is known as resonance Raman spectroscopy (RRS) [131, 132]. By doing this, the Raman scattering cross-section can be improved up to 10^6 compared to the non-resonant conditions [133].

1.5.1 Surface enhanced Raman scattering (SERS)

Another breakthrough in Raman spectroscopy was the discovery of SERS in the early 1970s [26]. The first ever SERS effect was observed for pyridine absorbed on electrochemically roughened silver electrodes. The phenomenon was initially explained as a ‘surface area effect’, related to the number of fractals on the interface [26]. After more careful experiments and demonstrations, it was concluded that the magnitude of the enhancement could not be explained by considering only the surface area. Two principal theories were

suggested to account for the SERS phenomena: (1) the electromagnetic (EM) [27, 28]; and (2) the charge transfer (CT) or chemical [29] mechanisms.

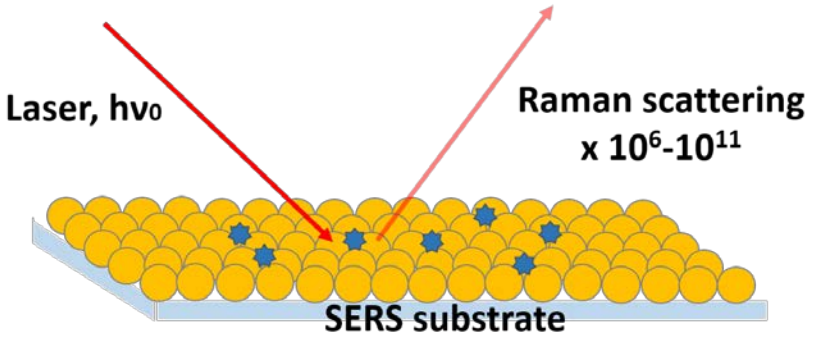

Figure 1.11 Schematic of a SERS substrate (supported gold NPs (yellow spheres) immobilized on glass). The blue particles depict the molecules of interest.

Figure 1.11 illustrates a typical SERS substrate. Surface enhanced Raman scattering is a Raman process that happens for molecules adsorbed on nanostructured metallic interfaces. The SERS effect amplifies Raman signals of the adsorbed molecules by a few orders of magnitude. It is reported that SERS allows up to 10^{11} enhancement factor (calculated as the magnitude of the SERS signal increment with respect to the normal Raman) for Rhodamine 6G [39] adsorbed on silver nanoparticle colloids. Since SERS is a surface-based process, the typical enhancements are accessible by the molecules located within 10 nm from the metal nanostructures (details of the mechanisms will be discussed in section 1.5.1.1 and 1.5.1.2). The greatly improved Raman cross-section observed in SERS (i.e. SERS cross-section of ~ 10^{-16} cm^2 for Rhodamine 6G versus the normal Raman cross-section of ~10^{-27} cm^2) [39, 40], is comparable to the fluorescence technique, with the additional benefit that SERS provides molecular fingerprinting vibrational spectra.

Research activity in the SERS field was vigorous at the first decade since its discovery, then it gradually plateaued until the first report of single-molecule detection using SERS by Kneipp et al. and Nie et al. [39, 41]. The SERS-based single molecule (SM) detection offer information-rich fingerprinting vibrational spectrum and present advantages over SM-detection by fluorescence [134, 135]. The single molecule capabilities of SERS have renewed the interest in the effect and led to accelerated developments in the SERS field.

1.5.1.1 The electromagnetic (EM) mechanism

The SERS EM theory is closely associated with LSPR. In a simplified version, the EM mechanism can be illustrated as the generation of a dipole field around metal nanoparticles (i.e. SERS substrate) when the excitation laser (ω_0) is in resonance with the metal free electrons oscillation (as discussed in Section 1.4.1). The molecules at the vicinity (within a few nanometers range) of the NPs experience a strong localized field confined at the metal-dielectric interface. The field is particular strong at the hot spot region formed in the gap between two nanoparticles, as presented in Figure 1.4. The electromagnetic energy may be lost (ω_0 - ω_{vib}) or gained (ω_0 + ω_{vib}) as the molecules vibrate, similar to a normal Raman scattering (refer to section 1.5). The emission field from the molecular vibrations then re-excites the surface plasmon on the metal nanoparticles, as the energy shift from the molecular vibration (compared to the incident field) is generally small relative to the broad surface plasmon absorption envelop.

The SERS phenomenon can then be thought as the combined contributions of two kinds of scatterings that take place simultaneously - inelastic scattering from the adsorbed molecules and an elastic scattering from the metal nanostructures. The electromagnetic enhancement factor (EF) can; therefore, be approximated using the following expressions:

$$EF \propto \left|E_{(\omega_0)}\right|^2 \left|E_{(\omega_0-\omega_{vib})}\right|^2 \quad (1.14)$$

$$\omega_0 - \omega_{vib} \approx \omega_0 \quad (1.15)$$

$$EF \propto \left|E_{(\omega_0)}\right|^4 \quad (1.16)$$

where $E_{(\omega_0)}$ corresponds to the local field associated with the incident laser and $E_{(\omega_0 - \omega_{vib})}$ is the local field at the scattered field modified by the molecular vibrations.

1.5.1.2 The charge transfer (CT) mechanism

The relationship demonstrated in Equation 1.12 shows that the efficiency of the normal Raman scattering is proportional to the light intensity (E^2 in Equation 1.12). This means that more scattering is obtained when the power of the excitation laser increases (keeping in mind that material decomposition sets the upper limit for the laser power). The EM enhancement mechanism, (discussed in Section 1.5.1.1, increases the local field by $E^4_{(\omega)}$, which can be thought as a power density increase in Equation 1.12. However, Equation 1.12 also emphasizes the dependence of the Raman intensity in the polarizability of the molecules (α). In other words, the efficiency of the Raman scattering is enhanced when the molecular polarizability is promoted. This concept was introduced in our discussion of the RRS in Section 1.5.

In the CT mechanism, the enhancement is believed to arise from new electronic transitions that arises from the interaction between the metal and the molecular orbitals, forming a charge transfer metal–molecule complex. This in turn modifies the molecular polarizability (refer to section 1.5) of the absorbate. When the charge transfer band is resonant to either the incident or the scattered field, the CT enhancement factor contributes to the order of ~$10 – 10^3$ to the overall SERS intensity [136].

Another point worth mentioning here is that the ability of the molecules to form the CT-complex with the metal(s) actually determines the extent or contribution of CT mechanism in SERS. The classical proof of the contribution of the CT effect arises from a comparison between the SERS intensities of CO and N_2 adsorbed on Ag under the same experimental conditions. The SERS signal of CO was observed to be 200 times higher than that from N_2 [137]. Since both molecules have similar polarizability, the larger SERS intensity from CO was proposed as a clear evident of the contribution from the CT mechanism in SERS.

1.5.2 SERS applications in analytical chemistry

The uncovering of the SM detection capability of SERS in the 1990s [39, 41, 138] (also discussed in section 1.5.1) provided an alternative for analytical chemists to perform measurements at ultra-low concentrations of analytes. In recent decades, there were various reports proposing real-world applications of SERS, particularly in the sensing of a variety of chemical species, ranging from environmental contaminants detection [43, 51, 78, 82, 139-144], security monitoring (e.g. food contaminants [145-149], chemical warfare agents [150-152]), forensic detections [153], to medical diagnostics [15, 73, 80, 154-164], and many others. It is known that all the polarizable molecules (i.e. the electron clouds of the species are easily distorted by the electric field) experiences Raman scattering (refer to section 1.5), and; therefore, can be detected by SERS. In the following section, some examples of SERS applications in analytical chemistry are discussed. The focus is on environmental-related applications, as those are closest to the interest of this work. Some examples of food contaminant detection using SERS are also reviewed, as most foodborne contaminants are introduced to the food source through either environmental pollution [53, 146, 149, 165-177] or as the food additives (mostly prohibited) during food processing [82, 148, 178-188].

1.5.2.1 Pesticides

The contamination of food source and environment by pesticides has been a longstanding global issue. Under the class of pesticides, there are herbicides, fungicides, insecticide etc. All these ‘-cide’ suffix-containing substances are designed to kill the entities as in their names. However, besides the initial purpose of killing ‘pests’, the wide applications of pesticides have caused the accumulation of the residues in food products [149, 172, 176] and in the ecosystem [189, 190]. These pesticide residues can be extremely toxic to humans and other living organisms [191].

There have been plenty of reports on the SERS detections of different types of pesticides residues in some real matrices (e.g. fruits and vegetable [149, 172, 174, 176]). A summary of those applications are provided in Table 1.1). As shown in Table 1.1, randomly distributed nanoparticles were the most commonly used SERS substrates for pesticides

detections [53, 146, 149, 165-173, 175-177]. These systems provide impressive LODs (i.e. parts per billion (ppb)-level and below). Some contributions had also reported the on-chip optofluidic detection of pesticides [166, 175]. One of the most interesting optofluidic setups was proposed by Yazdi and White. Their device was a pump-free microsystem with optical fiber cables integrated for sample excitation and signal collections. The optical fiber integrated design was reported to allow automation in sample alignment, as compared to the traditional Raman microscope measurements [175].

Table 1.1 Examples of SERS applications in pesticides detection

Pesticides	**SERS substrate**	**Sample matrix**	**LOD**	
methylparathion thiram chlorpyrifos	Au NPs decorated tape	vegetable and fruit	0.24-3.51 ng/cm^2	[146]
carbaryl phosmet methyl azinphos	Q-SERS™ G1	spiked apples skins	4.51 μg/mL 5.35 μg/mL 6.51 μg/mL	[174]
carbaryl phosmet methyl azinphos		spikes tomatoes skins	2.91 μg/mL 6.66 μg/mL 2.94 μg/mL	
thiabendazole	Ag NPs (portable Raman device)	citrus fruits and bananas		[176]
thiram ferbam ziram	Au nanorods		8.278 ng/mL 10.67 ng/mL 3.957 ng/mL	[171]
Thiram	dogbone shaped Au NPs		2.84 ng/mL	[170]
methamidophos	Ag NPs	vegetables	0.01 μg/mL	[172]
thiram	cube-like Fe_3O_4@SiO_2@Ag nanocomposites		0.24 μg/mL	[177]
thiram	clusters of Ag NPs		0.024 μg/mL	[53]
thiram	Au/Ag coreshell bypiramidal particles		2.0 ng/mL	[173]
methylparathion	mono-6-thio-β-cyclodextrin-decorated one-dimensional Au NPs		0.3 pg/mL	[168]
methyl parathion	optofluidic system with PDMS microfluidic channel (Ag NPs)		0.1 μg/mL	[165]
paraquat	optofluidic oil-phase microdroplet sensor (Ag NPs)		0.5 ng/mL	[192]

methyl parathion malachite green thiram	optofluidic pump-less microsystem (Ag NPs immobilized silica microspheres)	5 μg/mL 0.1 ng/mL 5 ng/mL	[175]
malathion	Ag NPs-immobilized filter membrane	61.5 ng/mL	[183]

1.5.2.2 Pharmaceuticals

The emergence of pharmaceuticals and personal care products (PCPPs) in the environment has become a worldwide issue. Despite of the unclear science (to-date) with respect to the risks of exposure, the monitoring of the identities of PCPPs and their quantities in the environment is still required for the societal well-beings [193].

SERS has been widely used for the detection of pharmaceuticals (or their metabolites or analogues) [14, 62, 74, 194-203]. Some illicit drugs (e.g. amphetamine, mephedrone) were reportedly detected by SERS [204-206]. A summary of examples of SERS applications in pharmaceutical detection is presented in Table 1.2. There were also reports of SERS measurements of pharmaceuticals using portable spectrometer [62, 194], which can be useful for on-site sampling and detection. The reported LODs achieved in SERS pharmaceutical detections were mostly in ppb or sub-ppm levels, presented in Table 1.2.

Table 1.2 Examples of SERS applications in pharmaceutical detection

Pharmaceuticals		**SERS substrate**	**Sample matrix**	**LOD**	
Antibiotics	enrofloxacin furazolidone	Klarites, Q-SERS	fish	800 ng/mL	[195]
	enrofloxacin	Ag NPs immobilized porous materials	chicken muscles	0.01 mg/kg	[199]
	enrofloxacin ciprofloxacin chloramphenic	dendritic Ag nanosubstrates		20 ng/mL 20 ng/mL 20 ng/mL	[194]
	moxifloxacin	Au NPs	artificial urine	0.085 μg/mL	[196]
	levofloxacin	droplet based microfluidic chip (Ag NPs)	human urine	25.3 μg/mL	[14]

Stimulants	nicotine cotinine anabasine	Au NPs	tertiary mixture	0.10 μg/mL 0.20 μg/mL 0.30 μg/mL	[197]
	nicotine cotinine trans-30-hydroxycotinine	Ag NPs	tertiary mixtures	2 ng/mL	[198]
anorexic drugs	sibutramine mono-desmethylsibutramine di-desmethylsibutramine	Ag NPs	tertiary mixtures	1.4 ng/mL 0.1_3 μg/mL 0.251 μg/mL	[202]
Illicit drugs	amphetamine methamphetamine	roughened Ag foil			[204]
	amphetamine methamphetamine 3,4-methylenedioxy-methamphetamine 3,4-methylenedioxyeth-amphetamine	matrix-stabilized Ag halide			[205]
	amphetamines sulfate	Ag NPs and Au NPs		3.7 μg/mL	[206]
	mephedrone	Au NPs (portable Raman device)			[62]

1.5.2.3 Polychlorinated biphenyls (PCBs)

Polychlorinated biphenyls (PCBs) is a group of synthetic organic molecules with 1 to 10 chlorine atoms detained to biphenyl rings. This group of chemicals were heavily used in the past (i.e. in the 1930s to 1970s), mainly for electrical transformers [207, 208]. It was later realized its toxicity and persistency in the ecosystem, where the compounds tend to bio-accumulate in fatty tissues of organisms [191, 209, 210]. Due to their resistance to environmental degradation, these compounds are classified as one of the persistent organic pollutants [211].

As mentioned in section 1.5.1.1, SERS detections rely largely on the close proximity distance between the molecules of interest and the plasmonic metal nanostructures. Approaches to adsorb PCBs molecules to SERS substrates were reported in previous studies [44, 57, 59, 69, 71, 212-217]. To make PCBs anchored to the SERS substrates, many of the reports presented ‘functionalized’ SERS substrates to ‘capture’ the PCBs molecules [44, 57, 59, 69, 71, 214-217], as seen in Table 1.3. These substrates were surface modified with ‘bridging’ molecules (e.g. cyclodextrin [57, 59, 69, 215, 216] and decanethiol [44, 214]).

As shown in Table 1.3, the LODs presented in the examples of SERS-based PCBs detections were varied with the systems. Yang et al. proposed a SERS platform consisting of spin-coated lubricated liquid (i.e. perfluorinated fluids) on porous support (silanized concave glass bowl). The analytes-containing liquid and Au colloid were then introduced to the system and dried. The SERS detections performed on the aggregates were reported to detect up to ~ 75 fM on the spiked soil samples [217].

Table 1.3 Examples of SERS applications in PCBs detection

Polychlorinated biphenyls (PCBs)	**SERS substrate**	**Sample matrix**	**LOD**	
PCB-77 PCB-101 PCB-29	AAO template-assisted Ag nanorod array (functionalized with HS-β-cyclodextrin)		5.8 μg/mL	[215]
PCB-47 PCB-77	decanethiol-modified AgFON substrates	Secondary mixture	0.015 ng/mL	[44]
PCB-77	decanethiol-modified vertically aligned Ag nanoplates		0.3 μg/mL	[214]
PCB-1 PCB-77	Ag nanosheet-assembled micro-hemispheres (functionalized with HS-β-cyclodextrin)	Secondary mixture	0.06 μg/mL	[59]
PCB-15	galvanic reaction prepared-Ag film (functionalized with β-cyclodextrin)			[57]
PCB-77	Ag NPs-decorated cone-shaped ZnO nanorods arrays		2.9 pg/mL	[213]
mixtures of PCBs	Ag nanorods	PCBs contaminated dry soil samples	5 μg/g	[212]
mixtures of PCBs	Au NPs (functionalized with β-cyclodextrin)	PCB contaminated soil		[69]
PCB-77	Microfluidic sensor with AAO templated PDMS (functionalized with HS-PCB-77 aptamer)		2.9 ng/mL	[71]
PCB-7 PCB-77 PCB-209	slippery liquid-infused porous substrate (a film of lubricating fluid locked in place by a micro/nanoporous substrate)	Spiked soil samples	0.016 pg/mL	[217]

1.5.2.4 Polyaromatic Hydrocarbons (PAHs)

Polyaromatic hydrocarbons (PAHs) are mainly generated during incomplete combustion [218]. As PCBs, PAHs also belongs to the class of persistent organic pollutants [211]. Among the hundreds types of PAHs, the Environmental Protection Agency (EPA) has included sixteen of them in a priority pollutant list, due to their carcinogenic nature towards living organisms [219]. PAHs molecules are highly lipophilic and surface functionalization of the substrates is crucial to detect PAHs successfully using SERS [45, 52, 60, 77, 220-227].

As seen in Table 1.4, these substrates were mostly surface-modified with long alkyl chain [45, 60, 77, 228] or some macromolecules [52, 220-225, 227]. The performance of the SERS-based PAHs detections proposed can be found in Table 1.4, where the reported LODs in assessing real world [226] or mimic-real world [229] matrices were in ppm or sub-ppm levels [226, 229].

Table 1.4 Examples of SERS applications in PAHs detection

Polyaromatic hydrocarbons (PAHs)	**SERS substrate**	**Sample matrix**	**LOD**	
benzo[*b*]fluoranthene fluoranthene benzo[*a*]anthracene pyrene	Alkyl chain-functionalized smooth gold film (Au NPs are added upon sample introduction)		3.0 ng/mL 4.0 ng/mL 13 ng/mL 13 ng/mL	[77]
anthracene pyrene	1,10-decanedithiol functionalized bowl-shaped Ag cavity		1.4 ng/mL 8.1 ng/mL	[60]
naphthalene anthracene pyrene benzo[*a*]pyrene benzo[*g,h,i*]perylene indeno[*1,2,3-cd*]pyrene	Au coffee ring on hydrophobic support	river water	0.6 μg/mL 0.2 μg/mL 0.1 μg/mL 0.1 μg/mL 0.07 μg/mL 0.07 μg/mL	[226]
naphthalene pyrene	Au NPs immobilized quartz substrates	artificial seawater	10 ng/mL 10 ng/mL	[229]
pyrene perylene	hexadecyl trimethyl ammonium bromide (CTAB) micelle-assisted reduced graphene oxide– Ag NPs		0.2 μg/mL 0.03 μg/mL	[72]

perylene	$Ag@SiO_2$ NPs (functionalized with β-cyclodextrin dimer)		2.5 ng/mL	[227]
anthracene pyrene triphenylene benzo[c]phenanthrene chrysene coronene	Ag NPs (functionalized with bis-acridinium dication lucigenin)	multi-component mixture	200 ng/mL 20 ng/mL 20 ng/mL 20 ng/mL 20 ng/mL 2 ng/mL	[224]
pyrene benzo[*a*]pyrene	Ag NPs (functionalized with calix[4]arene)		-	[220]
pyrene naphthalene phenanthrene	Ag NPs immobilized substrate (functionalized by C-18)		1 ng/mL 5 ng/mL	[228]
anthracene pyrene	Ag film-deposited nanospheres substrate (functionalized by 1-decanethiol)		0.05 ng/mL 0.1 ng/mL	[45]
fluoranthene fluorene acenaphthene naphthalene	Ag NPs immobilized copper foil (portable Raman spectrometer)		5 μg/mL 10 μg/mL 500 μg/mL 500 μg/mL	[225]
pyrene	Ag NPs (functionalized with dithiocarbamate calix[4]arene)		-	[221]
pyrene benzo[c]phenanthrene	Ag NPs (functionalized with viologen)		2 ng/mL 2 ng/mL	[222]
anthracene pyrene	Ag NPs (functionalized with per-6-deoxy-(6-thio)-β-cyclodextrin)		2 ng/mL 1.5 ng/mL	[223]
anthracene pyrene chrysene triphenylene coronene	Au NPs (functionalized with per-6-deoxy-(6-thio)-β-cyclodextrin)		20 ng/mL 2 ng/mL 20 ng/mL 200 ng/mL -	[52]

1.5.2.5 Food additives

Food and drinks safety is one of the utmost global concerns as unsafe food (including drinks) poses health risks to consumers that might cause illness or even deaths [230, 231]. In the recent decades, there have been multiple outbreaks of foodborne diseases worldwide [232-237]. One well-known example is the Chinese milk scandal in which melamine was found in various dairy products including infant formula [238]. In food industry, melamine is the adulterant added to milk and dairy products to increase the nitrogen content (a measure of protein content) [238]. The over-dosage of melamine in food products, nonetheless, can cause kidney damage [239-241]. It was reported that the contaminated dairy products have caused deaths of thousands babies and pets [238-241]. Another worldwide food safety concern is the presence of prohibited food colorants in some of the processed food. Food colorants are commonly added to food and drinks during the food processing to improve the visual aesthetic to the consumers [242]. Some of these colorants are reported to be carcinogenic to humans, especially in large consumption [243, 244]. These food additives are either prohibited in many countries, or the quantities added are restricted [242].

As an extremely sensitive technique, SERS has been reported to be employed in many of the food contaminants analysis, for instances, the prohibited food additives [82, 148, 178-188], as shown in Table 1.5. Based on Table 1.5, there have been a variety of SERS substrates employed in the applications, including colloidal metal nanoparticles [179], tailored-made nanoparticles [148, 180-182, 185, 188], solid supported metal nanoparticles [82, 183, 187], uniform SERS substrates [186] and so on. Some detections were attempted on real food [179] or drinks [148, 184, 186, 187] matrices, as seen in Table 1.5. The LODs reported were in the range of sub-ppm levels [148, 179, 186, 187].

Table 1.5 Examples of SERS applications in food colorants and melamine detection

Food additives		SERS substrate	Sample matrix	LOD	
Food colorants	Sudan I	Au NPs (portable Raman spectrometer)	spiked chilli powder	48 ng/g	[179]
	Sudan I	Au NPs-decorated Ag(Cl,Br) micro-necklaces		0.02 ng/mL	[82]
	Lemon Yellow Sunset Yellow Orange II chrysoidin Lemon Yellow Sunset Yellow Orange II chrysoidin	Au nanodumbells (portable Raman device)	spiked orange juice spiked coke	50 μg/mL 50 μg/mL 10 μg/mL 10 μg/mL 100 μg/mL 100 μg/mL 10 μg/mL 10 μg/mL	[148]
	Lemon Yellow Sunset Yellow	Ag NPs-decorated filter paper	spiked juices	5 μg/mL 5 μg/mL	[187]
	Sunset Yellow chrysoidine	SiO_2@Au nanoshells	secondary mixture	1 μg/mL 0.5 μg/mL	[185]
	amaranth erythrosine lemon yellow sunset yellow	graphene-Ag nanocomposite	quaternary mixture	6 μg/mL 0.9 μg/mL 5 μg/mL 5 μg/mL	[182]
	Azorubine (E122)	Au film over nanosphere arrays	sweet drinks	0.1 μg/mL	[186]
	Brilliant Green (E142) carmoisine (E-122) amaranth (E-123) Patent Blue V (E-131)	Ag film over nanospheres in microwell plates		500 pg per well -	[178]
	Sunset Yellow malachite Green	Fe_3O_4@SiO_2−Au	tertiary mixture	0.05 μg/mL 0.4 μg/mL	[188]
Food adulterant	melamine	4-mercaptopyridine-modified Au NPs	spiked milk powder	0.1 ng/mL	[181]
	melamine	Ag NPs-immobilized filter membrane		6.3 ng/mL	[183]
	melamine	Ag NPs-coated poly(styrene-co-acrylic acid) nanospheres		0.01 μg/mL	[180]
	melamine	vertically aligned Au nanorods	spiked orange juices	0.1 fg/mL	[184]

1.5.3 Problems of real applications of SERS

It is well known that a major advantage of SERS-based sensing is that it offers not only the required detection sensitivity (i.e. down to single molecule level [39, 41]), but also the benefit of vibrational spectroscopy. Like in normal Raman spectroscopy, SERS spectrum entails the fingerprinting qualitative information about the analytes. Nonetheless, despite of its ultimate potentials, SERS quantitation is still deemed too complicated for real applications. This is principally due to the technique's reproducibility issues in: (1) substrates fabrications and (2) spectral reproducibility during measurements [245-247].

Undeniably, the fabrication of SERS substrates has advanced a lot due to the introduction of new nanofabrication and synthetic tools [118, 119, 248-251]. The substrate fabrication has diversified from the classical metal nanoparticles colloids synthesized by wet chemistry [252, 253] to well defined uniform nanostructures [118, 119, 248-251]. The substrates produced using nanofabrication methods (e.g., focused ion beam (FIB) milling [119, 248, 251], electron beam lithography (EBL) [120, 249], laser interference lithography (LIL) [118], etc.) provide much better control over the geometry of the SERS hot spots; and, thus, improves the plasmonic enhancement reproducibility. It is, however, sometimes a trade-off between the reproducibility and the detection sensitivity (enhancement factors), since the nanoscale randomness on the substrate does support LSPR, which play a significant role in the enhancement mechanism. In addition to that, the low-throughput of the modern nanofabrication methods also complicates the possibility of real-life SERS applications.

The SERS spectral irreproducibility manifests itself particularly at trace level concentrations (e.g., the levels reported in single-molecule SERS observations [245, 246]). Since the SERS effect is highly location-sensitive (hot spots), the technique allows the SM detection out from the massive and complex environment. It is, however, very challenging to fabricate a homogeneous SERS substrate for the reliable quantification of the analytes. The extent of the enhancement is influenced by many factors, including the geometry of the nanostructures, the amount of aggregates/fractals, the locations where the adsorbed molecules are relative to the hot-spots, the surface coverage (surface concentration) and others [254]. In analytical chemistry, a reliable quantification should be designed in such a

way that the signal increment is only associated with the surface concentration. In that sense uniform SERS substrate, with more controlled enhancements, is the best option to help in achieving the ultimate goal of SERS-based quantifications. In the next chapter (Chapter 2), the classical and state-of-the-art fabrications of plasmonic substrates for SERS or other plasmonic applications, are reviewed. The top-down lithographic nanofabrications, which are commonly used in uniform substrate preparations, are the main focus of the review.

On the other hand, another means to improve SERS quantifications is through the utilization of more systematic and representative data analysis, e.g. chemometrics. In the following section, an introduction on chemometric applications in spectroscopic quantification is discussed in the following section.

1.6 Chemometrics applications in spectroscopic analysis

Chemometrics generally implies the use of mathematical and statistical methods to improve the understanding of chemical information [255, 256] . In analytical chemistry, it is commonly applied to correlate the quantities of chemicals or other quantity-related physical properties to analytical instrument data [256]. In most of the spectroscopic analysis (including SERS), chemometrics is useful in helping with multivariate data analysis, where simultaneous processing of multiple variables (e.g. hundreds of wavelengths in each full spectrum) in a number of large datasets is necessary. In other words, with the aid of chemometrics tools, the data analysis is no longer limited to univariate (e.g. select one wavelength and monitor the absorbance change over time), but the entire spectra can be employed [255].

In general, principal component regression (PCR) and partial least square (PLS) are two common chemometrics tools exploited in spectroscopic quantitative analysis [14, 195, 198]. PCR is a regression analysis that utilizes principle component analysis (PCA) in estimating the regression coefficients between spectral responses and concentrations of analytes. In brief, PCA decomposes the spectral sets into principle components (PCs) and scores through an orthogonal transformation. The number of principle components is normally less or equal to the number of original variables, with the ‘meaningfulness’ of each

PC (i.e. amount of the total variance) is given by the scores (scaled factors). Only those important PCs are retained for the further analysis and thus the dimensions of the datasets are reduced. As in the PCR, the factors/scores are regressed against the known concentrations of the components [255, 256]. On the other hand, PLS is an extension of the PCR where it finds a linear regression model by predicting variables with the prior information (i.e. dependent variable) from the datasets. The quality of the regression (calibration) is determined by calculating the errors (i.e. root mean square error in calibration) [255, 256].

To sum up, the advancement in chemometrics tools has greatly facilitated the high-quality data processing from different aspects of spectroscopy. In the context of spectroscopic analysis, the applications of chemometrics allow greater precision in data manipulation (particularly those multivariate datasets), or in resolving those complex data that are difficult to extract useful information manually. The choice of chemometrics techniques to be implemented is greatly associated to the types of samples or datasets (e.g., sample matrices involved, the complexity of the sample systems), the practicality (e.g., the user-friendliness of the methodology, the required operation time), and the most important aspects are the accuracy and precision yielded from the data analysis, which can be assessed through the validation step of any chemometrics methodology.

1.6.1 Multivariate curve resolution (MCR)

In recent years, multivariate curve resolution (MCR) has attracted attention in aiding spectral analysis. The technique utilizes bilinear additive model, which represents in the equation 1.17 [257-259]:

$$X = CS^T + E \qquad (1.17)$$

where X (i, j) is the data matrix from the spectra, C matrix consists of concentration profiles of all the components in the mixture, S^T is the pure spectra of the components and E corresponds to the errors or un-modelled variances from the datasets, as shown in Figure 1.11. With this modelling assumption, MCR is capable to calculate the pure spectra and determine the proportions of each component in the mixture. This is particularly beneficial

in situations where the pure spectra are impossible to obtain (complex matrices like environmental samples), since the prior information about the nature and composition of these mixtures is not required [257-259].

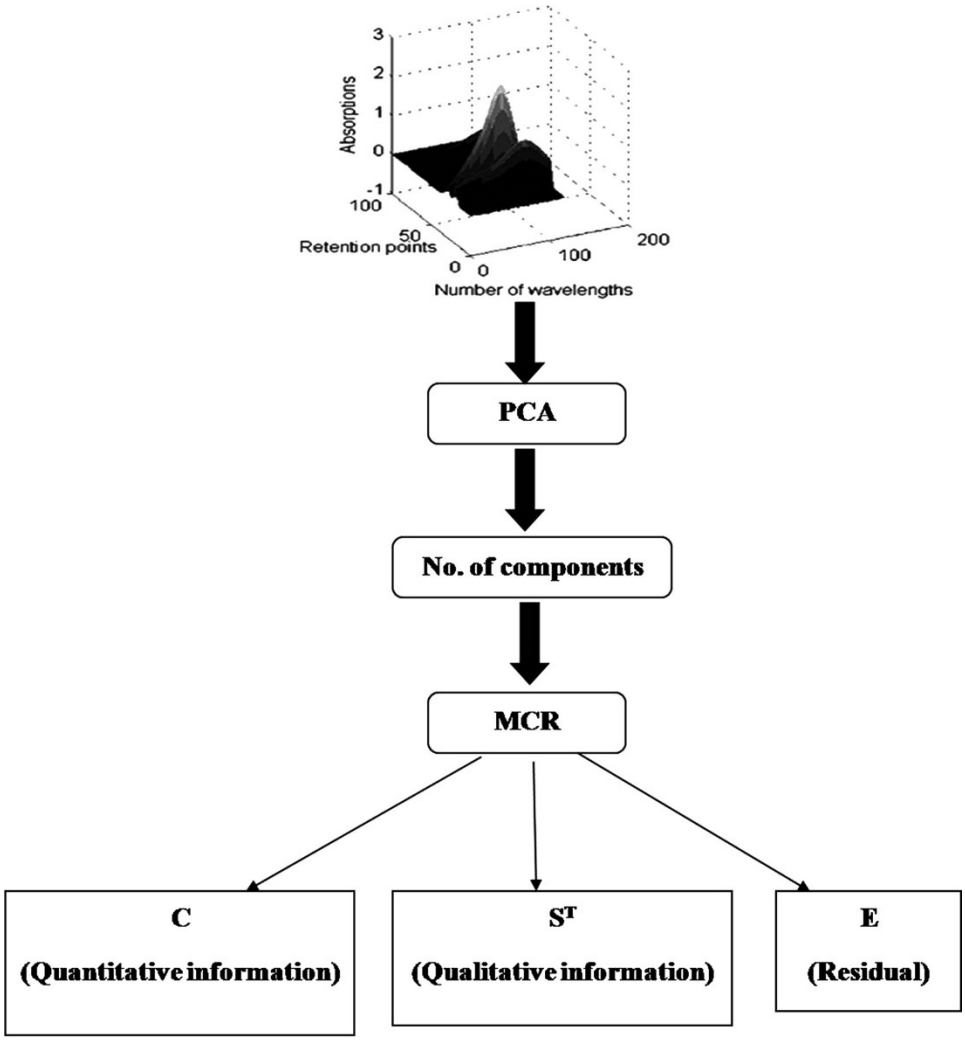

Figure 1.12 Flow chart illustrates the typical process in MCR execution. Reproduced with permission from [256].

In practice, MCR is mostly assisted by PCA at the early stage (refer to Figure 1.12), where PCA analysis provides information about the number of the chemical components contained in the samples (unknown mixtures) [256]. There are various MCR methods. Among them, MCR supported by the alternating least square (ALS) algorithm has been reported to be effective in resolving spectra in different complex matrices (e.g.

pharmaceuticals in environmental [260] and biological matrices [196]). This algorithm was reported to be able to improve the initial estimations of either spectral or concentration profiles of the chemical components under analysis. It is worth mentioning that the ALS algorithm is always optimized with some constraints applied (e.g. non negativity, unimodality, normalization etc.) to prevent uncertainties from different sources [256]. Non-negativity constraint is useful in spectroscopic quantifications, since both concentration and spectral profiles are always positive or zero [256].

The model eventually calculates the concentrations of the samples and the calibration curve (regression set) can then be constructed by plotting the calculated concentration (defined as scores in chapter 5) against the known concentration of the samples [256].

1.7 References

[1] R.P. Feynman, R.B. Leighton, M. Sands, S. Treiman, The Feynman lectures on physics, Physics Today, 17 (1964) 45.
[2] N. Mathur, Nanotechnology: Beyond the silicon roadmap, Nature, 419 (2002) 573-575.
[3] J.L. West, N.J. Halas, Engineered nanomaterials for biophotonics applications: Improving sensing, imaging, and therapeutics, Annual Review of Biomedical Engineering, 5 (2003) 285-292.
[4] S. Logothetidis, Nanotechnology: principles and applications, in: S. Logothetidis (Ed.) Nanostructured materials and their applications, Springer Berlin Heidelberg, Berlin, Heidelberg, 2012, pp. 1-22.
[5] H. Raether, Surface-plasmons on smooth and rough surfaces and on gratings, Springer Tracts in Modern Physics, 111 (1988) 1-133.
[6] Z.Q. Tian, B. Ren, D.Y. Wu, Surface-enhanced Raman scattering: From noble to transition metals and from rough surfaces to ordered nanostructures, Journal of Physical Chemistry B, 106 (2002) 9463-9483.
[7] Z. Jakšić, J. Matovic, Nanomembrane-enabled MEMS sensors: Case of Plasmonic Devices for Chemical and Biological Sensing, 2009.
[8] D.R. Hines, N.P. Siwak, L.A. Mosher, R. Ghodssi, MEMS lithography and micromachining techniques, in: R. Ghodssi, P. Lin (Eds.) MEMS materials and processes handbook, Springer US, Boston, MA, 2011, pp. 667-753.
[9] J. Homola, S.S. Yee, G. Gauglitz, Surface plasmon resonance sensors: review, Sensors and Actuators B: Chemical, 54 (1999) 3-15.
[10] W. Fritzsche, T.A. Taton, Metal nanoparticles as labels for heterogeneous, chip-based DNA detection, Nanotechnology, 14 (2003) R63-R73.
[11] R. Zia, J.A. Schuller, A. Chandran, M.L. Brongersma, Plasmonics: the next chip-scale technology, Materials Today, 9 (2006) 20-27.

[12] S. Lee, J. Choi, L. Chen, B. Park, J.B. Kyong, G.H. Seong, J. Choo, Y. Lee, K.H. Shin, E.K. Lee, S.W. Joo, K.H. Lee, Fast and sensitive trace analysis of malachite green using a surface-enhanced Raman microfluidic sensor, Analytica Chimica Acta, 590 (2007) 139-144.

[13] L.X. Quang, C. Lim, G.H. Seong, J. Choo, K.J. Do, S.K. Yoo, A portable surface-enhanced Raman scattering sensor integrated with a lab-on-a-chip for field analysis, Lab on a Chip, 8 (2008) 2214-2219.

[14] I.J. Hidi, M. Jahn, M.W. Pletz, K. Weber, D. Cialla-May, J. Popp, Toward levofloxacin monitoring in human urine samples by employing the LoC-SERS technique, The Journal of Physical Chemistry C, (2016).

[15] A. Muhlig, T. Bocklitz, I. Labugger, S. Dees, S. Henk, E. Richter, S. Andres, M. Merker, S. Stockel, K. Weber, D. Cialla-May, J. Popp, LOC-SERS: A promising closed system for the identification of mycobacteria, Analytical Chemistry, 88 (2016) 7998-8004.

[16] R. Choudhury, S. Panda, D.V. Singh, Emergence and dissemination of antibiotic resistance: A global problem, Indian Journal of Medical Microbiology, 30 (2012) 384-390.

[17] K.F. Rabe, S. Hurd, A. Anzueto, P.J. Barnes, S.A. Buist, P. Calverley, Y. Fukuchi, C. Jenkins, R. Rodriguez-Roisin, C. van Weel, J. Zielinski, Global strategy for the diagnosis, management, and prevention of chronic obstructive pulmonary disease - GOLD executive summary, American Journal of Respiratory and Critical Care Medicine, 176 (2007) 532-555.

[18] R.H. Ritchie, A.L. Marusak, Surface plasmon dispersion relation for an electron gas, Surface Science, 4 (1966) 234-240.

[19] R.H. Ritchie, E.T. Arakawa, J.J. Cowan, R.N. Hamm, Surface plasmon resonance effect in grating diffraction , Physical Review Letters, 21 (1968) 1530.

[20] A. Otto, Theory of plasmon excitation in thin films by electrons of non-normal incidence, Physica Status Solidi, 22 (1967) 401-406.

[21] E. Kretschmann, H. Raether, Plasma resonance emission in solids, Plasma resonance emission in solids, Zeitschrift Fur Naturforschung Part a-Astrophysik Physik Und Physikalische Chemie A, 23 (1968) 615-617.

[22] R.W. Wood, XXVII. Diffraction gratings with controlled groove form and abnormal distribution of intensity, Philosophical Magazine Series 6, 23 (1912) 310-317.

[23] U. Fano, Some theoretical considerations on anomalous diffraction gratings, Physical Review, 50 (1936) 573-573.

[24] U. Fano, The theory of anomalous diffraction gratings and of quasi-stationary waves on metallic surfaces (Sommerfeld's waves), Journal of the Optical Society of America, 31 (1941) 213-222.

[25] U. Fano, Effects of configuration interaction on intensities and phase shifts, Physical Review, 124 (1961) 1866-1878.

[26] M. Fleischmann, P.J. Hendra, A.J. McQuillan, Raman spectra of pyridine adsorbed at a silver electrode, Chemical Physics Letters, 26 (1974) 163-166.

[27] D.L. Jeanmaire, R.P. Vanduyne, Surface Raman spectroelectrochemistry. 1. Heterocyclic, aromatic, and aliphatic-amines adsorbed on anodized silver electrode, Journal of Electroanalytical Chemistry, 84 (1977) 1-20.

[28] M. Moskovits, Surface roughness and the enhanced intensity of Raman scattering by molecules adsorbed on metals, The Journal of Chemical Physics, 69 (1978) 4159-4161.
[29] M.G. Albrecht, J.F. Evans, J.A. Creighton, The nature of an electrochemically roughened silver surface and its role in promoting anomalous Raman scattering intensity, Surface Science, 75 (1978) L777-L780.
[30] M.E. Lippitsch, Observation of surface enhanced Raman spectra by adsorption to silver colloids, Chemical Physics Letters, 74 (1980) 125-127.
[31] M.E. Lippitsch, Surface enhanced Raman spectra of biliverdine and pyrromethenone adsorbed to silver colloids, Chemical Physics Letters, 79 (1981) 224-226.
[32] C.J. Murphy, T.K. Sau, A. Gole, C.J. Orendorff, Surfactant-directed synthesis and optical properties of one-dimensional plasmonic metallic nanostructures, Mrs Bulletin, 30 (2005) 349-355.
[33] Y.N. Xia, N.J. Halas, Shape-controlled synthesis and surface plasmonic properties of metallic nanostructures, Mrs Bulletin, 30 (2005) 338-344.
[34] C.J. Murphy, A.M. Gole, S.E. Hunyadi, C.J. Orendorff, One-dimensional colloidal gold and silver nanostructures, Inorganic Chemistry, 45 (2006) 7544-7554.
[35] H. Wang, D.W. Brandl, F. Le, P. Nordlander, N.J. Halas, Nanorice: A hybrid plasmonic nanostructure, Nano Letters, 6 (2006) 827-832.
[36] P. Drude, Zur Elektronentheorie der Metalle; II. Teil. Galvanomagnetische und thermomagnetische Effecte, Annalen der Physik, 308 (1900) 369-402.
[37] B. Liedberg, C. Nylander, I. Lunström, Surface plasmon resonance for gas detection and biosensing, Sensors and Actuators, 4 (1983) 299-304.
[38] D.J. Oshannessy, M. Brighamburke, K. Peck, Immobilization chemistries suitable for use in the BIACORE surface plasmon resonance detector, Analytical Biochemistry, 205 (1992) 132-136.
[39] K. Kneipp, Y. Wang, H. Kneipp, L.T. Perelman, I. Itzkan, R.R. Dasari, M.S. Feld, Single molecule detection using surface-enhanced Raman scattering (SERS), Physical Review Letters, 78 (1997) 1667-1670.
[40] K. Kneipp, H. Kneipp, H.G. Bohr, Single-molecule SERS spectroscopy, in: Surface-Enhanced Raman Scattering: Physics and Applications, vol. 103, ed. by K. Kneipp, M. Moskovits, H. Kneipp, Springer-Verlag, Berlin Heidelberg, 2006, pp. 261-277.
[41] S.M. Nie, S.R. Emery, Probing single molecules and single nanoparticles by surface-enhanced Raman scattering, Science, 275 (1997) 1102-1106.
[42] K.R. Ackermann, T. Henkel, J. Popp, Quantitative online detection of low-concentrated drugs via a SERS microfluidic system, Chemphyschem, 8 (2007) 2665-2670.
[43] R.A. Alvarez-Puebla, J.D.S. dos Santos, R.F. Aroca, SERS detection of environmental pollutants in humic acid-gold nanoparticle composite materials, Analyst, 132 (2007) 1210-1214.
[44] K.C. Bantz, C.L. Haynes, Surface-enhanced Raman scattering detection and discrimination of polychlorinated biphenyls, Vibrational Spectroscopy, 50 (2009) 29-35.
[45] C.L. Jones, K.C. Bantz, C.L. Haynes, Partition layer-modified substrates for reversible surface-enhanced Raman scattering detection of polycyclic aromatic hydrocarbons, Analytical and Bioanalytical Chemistry, 394 (2009) 303-311.

[46] A. Marz, K.R. Ackermann, D. Malsch, T. Bocklitz, T. Henkel, J. Popp, Towards a quantitative SERS approach - online monitoring of analytes in a microfluidic system with isotope-edited internal standards, Journal of Biophotonics, 2 (2009) 232-242.
[47] L.M. Tong, M. Righini, M.U. Gonzalez, R. Quidant, M. Kall, Optical aggregation of metal nanoparticles in a microfluidic channel for surface-enhanced Raman scattering analysis, Lab on a Chip, 9 (2009) 193-195.
[48] I.F. Cheng, C.C. Lin, D.Y. Lin, H. Chang, A dielectrophoretic chip with a roughened metal surface for on-chip surface-enhanced Raman scattering analysis of bacteria, Biomicrofluidics, 4 (2010) 034104
[49] S. Abalde-Cela, B. Auguie, M. Fischlechner, W.T.S. Huck, R.A. Alvarez-Puebla, L.M. Liz-Marzan, C. Abell, Microdroplet fabrication of silver-agarose nanocomposite beads for SERS optical accumulation, Soft Matter, 7 (2011) 1321-1325.
[50] M. Lee, S. Lee, J. Lee, H. Lim, G.H. Seong, E.K. Lee, S. Chang, C.H. Oh, J. Choo, Highly reproducible immunoassay of cancer markers on a gold-patterned microarray chip using surface-enhanced Raman scattering imaging, Biosensors and Bioelectronics, 26 (2011) 2135-2141.
[51] W. Ren, Y.X. Fang, E.K. Wang, A binary functional substrate for enrichment and ultrasensitive sers spectroscopic detection of folic acid using graphene oxide/Ag nanoparticle hybrids, ACS Nano, 5 (2011) 6425-6433.
[52] Y. Xie, X. Wang, X. Han, W. Song, W. Ruan, J. Liu, B. Zhao, Y. Ozaki, Selective SERS detection of each polycyclic aromatic hydrocarbon (PAH) in a mixture of five kinds of PAHs, Journal of Raman Spectroscopy, 42 (2011) 945-950.
[53] C. Yuan, R. Liu, S. Wang, G. Han, M.-Y. Han, C. Jiang, Z. Zhang, Single clusters of self-assembled silver nanoparticles for surface-enhanced Raman scattering sensing of a dithiocarbamate fungicide, Journal of Materials Chemistry, 21 (2011) 16264-16270.
[54] C. Farcau, N.M. Sangeetha, N. Decorde, S. Astilean, L. Ressier, Microarrays of gold nanoparticle clusters fabricated by Stop&Go convective self-assembly for SERS-based sensor chips, Nanoscale, 4 (2012) 7870-7877.
[55] I. Kim, I. Junejo, M. Lee, S. Lee, E.K. Lee, S. Chang, J. Choo, SERS-based multiple biomarker detection using a gold-patterned microarray chip, Journal of Molecular Structure, 1023 (2012) 197-203.
[56] M. Lee, K. Lee, K.H. Kim, K.W. Oh, J. Choo, SERS-based immunoassay using a gold array-embedded gradient microfluidic chip, Lab on a Chip, 12 (2012) 3720-3727.
[57] J. Yuan, Y. Lai, J. Duan, Q. Zhao, J. Zhan, Synthesis of a β-cyclodextrin-modified Ag film by the galvanic displacement on copper foil for SERS detection of PCBs, Journal of Colloid and Interface Science, 365 (2012) 122-126.
[58] J. Zhou, K. Ren, Y. Zhao, W. Dai, H. Wu, Convenient formation of nanoparticle aggregates on microfluidic chips for highly sensitive SERS detection of biomolecules, Analytical & Bioanalytical Chemistry, 402 (2012) 1601-1609.
[59] C. Zhu, G. Meng, Q. Huang, Z. Li, Z. Huang, M. Wang, J. Yuan, Large-scale well-separated Ag nanosheet-assembled micro-hemispheres modified with HS-[small beta]-CD as effective SERS substrates for trace detection of PCBs, Journal of Materials Chemistry, 22 (2012) 2271-2278.
[60] X. Gu, S. Tian, Q. Zhou, J. Adkins, Z. Gu, X. Li, J. Zheng, SERS detection of polycyclic aromatic hydrocarbons on a bowl-shaped silver cavity substrate, RSC Advances, 3 (2013) 25989-25996.

[61] Q. Li, B. Li, Y. Wang, Surface-enhanced Raman scattering microfluidic sensor, RSC Advances, 3 (2013) 13015-13026.
[62] S. Mabbott, E. Correa, D.P. Cowcher, J.W. Allwood, R. Goodacre, Optimization of parameters for the quantitative surface-enhanced Raman scattering detection of mephedrone using a fractional design and a portable Raman spectrometer, Analytical Chemistry, 85 (2013) 923-931.
[63] A. Gopalakrishnan, M. Chirumamilla, F. De Angelis, A. Toma, R.P. Zaccaria, R. Krahne, Bimetallic 3D nanostar dimers in ring cavities: recyclable and robust surface-enhanced Raman scattering substrates for signal detection from few molecules, ACS Nano, 8 (2014) 7986-7994.
[64] Y.L. Hu, J. Liao, D.M. Wang, G.K. Li, Fabrication of gold nanoparticle-embedded metal-organic framework for highly sensitive surface-enhanced Raman scattering detection, Analytical Chemistry, 86 (2014) 3955-3963.
[65] H.T. Ngo, H.-N. Wang, A.M. Fales, B.P. Nicholson, C.W. Woods, T. Vo-Dinh, DNA bioassay-on-chip using SERS detection for dengue diagnosis, Analyst, 139 (2014) 5655-5659.
[66] Y. Oh, K. Jeong, Optofluidic SERS chip with plasmonic nanoprobes self-aligned along microfluidic channels, Lab on a Chip, 14 (2014) 865-868.
[67] S. Picciolini, D. Mehn, C. Morasso, R. Vanna, M. Bedoni, P. Pellacani, G. Marchesini, A. Valsesia, D. Prosperi, C. Tresoldi, F. Ciceri, F. Gramatica, Polymer nanopillar–gold arrays as surface-enhanced Raman spectroscopy substrate for the simultaneous detection of multiple genes, ACS Nano, 8 (2014) 10496-10506.
[68] N. Qi, B.W. Li, H.Y. You, W. Zhang, L.W. Fu, Y.Q. Wang, L.X. Chen, Surface-enhanced Raman scattering on a zigzag microfluidic chip: towards high-sensitivity detection of As(III)ions, Analytical Methods, 6 (2014) 4077-4082.
[69] D. Arockia Jency, M. Umadevi, G.V. Sathe, SERS detection of polychlorinated biphenyls using β-cyclodextrin functionalized gold nanoparticles on agriculture land soil, Journal of Raman Spectroscopy, 46 (2015) 377-383.
[70] Y. Deng, M.N. Idso, D.D. Galvan, Q. Yu, Optofluidic microsystem with quasi-3 dimensional gold plasmonic nanostructure arrays for online sensitive and reproducible SERS detection, Analytica Chimica Acta, 863 (2015) 41-48.
[71] C. Fu, Y. Wang, G. Chen, L. Yang, S. Xu, W. Xu, Aptamer-based surface-enhanced Raman scattering-microfluidic sensor for sensitive and selective polychlorinated biphenyls detection, Analytical Chemistry, 87 (2015) 9555-9558.
[72] M. Jiang, Z. Qian, X. Zhou, X. Xin, J. Wu, C. Chen, G. Zhang, G. Xu, Y. Cheng, CTAB micelles assisted rGO-AgNP hybrids for SERS detection of polycyclic aromatic hydrocarbons, Physical Chemistry Chemical Physics, 17 (2015) 21158-21163.
[73] Z.W. Jiang, P.F. Gao, L. Yang, C.Z. Huang, Y.F. Li, Facile in situ synthesis of silver nanoparticles on the surface of metal-organic framework for ultrasensitive surface-enhanced Raman scattering detection of dopamine, Analytical Chemistry, 87 (2015) 12177-12182.
[74] L. Yang, X. Qin, X. Jiang, M. Gong, D. Yin, Y. Zhang, B. Zhao, SERS investigation of ciprofloxacin drug molecules on TiO_2 nanoparticles, Physical Chemistry Chemical Physics, 17 (2015) 17809-17815.

[75] M. Ye, Z. Wei, F. Hu, J. Wang, G. Ge, Z. Hu, M. Shao, S. Lee, J. Liu, Fast assembling microarrays of superparamagnetic Fe_3O_4@Au nanoparticle clusters as reproducible substrates for surface-enhanced Raman scattering, Nanoscale, 7 (2015) 13427-13437.
[76] X.L. Zong, R. Zhu, X.L. Guo, Nanostructured gold microelectrodes for SERS and EIS measurements by incorporating ZnO nanorod growth with electroplating, Scientific Reports, 5 (2015).
[77] H. Gu, K. Hu, D. Li, Y. Long, SERS detection of polycyclic aromatic hydrocarbons using a bare gold nanoparticles coupled film system, Analyst, 141 (2016) 4359-4365.
[78] L. Li, A.W. Zhao, D.P. Wang, H.Y. Guo, H.H. Sun, Q.Y. He, Fabrication of cube-like Fe_3O_4@SiO_2@Ag nanocomposites with high SERS activity and their application in pesticide detection, Journal of Nanoparticle Research, 18 (2016).
[79] Y.Q. Lv, Y.T. Qin, F. Svec, T.W. Tan, Molecularly imprinted plasmonic nanosensor for selective SERS detection of protein biomarkers, Biosensors and Bioelectronics, 80 (2016) 433-441.
[80] Y.M. Ma, H.L. Liu, M. Mao, J. Meng, L.B. Yang, J.H. Liu, Surface-enhanced Raman spectroscopy on liquid interfacial nanoparticle arrays for multiplex detecting drugs in urine, Analytical Chemistry, 88 (2016) 8145-8151.
[81] H.Z. Zhao, Y. Xu, C.Y. Wang, R. Wang, S.T. Xiang, L. Chen, Design and fabrication of a microfluidic SERS chip with integrated Ag film@nanoAu, RSC Advances, 6 (2016) 14105-14111.
[82] Q. Cao, X. Liu, K.P. Yuan, J. Yu, Q.H. Liu, J.J. Delaunay, R.C. Che, Gold nanoparticles decorated Ag(Cl,Br) micro-necklaces for efficient and stable SERS detection and visible-light photocatalytic degradation of Sudan I, Applied Catalysis B-Environmental, 201 (2017) 607-616.
[83] N.M.F. A. Olivieri, J. Ferré, R. Boqué, J.H. Kalivas and H. Mark, Guidelines for calibration in analytical chemistry Part 3. Uncertainty estimation and figures of merit for multivariate calibration, Pure & Applied Chemistry, 78 633-661.
[84] D.R. Thévenot, K. Toth, R.A. Durst, G.S. Wilson, Electrochemical biosensors: recommended definitions and classification1, Biosensors and Bioelectronics, 16 (2001) 121-131.
[85] C.I.L. Justino, T.A. Rocha-Santos, A.C. Duarte, T.A. Rocha-Santos, Review of analytical figures of merit of sensors and biosensors in clinical applications, TrAC Trends in Analytical Chemistry, 29 (2010) 1172-1183.
[86] C. Valsecchi, A.G. Brolo, Periodic metallic nanostructures as plasmonic chemical sensors, Langmuir, 29 (2013) 5638-5649.
[87] J.A. Huang, Y.L. Zhang, H. Ding, H.B. Sun, SERS-Enabled Lab-on-a-Chip Systems, Advanced Optical Materials, 3 (2015) 618-633.
[88] S. Umari, R.S. Moirangthem, Portable and economical plasmonic capillary sensor for biomolecular detection, Sensors and Actuators B-Chemical, 231 (2016) 203-210.
[89] D.M. Zhang, Q.J. Liu, Biosensors and bioelectronics on smartphone for portable biochemical detection, Biosens. Bioelectron., 75 (2016) 273-284.
[90] A.G. Brolo, Plasmonics for future biosensors, Nature Photonics, 6 (2012) 709-713.
[91] D. Cialla, K. Weber, R. Bohme, U. Hubner, H. Schneidewind, M. Zeisberger, R. Mattheis, R. Moller, J. Popp, Towards multiple readout application of plasmonic arrays, Beilstein J. Nanotechnol., 2 (2011) 501-508.

[92] A. Marz, T. Bocklitz, J. Popp, Online-calibration for reliable and robust lab-on-a-chip surface enhanced Raman spectroscopy measurement in a liquid/liquid segmented flow, Analytical Chemistry, 83 (2011) 8337-8340.
[93] I.J. Hidi, A. Muhlig, M. Jahn, F. Liebold, D. Cialla, K. Weber, J. Popp, LOC-SERS: towards point-of-care diagnostic of methotrexate, Analytical Methods, 6 (2014) 3943-3947.
[94] E. Kammer, K. Olschewski, S. Stockel, P. Rosch, K. Weber, D. Cialla-May, T. Bocklitz, J. Popp, Quantitative SERS studies by combining LOC-SERS with the standard addition method, Analytical and Bioanalytical Chemistry, 407 (2015) 8925-8929.
[95] L.S. Jung, C.T. Campbell, T.M. Chinowsky, M.N. Mar, S.S. Yee, Quantitative interpretation of the response of surface plasmon resonance sensors to adsorbed films, Langmuir, 14 (1998) 5636-5648.
[96] T.W. Ebbesen, H.J. Lezec, H.F. Ghaemi, T. Thio, P.A. Wolff, Extraordinary optical transmission through sub-wavelength hole arrays, Nature, 391 (1998) 667-669.
[97] E. Hutter, J.H. Fendler, Exploitation of localized surface plasmon resonance, Advanced Materials, 16 (2004) 1685-1706.
[98] P. Nordlander, C. Oubre, E. Prodan, K. Li, M.I. Stockman, Plasmon hybridizaton in nanoparticle dimers, Nano Letters, 4 (2004) 899-903.
[99] C.E. Talley, J.B. Jackson, C. Oubre, N.K. Grady, C.W. Hollars, S.M. Lane, T.R. Huser, P. Nordlander, N.J. Halas, Surface-enhanced Raman scattering from individual Au nanoparticles and nanoparticle dimer substrates, Nano Letters, 5 (2005) 1569-1574.
[100] M. Futamata, Single molecule sensitivity in SERS: importance of junction of adjacent Ag nanoparticles, Faraday Discussions, 132 (2006) 45-61.
[101] H. Xu, J. Aizpurua, M. Käll, P. Apell, Electromagnetic contributions to single-molecule sensitivity in surface-enhanced Raman scattering, Physical Review E, 62 (2000) 4318-4324.
[102] S. Lal, N.K. Grady, J. Kundu, C.S. Levin, J.B. Lassiter, N.J. Halas, Tailoring plasmonic substrates for surface enhanced spectroscopies, Chemical Society Reviews, 37 (2008) 898-911.
[103] F. Le, D.W. Brandl, Y.A. Urzhumov, H. Wang, J. Kundu, N.J. Halas, J. Aizpurua, P. Nordlander, Metallic nanoparticle arrays: A common substrate for both surface-enhanced Raman scattering and surface-enhanced infrared absorption, Acs Nano, 2 (2008) 707-718.
[104] M.K. Fan, A.G. Brolo, Self-assembled Au nanoparticles as substrates for surface-enhanced vibrational spectroscopy: Optimization and electrochemical stability, Chemphyschem, 9 (2008) 1899-1907.
[105] A.M. Funston, C. Novo, T.J. Davis, P. Mulvaney, Plasmon coupling of gold nanorods at short distances and in different geometries, Nano Letters, 9 (2009) 1651-1658.
[106] H. Wang, D.W. Brandl, P. Nordlander, N.J. Halas, Plasmonic nanostructures: artificial molecules, Accounts of Chemical Research, 40 (2007) 53-62.
[107] B. Liedberg, C. Nylander, I. Lundstrom, Biosensing with surface plasmon resonance - how it all started, Biosensors and Bioelectronics, 10 (1995) R1-R9.
[108] H.T. Baltar, E.M. Goldys, K. Drozdowicz-Tomsia, Propagating surface plasmons and dispersion relations for nanoscale multilayer metallic-dielectric films, INTECH Open Access Publisher, 2012.

[109] W.L. Barnes, A. Dereux, T.W. Ebbesen, Surface plasmon subwavelength optics, Nature, 424 (2003) 824-830.
[110] E.C. Le Ru, P.G. Etchegoin, Chapter 3 - Introduction to plasmons and plasmonics, in: Principles of Surface-Enhanced Raman Spectroscopy, Elsevier, Amsterdam, 2009, pp. 121-183.
[111] L.B. William, Surface plasmon–polariton length scales: a route to sub-wavelength optics, Journal of Optics A: Pure and Applied Optics, 8 (2006) S87.
[112] J.R. Sambles, G.W. Bradbery, F.Z. Yang, Optical-excitation of surface-plasmons - an introduction, Contemporary Physics, 32 (1991) 173-183.
[113] J. Pitarke, V. Silkin, E. Chulkov, P. Echenique, Theory of surface plasmons and surface-plasmon polaritons, Reports on progress in physics, 70 (2006) 1-87.
[114] A.V. Zayats, Smolyaninov, II, A.A. Maradudin, Nano-optics of surface plasmon polaritons, Physics Reports-Review Section of Physics Letters, 408 (2005) 131-314.
[115] R. Gordon, D. Sinton, K.L. Kavanagh, A.G. Brolo, A new generation of sensors based on extraordinary optical transmission, Accounts of Chemical Research, 41 (2008) 1049-1057.
[116] C. Escobedo, A.G. Brolo, R. Gordon, D. Sinton, Flow-through vs flow-over: analysis of transport and binding in nanohole array plasmonic biosensors, Analytical Chemistry, 82 (2010) 10015-10020.
[117] C. Escobedo, F. Eftekhari, J. Ferreira, P. Wood, R. Gordon, A.G. Brolo, D. Sinton, Nanohole arrays as optical and fluidic elements for sensing, ASME Proceedings, Vol 13: Nano-manufacturing Technology, and Micro and Nano systems, Parts A and B (2008), 965-969.
[118] J.W. Menezes, J. Ferreira, M.J.L. Santos, L. Cescato, A.G. Brolo, Large-area fabrication of periodic arrays of nanoholes in metal films and their application in biosensing and plasmonic-enhanced photovoltaics, Advanced Functional Materials, 20 (2010) 3918-3924.
[119] K. Sivashanmugan, J.-D. Liao, J.-W. You, C.-L. Wu, Focused-ion-beam-fabricated Au/Ag multilayered nanorod array as SERS-active substrate for virus strain detection, Sensors and Actuators B: Chemical, 181 (2013) 361-367.
[120] K.L. Lee, C.W. Lee, W.S. Wang, P.K. Wei, Sensitive biosensor array using surface plasmon resonance on metallic nanoslits, Journal of Biomedical Optics, 12 (2007).
[121] Y.L. Ho, M. Abasaki, J.J. Delaunay, Loop-turn optical flows with spectral selectivity in suspended plasmonic nanofin-cavity structure, ACS Photonics, 2 (2015) 730-737.
[122] B. Xiao, S.K. Pradhan, K.C. Santiago, G.N. Rutherford, A.K. Pradhan, Enhanced optical transmission and Fano resonance through a nanostructured metal thin film, Scientific Reports, 5 (2015).
[123] R. Gordon, A.G. Brolo, D. Sinton, K.L. Kavanagh, Resonant optical transmission through hole-arrays in metal films: physics and applications, Laser & Photonics Reviews, 4 (2010) 311-335.
[124] Y.P. Zhao, S.B. Chaney, S. Shanmukh, R.A. Dluhy, Polarized surface enhanced raman and absorbance spectra of aligned silver nanorod arrays, Journal of Physical Chemistry B, 110 (2006) 3153-3157.
[125] K.J. Alvine, B.E. Bernacki, W.D. Bennett, D.J. Edwards, A. Mendoza, J.D. Suter, Optical response of oriented and highly anisotropic subwavelength metallic nanostructure arrays, Applied Physics Letters, 102 (2013) 201115.

[126] C.L. Leverette, S.A. Jacobs, S. Shanmukh, S.B. Chaney, R.A. Dluhy, Y.P. Zhao, Aligned silver nanorod arrays as substrates for surface-enhanced infrared absorption spectroscopy, Applied Spectroscopy, 60 (2006) 906-913.
[127] C. V. Raman, K.S. Krishnan, A new type of secondary radiation, Nature, 121 (1928) 501-502.
[128] R. Singh, F. Riess, Sir C. V. Raman and the story of the Nobel prize, Current Science, 75 (1998) 965-971.
[129] J. Hecht, Short history of laser development, Optical Engineering, 49 (2010).
[130] H. J. Butler, L. Ashton, B. Bird, G. Cinque, K. Curtis, J. Dorney, K. Esmonde-White, N. J. Fullwood, B. Gardner, P.L. Martin-Hirsch, M.J. Walsh, M.R. McAinsh, N. Stone, F. L. Martin, Using Raman spectroscopy to characterize biological materials, Nature Protocols, 11 (2016) 664-687.
[131] W. Holzer, W.F. Murphy, H.J. Bernstein, Resonance Raman effect and resonance fluorescence in halogen gases, The Journal of Chemical Physics, 52 (1970) 399-407.
[132] R.J.H. Clark, T.J. Dines, Resonance Raman spectroscopy, and its application to inorganic chemistry. New Analytical Methods (27), Angewandte Chemie International Edition in English, 25 (1986) 131-158.
[133] M. Schmitt, J. Popp, Raman spectroscopy at the beginning of the twenty-first century, Journal of Raman Spectroscopy, 37 (2006) 20-28.
[134] N. J. Dovichi, J.C. Martin, J.H. Jett, R.A. Keller, Attogram detection limit for aqueous dye samples by laser-induced fluorescence, Science, 219 (1983) 845.
[135] W.P. Ambrose, W.E. Moerner, Fluorescence spectroscopy and spectral diffusion of single impurity molecules in a crystal, Nature, 349 (1991) 225-227.
[136] H. Yamada, H. Nagata, K. Toba, Y. Nakao, Charge-transfer band and SERS mechanism for the pyridine-Ag system, Surface Science, 182 (1987) 269-286.
[137] A. Campion, P. Kambhampati, Surface-enhanced Raman scattering, Chemical Society Reviews, 27 (1998) 241-250.
[138] X.M. Qian, S.M. Nie, Single-molecule and single-nanoparticle SERS: from fundamental mechanisms to biomedical applications, Chemical Society Reviews, 37 (2008) 912-920.
[139] T. Vo-Dinh, SERS chemical sensors and biosensors: new tools for environmental and biological analysis, Sensors and Actuators B: Chemical, 29 (1995) 183-189.
[140] R. A. Halvorson, P. J. Vikesland, Surface-Enhanced Raman Spectroscopy (SERS) for Environmental Analyses, Environmental Science & Technology, 44 (2010) 7749-7755.
[141] Z.L. Huang, G.W. Meng, Q. Huang, B. Chen, C.H. Zhu, Z. Zhang, Large-area Ag nanorod array substrates for SERS: AAO template-assisted fabrication, functionalization, and application in detection PCBs, Journal of Raman Spectroscopy, 44 (2013) 240-246.
[142] D.W. Li, W.L. Zhai, Y.T. Li, Y.T. Long, Recent progress in surface enhanced Raman spectroscopy for the detection of environmental pollutants, Microchimica Acta, 181 (2014) 23-43.
[143] Y. Li, J.S. Church, Raman spectroscopy in the analysis of food and pharmaceutical nanomaterials, Journal of Food and Drug Analysis, 22 (2014) 29-48.
[144] G. Persichetti, R. Bernini, Water monitoring by optofluidic Raman spectroscopy for in situ applications, Talanta, 155 (2016) 145-152.

[145] B. Peng, G.Y. Li, D.H. Li, S. Dodson, Q. Zhang, J. Zhang, Y.H. Lee, H.V. Demir, X.Y. Ling, Q.H. Xiong, Vertically aligned gold nanorod monolayer on arbitrary substrates: self-assembly and femtomolar detection of food contaminants, ACS Nano, 7 (2013) 5993-6000.
[146] J.M. Chen, Y.J. Huang, P. Kannan, L. Zhang, Z.Y. Lin, J.W. Zhang, T. Chen, L.H. Guo, Flexible and adhesive surface enhance Raman scattering active tape for rapid detection of pesticide residues in fruits and vegetables, Analytical Chemistry, 88 (2016) 2149-2155.
[147] N. Duan, B.Y. Chang, H. Zhang, Z.P. Wang, S.J. Wu, Salmonella typhimurium detection using a surface-enhanced Raman scattering-based aptasensor, International Journal of Food Microbiology, 218 (2016) 38-43.
[148] J. Meng, S. Qin, L. Zhang, L.B. Yang, Designing of a novel gold nanodumbbells SERS substrate for detection of prohibited colorants in drinks, Applied Surface Science, 366 (2016) 181-186.
[149] T.X. Yang, Z.Y. Zhang, B. Zhao, R.Y. Hou, A. Kinchla, J.M. Clark, L.L. He, Real-time and in situ monitoring of pesticide penetration in edible leaves by surface-enhanced Raman scattering mapping, Analytical Chemistry, 88 (2016) 5243-5250.
[150] T.Y. Han, C.A. Valdez, T.Y. Olson, S.H. Kim, J.H. Satcher Jr, Rapid detection and identification of energetic materials with surface enhanced raman spectrometry (SERS), Google Patents, 2015.
[151] T. Yang, X. Guo, H. Wang, S. Fu, H. Yang, Magnetically optimized SERS assay for rapid detection of trace drug-related biomarkers in saliva and fingerprints, Biosensors and Bioelectronics, 68 (2015) 350-357.
[152] A. Hakonen, T. Rindzevicius, M.S. Schmidt, P.O. Andersson, L. Juhlin, M. Svedendahl, A. Boisen, M. Käll, Detection of nerve gases using surface-enhanced Raman scattering substrates with high droplet adhesion, Nanoscale, 8 (2016) 1305-1308.
[153] C. Muehlethaler, M. Leona, J.R. Lombardi, Review of surface enhanced Raman scattering applications in forensic science, Analytical Chemistry, 88 (2016) 152-169.
[154] J.P. Xie, Q.B. Zhang, J.Y. Lee, D.I.C. Wang, The synthesis of SERS-active gold nanoflower tags for in vivo applications, ACS Nano, 2 (2008) 2473-2480.
[155] R.A. Alvarez-Puebla, L.M. Liz-Marzán, SERS-based diagnosis and biodetection, Small, 6 (2010) 604-610.
[156] J.M. Yuen, N.C. Shah, J.T. Walsh, M.R. Glucksberg, R.P. Van Duyne, Transcutaneous glucose sensing by surface-enhanced spatially offset Raman spectroscopy in a rat model, Analytical Chemistry, 82 (2010) 8382-8385.
[157] J.B. Song, J.J. Zhou, H.W. Duan, Self-assembled plasmonic vesicles of SERS-encoded amphiphilic gold nanoparticles for cancer cell targeting and traceable intracellular drug delivery, Journal of the American Chemical Society, 134 (2012) 13458-13469.
[158] X.J. Wang, C. Wang, L. Cheng, S.T. Lee, Z. Liu, Noble metal coated single-walled carbon nanotubes for applications in surface enhanced Raman scattering imaging and photothermal therapy, Journal of the American Chemical Society, 134 (2012) 7414-7422.
[159] P. Wu, Y. Gao, H. Zhang, C.X. Cai, Aptamer-guided silver-gold bimetallic nanostructures with highly active surface-enhanced Raman scattering for specific

detection and near-infrared photothermal therapy of human breast cancer cells, Analytical Chemistry, 84 (2012) 7692-7699.

[160] J.S. Sun, Y.L. Xianyu, X.Y. Jiang, Point-of-care biochemical assays using gold nanoparticle-implemented microfluidics, Chemical Society Reviews, 43 (2014) 6239-6253.

[161] C. Andreou, V. Neuschmelting, D.F. Tschaharganeh, C.H. Huang, A. Oseledchyk, P. Iacono, H. Karabeber, R.R. Colen, L. Mannelli, S.W. Lowe, M.F. Kircher, Imaging of liver tumors using surface-enhanced Raman scattering nanoparticles, ACS Nano, 10 (2016) 5015-5026.

[162] Y. Chen, J.Q. Ren, X.G. Zhang, D.Y. Wu, A.G. Shen, J.M. Hu, Alkyne-modulated surface-enhanced Raman scattering-palette for optical interference-free and multiplex cellular imaging, Analytical Chemistry, 88 (2016) 6115-6119.

[163] A.I. Henry, B. Sharma, M.F. Cardinal, D. Kurouski, R.P. Van Duyne, Surface-enhanced Raman spectroscopy biosensing: in vivo diagnostics and multimodal imaging, Analytical Chemistry, 88 (2016) 6638-6647.

[164] N.B. Yi, C. Zhang, Q.H. Song, S.M. Xiao, A hybrid system with highly enhanced graphene SERS for rapid and tag-free tumor cells detection, Scientific Reports, 6 (2016).

[165] D. Lee, S. Lee, G.H. Seong, J. Choo, E.K. Lee, D. Gweon, S. Lee, Quantitative analysis of methyl parathion pesticides in a polydimethylsiloxane microfluidic channel using confocal surface-enhanced Raman spectroscopy, Applied Spectroscopy, 60 (2006) 373-377.

[166] R. Gao, N. Choi, S. Chang, S.H. Kang, J.M. Song, S.I. Cho, D.W. Lim, J. Choo, Highly sensitive trace analysis of paraquat using a surface-enhanced Raman scattering microdroplet sensor, Analytica Chimica Acta, 681 (2010) 87-91.

[167] J. Vongsvivut, E.G. Robertson, D. McNaughton, Surface-enhanced Raman spectroscopic analysis of fonofos pesticide adsorbed on silver and gold nanoparticles, Journal of Raman Spectroscopy, 41 (2010) 1137-1148.

[168] J. Wang, L. Kong, Z. Guo, J. Xu, J. Liu, Synthesis of novel decorated one-dimensional gold nanoparticle and its application in ultrasensitive detection of insecticide, Journal of Materials Chemistry, 20 (2010) 5271-5279.

[169] L. Guerrini, S. Sanchez-Cortes, V.L. Cruz, S. Martinez, S. Ristori, A. Feis, Surface-enhanced Raman spectra of dimethoate and omethoate, Journal of Raman Spectroscopy, 42 (2011) 980-985.

[170] B. Saute, R. Narayanan, Solution-based direct readout surface enhanced Raman spectroscopic (SERS) detection of ultra-low levels of thiram with dogbone shaped gold nanoparticles, Analyst, 136 (2011) 527-532.

[171] B. Saute, R. Premasiri, L. Ziegler, R. Narayanan, Gold nanorods as surface enhanced Raman spectroscopy substrates for sensitive and selective detection of ultra-low levels of dithiocarbamate pesticides, Analyst, 137 (2012) 5082-5087.

[172] Y. Xie, G. Mukamurezi, Y. Sun, H. Wang, H. Qian, W. Yao, Establishment of rapid detection method of methamidophos in vegetables by surface enhanced Raman spectroscopy, European Food Research and Technology, 234 (2012) 1091-1098.

[173] X. Zheng, Y. Chen, Y. Chen, N. Bi, H. Qi, M. Qin, D. Song, H. Zhang, Y. Tian, High performance Au/Ag core/shell bipyramids for determination of thiram based on surface-enhanced Raman scattering, Journal of Raman Spectroscopy, 43 (2012) 1374-1380.

[174] B. Liu, P. Zhou, X. Liu, X. Sun, H. Li, M. Lin, Detection of pesticides in fruits by surface-enhanced Raman spectroscopy coupled with gold nanostructures, Food and Bioprocess Technology, 6 (2013) 710-718.
[175] S.H. Yazdi, I.M. White, Multiplexed detection of aquaculture fungicides using a pump-free optofluidic SERS microsystem, Analyst, 138 (2013) 100-103.
[176] C. Müller, L. David, V. Chiş, S.C. Pînzaru, Detection of thiabendazole applied on citrus fruits and bananas using surface enhanced Raman scattering, Food Chemistry, 145 (2014) 814-820.
[177] L. Li, A. Zhao, D. Wang, H. Guo, H. Sun, Q. He, Fabrication of cube-like Fe_3O_4@SiO_2@Ag nanocomposites with high SERS activity and their application in pesticide detection, Journal of Nanoparticle Research, 18 (2016) 178.
[178] J. Stropp, G. Trachta, G. Brehm, S. Schneider, A new version of AgFON substrates for high-throughput analytical SERS applications, Journal of Raman Spectroscopy, 34 (2003) 26-32.
[179] W. Cheung, I.T. Shadi, Y. Xu, R. Goodacre, Quantitative analysis of the banned food dye Sudan-1 using surface enhanced Raman scattering with multivariate chemometrics, The Journal of Physical Chemistry C, 114 (2010) 7285-7290.
[180] J. Li, W. Ma, C. Wei, L. You, J. Guo, J. Hu, C. Wang, Detecting trace melamine in solution by SERS using Ag nanoparticle coated poly(styrene-co-acrylic acid) nanospheres as novel active substrates, Langmuir, 27 (2011) 14539-14544.
[181] T. Lou, Y. Wang, J. Li, H. Peng, H. Xiong, L. Chen, Rapid detection of melamine with 4-mercaptopyridine-modified gold nanoparticles by surface-enhanced Raman scattering, Analytical and Bioanalytical Chemistry, 401 (2011) 333-338.
[182] Y. Xie, Y. Li, L. Niu, H. Wang, H. Qian, W. Yao, A novel surface-enhanced Raman scattering sensor to detect prohibited colorants in food by graphene/silver nanocomposite, Talanta, 100 (2012) 32-37.
[183] W.W. Yu, I.M. White, A simple filter-based approach to surface enhanced Raman spectroscopy for trace chemical detection, The Analyst, 137 (2012) 1168-1173.
[184] B. Peng, G. Li, D. Li, S. Dodson, Q. Zhang, J. Zhang, Y.H. Lee, H.V. Demir, X. Yi Ling, Q. Xiong, Vertically aligned gold nanorod monolayer on arbitrary substrates: self-assembly and femtomolar detection of food contaminants, ACS Nano, 7 (2013) 5993-6000.
[185] Y. Xie, T. Chen, Y. Cheng, H. Wang, H. Qian, W. Yao, SiO_2@Au nanoshells-based SERS method for detection of sunset yellow and chrysoidine, Spectrochimica Acta Part A: Molecular and Biomolecular Spectroscopy, 132 (2014) 355-360.
[186] V. Peksa, M. Jahn, L. Štolcová, V. Schulz, J. Proška, M. Procházka, K. Weber, D. Cialla-May, J. Popp, Quantitative SERS analysis of azorubine (E 122) in sweet drinks, Analytical Chemistry, 87 (2015) 2840-2844.
[187] Y. Zhu, L. Zhang, L. Yang, Designing of the functional paper-based surface-enhanced Raman spectroscopy substrates for colorants detection, Materials Research Bulletin, 63 (2015) 199-204.
[188] Z. Sun, J. Du, L. Yan, S. Chen, Z. Yang, C. Jing, Multifunctional Fe_3O_4@SiO_2–Au satellite structured SERS probe for charge selective detection of food dyes, ACS Applied Materials & Interfaces, 8 (2016) 3056-3062.
[189] K.R. Solomon, D.B. Baker, R.P. Richards, D.R. Dixon, S.J. Klaine, T.W. LaPoint, R.J. Kendall, C.P. Weisskopf, J.M. Giddings, J.P. Giesy, L.W. Hall, W.M. Williams,

Ecological risk assessment of atrazine in North American surface waters, Environmental Toxicology and Chemistry, 15 (1996) 31-74.
[190] D.W. Kolpin, E.T. Furlong, M.T. Meyer, E.M. Thurman, S.D. Zaugg, L.B. Barber, H.T. Buxton, Pharmaceuticals, hormones, and other organic wastewater contaminants in US streams, 1999-2000: A national reconnaissance, Environmental Science & Technology, 36 (2002) 1202-1211.
[191] M.S. Wolff, P.G. Toniolo, E.W. Lee, M. Rivera, N. Dubin, Blood-levels of organochlorine residues and risk of breast-cancer, Journal of the National Cancer Institute, 85 (1993) 648-652.
[192] R. Gao, N. Choi, S.I. Chang, S.H. Kang, J.M. Song, S.I. Cho, D.W. Lim, J. Choo, Highly sensitive trace analysis of paraquat using a surface-enhanced Raman scattering microdroplet sensor, Analytica Chimica Acta, 681 (2010) 87-91.
[193] C.G. Daughton, T.A. Ternes, Pharmaceuticals and personal care products in the environment: agents of subtle change?, Environmental Health Perspectives, 107 (1999) 907-938.
[194] L. He, M. Lin, H. Li, N. Kim, Surface-enhanced Raman spectroscopy coupled with dendritic silver nanosubstrate for detection of restricted antibiotics, Journal of Raman Spectroscopy, 41 (2010) 739-744.
[195] Y. Zhang, Y. Huang, F. Zhai, R. Du, Y. Liu, K. Lai, Analyses of enrofloxacin, furazolidone and malachite green in fish products with surface-enhanced Raman spectroscopy, Food Chemistry, 135 (2012) 845-850.
[196] M. Mamián-López, R. Poppi, Quantification of moxifloxacin in urine using surface-enhanced Raman spectroscopy (SERS) and multivariate curve resolution on a nanostructured gold surface, Analytical & Bioanalytical Chemistry, 405 (2013) 7671-7677.
[197] M.B. Mamián-López, R.J. Poppi, Standard addition method applied to the urinary quantification of nicotine in the presence of cotinine and anabasine using surface enhanced Raman spectroscopy and multivariate curve resolution, Analytica Chimica Acta, 760 (2013) 53-59.
[198] O. Alharbi, Y. Xu, R. Goodacre, Simultaneous multiplexed quantification of nicotine and its metabolites using surface enhanced Raman scattering, Analyst, 139 (2014) 4820-4827.
[199] Y. Xu, Y. Du, Q. Li, X. Wang, Y. Pan, H. Zhang, T. Wu, H. Hu, Ultrasensitive Detection of enrofloxacin in chicken muscles by surface-enhanced Raman spectroscopy using amino-modified glycidyl methacrylate-ethylene dimethacrylate (GMA-EDMA) powdered porous material, Food Analytical Methods, 7 (2014) 1219-1228.
[200] S.L. Clauson, J.M. Sylvia, T.A. Arcury, P. Summers, K.M. Spencer, Detection of pesticides and metabolites using surface-enhanced raman spectroscopy (sers): acephate, Applied Spectroscopy, 69 (2015) 785-793.
[201] S. Liu, J. Huang, Z. Chen, N. Chen, F. Pang, T. Wang, L. Hu, Raman spectroscopy measurement of levofloxacin lactate in blood using an optical fiber nano-probe, Journal of Raman Spectroscopy, 46 (2015) 197-201.
[202] H. Mao, M. Qi, Y. Zhou, X. Huang, L. Zhang, Y. Jin, Y. Peng, S. Du, Discrimination of sibutramine and its analogues based on surface-enhanced Raman spectroscopy and chemometrics: toward the rapid detection of synthetic anorexic drugs in natural slimming products, RSC Advances, 5 (2015) 5886-5894.

[203] C.Y. Liu, Y.Y. Han, P.H. Shih, W.N. Lian, H.H. Wang, C.H. Lin, P.R. Hsueh, J.K. Wang, Y.L. Wang, Rapid bacterial antibiotic susceptibility test based on simple surface-enhanced Raman spectroscopic biomarkers, Scientific Reports, 6 (2016).
[204] R.A. Sulk, R.C. Corcoran, K.T. Carron, Surface-enhanced Raman scattering detection of amphetamine and methamphetamine by modification with 2-mercaptonicotinic acid, Applied Spectroscopy, 53 (1999) 954-959.
[205] B. Sagmuller, B. Schwarze, G. Brehm, S. Schneider, Application of SERS spectroscopy to the identification of (3,4-methylenedioxy)amphetamine in forensic samples utilizing matrix stabilized silver halides, Analyst, 126 (2001) 2066-2071.
[206] K. Faulds, W.E. Smith, D. Graham, R.J. Lacey, Assessment of silver and gold substrates for the detection of amphetamine sulfate by surface enhanced Raman scattering (SERS), Analyst, 127 (2002) 282-286.
[207] P.O. Darnerud, G.S. Eriksen, T. Johannesson, P.B. Larsen, M. Viluksela, Polybrominated diphenyl ethers: Occurrence, dietary exposure, and toxicology, Environmental Health Perspectives, 109 (2001) 49-68.
[208] C.A. de Wit, An overview of brominated flame retardants in the environment, Chemosphere, 46 (2002) 583-624.
[209] F. Falck, A. Ricci, M.S. Wolff, J. Godbold, P. Deckers, Pesticides and polychlorinated biphenyl residues in human breast lipids and their relation to breast-cancer, Archives of Environmental Health, 47 (1992) 143-146.
[210] R.A. Hites, Polybrominated diphenyl ethers in the environment and in people: A meta-analysis of concentrations, Environmental Science & Technology, 38 (2004) 945-956.
[211] K.C. Jones, P. De Voogt, Persistent organic pollutants (POPs): state of the science, Environmental pollution, 100 (1999) 209-221.
[212] Q. Zhou, X. Zhang, Y. Huang, Z. Li, Z. Zhang, Rapid detection of polychlorinated biphenyls at trace levels in real environmental samples by surface-enhanced Raman scattering, Sensors, 11 (2011) 10851.
[213] H. Tang, G. Meng, Q. Huang, Z. Zhang, Z. Huang, C. Zhu, Arrays of cone-shaped ZnO nanorods decorated with Ag nanoparticles as 3D surface-enhanced Raman scattering substrates for rapid detection of trace polychlorinated biphenyls, Advanced Functional Materials, 22 (2012) 218-224.
[214] C. Zhu, G. Meng, Q. Huang, Z. Huang, Vertically aligned Ag nanoplate-assembled film as a sensitive and reproducible SERS substrate for the detection of PCB-77, Journal of Hazardous Materials, 211–212 (2012) 389-395.
[215] Z. Huang, G. Meng, Q. Huang, B. Chen, C. Zhu, Z. Zhang, Large-area Ag nanorod array substrates for SERS: AAO template-assisted fabrication, functionalization, and application in detection PCBs, Journal of Raman Spectroscopy, 44 (2013) 240-246.
[216] K. Sun, Q. Huang, G. Meng, Y. Lu, Highly sensitive and selective surface-enhanced Raman spectroscopy label-free detection of 3,3′,4,4′-tetrachlorobiphenyl using DNA aptamer-modified Ag-nanorod arrays, ACS Applied Materials & Interfaces, 8 (2016) 5723-5728.
[217] S. Yang, X. Dai, B. B. Stogin, T. Wong, Ultrasensitive surface-enhanced Raman scattering detection in common fluids, Proceedings of the National Academy of Sciences, 113 (2016) 268-273.

[218] N.R. Khalili, P.A. Scheff, T.M. Holsen, PAH Source fingerprints for coke ovens, diesel and gasoline-engines, highway tunnels, and wood combustion emissions, Atmospheric Environment, 29 (1995) 533-542.
[219] I.C. Nisbet, P.K. LaGoy, Toxic equivalency factors (TEFs) for polycyclic aromatic hydrocarbons (PAHs), Regulatory toxicology and pharmacology, 16 (1992) 290-300.
[220] P. Leyton, S. Sanchez-Cortes, J.V. Garcia-Ramos, C. Domingo, M. Campos-Vallette, C. Saitz, R.E. Clavijo, Selective molecular recognition of polycyclic aromatic hydrocarbons (PAHs) on calix[4]arene-functionalized Ag nanoparticles by surface-enhanced Raman scattering, The Journal of Physical Chemistry B, 108 (2004) 17484-17490.
[221] L. Guerrini, J.V. Garcia-Ramos, C. Domingo, S. Sanchez-Cortes, functionalization of Ag nanoparticles with dithiocarbamate calix[4]arene as an effective supramolecular host for the surface-enhanced Raman scattering detection of polycyclic aromatic hydrocarbons, Langmuir, 22 (2006) 10924-10926.
[222] L. Guerrini, J.V. Garcia-Ramos, C. Domingo, S. Sanchez-Cortes, Nanosensors based on viologen functionalized silver nanoparticles: few molecules surface-enhanced Raman spectroscopy detection of polycyclic aromatic hydrocarbons in interparticle hot spots, Analytical Chemistry, 81 (2009) 1418-1425.
[223] Y. Xie, X. Wang, X. Han, X. Xue, W. Ji, Z. Qi, J. Liu, B. Zhao, Y. Ozaki, Sensing of polycyclic aromatic hydrocarbons with cyclodextrin inclusion complexes on silver nanoparticles by surface-enhanced Raman scattering, Analyst, 135 (2010) 1389-1394.
[224] I. López-Tocón, J.C. Otero, J.F. Arenas, J.V. Garcia-Ramos, S. Sanchez-Cortes, Multicomponent direct detection of polycyclic aromatic hydrocarbons by surface-enhanced Raman spectroscopy using silver nanoparticles functionalized with the viologen host lucigenin, Analytical Chemistry, 83 (2011) 2518-2525.
[225] X. Jiang, Y. Lai, M. Yang, H. Yang, W. Jiang, J. Zhan, Silver nanoparticle aggregates on copper foil for reliable quantitative SERS analysis of polycyclic aromatic hydrocarbons with a portable Raman spectrometer, Analyst, 137 (2012) 3995-4000.
[226] J. Xu, J. Du, C. Jing, Y. Zhang, J. Cui, Facile Detection of Polycyclic aromatic hydrocarbons by a surface-enhanced Raman scattering sensor based on the Au coffee ring effect, ACS Applied Materials & Interfaces, 6 (2014) 6891-6897.
[227] E. Hahm, D. Jeong, M.G. Cha, J.M. Choi, X. Pham, H. Kim, H. Kim, Y. Lee, D.H. Jeong, S. Jung, B. Jun, β-CD dimer-immobilized Ag assembly embedded silica nanoparticles for sensitive detection of polycyclic aromatic hydrocarbons, Scientific Reports, 6 (2016) 26082.
[228] L.G. Olson, R.H. Uibel, J.M. Harris, C18-modified metal-colloid substrates for surface-enhanced Raman detection of trace-level polycyclic aromatic hydrocarbons in aqueous solution, Applied Spectroscopy, 58 (2004) 1394-1400.
[229] O. Péron, E. Rinnert, M. Lehaitre, P. Crassous, C. Compère, Detection of polycyclic aromatic hydrocarbon (PAH) compounds in artificial sea-water using surface-enhanced Raman scattering (SERS), Talanta, 79 (2009) 199-204.
[230] P.S. Mead, L. Slutsker, V. Dietz, L.F. McCaig, J.S. Bresee, C. Shapiro, P.M. Griffin, R.V. Tauxe, Food-related illness and death in the United States, Emerging infectious diseases, 5 (1999) 607.

[231] S.P. Oliver, B.M. Jayarao, R.A. Almeida, Foodborne pathogens in milk and the dairy farm environment: food safety and public health implications, Foodbourne Pathogens & Disease, 2 (2005) 115-129.
[232] E. Scallan, R.M. Hoekstra, F.J. Angulo, R.V. Tauxe, M.A. Widdowson, S.L. Roy, J.L. Jones, P.M. Griffin, Foodborne Illness Acquired in the United States-major pathogens, Emerging Infectious Diseases, 17 (2011) 7-15.
[233] M.M.M. Guerra, A.M. de Almeida, A.L. Willingham, An overview of food safety and bacterial foodborne zoonoses in food production animals in the Caribbean region, Tropical Animal Health and Production, 48 (2016) 1095-1108.
[234] R.R. Harvey, C.M. Zakhour, L.H. Gould, Foodborne disease outbreaks associated with organic foods in the United States, Journal of Food Protection, 79 (2016) 1953-1958.
[235] B.T. Lunestad, A. Maage, I.S. Roiha, M. Myrmel, C.S. Svanevik, A. Duinker, An outbreak of norovirus infection from shellfish soup due to unforeseen insufficient heating during preparation, Food and Environmental Virology, 8 (2016) 231-234.
[236] C.R.M. Moffatt, A. Greig, M. Valcanis, W. Gao, T. Seemann, B.P. Howden, M.D. Kirk, A large outbreak of Campylobacter jejuni infection in a university college caused by chicken liver pate Australia, 2013, Epidemiology and Infection, 144 (2016) 2971-2978.
[237] A. White, A. Cronquist, E.J. Bedrick, E. Scallan, Food Source prediction of shiga toxin-producing escherichia coli outbreaks using demographic and outbreak characteristics, United States, 1998-2014, Foodborne Pathogens and Disease, 13 (2016) 527-534.
[238] K. Everstine, J. Spink, S. Kennedy, Economically motivated adulteration (EMA) of food: Common characteristics of EMA incidents, Journal of Food Protection, 76 (2013) 723-735.
[239] C.A. Brown, K.S. Jeong, R.H. Poppenga, B. Puschner, D.M. Miller, A.E. Ellis, K.I. Kang, S. Sum, A.M. Cistola, S.A. Brown, Outbreaks of renal failure associated with melamine and cyanuric acid in dogs and cats in 2004 and 2007, Journal of Veterinary Diagnostic Investigation, 19 (2007) 525-531.
[240] R.L.M. Dobson, S. Motlagh, M. Quijano, R.T. Cambron, T.R. Baker, A.M. Pullen, B.T. Regg, A.S. Bigalow-Kern, T. Vennard, A. Fix, R. Reimschuessel, G. Overmann, Y. Shan, G. P. Daston, Identification and characterization of toxicity of contaminants in pet food leading to an outbreak of renal toxicity in cats and dogs, Toxicological Sciences, 106 (2008) 251-262.
[241] A.K.C. Hau, T. H. Kwan, P.K.T. Li, Melamine toxicity and the kidney, Journal of the American Society of Nephrology, 20 (2009) 245-250.
[242] N. Martins, C. L. Roriz, P. Morales, L. Barros, I. Ferreira, Food colorants: Challenges, opportunities and current desires of agro-industries to ensure consumer expectations and regulatory practices, Trends in Food Science & Technology, 52 (2016) 1-15.
[243] M.L.T. Polonio, F. Peres, Food additive intake and health effects: public health challenges in Brazil, Cadernos De Saude Publica, 25 (2009) 1653-1666.
[244] P. Amchova, H. Kotolova, J. Ruda-Kucerova, Health safety issues of synthetic food colorants, Regulatory Toxicology and Pharmacology, 73 (2015) 914-922.
[245] N.P.W. Pieczonka, R.F. Aroca, Single molecule analysis by surfaced-enhanced Raman scattering, Chemical Society Reviews, 37 (2008) 946-954.

[246] A. Otto, What is observed in single molecule SERS, and why?, Journal of Raman Spectroscopy, 33 (2002) 593-598.
[247] S. R. Emory, R. A. Jensen, T. Wenda, M. Han, S. Nie, Re-examining the origins of spectral blinking in single-molecule and single-nanoparticle SERS, Faraday Discussions, 132 (2006) 249-259.
[248] Y. Lin, J. Liao, Y. Ju, C. Chang, A. Shiau, Focused ion beam-fabricated Au micro/nanostructures used as a surface enhanced Raman scattering-active substrate for trace detection of molecules and influenza virus, Nanotechnology, 22 (2011) 185308.
[249] N. A. Abu Hatab, J. M. Oran, M. J. Sepaniak, Surface-enhanced Raman spectroscopy substrates created via electron beam lithography and nanotransfer printing, ACS Nano, 2 (2008) 377-385.
[250] A. Dhawan, M. Gerhold, A. Madison, J. Fowlkes, P.E. Russell, T. Vo-Dinh, D.N. Leonard, Fabrication of nanodot plasmonic waveguide structures using FIB milling and electron beam-induced deposition, Scanning, 31 (2009) 139-146.
[251] J. R. Anema, A. G. Brolo, P. Marthandam, R. Gordon, Enhanced Raman scattering from nanoholes in a copper film, Journal of Physical Chemistry C, 112 (2008) 17051-17055.
[252] R. G. Freeman, K. C. Grabar, K. J. Allison, R. M. Bright, Self-assembled metal colloid monolayers: An approach to SERS substrates, Science, 267 (1995) 1629.
[253] D. Philip, G. Aruldhas, SERS Spectra of 2-Aminophenol in Silver Colloids, Journal of Solid State Chemistry, 116 (1995) 427-431.
[254] J.A. Dieringer, A.D. McFarland, N.C. Shah, D.A. Stuart, A.V. Whitney, C.R. Yonzon, M.A. Young, X.Y. Zhang, R.P. Van Duyne, Surface enhanced Raman spectroscopy: new materials, concepts, characterization tools, and applications, Faraday Discussions, 132 (2006) 9-26.
[255]P. Geladi, Chemometrics in spectroscopy. Part 1. Classical chemometrics, Spectrochimica Acta Part B: Atomic Spectroscopy, 58 (2003) 767-782.
[256] N. Kumar, A. Bansal, G.S. Sarma, R.K. Rawal, Chemometrics tools used in analytical chemistry: An overview, Talanta, 123 (2014) 186-199.
[257] T. Azzouz, R. Tauler, Application of multivariate curve resolution alternating least squares (MCR-ALS) to the quantitative analysis of pharmaceutical and agricultural samples, Talanta, 74 (2008) 1201-1210.
[258] A. de Juan, J. Jaumot, R. Tauler, Multivariate curve resolution (MCR). Solving the mixture analysis problem, Analytical Methods, 6 (2014) 4964-4976.
[259] J.R. Schoonover, R. Marx, S.L. Zhang, Multivariate curve resolution in the analysis of vibrational spectroscopy data files, Applied Spectroscopy, 57 (2003) 154A-170A.
[260] H. Parastar, H. Shaye, Comparative study of partial least squares and multivariate curve resolution for simultaneous spectrophotometric determination of pharmaceuticals in environmental samples, RSC Advances, 5 (2015) 70017-70024.

Chapter 2

State-of-the-Art on the Fabrication of Plasmonic Nanostructures

As discussed in Chapter 1 (Section 1.7), uniform plasmonic substrates are required to realize reliable SERS or other surface plasmon resonance-based detection schemes (and quantification methods). In this chapter, the state-of-the-art fabrication of plasmonic nanostructures are reviewed. These encompass classical wet chemistry preparation, modern nanofabrication methods, as well as the hybrid strategies for mass fabrication. The goal is to provide the reader with an overview of the nanofabrication as a context for our own work that will be presented in Chapters 3 to 5.

2.1 Classical nanofabrication

2.1.1 Solution-based synthesis

Solution-based (wet chemistry) synthesis has been the most widely used approach to prepare metal nanostructures that support plasmonic interactions. The colloidal-based syntheses can be tuned to tailor-make different nanoparticles geometries, ranging from the common nanospheres [1] to nano-dendritric [2, 3], nanorods [4-7], hollow nanostructures [8-10], nanowires [11], nanorices [12], nanoplates [13] and others. The different types of plasmonic nanoparticles generated by wet chemistry are depicted in Figure 2.1.

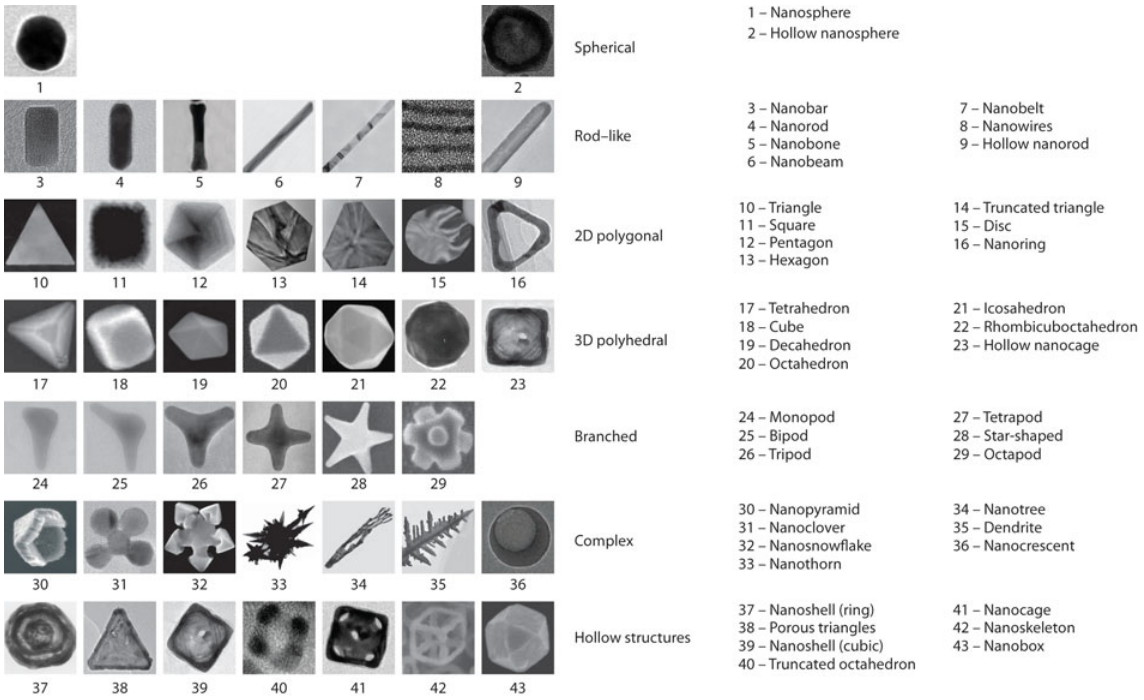

Figure 2.1 Summary of plasmonic nanoparticles fabricated by wet chemistry. Reproduced with permission from [14].

2.1.1.1 Nanospheres

The most common geometry for the metal nanoparticles is nanospheres (refer to Figure 2.1 under the ‘spherical’ category). The earliest colloidal synthesis of metal nanospheres starts with a soluble metal salt (e.g. silver nitrate and gold chloride) and reducing agents. Their mixture leads to the production of metal nanoparticles [15, 16].

As in Section 1.4.1, the localized field in the nanometer-sized gaps between the nanoparticles in the aggregates (oligomers can be thought as ‘controlled’ aggregates) is enhanced, as compared to those single nanoparticles [17, 18]. The localized field enhancement between a dimer of gold nanospheres is well-illustrated in the simulation reported by Talley et al., as presented in Figure 2.2. There are many reports on the preparation of oligomers metal nanoparticles (e.g. dimers [19, 20], trimers [20], other chained structures [21, 22]) as potential SERS substrates. These oligomers are made through surface chemistry modifications (e.g. DNA linkage [19]), and laser welding [23] to nano-join the nanoparticles.

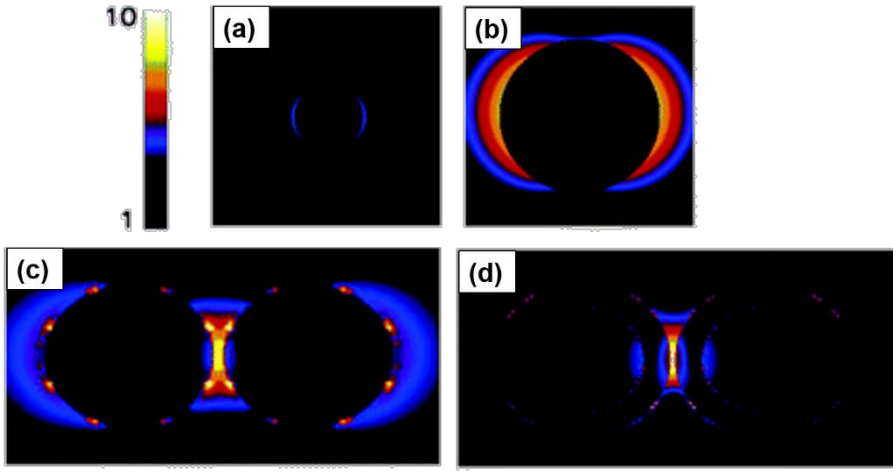

Figure 2.2 The simulated near-field enhancement at an excitation laser of 633 nm for (a) an isolated Au nanosphere, (b) an isolated Au nanoshell. The field localization for a dimer of Au nanospheres in shown in (c), and for Au nanoshells in (d) The inter-particles axis was parallel to the incident polarization. The color scale represents the electric field enhancement $,|E|$ (dimensionless, normalized to the amplitude of the incident field). Reproduced with permission from [18].

2.1.1.2 Tipped nanoparticles

In the case of tipped structures, classified in Figure 2.1 as 2D polygonal, 3D polyhedral and branched, such as, nanotriangles [24-26], nanocubes [27-29], nanotriisohedral [24, 29], and nanostars [29], the syntheses are radically different in terms of reaction times, and the choices of reducing and protecting agents to control the nucleation and growing rate of the nanoparticles [4, 30-32]. One popular methodology is polymer-mediated polyol process, in which Ag nanostructures in well-defined shapes were successfully synthesized. Briefly, the process employed different ratios of poly(vinylpyrrolidone) (PVP) (as reducing and capping agents) and $AgNO_3$ to modify the level of surface coverage of PVP on Ag seeds. This in turn led to the directional growth of the seeds into nanostructures in specific shapes (e.g. nanocubes, nanotriangles) [32]. The sharp edges are particularly good for field localization, since they behave as nanoscale antennas [29].

2.1.1.3 Alloys

Beyond the nanoparticles that consist of a single metallic element, both nano-alloys (e.g. Ag-Au [33-36], Au-Cu [35], Cu-Ag [35]) and core-shell structures (e.g. silica core with Au or Ag shells [37-41]) have also been reported. These clusters are useful to improve the surface plasmon (LSPR more specifically) tunability through the variation of optical properties from different metallic components (by either varying the types of metals or their compositions) [42-49]. Since these 'nanometric-mixures of metals' demonstrate hybrid optical properties, the LSPR band of nano-alloys (e.g., Ag-Au alloys) is broader as compared to pure metals. This can be useful for many plasmonic applications, for instances, better coupling of surface plasmon and laser excitation line in SERS optimization [42] or promoting light absorption in plasmonic-enhanced solar cells [43].

2.1.1.4 Two-dimensional planar substrates from nanoparticles

In addition, three-dimensional metal nanoparticles assemblies can also be immobilized onto solid supports (e.g. glass slides [50-53], rubber membrane [54, 55], optical fiber tips [56], plastic strip [57], PDMS [58], cured epoxy [59]), using different surface chemistry modification (e.g. sol-gel self-assembly). This eventually leads to planar plasmonic substrates that are more stable and convenient to certain applications. There are also reports on metallic nanoparticle assemblies supported by electrostatic interactions on other organic or inorganic frameworks (e.g. ZnO [60, 61], MoS_2 [62], graphite [63]), as plasmonic substrates. Our group has reported a number of methodologies in fabrication of solid-supported SERS substrates [51-53, 56]. Figure 2.3 demonstrated one of the methodologies based on surface chemistry modifications [52]. Firstly, a piranha acid-cleaned Au slide was surface modified with monolayer of linker molecules, 1,3-propanedithiol (PDT) (step 1 in Figure 2.3). Since PDT consists of two thiol groups, ideally, one thiol group is bound to gold slide and the other is free for subsequent step (i.e. linking with Au NPs). As many Au NPs attracted to the free thiol groups on the Au slide, as seen in step 2 of Figure 2.3, they eventually formed a film containing nanometric roughness (i.e. hot-spots). The process was repeated (step 3 in Figure 2.3) to increase the roughness (aggregation) as to optimize the SERS responses [52].

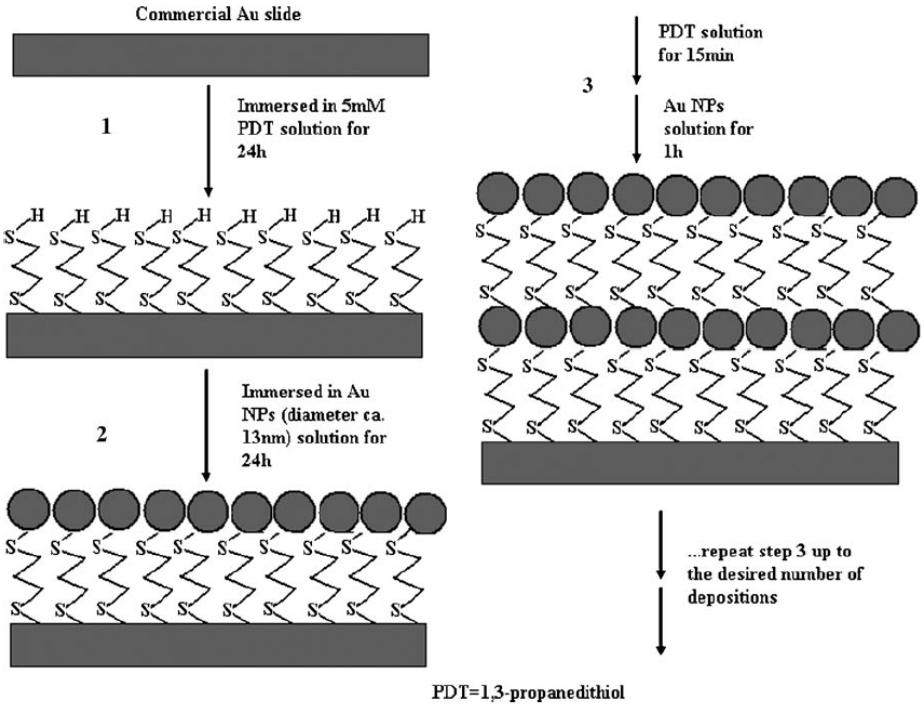

Figure 2.3 Schematic of the sol-gel immobilization of Au nanoparticles on the solid support. Reproduced with permission from [52].

2.1.2 Anisotopic chemical etching

Etching, which is a normal intermediate step in nanofabrication, is useful to remove surplus materials. There are two types of etching: dry etching (using plasma or reactive ions) and wet etching (using etchant solutions that are capable of dissolving the materials). Both types of etching are isotropic (i.e. the degree of etching is equal on the entire substrate interface). Conversely, the etching process can be tuned to be directional and anisotropic. One way to do this is to employ highly crystalline materials (e.g. Si). In the case of Si, the existence of different bond density in each of the crystal packings (111), (110), (100)) affects the etching rate of the interface contacting the etchant solution (e.g. KOH solution, HF solution). Since the crystal-packing in (111) plane presents the greatest bond density, its etching rate is considerably slower, when compared to the other packing structures. This provides the selective anisotropy during the etching that subsequently contributes to the formation of patterned nanostructures (e.g. nanowires) [64].

Lo et al. fabricated silicon tips (i.e. silicon nanowires) from single-crystalline silicon wafers using plasma etching [i.e. electron cyclotron resonance microwave plasma enhanced chemical vapor deposition (ECR-MWPECVD)]. The Au film deposited on these Si nanotips was then surface-modified in order to immobilize single strand DNAs. Subsequent AgNPs were added to the system to improve the SERS measurement sensitivity of DNAs [65]. The SEM images of the gold nanotips fabricated through the chemical etching of Si can be seen in Figure 2.4.

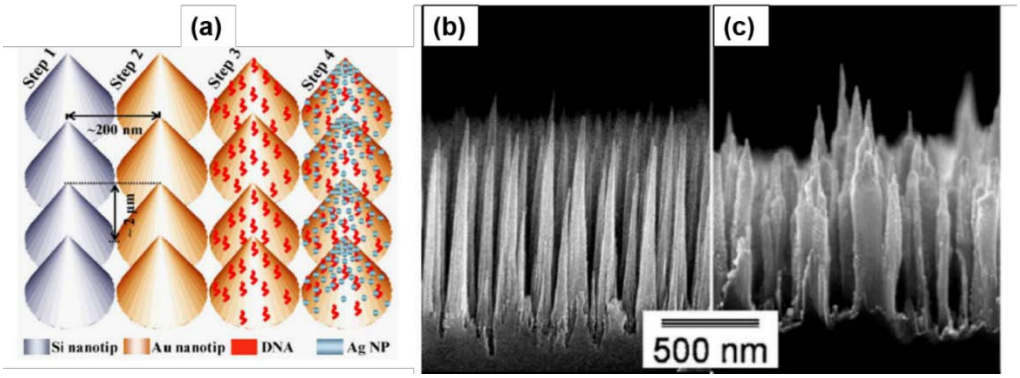

Figure 2.4 (a) The SERS detection scheme of DNA using Au nanotips fabricated through etching process. The SEM images of the fabricated Au nanotips, **(b)** before and **(c)** after the immobilization of Ag NPs. Reproduced with permission from [65].

2.1.3 Electrochemical roughening

The approach used in the SERS discovery in the 1970s [66], electrochemical roughening (or texturing), is still one of the most widely used technique to perform SERS measurements. There are reported studies showing the optimization of the SERS responses by modifying the roughening morphology of the electrodes. The degree of roughening on the electrodes can be controlled through the alteration of electrochemical pre-treatment conditions [67-69], including the concentration of the electrolyte solutions [69]. Figure 2.5 shows the SEM images of the electrochemical roughened Ag substrates reported by Yang et al. [69].

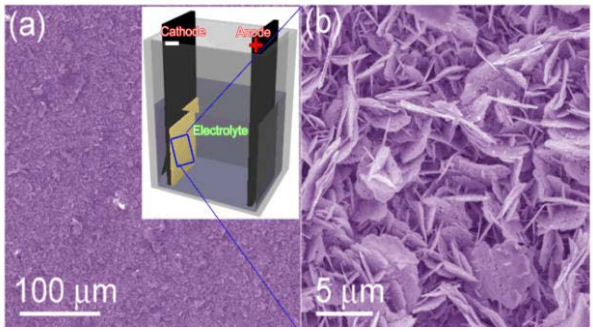

Figure 2.5 SEM images shows the highly roughened Ag substrate in different magnifications. The H_3BO_3 in the electrolyte played a role in controlling the level of electrochemical roughening. Reproduced with permission from [69].

Additionally, there are reports demonstrating the *in-situ* production of nanostructures with specific geometries (e.g. nanospheres, nanostars) by electrochemistry. These nanostructures were reported as effective SERS platforms [70-72]. Park et al. reported a galvanic replacement-based fabrication of the gold hollow nanostructures (named as three-dimensional nanoporous gold), as depicted in Figure 2.6. The substrates fabricated were reported to effectively detect the SERS from Rhodamine 6G at the concentration as low as 10^{-8} M.

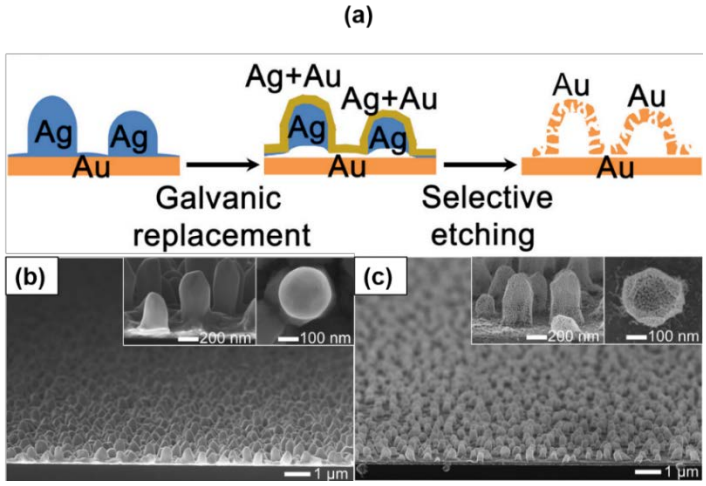

Figure 2.6 (a) Schematic illustrating the galvanic replacement-based fabrication of the three-dimensional gold nanoporous structures. SEM images of **(b)** three-dimensional Ag nanoislands fabricated through the electrochemical replacement reaction and **(c)** the hollow gold nanoporous structures after selective etching of Ag. Reproduced with permission from [71] (copyright information: Creative Common Attribution 4.0 International).

2.2 Nanolithography

2.2.1 Focused ion beam (FIB)

Focused ion beam (FIB) milling is a top-down fabrication technique that involves bombarding a smooth surface with gallium (Ga) ion. The controlled impacts of the Ga ions mill away the top surface atoms, allowing nanostructures of desired geometries (e.g. nanoholes [73-76], nanopillars [77-79], nano-gratings [80, 81], nanostars [82], nano-bowties [83, 84], double-hole with concentric rings [85]) to be fabricated. The resolution of FIB fabrication depends on the probe size of the Ga ion, but it routinely achieves levels below 10 nm [86].

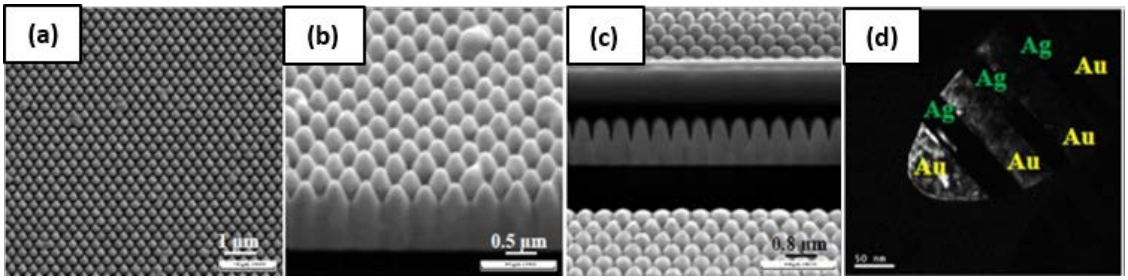

Figure 2.7 (a-c) SEM images of FIB-fabricated nanorod arrays on Au/Ag hybrid film. **(d)** Backscattering electron image of the respective samples with Au/Ag multilayered nanorods. Reproduced with permission from [79].

Generally, FIB-milling of plasmonic nanostructures are carried out on smooth metallic films (e.g. gold [78, 87, 88], copper [73], silver [82], hybrid metallic layers with alternating Ag and Au film, as seen in Figure 2.7 [79]) supported on planar solid substrates. The milled substrates consist mostly of periodic arrays of metal nanostructures supported on glass. There are also reports of FIB milling on the facets of optical fiber tips for SERS remote sensing [89, 90]. The nanostructures demonstrated in Figure 2.7 with the embedded Ag (or Au) layers in the structures was developed by Sivashanmugan et al. The authors correlated the improved SERS enhancements from the hybrid Ag/Au nanorod substrates to the induced LSPR resonance by the thin sandwiched Ag or Au film within each nanorod array. FIB-fabricated nanoholes arrays combined with materials of unique optical properties (e.g. quantum dots [91], liquid crystals [87]) have been reported. A typical FIB-milled nanoholes array can be viewed in Figure 2.8(a). As in Equation 1.9 (refer to Chapter 1,

Section 1.4.2.2), the position of the SPR band is closely related to the periodicity of the nanogratings. This explains Figure 2.8(b) where EOT spectra were red-shifted as the periodicity of nanoholes increased.

Various plasmonic sensing applications have been reported, including the use of hybrid Ag-Au nanogaps arrays (refer to Figure 2.7) in SERS influenza virus detection [79], on-chip SPR sensing of cancer biomarkers using Au nanoholes arrays [92], and others. There have also been studies on SPR detection optimization using different microfluidic flow modes (e.g. flow-through [93, 94] and flow-over [94] modes).

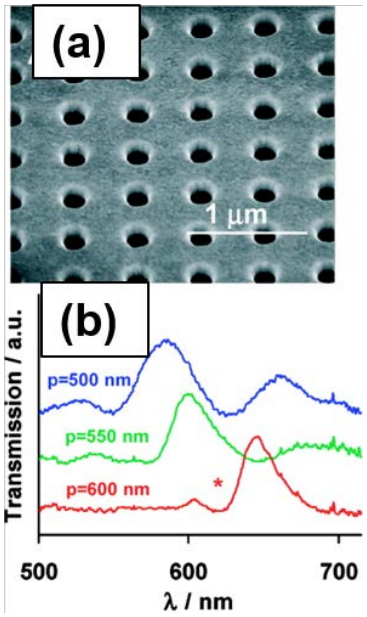

Figure 2.8 (a) A typical FIB-milled nanoholes arrays. **(b)** EOT spectra show wavelength shifts as the periodicity of the nanoholes varies. The transmission minimum marked with asterisks corresponds to the Wood's diffraction anomaly. Reproduced with permission from [74].

FIB has been a versatile fabrication technique to produce metallic nanostructures that are useful in supporting both SERS and SPR. Nonetheless, the main hindrances behind the mass production of substrates using this technique are related to high fabrication cost and long fabrication time. Moreover, FIB fabrication restricts the pattern area to the micron-

scale. For those reasons, FIB is more suitable for proof-of-concept studies and for structures that require high precision in the fabrication parameters.

2.2.2 Electron beam lithography (EBL)

EBL is another state-of-the-art nanofabrication tool available to precisely fabricate nanostructures. This technique utilizes the interaction between the electron beam and an "electron beam resist" polymer for nanostructuring patterning. Electron beam resists can be categorized into positive resists (i.e. electron-exposed area of the resist is removed after the development step) and negative resists (i.e. electron-exposed area of the resist stays after the development step). Figure 2.9 shows a vast variety of different plasmonic nanostructures designs that have been fabricated through EBL, including three-dimensional metallic structures (e.g. gold cubical nano-posts and pits [95, 96],), nano-vortex lens (spiral structures) with sharp tip apex [97], nanogaps with less than 10 nm [98], nano-rhombic arrays [99], and nano-rings/split rings [100].

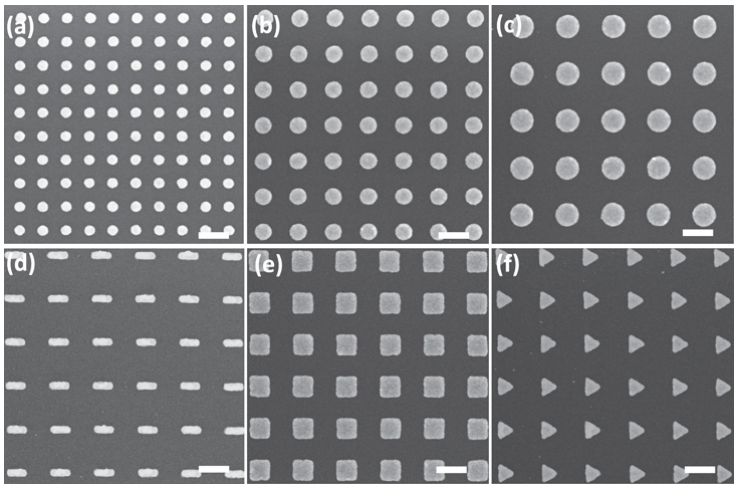

Figure 2.9 SEM images for the nanostructures fabricated through EBL using the PMMA-based dry lift-off, (a - c) gold nanodisks with different periodicities, (d) gold nanorods, (e) gold nanosquares and (f) nanotriangles. All the scale bars show 200 nm. Reproduced with permission from [101].

Gopalakrishnan et al. developed few-molecules sensitive SERS substrates (enhancement factor of 10^{10} for Rhodamine and adenine molecules) using EBL technique. The authors fabricated arrays containing bimetallic nanostar dimer in ring cavities [102], as

presented in Figure 2.10. The three-dimensional SERS substrates were reported to be recyclable, up to five cycles, without degrading the SERS performance.

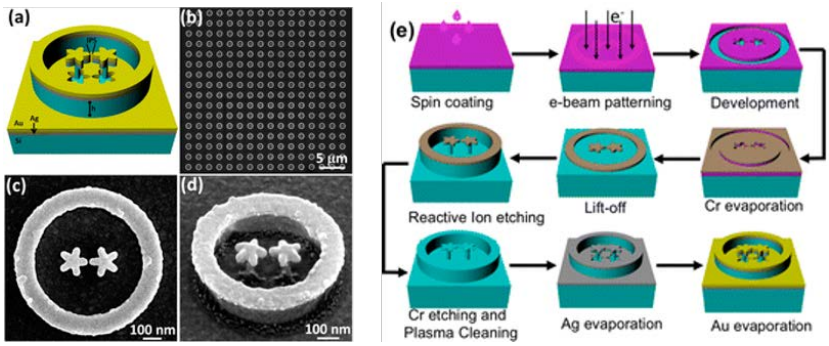

Figure 2.10 (a) Schematic and **(b-d)** SEM images for Ag-Au bimetallic three-dimensional nanostar dimers fabricated through EBL. **(e)** Schemes illustrates the steps during the fabrication. Reproduced with permission from [102].

As in FIB milling, EBL-fabricated nanostructures are frequently employed in proof of concept plasmonic evaluations. The technique faces similar throughput limitations as the FIB method. To deal with those constraints, a lot of research has then been geared towards indirect fabrication strategies, for instance, using EBL to produce reusable nanostructured-templates (e.g. stencil-mask [103, 104]) and molds [105-109]). These strategies, including template-stripping and nanoimprinting, transfer the nanostructure patterns from the EBL templates to the target substrates [106-110]. The transferred nanostructures are normally a plasmonic metal feature.

EBL has gained popularity as a nanofabrication tool. EBL can be combined to other microfabrication techniques, like reactive-ion etching and lift-off, to produce variety of nanostructures that are required as platforms for plasmon-enhanced chemical sensing.

2.3 Large area lithography

2.3.1 Laser interference lithography (LIL)

Laser interference lithography (LIL) technique is a rapid, large-area and maskless fabrication method. It utilizes the constructive optical interference between two coherent laser beams to produce a periodic nanostructured pattern in a photoresist [111, 112]. Since this technique relies on the interaction between the photons and the photoresist, the wavelength of the operating laser must be within the optimum absorption region of the photoresist polymer [112]. LIL also has high geometry manipulation capabilities and allow the fabrication of different nanostructures (e.g. nanogratings [113-115], nanopillars [116-118] and nano-rhombus/diamonds [119]).

One of the instrumentations employed in LIL is the Lloyd's mirror interferometer [(refer to Figure 2.11(a)] [116, 120]. Figure 2.11(a) depicts a LIL instrumentation based on a single laser beam setup (diverging beam from pinhole of spatial filter). From Figure 2.11(a), we can see that the substrate (photoresist substrate) is exposed to two part of the laser beam (from the same coherent source), with one of the parts reaches directly from laser source. As the interferometer has a mirror integrated perpendicular (i.e. 90^o) to the substrate, the second part of the beam is from the mirror's reflection, and is constructively interfered with the first part of the beam. This results in the formation of periodic fringes on the substrate, and the periodicity of the structures, p can be estimated from equation 2.1 [116, 120] :

$$p = \frac{\lambda}{2 \sin\theta} \qquad (2.1)$$

where λ is the wavelength of laser and refer Figure 2.11 (a) for θ (both θ's are the same), as indicated in Figure 2.11(a). Figure 2.11(b, c) shows a typical LIL-fabricated photoresist substrates consisting of nanopillars structure. In that case, the substrate was exposed twice to the laser under Lloyd's interferometers, with the second exposure at a position 90^o away from the first one [116].

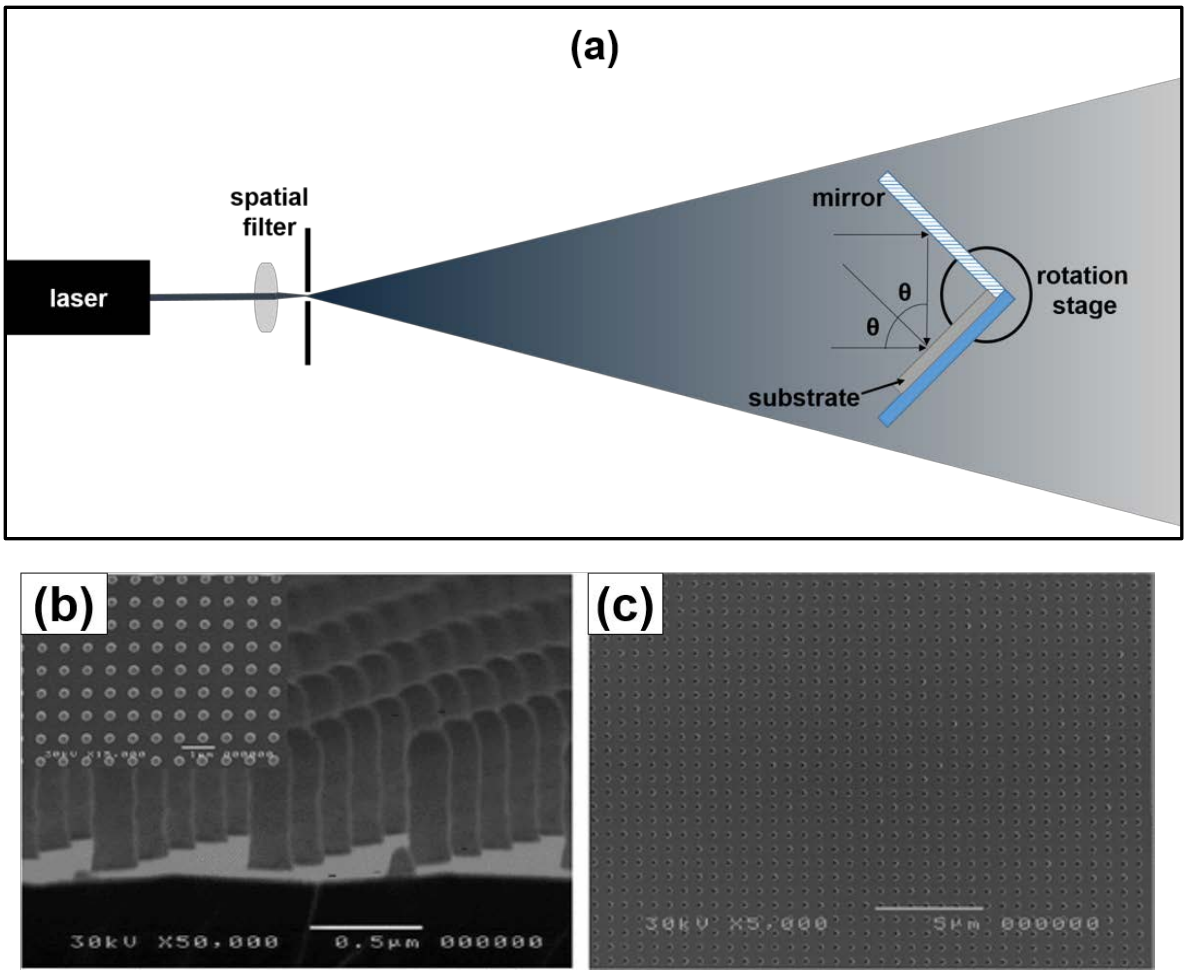

Figure 2.11 (a) Schematic of LIL using Lloyd's mirror interferometer setup. **(b, c)** The photoresist nanopillars template fabricated through LIL. Reproduced with permission from [116].

Menezes et al. reported the SPR application of LIL generated substrates (gold nanopillars (refer Figure 2.11 (b, c)) and nanoholes arrays) to detect biotin-streptavidin binding in a microfluidic platform [116]. The sensitivity of the bio-sensing using the gold nanoholes arrays was then improved by manipulating the optical collimation [121]. Menezes et al. also compared the optical sensing resolutions of FIB and LIL-fabricated nanoholes arrays of similar dimensions. The LIL- substrates demonstrated a better optical resolution in a large area compared to the FIB [117].

Yang et al. mounted optical fiber tips (OPTs) on ceramic ferrules to allow the direct LIL-patterning of the tips, as shown in Figure 2.12. The gold nanopillars patterned OPTs were used for SERS measurements of pyridine-containing molecules [118].

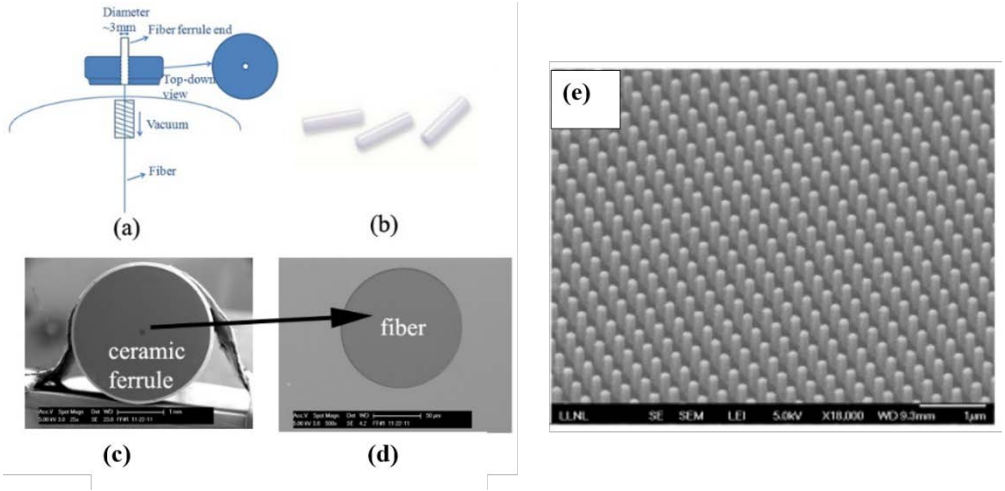

Figure 2.12 (a) Schematic and **(b-d)** photographs show the setup used in direct LIL on optical fiber tips. **(e)** SEM images of the nanopillars on the optical fiber tip. Reproduced with permission from [118].

Siegfried et al. prepared reusable gold nanoslits substrates using an LIL setup equipped with deep-UV laser. The substrates were applied for the SERS detections of thiol-containing chained molecules. After the experiments, the SERS substrates were cleaned with UV-ozone and reused [115]. Mandal et al. compared the SERS responses of rhodamine 6G dye under different geometries of nanostructures fabricated by LIL (e.g., square, hexagonal and rectangular). Among the examined shapes, the nano-hexagonal arrays demonstrated superior Raman enhancement [122]. Ahn et al. optimized LIL-fabricated Au nano-diamonds for SERS detections by immobilizing Au NPs onto the substrates. The optimized geometry demonstrated a SERS enhancement factor of ~ 10^9 [119].

2.3.2 Nanosphere lithography (NSL)

Nanosphere lithography is a large area fabrication technique, which relies on mono-disperse (homogeneous size distribution) spherical particles in colloidal suspensions (i.e. polystyrene [123-148], silica beads [149], latex [150]) to self-organize into periodic structures. A typical approach for NSL fabrication is through solvent evaporation that directs the self-assembly of the nanospheres onto a solid support [151]. Metal films can be directly deposited on top of the self-assembled nanospheres (used as templates) to generate plasmonic substrates. Alternatively, the organized assembly of spheres can be further treated to produce nanostructures in other geometries. For instance, a plasma etching process reduces the nanospheres to tune the periodicity of the resulting nanostructures [144, 147, 149, 150]. On the other hand, etching with reactive ion sources may be used to develop different nanostructures or to remove the colloidal beads [131, 137]. The self-assembled nanospheres can also be microwave-heated to partially melt and form nano-hexagonal layers [123]. NSL has been reported to be the precursor to fabricate a variety of nanostructures geometries, for instances nanocavities [125, 136], nanoposts [144], nanorings [127, 131], nanocrescents [131], nanocoreshells/semi-shells [137], nanocups [149], nanowaves [132] or honeycomb nanostructures [141].

For instance, Zhu et al. fabricated localized SPR based nanosensors using a thin film (i.e. 30 nm) of Ag deposited on self-assembled PS beads on glass [124]. Figure 2.13 shows another interesting example by Liu et al, who prepared nano-metallic petri dishes using the nanosphere template procedure. Polymer-dispersed silica nanospheres were spin-coated onto silicon wafer. After the polymer was partially etched away, a chromium layer was deposited, following the removal of the silica beads. A second plasma etching produced a chromium capped-polymer nano-posts structures. After Au/Ti deposition and a third round of plasma etching, the nano-sized gold petri dishes were fabricated, and used in SERS detection of thiolated molecules [149].

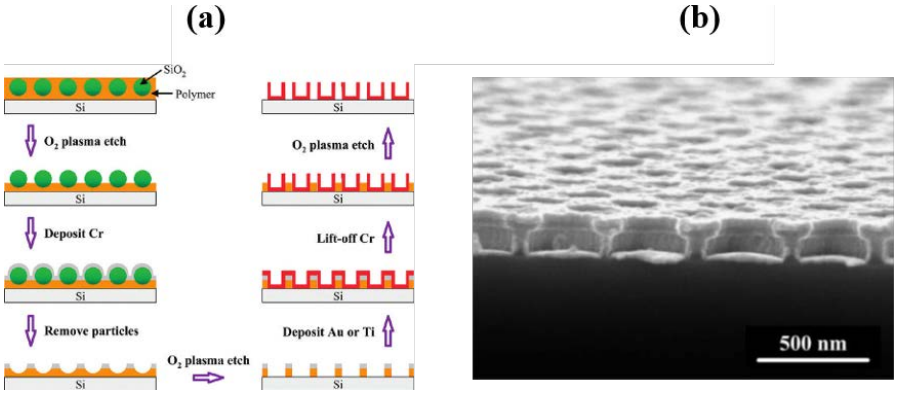

Figure 2.13 (a) Schematic of PS beads-templated fabrication of Au nanocups. **(b)** SEM cross-section of Au nanocups. Reproduced with permission from [149].

Live et al. successfully employed continuous Au films, consisting of triangles microholes arrays fabricated through latex nanosphere lithography, for SPR detection of IgG antibodies [150]. Lewika et al. reported a tape-enhanced selective etching of gold-coated semi-shells of nanospheres (from previous etching) arrays to prepare nanorings and nanocrescents structures [131]. Liu et al. applied a similar procedure to fabricate gold core-shells and semi-shells using NSL, without the final step of selective etching [137], as demonstrated in Figure 2.14.

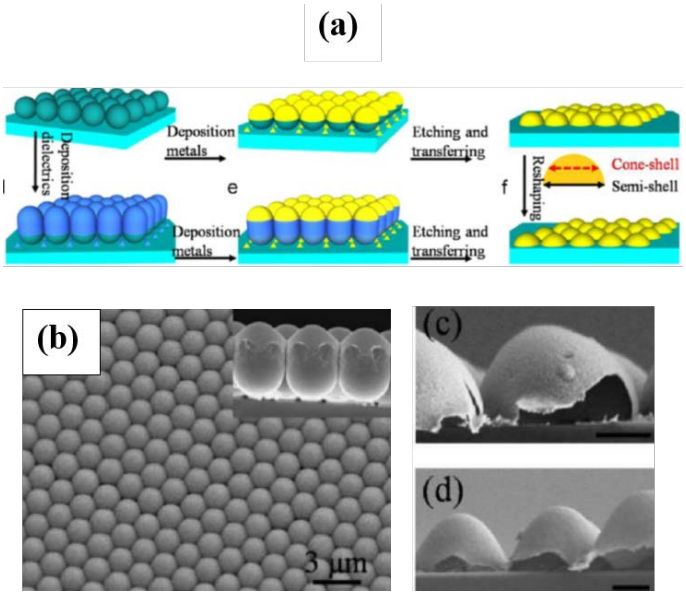

Figure 2.14 (a) Schematic of Au cones and semicones preparation. **(b-d)** SEM images of the fabricated substrates. The scale bars in (c, d) show 0.5 μm. Reproduced with permission from [137].

Ngo et al. performed SERS detection of DNA and sentinel molecules using ordered nanodome (nanowave) chips produced from NSL-based technology. The nanodome structures were prepared by direct-deposition of metal films on the nanospheres arrays [132, 138, 139]. On the other hand, Zhao et al. designed an SPR-based cell detector using self-organized PS spheres mounted on a triple-layer film (Au/SiO_2/Au). The nanospheres acted as protectors during reactive ion etching of the gold interface, producing Au nanodisks for SPR cell-trapping experiments [144], as seen in Figure 2.15.

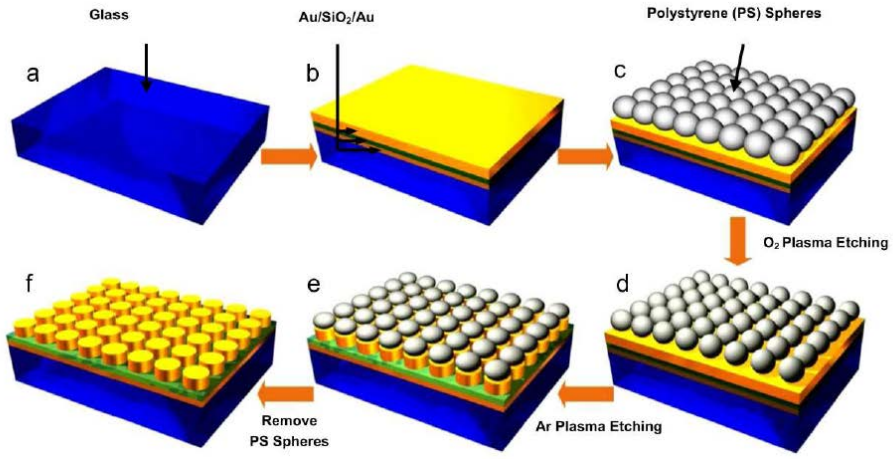

Figure 2.15 Schematic shows the fabrication procedure of the three-layered (Au/SiO_2/Au) nanodisks. Reproduced with permission from [144].

2.3.3 Template-assisted lithography

Template-assisted nanofabrication encompasses all the procedures that incorporate transfer of nanostructured patterns using a pre-fabricated template (master). These also include those procedures involving relocation of the nanostructured pattern from a primary template (or mold when shaping is performed on the molten liquids in the pre-manufactured template) to a target substrate, for instances, nanoimprinting, template-stripping, micro-contact and others. A few examples of the template-assisted nanofabrication are selected to be discussed below.

2.3.3.1 Anodized aluminum oxide (AAO) template

Highly ordered AAO templates have been widely utilized for the fabrication of plasmonic substrates. An example of the fabrication procedure is shown in Figure 2.16. A variety of nanostructured shapes have been prepared using this technique, including nanomeshes [152, 153], nanobowls [154], nanodots [152, 155, 156], nanocaps [157], microflowers [158], nanotubes/canals [159], nanowires [160-162] and nanorods [163-165]. Generally, there are two ways to prepare the AAO film: the first one involves a long period of anodization, while the second one is a two-step process, which is more time-efficient. In the two-step process, a concave template is initially formed after the first anodization, followed by a subsequent etching procedure. The previously etched template is then submitted to a second anodization step. Both anodization methods (single step and two-steps) eventually lead to the formation of AAO structures consisting of highly ordered hexagonal arrays, as shown in Figure 2.16(b). The self-organized hexagonal geometry is believed to result from the close packing orientation of the aluminium oxide [166].

One of the earlier reports on the utilization of AAO for SERS applications was related to their use as templates for the fabrication of high aspect ratios silver nanowires (nanorods) arrays [163]. Yao et al. concluded that SERS enhancements were influenced by the length of the nanorods [163]. Schierhorn et al. fabricated ordered 2D metal nanoparticles arrays of hybrid structures consisting of silver nanoparticles (i.e. ~ 35 nm) and silica rods using pored-enlarged AAO templates, as seen in Figure 2.16. The silver nanoparticles were electrochemically deposited and the silica rods were then grown in the AAO pores template through sol-gel chemistry. The best SERS performance obtained was up to sub-attomolar detection limits [167].

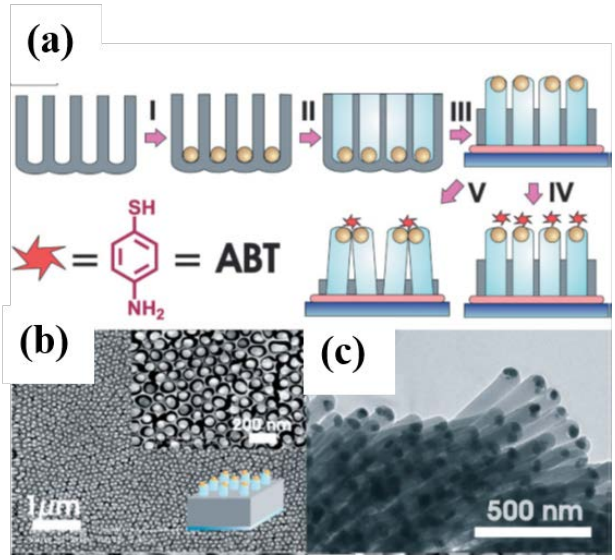

Figure 2.16 (a) Schematics and **(b, c)** SEM images of Ag NPs encapsulated silica rods fabricated through the AAO template. Reproduced with permission from [167].

Lombardi et al. demonstrated the use of thin (i.e. 300-nm thickness) AAO membrane as a template to form Ag NPs arrays (i.e. nanodisks) on a silicon wafer [168]. A few research groups (i.e. Ko and Tsukruk [159], Lu et al. [169] and Ji et al. [170]) fabricated three-dimensional SERS substrates using AAO templates, where the AAO nanotubes were decorated with either gold [159] or silver nanoparticles [169, 170]. An example of this approach is shown in Figure 2.17. Ko and Tsukruk also utilized the AuNPs-decorated AAO nanotubes for SERS detections of explosive molecules (i.e. DNT) [159] (Figure 2.17).

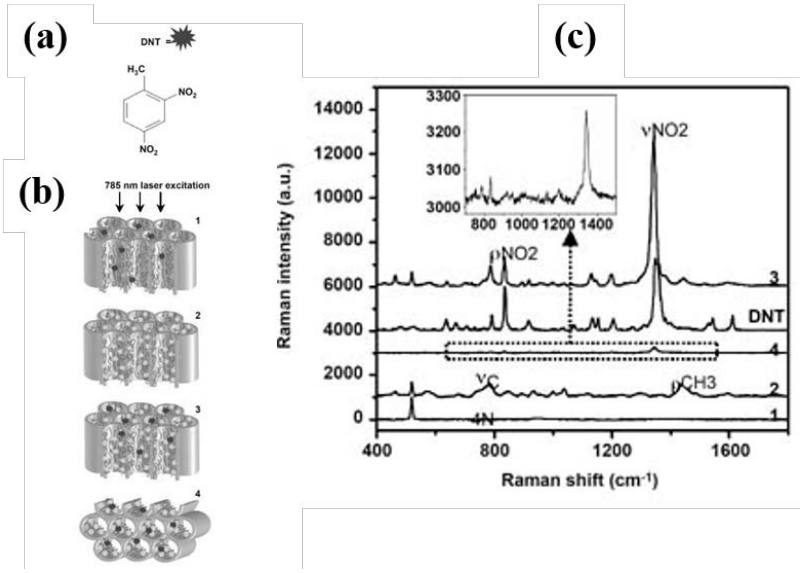

Figure 2.17 (a) Explosive chemical, DNT. **(b)** Schematic shows the AAO template with the back removed forming nanotubes, which were then decorated with Au NPs, indicated by the bright dots in case 2 – 4. The black dots represent the DNT molecules (as seen in case 1, 3 and 4). The SERS measurements in **(c)** were performed in: case 1, DNT molecules in nanotubes under parallel excitation incidence; case 2, Au NPs in nanotubes under parallel excitation; case 3, DNT molecules in Au NPs deposited nanotubes under parallel excitation, and case 4, DNT molecules in Au NPs deposited nanotubes under perpendicular excitation. Reproduced with permission from [159].

Zakaria et al. deposited thin hybrid layers of Au and Ag on an AAO template. This was followed by Cu tape stripping to transfer the pattern from the template. This resulted in the formation of long-range organized Au/Ag microflowers, which has potential to be a cheap, and easy alternative to fabricate large area plasmonic substrates [158]. Jang et al. prepared multistacks of Au/Ag nanomesh arrays (supported on silicon wafer) through the AAO-templated pattern transfer procedure, as seen in Figure 2.18. The SERS electromagnetic enhancements was controlled through the number of the nanomesh layers and the choice of metal (or hybrid of different metals in the layers) used in the fabrication [153].

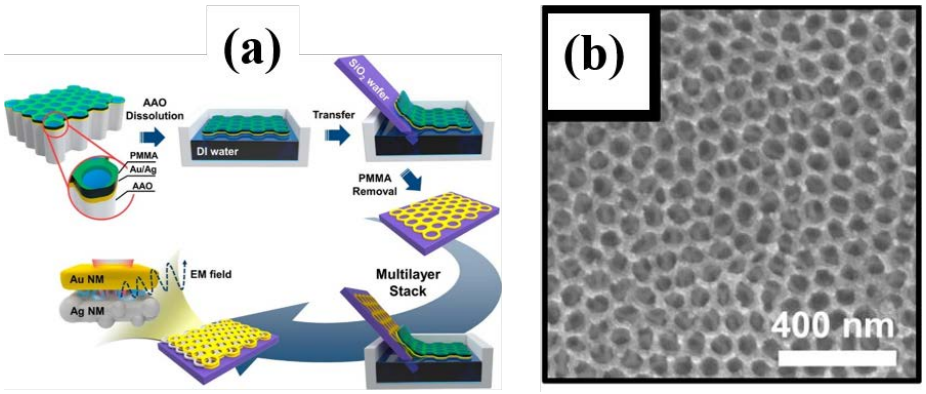

Figure 2.18 (a) Schematic of the fabrication process for multilayer Au/Ag nanomesh structures. **(b)** SEM image of the 4-layer of Au nanomesh structures. Reproduced with permission from [153].

A versatile nanofabrication based on AAO templates is demonstrated by Al-Haddad et al. The authors used AAO membranes to prepare (1) Au nanodots arrays (direct Au evaporation on porous AAO membrane supported on Si wafer), (2) Au nanocages arrays (imprinting procedure of the Au film on the edges of porous AAO membrane onto another target), and (3) Si nanowires arrays (HF-etching of the Au nanocages arrays) [152].

2.3.3.2 LIL-template

Instead of direct patterning using LIL, there are reports using LIL-fabricated substrates as the templates for pattern transfer. Du et al. utilized LIL templates to transfer patterned metallic nanostructures to a target substrate (e.g. PDMS). This large-area (i.e. wafer scale) fabrication process was reported to be cost-effective, simple and non-destructive [171]. Figure 2.19 depicts the approach of Pang et al. who demonstrated the use of LIL-fabricated grating structures as the mold to pattern colloidal gold nanoparticles into highly ordered arrays. The resulting structure (Figure 2.19) has the properties of a metallic photonic crystal (nanogratings) [172].

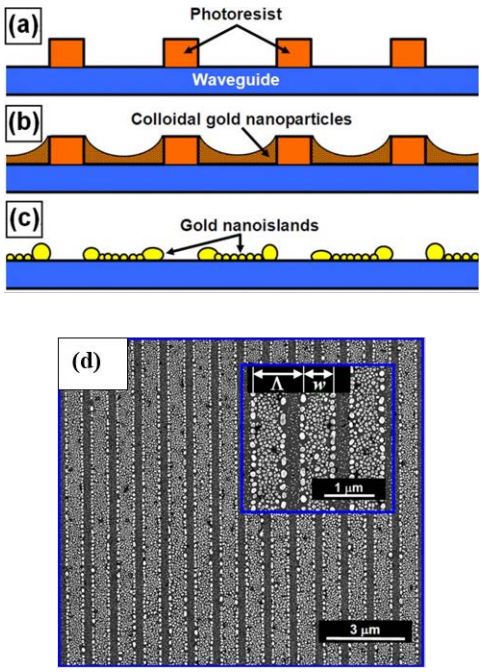

Figure 2.19 (a-c) Illustration of LIL template-assisted fabrication of the ordered grating arrays from the non-ordered gold nanoparticles. **(d)** SEM image of the fabricated structures. Reproduced with permission from [172].

2.3.3.3 NSL-template

NSL template can also be used for pattern transfer. An intermediate sacrificial template was used in the pattern transfer process. In Figure 2.20, Wang et al. used a pattern transfer procedure from gold-coated nanosphere arrays (prepared through the NSL) with the aid of polylactic acid (PLA) polymer as sacrificial template. The proposed peel-assembly-transfer procedure (Figure 2.20) successfully fabricated Au triangle arrays and Ag nanohole arrays supported on an adhesive polymer layer. The presence of the polymer layer underneath the metal nanostructures is reported to be an alternative to improve the mechanical stability of the nanostructures [146].

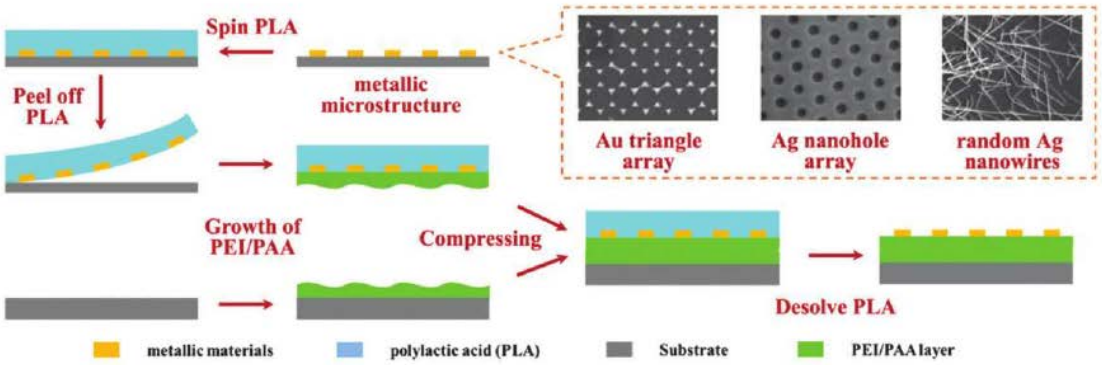

Figure 2.20 Pattern transfer of gold nanostructures made from NSL template to the target substrate. A sacrificial template (i.e. PLA) is employed at the intermediate steps. The inset shows the typical fabricated metal nanostructures. Reproduced with permission from [146].

Eriksen et al. demonstrated a template stripping procedure (aided by an epoxy layer) to transfer gold nanostructures based on self-organized PS nanospheres to a glass substrate, similar to Figure 2.20. The final substrates consisted of Au nanocavities supported on glass [125]. Ye et al. prepared PDMS-based gold semi-shells arrays. Self-organized nanospheres supported on a Ti-coated glass were first coated with Au and Cu films. A peeling procedure involving PDMS was implemented to detach the metal-coated nanospheres from the glass. This resulted in the formation of gold nanoring structures on the PDMS substrate [127], as seen in Figure 2.21(d).

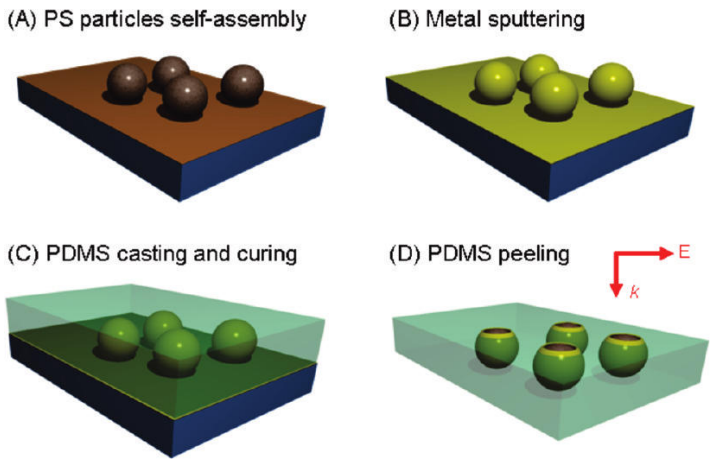

Figure 2.21 Schematics of the procedure fabricating the metallic semishells supported on PDMS. The primary template is formed through NSL procedure. Reproduced with permission from [127].

Hall et al. prepared wafer-scale silicon-based reusable templates by NSL-reactive ion etching process. The templates can be used in the large-area nanofabrication of nanowells and nanopillars combined to the template-stripping procedure enabled by an epoxy adhesive [130]. The final large area substrates fabricated are shown in Figure 2.22.

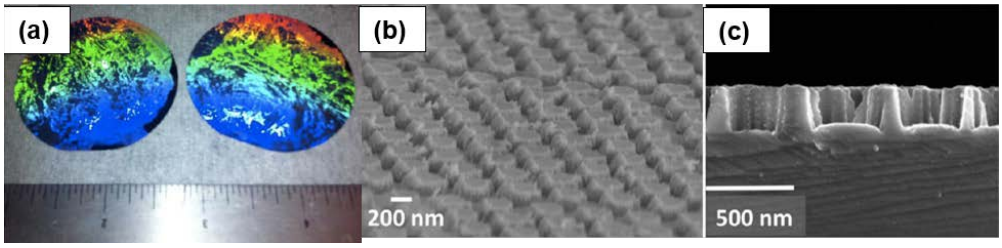

Figure 2.22 (a) The wafer-scale PS substrate fabricated through the process**. (b, c)** SEM images of the nanopillars and nanoholes arrays. Reproduced with permission from [130].

2.3.3.4 EBL-template

Figure 2.23 shows an integrated strategy (i.e. template stripping) developed by Cherukulappurath et al. to fabricate large-area pyramidal pits for tip-enhanced Raman spectroscopy. A Si template consisting of pyramidal pit arrays was generated by combining EBL and chemical etching (both reactive ion etching and KOH-based wet etching) of an oxide-coated Si wafer (Fig. 2.23(a)). The area exposed to the chemical etching was previously defined by EBL. The formation of pits was a consequence of the anisotropic etching of Si in KOH (discussed in Section 2.1.2). Another key step to maintain the sharpness of the pyramidal tips was to utilize an angled metal deposition (Fig. 2.23(b)), which resulted in an asymmetric thickness of metal on the Si mold. The metallic nanostructures were then stripped from the Si mold using UV-cured epoxy adhesive, as seen in Figure 2.23 (c and d). The final nanostructures are shown in Fig. 2.23 (e and f) [109].

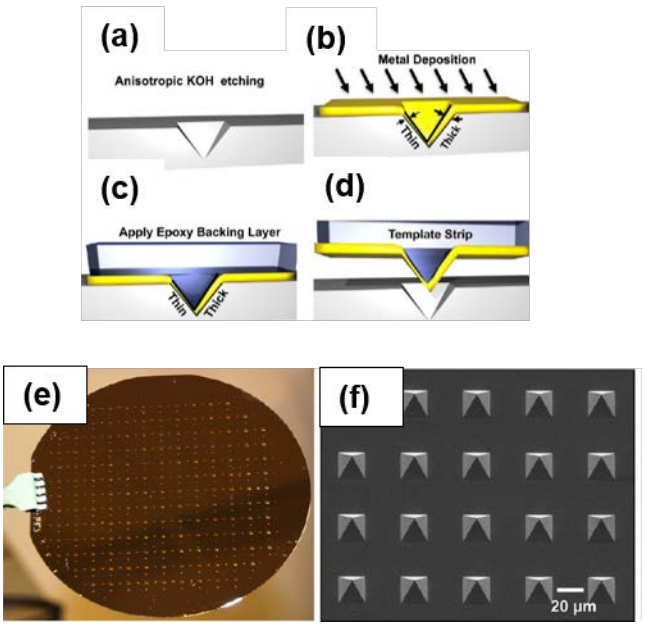

Figure 2.23 (a-d) Schematic illustration for the fabrication of sharp pyramidal tips. **(e)** The wafer-size tipped arrays fabricated through the combined EBL and chemical etching. **(f)** SEM image of the tipped arrays. Reproduced with permission from [109].

2.3.3.5 Molecular micro-stamp

Figure 2.24(a) shows the steps developed by Xi et al. to fabricate SERS micro-arrays. A micro-contact based electrochemical procedure was implemented in Fig. 2.24(a). The Au film was first patterned with an alkane-thiol monolayer via microstamping on a smooth Au film. The presence of the organic arrays on the Au surface provided the area-selectivity for the following electrochemical steps (Cu electrodeposition and Ag displacement) [173]. The resulting Ag microarrays are shown in Figure 2.24 (b and c).

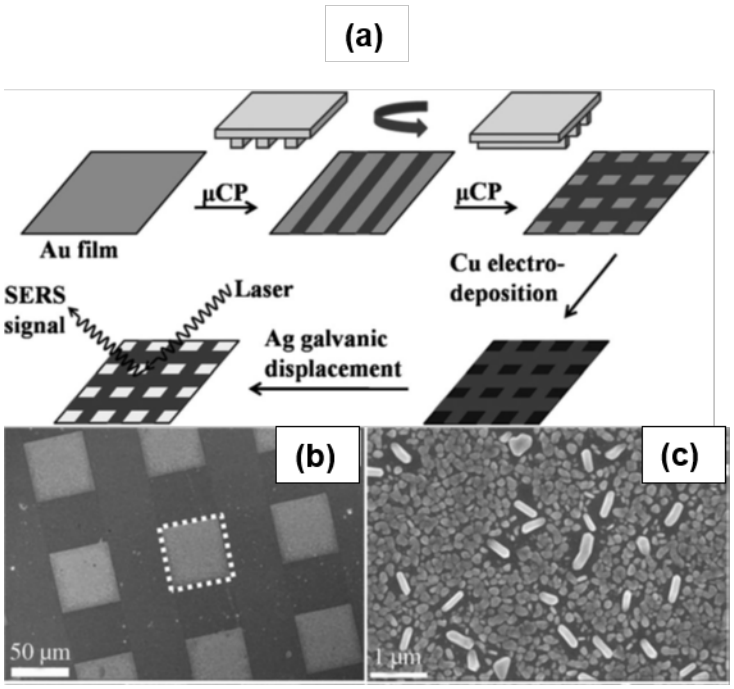

Figure 2.24 (a) Schematic shows the micro-contact electrochemical procedure to prepare SERS arrays. **(b, c)** The SEM images of the arrays fabricated. Reproduced with permission from [173].

2.3.4 Inkjet printing

Inkjet printing SERS metal nanoparticle arrays was first attempted by Yu and White using a mixture of concentrated citrate-based silver nanoparticles colloidal suspension in glycerol as ‘ink’ in the cartridge of a commercial inkjet printer [174]. The main purpose of the glycerol was to thicken the mixture, so that it would only wet the desired areas determined by the computer [174]. The printing-based fabrication was initially done on cellulose papers but the outcome suffered from the ‘coffee ring effect’, as most of the metal nanoparticles were accumulated at the edges of the spots. Yang et al. and Meier et al. demonstrated improved printing quality by using different supporting materials (i.e. ITO strips [175] and alkane-silane modified silicon wafer [176]) to modify the hydrophobicity of the surface in order to avoid the formation of coffee rings. The SEM images of the inkjet-printed Au nanoparticles arrays are shown in Figure 2.25.

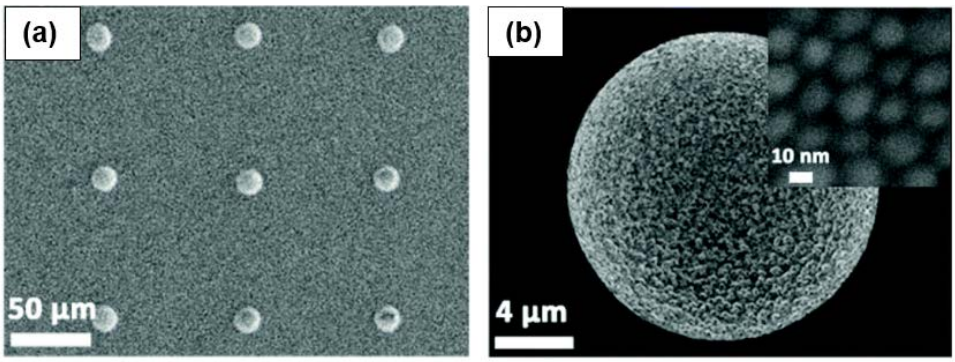

Figure 2.25 (a, b) SEM images of the SERS active Au nanoparticles spots produced by inkjet printing on the hydrophobic surface. Reproduced with permission from [176].

2.4 Nanostructures patterning into plasmonic microarrays

Nanostructure patterning has been attractive for many plasmonic applications. The most apparent benefit from microarrays patterning is that it greatly improves the throughput of the fabrication. In the ideal scenario, multiple microarrays, produced through large area substrate patterning, would contain identical nanostructures. This should enable each of the arrays to operate as an individual chemical sensing unit.

In analytical chemistry, microarray patterning has great potential to improve the statistics of the quantification, since the presence of many sensing elements allows a more systematic analysis of the outcome (e.g. by taking the averages from a few arrays). Moreover, nanostructured-microarrays supported on planar substrate are also ready to be integrated with microfluidic system for on-chip sensing applications, as well as multiplexing detections when necessary.

Most of the nanofabrication methods (e.g. FIB and EBL, discussed in Section 2.2.1 and 2.2.2) can be used for the production of microarrays through the programming of the desired design. This approach, nonetheless, is high-cost and time-consuming. Many researchers have then reported the preparation of microarrays through the combination of nanofabrication with other complementary processes, for instance, photolithography [116, 177, 178]. Other template-assisted procedures, including nano-imprint [107, 179-185] and template stripping [109, 130] (refer to Section 2.3.3), are also useful to reduce the fabrication costs.

2.4.1 Photolithography for microarrays fabrication

The photolithography (i.e. UV lithography) integrated with photoresist-based LIL has been used for the fabrication of microarrays. In addition, photolithography has been applied to prepare microscale patches within a larger area substrate (e.g. ~ an $inch^2$ to wafer size) as a preliminary step for subsequent nanostructure fabrication steps (e.g. etching process). The photolithography step defines the specific areas for the growth or integration of the nanostructures.

2.4.1.1 Combination of LIL and photolithography

Menezes et al. reported the combination of LIL and photolithography for microarray fabrication, as depicted in Figure 2.26. The microarrays consisted of 200 μm diameter circles and were utilized in a microfluidic biosensing experiment [116].

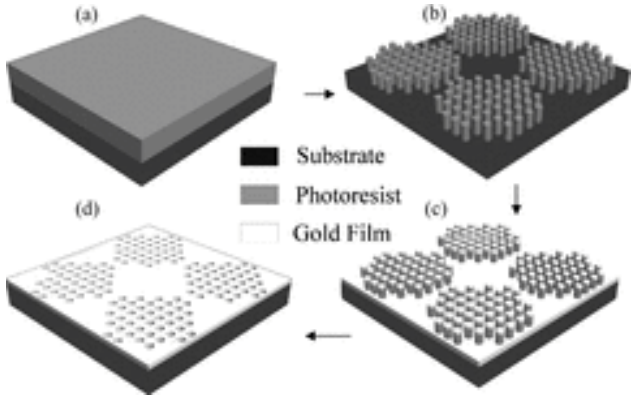

Figure 2.26 Schematic presents the fabrication of microarrays circles through the combination of IL and photolithography. Reproduced with permission from [116].

2.4.1.2 Combination of chemical etching and photolithography

Yi et al. used a combination of photolithography and wet etching to selectively grow Ag NPs decorated-silicon nanowires arrays (refer to Figure 2.27(a)). The etchant used was a mixture of HF, H_2O_2, and $AgNO_3$. The simultaneous Ag NPs deposition during the wet etching facilitated the galvanic displacement of Si by the HF/$AgNO_3$ solution. The resulting platform, as seen in Figure 2.27(b), was then utilized for label-free SERS detection of DNA [186].

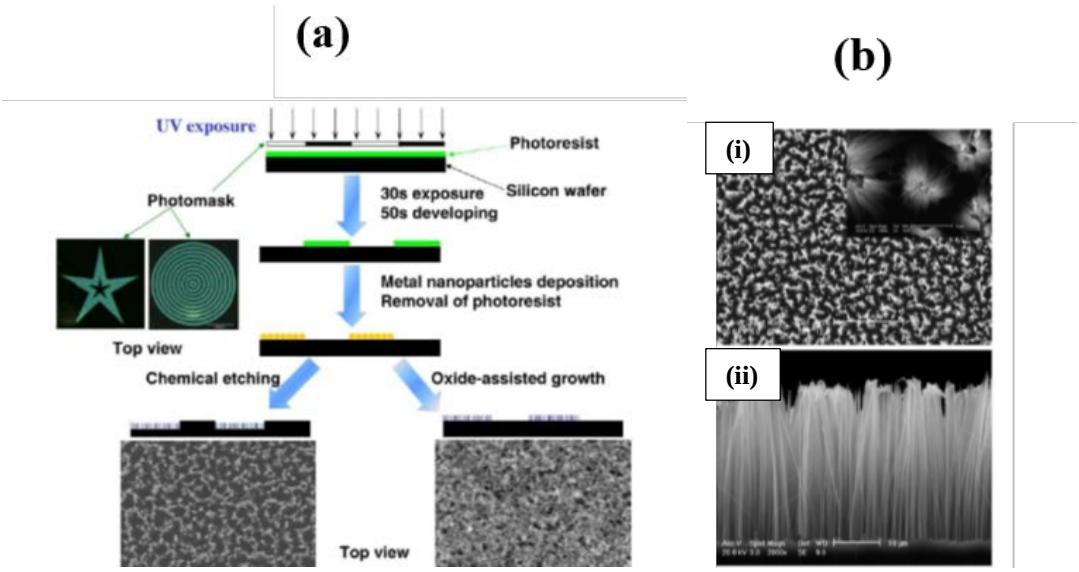

Figure 2.27 (a) Schematic illustration of silicon nanowire arrays with combined strategy of UV lithography and chemical etching. **(b)** Top and cross-sectional view of the silicon nanowires. The scale bars show 50 μm in (b)(i), 1 μm in the inset of (b)(i), and 10 μm in (b)(ii). Reproduced with permission from [186].

Wang et al. developed a wafer scale nanowire structure with sub-10nm gaps, using a combined strategy consisting of UV-lithography and chemical etching. The photolithography (with positive photoresist) defined the microscale regions in Si wafer and it was followed by a chemical etching step. The etching process provided the pit-shaped structure. The subsequent metal deposition partially closed the gaps between the nanowires into less than 10-nm spacing. The microarrays substrates, as shown in Figure 2.28, were then used for on-chip SERS-based DNA detections [178].

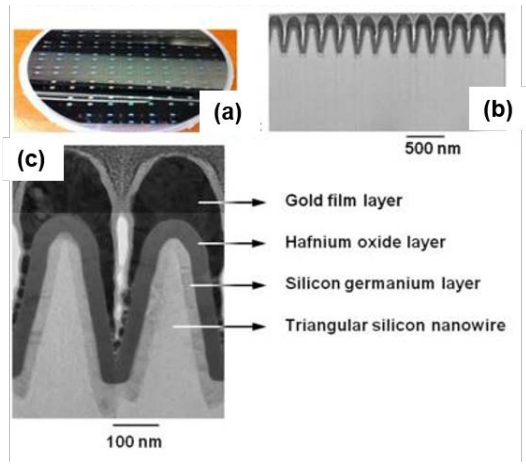

Figure 2.28 (a) The picture of 6 inch^2 chemical-etched silicon nanowire microarrays. **(b, c)** The cross-sectional view of the metal deposited nanowires. Reproduced with permission from [178].

2.4.1.3 Combination of NSL and photolithography

Figure 2.29 illustrates the work of Tabatabaei et al. who reported combining NSL and photolithography to produce single pockets to immobilize cells for SERS measurements. The finished platform (Figure 2.29) was modified with 4-mercaptophenylboronic acid (a Raman reporter) before the cells attachment. The SERS detection using this platform successfully distinct glycan expressions from cells closely associated with cancer [145].

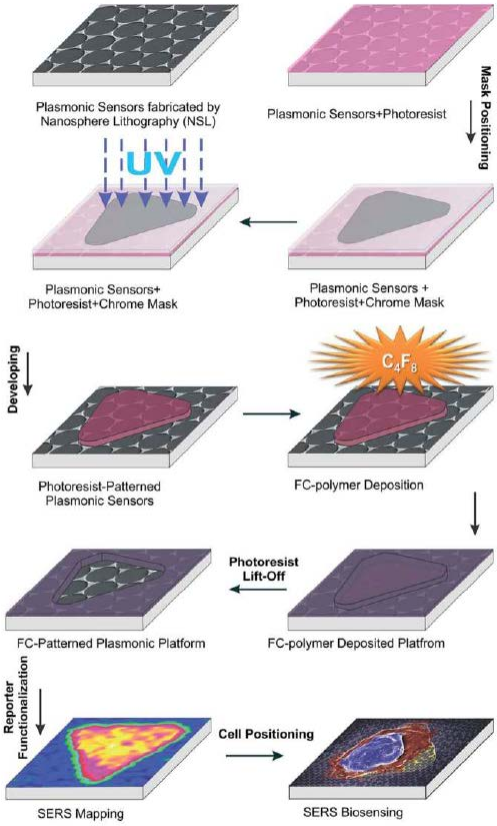

Figure 2.29 Schematic illustration of combined NSL – photolithography fabrication. Reproduced with permission from [145] (copyright information: Creative Commons Attribution 3.0 Unported Licence).

2.5 Optofluidic platforms for plasmonic microarrays

In the past decade, there has been growing interest in applying optofluidic platforms in different applications. In most prospective, optofluidic platforms are defined as the convergence of the optical detections (photonic-based measurements) to the microfluidic systems, which can potentially be advantageous as compared to those classical static detection systems.

Similarly, in the context of plasmonic sensing, the conjunction of the active fluidic system to the plasmonic microsystem (i.e. microarrays of metallic nanostructures) leads to several improvements. For instance, it allows more flexibility in sample manipulation; it also increase the number of the analyte molecules that reach the sensing surface by continuous flow; and, if necessary, it can enable on-chip pre-concentration or separation

steps. All these translate into an all-around improved sensing platform. In addition, the presence of the continuous flow helps to prevent local heating at the detection region, which might be important, especially when the sample is probed by laser illumination.

A few of the recent developments in optofluidic platforms used for plasmonic sensing will be discussed in the following sections (Section 2.5.1-2.5.4).

2.5.1 Optofluidic setup based on direct laser writing on glass micro-channels

Figure 2.30 shows that on-chip simultaneous patterning and metal nanoparticles deposition can be achieved with the help of a femtosecond laser at NIR wavelength (i.e. ~800 nm) [187, 188]. A mixture containing the metal salt solution, a reducing agent and a stabilizing agent are the precursor of the fabrication. The mixture can be either dry (i.e. spin-coated on solid support) or in solution form. The Ag (i.e. Ag^{+}) precursor has a maximum absorption at ~ 300 nm, it is photo-reduced to Ag (in the form of silver nanoparticles) through a two-photon absorption [187, 188]. Xu et al. employed a motorized stage to control the position of the substrate (i.e. the glass micro-channels) so that the photon-reduction can be manipulated on specific locations to form arrays of silver nanoparticles. The process is similar to the direct write of silver nanoparticles using a laser [188], as illustrated in Figure 2.30(a). The optofluidic integration to the platform was straightforward with aid of poly-dimethylsiloxane (PDMS), since those plasmonic active arrays were already drawn on the channelled microsystem.

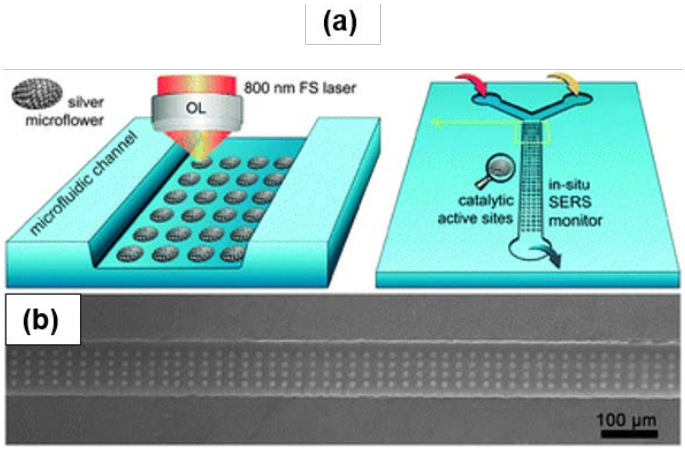

Figure 2.30 (a) Schematic illustrates the laser writing process to fabricate the Ag nanoparticles arrays. **(b)** The SEM image of the arrays fabricated. Reproduced with permission from [189].

2.5.2 Optofluidic setup based on Ag nanostructured-PDMS micro-channels

Oh and Jeong developed a convenient optofluidic SERS chips based on PDMS micro-channels. The active plasmonic elements were the random nanotips and nanodots formed on the PDMS channels through the plasma etching of the previously evaporated Ag on the PDMS, as shown in Figure 2.31. The system was sealed through the irreversible bonding (-Si-O-Si-) between the PDMS and glass. The proposed setup was employed in benzenethiol SERS detection and was reported to be highly selective and cost effective [190].

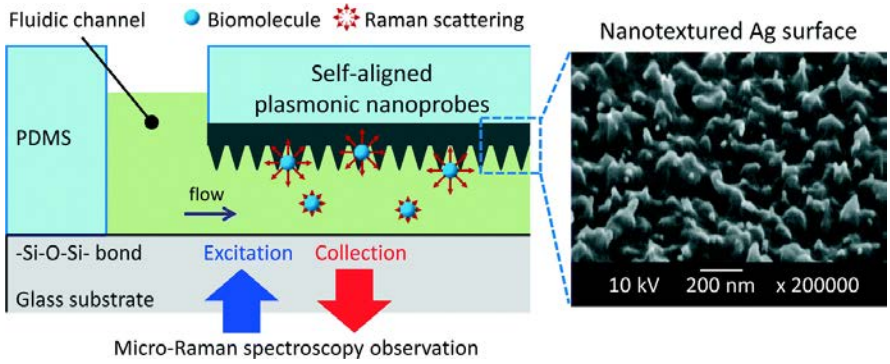

Figure 2.31 Schematic illustrates the optofluidic SERS chip with plasma-induced Ag nanostructures along PDMS microfluidic channels. The inset is the SEM image of the nanotips and nanodots induced by the oxygen plasma treatment. Reproduced with permission from [190].

2.5.3 Optofluidic setup using perforated adhesive

Deng et al. proposed a three-layer optofluidic setup, as seen in Figure 2.32, for online SERS detection of rhodamine 6G and malathion. The plasmonic nanostructures were the EBL-lithographed uniform gold nanopillars and nanodots supported on micro-channelled PDMS. Instead of sealing the system through irreversible bonding between PDMS and glass as the example in Section 2.5.2, the authors recruited the precisely laser-cut perforated adhesive to conjoin the system with the cover glass, as illustrated in Figure 2.32(a) [191].

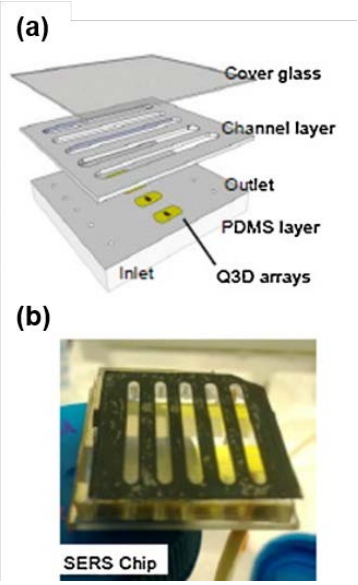

Figure 2.32 (a, b) The three-layer SERS optofluidic chip, with the centre layer made up of perforated adhesive and SERS substrate, the quasi three-dimensional (Q3D) arrays located underneath. Reproduced with permission from [191].

2.6 Implications from the nanofabrication advances

From this review, we can see that amazing progress has been taken place in the last decade for both bottom-up and top-down nanofabrication. All the techniques have their own unprecedented benefits and have demonstrated their competences in fabricating excellent nanostructures in a variety of geometries and shapes (refer to Section 2.1 to 2.5). The advances in lithographic-based nanofabrication has greatly favored the use of uniform substrates to support plasmonic applications (e.g. SERS and SPR-sensing). In the following chapters (chapter 3-5), proof-of-concept SERS and SPR-based sensing with uniform substrates generated by LIL will be presented.

2.7 References

[1] J. Nedeljkovic, R.C. Patel, Observation of plasmon-enhanced optical extinction in silver-coated silver bromide nanoparticles, Applied Physics Letters, 58 (1991) 2461-2463.
[2] C.T. Lin, M.H. Shiao, M.N. Chang, N. Chu, Y.W. Chen, Y.H. Peng, B.H. Liao, H.J. Huang, C.N. Hsiao, F.G. Tseng, A facile approach to prepare silicon-based Pt-Ag tubular dendritic nano-forests (tDNFs) for solar-light-enhanced methanol oxidation reaction, Nanoscale Research Letters, 10 (2015) 1-8.
[3] C.T. Lin, M.N. Chang, H.J. Huang, C.H. Chen, R.J. Sun, B.H. Liao, Y.F.C. Chau, C.N. Hsiao, M.H. Shiao, F.G. Tseng, Rapid fabrication of three-dimensional gold dendritic nanoforests for visible light-enhanced methanol oxidation, Electrochimica Acta, 192 (2016) 15-21.
[4] C.J. Murphy, T.K. Sau, A. Gole, C.J. Orendorff, Surfactant-directed synthesis and optical properties of one-dimensional plasmonic metallic nanostructures, Mrs Bulletin, 30 (2005) 349-355.
[5] C.J. Murphy, A.M. Gole, S.E. Hunyadi, C.J. Orendorff, One-dimensional colloidal gold and silver nanostructures, Inorganic Chemistry, 45 (2006) 7544-7554.
[6] Z.J. Yang, Z.H. Hao, H.Q. Lin, Q.Q. Wang, Plasmonic Fano resonances in metallic nanorod complexes, Nanoscale, 6 (2014) 4985-4997.
[7] Q.F. Zhang, H. Jing, G.G. Li, Y. Lin, D.A. Bloni, H. Wang, Intertwining roles of silver ions, surfactants, and reducing agents in gold nanorod overgrowth: pathway switch between silver underpotential deposition and gold-silver codeposition, Chemistry of Materials, 28 (2016) 2728-2741.
[8] S. Stasienko, J. Krajczewski, S. Wojtysiak, K. Czajkowski, A. Kudelski, Preparation of silver hollow nanostructures by plasmon-driven transformation, Colloids and Surfaces a-Physicochemical and Engineering Aspects, 443 (2014) 102-108.
[9] Y.G. Sun, B.T. Mayers, Y.N. Xia, Template-engaged replacement reaction: A one-step approach to the large-scale synthesis of metal nanostructures with hollow interiors, Nano Letters, 2 (2002) 481-485.
[10] Y.G. Sun, Y.N. Xia, Increased sensitivity of surface plasmon resonance of gold nanoshells compared to that of gold solid colloids in response to environmental changes, Analytical Chemistry, 74 (2002) 5297-5305.
[11] Y.G. Sun, Silver nanowires - unique templates for functional nanostructures, Nanoscale, 2 (2010) 1626-1642.
[12] H. Wang, D.W. Brandl, F. Le, P. Nordlander, N.J. Halas, Nanorice: A hybrid plasmonic nanostructure, Nano Letters, 6 (2006) 827-832.
[13] Q. Zhang, N. Li, J. Goebl, Z.D. Lu, Y.D. Yin, A systematic study of the synthesis of silver nanoplates: is citrate a "magic" reagent?, Journal of the American Chemical Society, 133 (2011) 18931-18939.
[14] S.J. Tan, M.J. Campolongo, D. Luo, W. Cheng, Building plasmonic nanostructures with DNA, Nat Nano, 6 (2011) 268-276.
[15] M.E. Lippitsch, Observation of surface enhanced Raman-spectra by adsorption to silver colloids, Chemical Physics Letters, 74 (1980) 125-127.
[16] M.E. Lippitsch, Surface enhanced Raman-spectra of biliverdine and pyrromethenone adsorbed to silver colloids, Chemical Physics Letters, 79 (1981) 224-226.
[17] N.J. Halas, S. Lal, W.-S. Chang, S. Link, P. Nordlander, Plasmons in strongly coupled metallic nanostructures, Chemical Reviews, 111 (2011) 3913-3961.

[18] C.E. Talley, J.B. Jackson, C. Oubre, N.K. Grady, C.W. Hollars, S.M. Lane, T.R. Huser, P. Nordlander, N.J. Halas, Surface-enhanced Raman scattering from individual Au nanoparticles and nanoparticle dimer substrates, Nano Letters, 5 (2005) 1569-1574.
[19] H.J. Yin, L. Liu, C.A. Shi, X. Zhang, M.Y. Lv, Y.M. Zhao, H.J. Xu, Study of surface-enhanced Raman scattering activity of DNA-directed self-assembled gold nanoparticle dimers, Applied Physics Letters, 107 (2015).
[20] H. Zhang, S. Yang, Q. Zhou, L. Yang, P. Wang, Y. Fang, The suitable condition of using LSPR model in SERS: LSPR effect versus chemical effect on microparticles surface-modified with nanostructures, Plasmonics, (2016) 1-5.
[21] Y. Yang, J.L. Shi, T. Tanaka, M. Nogami, Self-assembled silver nanochains for surface-enhanced Raman scattering, Langmuir, 23 (2007) 12042-12047.
[22] R.W. Taylor, R. Esteban, S. Mahajan, J. Aizpurua, J.J. Baumberg, Optimizing SERS from gold nanoparticle clusters: addressing the near field by an embedded chain plasmon model, Journal of Physical Chemistry C, 120 (2016) 10512-10522.
[23] A. Hu, P. Peng, H. Alarifi, X.Y. Zhang, J.Y. Guo, Y. Zhou, W.W. Duley, Femtosecond laser welded nanostructures and plasmonic devices, Journal of Laser Applications, 24 (2012) 042001.
[24] M.R. Langille, M.L. Personick, C.A. Mirkin, Plasmon-mediated syntheses of metallic nanostructures, Angewandte Chemie (International ed.), 52 (2013) 13910-13940.
[25] M.A. Huergo, C.M. Maier, M.F. Castez, C. Vericat, S. Nedev, R.C. Salvarezza, A.S. Urban, J. Feldmann, Optical nanoparticle sorting elucidates synthesis of plasmonic nanotriangles, ACS Nano, 10 (2016) 3614-3621.
[26] K.G. Li, K. Jiang, L. Zhang, Y. Wang, L. Mao, J. Zeng, Y.H. Lu, P. Wang, Raman scattering enhanced within the plasmonic gap between an isolated Ag triangular nanoplate and Ag film, Nanotechnology, 27 (2016).
[27] B. Chen, X.L. Jiao, D.R. Chen, Fabrication of hollow cubic Ag microboxes with net-like nanofiber structures and their surface plasmon resonance, Crystengcomm, 13 (2011) 204-211.
[28] S.P. Zhang, K. Bao, N.J. Halas, H.X. Xu, P. Nordlander, Substrate-induced Fano resonances of a plasmonic: nanocube: a route to increased-sensitivity localized surface plasmon resonance sensors revealed, Nano Letters, 11 (2011) 1657-1663.
[29] Q.F. Zhang, N. Large, H. Wang, Gold nanoparticles with tipped surface structures as substrates for single-particle surface-enhanced Raman spectroscopy: concave nanocubes, nanotrisoctahedra, and nanostars, ACS Applied Materials & Interfaces, 6 (2014) 17255-17267.
[30] Y.N. Xia, N.J. Halas, Shape-controlled synthesis and surface plasmonic properties of metallic nanostructures, Mrs Bulletin, 30 (2005) 338-344.
[31] S. Barbosa, A. Agrawal, L. Rodríguez-Lorenzo, I. Pastoriza-Santos, R.A. Alvarez-Puebla, A. Kornowski, H. Weller, L.M. Liz-Marzán, Tuning size and sensing properties in colloidal gold nanostars, Langmuir, 26 (2010) 14943-14950.
[32] B. Wiley, Y. Sun, B. Mayers, Y. Xia, Shape-controlled synthesis of metal nanostructures: the case of silver, Chemistry – A European Journal, 11 (2005) 454-463.
[33] R.G. Freeman, M.B. Hommer, K.C. Grabar, M.A. Jackson, M.J. Natan, Ag-clad Au nanoparticles: novel aggregation, optical, and surface-enhanced Raman scattering properties, The Journal of Physical Chemistry, 100 (1996) 718-724.

[34] M. Sharma, P.R. Pudasaini, F. Ruiz-Zepeda, E. Vinogradova, A.A. Ayon, Plasmonic effects of Au/Ag bimetallic multispiked nanoparticles for photovoltaic applications, ACS Applied Materials & Interfaces, 6 (2014) 15472-15479.
[35] C. Gong, M.S. Leite, Noble metal alloys for plasmonics, ACS Photonics, 3 (2016) 507-513.
[36] H.M. Qian, M. Xu, X.W. Li, M.W. Ji, L. Cheng, A. Shoaib, J.J. Liu, L. Jiang, H.S. Zhu, J.T. Zhang, Surface micro/nanostructure evolution of Au-Ag alloy nanoplates: Synthesis, simulation, plasmonic photothermal and surface-enhanced Raman scattering applications, Nano Research, 9 (2016) 876-885.
[37] F. Le, D.W. Brandl, Y.A. Urzhumov, H. Wang, J. Kundu, N.J. Halas, J. Aizpurua, P. Nordlander, Metallic nanoparticle arrays: A common substrate for both surface-enhanced Raman scattering and surface-enhanced infrared absorption, ACS Nano, 2 (2008) 707-718.
[38] J. Zhu, Y.J. Ren, The effect of negative curvature on the plasmonic coupling of concentric core-shell metallic nanostructures, Plasmonics, 9 (2014) 1077-1084.
[39] N. Zhou, M. Yuan, Y.H. Gao, D.S. Li, D.R. Yang, Silver nanoshell plasmonically controlled emission of semiconductor quantum dots in the strong coupling regime, ACS Nano, 10 (2016) 4154-4163.
[40] Y. Zhang, A. Manjavacas, N.J. Hogan, L.N. Zhou, C. Ayala-Orozco, L.L. Dong, J.K. Day, P. Nordlander, N.J. Halas, Toward Surface plasmon-enhanced optical parametric amplification (SPOPA) with engineered nanoparticles: a nanoscale tunable infrared source, Nano Letters, 16 (2016) 3373-3378.
[41] J.B. Lassiter, M.W. Knight, N.A. Mirin, N.J. Halas, Reshaping the plasmonic properties of an individual nanoparticle, Nano Letters, 9 (2009) 4326-4332.
[42] R.A. Alvarez-Puebla, J.P. Bravo-Vasquez, P. Cheben, D. Xu, P. Waldron, H. Fenniri, SERS-active Ag/Au bimetallic nanoalloys on Si/SiOx, Journal of Colloid and Interface Science, 333 (2009) 237-241.
[43] A. Bansal, J.S. Sekhon, S.S. Verma, Scattering Efficiency and LSPR Tunability of Bimetallic Ag, Au, and Cu Nanoparticles, Plasmonics, 9 (2014) 143-150.
[44] A. Bansal, S.S. Verma, Simulated study of plasmonic coupling in noble bimetallic alloy nanosphere arrays, AIP Advances, 4 (2014).
[45] F. Hubenthal, N. Borg, F. Trager, Optical properties and ultrafast electron dynamics in gold-silver alloy and core-shell nanoparticles, Applied Physics B-Lasers and Optics, 93 (2008) 39-45.
[46] F. Hubenthal, T. Ziegler, C. Hendrich, M. Alschinger, F. Trager, Tuning the surface plasmon resonance by preparation of gold-core/silver-shell and alloy nanoparticles, European Physical Journal D, 34 (2005) 165-168.
[47] N. Kumar, F. Alam, V. Dutta, Deposition of Ag and Au-Ag alloy nanoparticle films by spray pyrolysis technique with tuned plasmonic properties, Journal of Alloys and Compounds, 585 (2014) 312-317.
[48] R.H. Magruder, J.E. Wittig, R.A. Zuhr, Wavelength tunability of the surface-plasmon resonance of nanosize metal colloids in glass, Journal of Non-Crystalline Solids, 163 (1993) 162-168.
[49] F.A.A. Nugroho, B. Iandolo, J.B. Wagner, C. Langhammer, Bottom-up nanofabrication of supported noble metal alloy nanoparticle arrays for plasmonics, ACS Nano, 10 (2016) 2871-2879.

[50] R.G. Freeman, K.C. Grabar, K.J. Allison, R.M. Bright, et al., Self-assembled metal colloid monolayers: An approach to SERS substrates, Science, 267 (1995) 1629.
[51] C.J. Addison, A.G. Brolo, Nanoparticle-containing structures as a substrate for surface-enhanced Raman scattering, Langmuir, 22 (2006) 8696-8702.
[52] M.K. Fan, A.G. Brolo, Self-assembled Au nanoparticles as substrates for surface-enhanced vibrational spectroscopy: Optimization and electrochemical stability, Chemphyschem, 9 (2008) 1899-1907.
[53] M. Fan, A.G. Brolo, Silver nanoparticles self assembly as SERS substrates with near single molecule detection limit, Physical Chemistry Chemical Physics, 11 (2009) 7381-7389.
[54] F.C. Cabrera, P.H.B. Aoki, R.F. Aroca, C.J.L. Constantino, D.S. dos Santos, A.E. Job, Portable smart films for ultrasensitive detection and chemical analysis using SERS and SERRS, Journal of Raman Spectroscopy, 43 (2012) 474-477.
[55] E.A. Batista, D.P. dos Santos, G.F.S. Andrade, A.C. Sant'Ana, A.G. Brolo, M.L.A. Temperini, Using polycarbonate membranes as templates for the preparation of au nanostructures for surface-enhanced Raman scattering, Journal of Nanoscience and Nanotechnology, 9 (2009) 3233-3238.
[56] G.F.S. Andrade, M.K. Fan, A.G. Brolo, Multilayer silver nanoparticles-modified optical fiber tip for high performance SERS remote sensing, Biosensors and Bioelectronics, 25 (2010) 2270-2275.
[57] M.K. Fan, M. Thompson, M.L. Andrade, A.G. Brolo, Silver nanoparticles on a plastic platform for localized surface plasmon resonance biosensing, Analytical Chemistry, 82 (2010) 6350-6352.
[58] H. Wang, N.J. Halas, Plasmonic nanoparticle heterodimers in a semiembedded geometry fabricated by stepwise upright assembly, Nano Letters, 6 (2006) 2945-2948.
[59] B.J. Wiley, D.J. Lipomi, J.M. Bao, F. Capasso, G.M. Whitesides, Fabrication of surface plasmon resonators by nanoskiving single-crystalline gold microplates, Nano Letters, 8 (2008) 3023-3028.
[60] B.C.P. Massola, N.M.P. de Souza, F.F.F. Stachack, E. Oliveira, J.C. Germino, A.J. Terezo, F.J. Quites, Au-ZnO prepared by simple in situ reduction and spontaneous of gold nanoparticles on the surface of the layered zinc hydroxide using a novel one-pot method, Materials Chemistry and Physics, 167 (2015) 152-159.
[61] G. Bertoni, F. Fabbri, M. Villani, L. Lazzarini, S. Turner, G. Van Tendeloo, D. Calestani, S. Gradecak, A. Zappettini, G. Salviati, Nanoscale mapping of plasmon and exciton in ZnO tetrapods coupled with Au nanoparticles, Scientific Reports, 6 (2016).
[62] A.M. Yan, Y. Hua, V.P. Dravid, Locally enhanced surface plasmons and modulated "hot-spots" in nanoporous gold patterns on atomically thin MoS_2 with a comparison to SiO_2 substrate, Applied Physics Letters, 108 (2016).
[63] G. Lu, H. Li, C. Liusman, Z.Y. Yin, S.X. Wu, H. Zhang, Surface enhanced Raman scattering of Ag or Au nanoparticle-decorated reduced graphene oxide for detection of aromatic molecules, Chemical Science, 2 (2011) 1817-1821.
[64] N.C. Lindquist, P. Nagpal, K.M. McPeak, D.J. Norris, S. Oh, Engineering metallic nanostructures for plasmonics and nanophotonics, Reports on Progress in Physics. Physical Society (Great Britain), 75 (2012) 036501-036501.
[65] H. Lo, H. Hsiung, S. Chattopadhyay, H. Han, C. Chen, J.P. Leu, K. Chen, L. Chen, Label free sub-picomole level DNA detection with Ag nanoparticle decorated Au

nanotip arrays as surface enhanced Raman spectroscopy platform, Biosensors and Bioelectronics, 26 (2011) 2413-2418.
[66] M. Fleischmann, P.J. Hendra, A.J. McQuillan, Raman-spectra of pyridine adsorbed at a silver electrode, Chemical Physics Letters, 26 (1974) 163-166.
[67] P. Gao, D. Gosztola, L.-W.H. Leung, M.J. Weaver, Surface-enhanced Raman scattering at gold electrodes: Dependence on electrochemical pretreatment conditions and comparisons with silver, Journal of Electroanalytical Chemistry and Interfacial Electrochemistry, 233 (1987) 211-222.
[68] P.L. Redmond, A.J. Hallock, L.E. Brus, Electrochemical Ostwald ripening of colloidal Ag particles on conductive substrates, Nano Letters, 5 (2005) 131-135.
[69] S. Yang, D. Slotcavage, J.D. Mai, F. Guo, S. Li, Y. Zhao, Y. Lei, C.E. Cameron, T.J. Huang, Electrochemically created highly surface roughened Ag nanoplate arrays for SERS biosensing applications, Journal of Materials Chemistry C, 2 (2014) 8350-8356.
[70] D. Lis, Y. Caudano, M. Henry, S. Demoustier-Champagne, E. Ferain, F. Cecchet, Selective plasmonic platforms based on nanopillars to enhance vibrational sum-frequency generation spectroscopy, Advanced Optical Materials, 1 (2013) 244-255.
[71] S.H. Park, J.G. Son, T.G. Lee, J. Kim, S.Y. Han, H.M. Park, J.Y. Song, Galvanic synthesis of three-dimensional and hollow metallic nanostructures, Nanoscale Research Letters, 9 (2014) 679.
[72] W. Nogala, P. Kannan, S. Gawinkowski, M. Jonsson-Niedziolka, M. Kominiak, J. Waluk, M. Opallo, Tailored gold nanostructure arrays as catalysts for oxygen reduction in alkaline media and a single molecule SERS platform, Nanoscale, 7 (2015) 10767-10774.
[73] J.R. Anema, A.G. Brolo, P. Marthandam, R. Gordon, Enhanced Raman scattering from nanoholes in a copper film, Journal of Physical Chemistry C, 112 (2008) 17051-17055.
[74] R. Gordon, D. Sinton, K.L. Kavanagh, A.G. Brolo, A new generation of sensors based on extraordinary optical transmission, Accounts of Chemical Research, 41 (2008) 1049-1057.
[75] C. Escobedo, F. Eftekhari, J. Ferreira, P. Wood, R. Gordon, A.G. Brolo, D. Sinton, ASME, Nanohole arrays as optical and fluidic elements for sensing, 2009.
[76] A.G. Brolo, R. Gordon, D. Sinton, Nanohole Arrays in Metal Films as Integrated Chemical Sensors and Biosensors, in: M. Zourob, A. Lakhtakia (Eds.) Optical guided-wave chemical and biosensors, 2010, pp. 155-179.
[77] A. Dhawan, M. Gerhold, A. Madison, J. Fowlkes, P.E. Russell, T. Vo-Dinh, D.N. Leonard, Fabrication of nanodot plasmonic waveguide structures using FIB milling and electron beam-induced deposition, Scanning, 31 (2009) 139-146.
[78] Y. Lin, J. Liao, Y. Ju, C. Chang, A. Shiau, Focused ion beam-fabricated Au micro/nanostructures used as a surface enhanced Raman scattering-active substrate for trace detection of molecules and influenza virus, Nanotechnology, 22 (2011) 185308.
[79] K. Sivashanmugan, J. Liao, J. You, C. Wu, Focused-ion-beam-fabricated Au/Ag multilayered nanorod array as SERS-active substrate for virus strain detection, Sensors and Actuators B: Chemical, 181 (2013) 361-367.
[80] B. Zeng, Y. Gao, F. Bartoli, Ultrathin nanostructured metals for highly transmissive plasmonic subtractive color filters,Scientific Reports, 3:2840 (2013) 1 - 9

[81] B. Zeng, Y. Gao, F.J. Bartoli, Rapid and highly sensitive detection using Fano resonances in ultrathin plasmonic nanogratings, Applied Physics Letters, 105 (2014) 161106.
[82] S.L. Zhu, W. Zhou, Plasmonic properties of two-dimensional metallic nanoholes fabricated by focused ion beam lithography, Journal of Nanoparticle Research, 14 (2012).
[83] L. Wang, X. Xu, High transmission nanoscale bowtie-shaped aperture probe for near-field optical imaging, Applied Physics Letters, 90 (2007) 261105.
[84] E.X. Jin, X. Xu, Enhanced optical near field from a bowtie aperture, Applied Physics Letters, 88 (2006) 153110.
[85] Q. Min, M.J.L. Santos, E.M. Girotto, A.G. Brolo, R. Gordon, Localized Raman enhancement from a double-hole nanostructure in a metal film, Journal of Physical Chemistry C, 112 (2008) 15098-15101.
[86] K. Kant anf D. Losic, Focused ion bean (FIB) technology for micro- and nanoscale fabrications, in: Z.M. Wang (Ed.), FIB Nanostructures, Springer International (2013) 1-22
[87] W. Dickson, G.A. Wurtz, P.R. Evans, R.J. Pollard, A.V. Zayats, Electronically controlled surface plasmon dispersion and optical transmission through metallic hole arrays using liquid crystal, Nano Letters, 8 (2008) 281-286.
[88] F. Eftekhari, C. Escobedo, J. Ferreira, X. Duan, E.M. Girotto, A.G. Brolo, R. Gordon, D. Sinton, Nanoholes As Nanochannels: Flow-through plasmonic sensing, analytical chemistry, 81 (2009) 4308-4311.
[89] A. Dhawan, J.F. Muth, D.N. Leonard, M.D. Gerhold, J. Gleeson, T. Vo-Dinh, P.E. Russell, FIB Fabrication of metallic nanostructures on end-faces of optical fibers for chemical sensing applications, Journal of Vacuum Science & Technology. B, 26 (2008) 2168-2173.
[90] G.F. Andrade, J.G. Hayashi, M.M. Rahman, W.J. Salcedo, C.M. Cordeiro, A.G. Brolo, Surface-enhanced resonance Raman scattering (SERRS) using Au nanohole arrays on optical fiber tips, Plasmonics, 8 (2013) 1113-1121.
[91] A.G. Brolo, S.C. Kwok, M.D. Cooper, M.G. Moffitt, C.W. Wang, R. Gordon, J. Riordon, K.L. Kavanagh, Surface plasmon−quantum dot coupling from arrays of nanoholes, The Journal of Physical Chemistry B, 110 (2006) 8307-8313.
[92] C. Escobedo, Y.W. Chou, M. Rahman, X.B. Duan, R. Gordon, D. Sinton, A.G. Brolo, J. Ferreira, Quantification of ovarian cancer markers with integrated microfluidic concentration gradient and imaging nanohole surface plasmon resonance, Analyst, 138 (2013) 1450-1458.
[93] C. Escobedo, A.G. Brolo, R. Gordon, D. Sinton, Optofluidic concentration: plasmonic nanostructure as concentrator and sensor, Nano Letters, 12 (2012) 1592-1596.
[94] C. Escobedo, A.G. Brolo, R. Gordon, D. Sinton, Flow-through vs flow-over: analysis of transport and binding in nanohole array plasmonic biosensors, Analytical Chemistry, 82 (2010) 10015-10020.
[95] T.D. Corrigan, S. Guo, R.J. Phaneuf, H. Szmacinski, Enhanced fluorescence from periodic arrays of silver nanoparticles, Journal of Fluorescence, 15 (2005) 777-784.
[96] Y. Yokota, K. Ueno, S. Juodkazis, V. Mizeikis, N. Murazawa, H. Misawa, H. Kasa, K. Kintaka, J. Nishii, Nano-textured metallic surfaces for optical sensing and detection

applications, Journal of Photochemistry and Photobiology A-Chemistry, 207 (2009) 126-134.
[97] D. Garoli, T. Ongarello, P. Zilio, M. Carli, F. Romanato, Nanofocusing on circularly distributed tapered metallic waveguides by means of plasmonic vortex lenses, Applied Optics, 54 (2015) 1161-1166.
[98] S.J. Bauman, E.C. Novak, D.T. Debu, D. Natelson, J.B. Herzog, Fabrication of sub-lithography-limited structures via nanomasking technique for plasmonic enhancement applications, IEEE Transactions on Nanotechnology, 14 (2015) 790-793.
[99] D. Cialla, K. Weber, R. Bohme, U. Hubner, H. Schneidewind, M. Zeisberger, R. Mattheis, R. Moller, J. Popp, Towards multiple readout application of plasmonic arrays, Beilstein Journal of Nanotechnoly, 2 (2011) 501-508.
[100] A.K. Sheridan, A.W. Clark, A. Glidle, J.M. Cooper, D.R.S. Cumming, Multiple plasmon resonances from gold nanostructures, Applied Physics Letters, 90 (2007).
[101] Y.Q. Chen, Z.Q. Li, Q. Xiang, Y.S. Wang, Z.Q. Zhang, H.G. Duan, Reliable fabrication of plasmonic nanostructures without an adhesion layer using dry lift-off, Nanotechnology, 26 (2015).
[102] A. Gopalakrishnan, M. Chirumamilla, F. De Angelis, A. Toma, R.P. Zaccaria, R. Krahne, Bimetallic 3D nanostar dimers in ring cavities: recyclable and robust surface-enhanced Raman scattering substrates for signal detection from few molecules, ACS Nano, 8 (2014) 7986-7994.
[103] O. Vazquez-Mena, T. Sannomiya, M. Tosun, L.G. Villanueva, V. Savu, J. Voros, J. Brugger, High-resolution resistless nanopatterning on polymer and flexible substrates for plasmonic biosensing using stencil masks, ACS Nano, 6 (2012) 5474-5481.
[104] O. Vazquez-Mena, T. Sannomiya, L.G. Villanueva, J. Voros, J. Brugger, Metallic nanodot arrays by stencil lithography for plasmonic biosensing applications, ACS Nano, 5 (2011) 844-853.
[105] A. Bouvrée, A. D'Orlando, T. Makiabadi, S. Martin, G. Louarn, J.Y. Mevellec, B. Humbert, Nanostructured and nanopatterned gold surfaces: application to the surface-enhanced Raman spectroscopy, Gold Bulletin, 46 (2013) 283-290.
[106] H.L. Chen, S.Y. Chuang, W.H. Lee, S.S. Kuo, W.F. Su, S.L. Ku, Y.F. Chou, Extraordinary transmittance in three-dimensional crater, pyramid, and hole-array structures prepared through reversal imprinting of metal films, Optics Express, 17 (2009) 1636-1645.
[107] C. Liang, M. Liao, W. Chen, T. Cheng, W. Chang, C. Lin, Plasmonic metallic nanostructures by direct nanoimprinting of gold nanoparticles, Optics Express, 19 (2011) 4768-4776.
[108] K.L. Lee, J.B. Huang, J.W. Chang, S.H. Wu, P.K. Wei, Ultrasensitive biosensors using enhanced Fano resonances in capped gold nanoslit arrays, Scientific Reports, 5 (2015).
[109] S. Cherukulappurath, T.W. Johnson, N.C. Lindquist, S.H. Oh, Template-stripped asymmetric metallic pyramids for tunable plasmonic nanofocusing, Nano Letters, 13 (2013) 5635-5641.
[110] J. Peipei, J. Hao, S. Jayshri, Y. Jun, Plasmonic nanohole array sensors fabricated by template transfer with improved optical performance, Nanotechnology, 24 (2013) 195501.

[111] Q. Xie, M.H. Hong, H.L. Tan, G.X. Chen, L.P. Shi, T.C. Chong, Fabrication of nanostructures with laser interference lithography, Journal of Alloys and Compounds, 449 (2008) 261-264.
[112] C. Lu, R.H. Lipson, Interference lithography: a powerful tool for fabricating periodic structures, Laser & Photonics Reviews, 4 (2010) 568-580.
[113] K. Du, I. Wathuthanthri, W.D. Mao, W. Xu, C.H. Choi, Large-area pattern transfer of metallic nanostructures on glass substrates via interference lithography, Nanotechnology, 22 (2011).
[114] A. Arriola, A. Rodriguez, N. Perez, T. Tavera, M.J. Withford, A. Fuerbach, S.M. Olaizola, Fabrication of high quality sub-micron Au gratings over large areas with pulsed laser interference lithography for SPR sensors, Optical Materials Express, 2 (2012) 1571-1579.
[115] T. Siegfried, M. Kind, A. Terfort, O.J. Martin, M. Zharnikov, N. Ballav, H. Sigg, Reusable plasmonic substrates fabricated by interference lithography: a platform for systematic sensing studies, Journal of Raman Spectroscopy, 44 (2013) 170-175.
[116] J.W. Menezes, J. Ferreira, M.J.L. Santos, L. Cescato, A.G. Brolo, Large-area fabrication of periodic arrays of nanoholes in metal films and their application in biosensing and plasmonic-enhanced photovoltaics, Advanced Functional Materials, 20 (2010) 3918-3924.
[117] J.W. Menezes, L.A.M. Barea, E.F. Chillcce, N. Frateschi, L. Cescato, Comparison of plasmonic arrays of holes recorded by interference lithography and focused ion beam, IEEE Photonics Journal, 4 (2012) 544-551.
[118] X. Yang, N. Ileri, C.C. Larson, T.C. Carlson, J.A. Britten, A.S.P. Chang, C. Gu, T.C. Bond, Nanopillar array on a fiber facet for highly sensitive surface-enhanced Raman scattering, Optics Express, 20 (2012) 24819-24826.
[119] H. Ahn, P. Thiyagarajan, L. Jia, S. Kim, J. Yoon, E.L. Thomas, J. Jang, An optimal substrate design for SERS: dual-scale diamond-shaped gold nano-structures fabricated via interference lithography, Nanoscale, 5 (2013) 1836-1842.
[120] H. Wolferen, L. Abelmann, Laser interference lithography, (2011) 133-148
[121] J. Weber de Menezes, A. Thesing, C. Valsecchi, L.E.G. Armas, A.G. Brolo, Improving the performance of gold nanohole array biosensors by controlling the optical collimation conditions, Applied Optics, 54 (2015) 6502-6507.
[122] P. Mandal, A. Nandi, S.A. Ramakrishna, Propagating surface plasmon resonances in two-dimensional patterned gold-grating templates and surface enhanced Raman scattering, Journal of Applied Physics, 112 (2012) 044314-044314-044312.
[123] A. Kosiorek, W. Kandulski, H. Glaczynska, M. Giersig, Fabrication of nanoscale rings, dots, and rods by combining shadow nanosphere lithography and annealed polystyrene nanosphere masks, Small, 1 (2005) 439-444.
[124] S.L. Zhu, C.L. Du, Y.Q. Fu, Biochemistry nanosensor-based hybrid metallic nanostructures array, Sensors and Actuators B-Chemical, 137 (2009) 345-349.
[125] R.L. Eriksen, A. Pors, J. Dreier, A.C. Simonsen, O. Albrektsen, Fabrication of large area homogeneous metallic nanostructures for optical sensing using colloidal lithography, Microelectronic Engineering, 87 (2010) 1471-1474.
[126] S.K. Yang, W.P. Cai, L.C. Kong, Y. Lei, Surface Nanometer-scale patterning in realizing large-scale ordered arrays of metallic nanoshells with well-defined structures and controllable properties, Advanced Functional Materials, 20 (2010) 2527-2533.

[127] J. Ye, N. Verellen, W. Van Roy, L. Lagae, G. Maes, G. Borghs, P. Van Dorpe, Plasmonic modes of metallic semishells in a polymer film, ACS Nano, 4 (2010) 1457-1464.
[128] S.Y. Lee, S.H. Kim, S.G. Jang, C.J. Heo, J.W. Shim, S.M. Yang, High-fidelity optofluidic on-chip sensors using well-defined gold nanowell crystals, Analytical Chemistry, 83 (2011) 9174-9180.
[129] S.K. Yang, F. Xu, S. Ostendorp, G. Wilde, H. Zhao, Y. Lei, Template-confined dewetting process to surface nanopatterns: Fabrication, structural tunability, and structure-related properties, Advanced Functional Materials, 21 (2011) 2446-2455.
[130] A.S. Hall, S.A. Friesen, T.E. Mallouk, Wafer-scale fabrication of plasrnonic crystals from patterned silicon templates prepared by nanosphere lithography, Nano Letters, 13 (2013) 2623-2627.
[131] Z.A. Lewicka, Y. Li, A. Bohloul, W.W. Yu, V.L. Colvin, Nanorings and nanocrescents formed via shaped nanosphere lithography: a route toward large areas of infrared metamaterials, Nanotechnology, 24 (2013).
[132] H.T. Ngo, H.-N. Wang, A.M. Fales, T. Vo-Dinh, Label-free DNA biosensor based on sers molecular sentinel on nanowave chip, Analytical Chemistry, 85 (2013) 6378-6383.
[133] S.P. Scheeler, S. Muhlig, C. Rockstuhl, S. Bin Hasan, S. Ullrich, F. Neubrech, S. Kudera, C. Pacholski, Plasmon coupling in self-assembled gold nanoparticle-based honeycomb islands, Journal of Physical Chemistry C, 117 (2013) 18634-18641.
[134] B. Ai, Y. Yu, H. Mohwald, G. Zhang, B. Yang, Plasmonic films based on colloidal lithography, Advances in Colloid and Interface Science, 206 (2014) 5-16.
[135] X. Gu, Y. Yan, G. Jiang, J. Adkins, J. Shi, Using a silver-enhanced microarray sandwich structure to improve SERS sensitivity for protein detection, Analytical and bioanalytical chemistry, 406 (2014) 1885-1894.
[136] X.F. Gu, Y.R. Yan, G.Q. Jiang, J. Adkins, J. Shi, G.M. Jiang, S. Tian, Using a silver-enhanced microarray sandwich structure to improve SERS sensitivity for protein detection, Analytical and Bioanalytical Chemistry, 406 (2014) 1885-1894.
[137] Z.Q. Liu, H.B. Shao, X.S. Liu, J. Chen, M.L. Liu, G.L. Fu, H.L. Xu, G.Q. Liu, Fabrication and optical properties of novel plasmonic cone-shell crystal, Materials Letters, 134 (2014) 165-167.
[138] H.T. Ngo, H.N. Wang, T. Burke, G.S. Ginsburg, T. Vo-Dinh, Multiplex detection of disease biomarkers using SERS molecular sentinel-on-chip, Analytical and Bioanalytical Chemistry, 406 (2014) 3335-3344.
[139] H.T. Ngo, H.-N. Wang, A.M. Fales, B.P. Nicholson, C.W. Woods, T. Vo-Dinh, DNA bioassay-on-chip using SERS detection for dengue diagnosis, Analyst, 139 (2014) 5655-5659.
[140] S. Picciolini, D. Mehn, C. Morasso, R. Vanna, M. Bedoni, P. Pellacani, G. Marchesini, A. Valsesia, D. Prosperi, C. Tresoldi, F. Ciceri, F. Gramatica, Polymer nanopillar–gold arrays as surface-enhanced Raman spectroscopy substrate for the simultaneous detection of multiple genes, ACS Nano, 8 (2014) 10496-10506.
[141] D. Qi, L. Lu, L. Wang, J. Zhang, Improved SERS sensitivity on plasmon-free TiO_2 photonic microarray by enhancing light-matter coupling, Journal of the American Chemical Society, 136 (2014) 9886-9889.

[142] D. Volpati, E.R. Spada, C.C.P. Cid, M.L. Sartorelli, R.F. Aroca, C.J.L. Constantino, Exploring copper nanostructures as highly uniform and reproducible substrates for plasmon-enhanced fluorescence, Analyst, 140 (2015) 476-482.
[143] S. Xie, J. Yang, X. Xiao, Y. Hou, J. Du, L. Pang, X. Li, F. Gao, Scalable Fabrication of quasi-three-dimensional chiral plasmonic oligomers based on stepwise colloid sphere lithography technology, Nanoscale Research Letters, 10 (2015) 1-9.
[144] X.H. Zhao, M.M.K. Wong, S.K. Chiu, S.W. Pang, Effects of three-layered nanodisk size on cell detection sensitivity of plasmon resonance biosensors, Biosensors and Bioelectronics, 74 (2015) 799-807.
[145] M. Tabatabaei, G.Q. Wallace, F.A. Caetano, E.R. Gillies, S.S.G. Ferguson, F. Lagugne-Labarthet, Controlled positioning of analytes and cells on a plasmonic platform for glycan sensing using surface enhanced Raman spectroscopy, Chemical Science, 7 (2016) 575-582.
[146] T.Q. Wang, G.S. Song, F.C. Liu, Y.Q. Qi, C.S. Luo, X.M. Zhang, Y.N. Li, E.H. Han, Y. Fu, Y.H. Jiao, Mechanical stabilization of metallic microstructures by insertion of an adhesive polymer underlayer for further optical and electrical applications, Journal of Materials Chemistry C, 4 (2016) 3231-3237.
[147] Q.Y. Xiong, J. Wei, S.M. Mahpeykar, L.J. Meng, X.H. Wang, Observation of localized surface plasmons and hybridized surface plasmon polaritons on self-assembled two-dimensional nanocavities, Optics Letters, 41 (2016) 1506-1509.
[148] H.B. Zheng, R. Vallee, I. Ly, R.M. Almeida, T. Rivera, S. Ravaine, Morphological design of gold nanopillar arrays and their optical properties, Journal of Physical Chemistry C, 120 (2016) 1178-1185.
[149] X.F. Liu, C.H. Sun, P. Jiang, Templated fabrication of periodic arrays of metallic attoliter petri dishes, Chemistry of Materials, 22 (2010) 1768-1775.
[150] L.S. Live, O.R. Bolduc, J.F. Masson, Propagating surface plasmon resonance on microhole arrays, Analytical Chemistry, 82 (2010) 3780-3787.
[151] P. Colson, C. Henrist, R. Cloots, Nanosphere lithography: A powerful method for the controlled manufacturing of nanomaterials, Journal of Nanomaterials, 2013 (2013) 19.
[152] A. Al-Haddad, Z. Zhan, C. Wang, S. Tarish, R. Vellacheria, Y. Lei, Facile transferring of wafer-scale ultrathin alumina membranes onto substrates for nanostructure patterning, ACS Nano, 9 (2015) 8584-8591.
[153] H.Y. Jang, S.K. Kim, S. Park, Electromagnetic field enhancement in the multilayer of metallic nanomesh films: Synthesis and application as surface-enhanced Raman scattering substrates, Journal of Physical Chemistry C, 119 (2015) 10585-10591.
[154] M.Y. Kang, X.Y. Zhang, L.W. Liu, Q.W. Zhou, M.L. Jin, G.F. Zhou, X.S. Gao, X.B. Lu, Z. Zhang, J.M. Liu, High-density ordered Ag@Al_2O_3 nanobowl arrays in applications of surface-enhanced Raman spectroscopy, Nanotechnology, 27 (2016).
[155] A. Sangar, A. Merlen, P. Torchio, S. Vedraine, F. Flory, L. Escoubas, L. Patrone, G. Delafosse, V. Chevallier, E. Moyen, M. Hanbucken, Fabrication and characterization of large metallic nanodots arrays for organic thin film solar cells using anodic aluminum oxide templates, Solar Energy Materials and Solar Cells, 117 (2013) 657-662.
[156] D.L. Yu, H.T. Huang, L.F. Lu, J.F. Che, X.Y. Chen, X.F. Zhu, Y. Song, D.D. Li, Templated deposition of multiscale periodic metallic nanodot arrays with sub-10 nm gaps on rigid and flexible substrates, Nanotechnology, 25 (2014).

[157] T. Qiu, W.J. Zhang, X.Z. Lang, Y.J. Zhou, T.J. Cui, P.K. Chu, Controlled assembly of highly Raman-enhancing silver nanocap arrays templated by porous anodic alumina membranes, Small, 5 (2009) 2333-2337.
[158] R. Zakaria, K.S. Hamdan, S.M.C. Noh, A. Supangat, M. Sookhakian, Surface plasmon resonance and photoluminescence studies of Au and Ag micro-flowers, Optical Materials Express, 5 (2015) 943-950.
[159] H. Ko, V.V. Tsukruk, Nanoparticle-decorated nanocanals for surface-enhanced Raman scattering, Small, 4 (2008) 1980-1984.
[160] G. Sauer, G. Brehm, S. Schneider, H. Graener, G. Seifert, K. Nielsch, J. Choi, P. Goring, U. Gosele, P. Miclea, R.B. Wehrspohn, In situ surface-enhanced Raman spectroscopy of monodisperse silver nanowire arrays, Journal of Applied Physics, 97 (2005).
[161] S.J. Lee, A.R. Morrill, M. Moskovits, Hot spots in silver nanowire bundles for surface-enhanced Raman spectroscopy, Journal of the American Chemical Society, 128 (2006) 2200-2201.
[162] L.S. Zhang, P.X. Zhang, Y. Fang, Magnetron sputtering of silver nanowires using anodic aluminum oxide template: A new active substrate of surface enhanced Raman scattering and an investigation of its enhanced mechanism, Analytica Chimica Acta, 591 (2007) 214-218.
[163] J. Yao, G. Pan, K. Xue, D. Wu, B. Ren, D. Sun, J. Tang, X. Xu, Z. Tian, A complementary study of surface-enhanced Raman scattering and metal nanorod arrays, Pure and applied chemistry, 72 (2000) 221-228.
[164] B.L. Broglin, A. Andreu, N. Dhussa, J.A. Heath, J. Gerst, B. Dudley, D. Holland, M. El-Kouedi, Investigation of the effects of the local environment on the surface-enhanced Raman spectra of striped gold/silver nanorod arrays, Langmuir, 23 (2007) 4563-4568.
[165] G.H. Gu, J.S. Suh, Silver nanorods used to promote SERS as a quantitative analytical tool, Journal of Raman Spectroscopy, 41 (2010) 624-627.
[166] C. Lu, Z. Chen, Anodic Aluminum Oxide-Based Nanostructures and Devices, Encyclopedia of Nanoscience and Nanotechnology, 11 (2011) 235-259.
[167] M. Schierhorn, S.J. Lee, S.W. Boettcher, G.D. Stucky, M. Moskovits, Metal–Silica Hybrid Nanostructures for Surface-Enhanced Raman Spectroscopy, Advanced Materials, 18 (2006) 2829-2832.
[168] I. Lombardi, P.L. Cavallotti, C. Carraro, R. Maboudian, Template assisted deposition of Ag nanoparticle arrays for surface-enhanced Raman scattering applications, Sensors and Actuators B-Chemical, 125 (2007) 353-356.
[169] Z. Lu, W. Ruan, J. Yang, W. Xu, C. Zhao, B. Zhao, Deposition of Ag nanoparticles on porous anodic alumina for surface enhanced Raman scattering substrate, Journal of Raman Spectroscopy, 40 (2009) 112-116.
[170] N. Ji, W.D. Ruan, C.X. Wang, Z.C. Lu, B. Zhao, Fabrication of silver decorated anodic aluminum oxide substrate and its optical properties on surface-enhanced Raman scattering and thin film interference, Langmuir, 25 (2009) 11869-11873.
[171] K. Du, I. Wathuthanthri, Y. Liu, W. Xu, C. Choi, Wafer-scale pattern transfer of metal nanostructures on polydimethylsiloxane (PDMS) substrates via holographic nanopatterns, ACS Applied Materials & Interfaces, 4 (2012) 5505-5514.
[172] Z.G. Pang, X.P. Zhang, T.R. Zhai, Hybrid metallic photonic crystals with higher-order coupling processes, Journal of Applied Physics, 110 (2011) 0743131-0743135

[173] X. Ke, B. Lu, J. Hao, J. Zhang, H. Qiao, Facile fabrication of SERS arrays through galvanic replacement of silver onto electrochemically deposited copper micropatterns, Chemphyschem, 13 (2012) 3786-3789.
[174] W.W. Yu, I.M. White, Inkjet printed surface enhanced Raman spectroscopy array on cellulose paper, Analytical Chemistry, 82 (2010) 9626-9630.
[175] T.A. Meier, E. Poehler, F. Kemper, O. Pabst, H.G. Jahnke, E. Beckert, A. Robitzki, D. Belder, Fast electrically assisted regeneration of on-chip SERS substrates, Lab on a Chip, 15 (2015) 2923-2927.
[176] Q. Yang, M. Deng, H. Li, M. Li, C. Zhang, W. Shen, Y. Li, D. Guo, Y. Song, Highly reproducible SERS arrays directly written by inkjet printing, Nanoscale, 7 (2015) 421-425.
[177] I. Kim, I. Junejo, M. Lee, S. Lee, E.K. Lee, S. Chang, J. Choo, SERS-based multiple biomarker detection using a gold-patterned microarray chip, Journal of Molecular Structure, 1023 (2012) 197-203.
[178] H. Wang, A. Dhawan, Y. Du, D. Batchelor, D.N. Leonard, V. Misra, T. Vo-Dinh, Molecular sentinel-on-chip for SERS-based biosensing, Physical Chemistry Chemical Physics, 15 (2013) 6008-6015.
[179] A. Camposeo, L. Persano, R. Manco, Y. Wang, P. Del Carro, C. Zhang, Z.Y. Li, D. Pisignano, Y.N. Xia, Metal-enhanced near-infrared fluorescence by micropatterned gold nanocages, ACS Nano, 9 (2015) 10047-10054.
[180] J. Henzie, M.H. Lee, T.W. Odom, Multiscale patterning of plasmonic metamaterials, Nature Nanotechnology, 2 (2007) 549-554.
[181] M. Kovylina, N. Alayo, A. Conde-Rubio, X. Borrise, G. Hibbard, A. Labarta, X. Batlle, F. Perez-Murano, Au cylindrical nanocup: A geometrically, tunable optical nanoresonator, Applied Physics Letters, 107 (2015).
[182] C.C. Liang, M.Y. Liao, W.Y. Chen, T.C. Cheng, W.H. Chang, C.H. Lin, Plasmonic metallic nanostructures by direct nanoimprinting of gold nanoparticles, Optics Express, 19 (2011) 4768-4776.
[183] B.D. Lucas, J.S. Kim, C. Chin, L.J. Guo, Nanoimprint lithography based approach for the fabrication of large-area, uniformly oriented plasmonic arrays, Advanced Materials, 20 (2008) 1129-1134.
[184] C. Wang, S.Y. Chou, Integration of metallic nanostructures in fluidic channels for fluorescence and Raman enhancement by nanoimprint lithography and lift-off on compositional resist stack, Microelectronic Engineering, 98 (2012) 693-697.
[185] J. Zhu, M.Q. Xue, D. Zhao, M.N. Zhang, L. Duan, Y. Qiu, T.B. Cao, Facile fabrication of metallic nanostructures by tunable cracking and transfer printing, Angewandte Chemie-International Edition, 50 (2011) 12478-12482.
[186] C.Q. Yi, C.W. Li, H.Y. Fu, M.L. Zhang, S.J. Qi, N.B. Wong, S.T. Lee, M.S. Yang, Patterned growth of vertically aligned silicon nanowire arrays for label-free DNA detection using surface-enhanced Raman spectroscopy, Analytical and Bioanalytical Chemistry, 397 (2010) 3143-3150.
[187] R. Kuladeep, L. Jyothi, S. Chakradhar, D.N. Rao, Fabrication of metal nanostructures in a polymer matrix using femtosecond laser writing technique, Optical Engineering, 53 (2014) 0718231-0718234.
[188] B. Xu, R. Zhang, X. Liu, H. Wang, Y. Zhang, H. Jiang, L. Wang, Z. Ma, J. Ku, F. Xiao, H. Sun, On-chip fabrication of silver microflower arrays as a catalytic

microreactor for allowing in situ SERS monitoring, Chemical Communications, 48 (2012) 1680-1682.
[189] B.B. Xu, R. Zhang, X.Q. Liu, H. Wang, Y.L. Zhang, H.B. Jiang, L. Wang, Z.C. Ma, J.F. Ku, F.S. Xiao, H.B. Sun, On-chip fabrication of silver microflower arrays as a catalytic microreactor for allowing in situ SERS monitoring, Chemical Communications, 48 (2012) 1680-1682.
[190] Y. Oh, K. Jeong, Optofluidic SERS chip with plasmonic nanoprobes self-aligned along microfluidic channels, Lab on a Chip, 14 (2014) 865-868.
[191] Y. Deng, M.N. Idso, D.D. Galvan, Q. Yu, Optofluidic microsystem with quasi-3 dimensional gold plasmonic nanostructure arrays for online sensitive and reproducible SERS detection, Analytica Chimica Acta, 863 (2015) 41-48.

Chapter 3

Polarization-dependent SERS from Microarrays

(This chapter is based on the manuscript submitted to Analytica Chimica Acta.)

3.1 Introduction

Surface-enhanced Raman scattering (SERS), a technique that allows a large increase in the Raman scattering efficiency from molecules adsorbed on certain metallic nanostructures, has been attractive for a variety of real-life applications in analytical chemistry, including environmental sensing [1-3]; medical diagnosis and prognosis [4-6]; security detection [7-9]; and many others. The popularity of SERS is mainly attributed to two major advantages offered by the technique: (1) molecular-specific vibrational information; and (2) extraordinary detection sensitivity down to the single molecule level [10-12].

SERS substrates, consisting of the metallic nanostructures, and the molecule(s) of interest are required for SERS measurement(s). The most classical SERS substrate is generated from the aggregation of metal nanoparticles from a colloidal suspension [13, 14]. In this case, batch-to-batch variations in both spectral features and SERS intensities are among the major challenges for their application in analytical chemistry. Supported SERS substrates have been developed through different approaches, including immobilization of metal nanoparticles on solid surfaces (such as glass) via surface chemistry modification [15-18]; fabrication of organized nanostructures through lithographic techniques [19-21]; and other sophisticated nanofabrication methods [22, 23]. Top-down lithography techniques, such as electron-beam lithography [20, 21, 24], laser interference lithography [25, 26], focused ion beam milling [27-29] and others have been used to fabricate nanostructures with well-controlled dimensions. The immobilization of the nanostructures in a solid platform improves the reproducibility and the integrity of the SERS measurements [30]. Another advantage of a solid SERS platform is that it is relatively simple and straightforward to pattern them in a series of regular patches of organized nanostructures, generating microarrays (μarrays). SERS μarrays can be useful in analytical chemistry to achieve multiplexing (i.e. simultaneous sensing from different patches). SERS μarrays can be

integrated in microfluidics architectures. They can even provide an approach to tackle the inhomogeneity issues that have plagued the SERS field, since the results from several μarrays can be averaged in an attempt to control and quantify the SERS variabilities.

In this work, large area (~1 $inch^2$) SERS μarrays were fabricated through a combination of laser interference lithography (LIL) and laser photolithography (LPL). The basic structural design of the nanostructure is a one-dimensional periodic grid, with clear ridges and troughs (nanogratings). The optical characteristic of this type of structure is naturally polarization-dependent. Previous studies have demonstrated the potential of polarization-dependent substrates to eliminate intrinsic interferences arising from solvent [31], temperature [32], and other polarization-independent variables. This ability to self-reference using the proper choice of light polarization could prevent systematic errors. Proof-of-concept demonstration of on-chip SERS detection capability of our μarrays was achieved using an epoxy-perforated membrane [33] that isolated the nanostructures patches into multiple detection channels. There are several previous reports of SERS optofluidic lab-on-chip devices, where the fluidic systems were handled through PDMS micro-channels [34-36], etched-glass microchannels [37], laser-cut channels on different materials, like double-sided tapes [38], and others. The epoxy membrane prepared through deep UV-lithography used in this work offers simplicity and reasonable precision to ensure the proper alignment between the channels and the μarrays. A quinolone derivative antibiotics, 8-quinolinol, which is considered an emergent organic contaminant found in fresh waters, was chosen as analyte for the proof of concept measurements.

3.2 Experimental section

3.2.1 Chemicals and materials

Microposit SC 1827 positive photoresist, Microposit thinner type P, Microposit 351 developer, deionized water (produced through Barnstead Millipore system with resistivity of 18.2 MΩcm), epoxy resin adhesive (NOA 73 from Norland Products Inc.), acetone (ACS reagent grade, supplied by VWR), anhydrous ethanol (ACS reagent grade, supplied by VWR), methanol (ACS reagent grade, supplied by VWR), 4-mercaptopyridine solid (95 % assay, supplied by Sigma-Aldrich) and 8-quinolinol solid (analytical grade, supplied by Sigma-Aldrich), microscope slides.

3.2.2 Substrate fabrication

The 1 inch^2 microscope glass slides (cut from 3 inch x 1 inch slides) were first cleaned by sonication in copious amount of acetone, methanol, ethanol and isopropanol, sequentially, to remove any contaminants on the glass. After oven-dried to remove all the solvents and cooled to room temperature, the glass slides were spin-coated with diluted Microposit SC 1827 positive photoresist (in 1:1 ratio with Microposit thinner type P) at 2000 rpm for 30 seconds. The coated glass slides were pre-baked at temperature of 120 ^{o}C for 10 minutes to remove the solvent from the photoresist layer. The photoresist-coated glass was next mounted on the interference lithography setup (refer to Section 2.3.1) and exposed to a Coherent Ar^+ laser line (λ = 458 nm) at 100 mJ cm^{-2} for 45 seconds. The overall fabrication procedure is illustrated in Figure 3.1. The fabrication of a large area periodic pattern (i.e. nanostructures on the entire 1 inch^2 substrate) was completed after the IL-treated photoresist substrates were developed in diluted Microposit 351 developer (in 1:3 ratio with deionized water), as shown in step 1(b) and (c) in the scheme of Figure 3.1. The solvent development lasted 45 seconds under gentle motion parallel to the main grating axis.

As for the μarrays (i.e. multiple ~900 μm^2 patches of nanostructures on the 1 inch^2 substrate), a second laser exposure of 1.5 minutes was proceeded through a Mylar based photomask which defined the μarrays dimension as illustrated in steps 1(d) and (e). The photoresist substrates were then developed the same way as the large area substrates to ravel the patches of nanostructured μarrays. To add on, the photomask design was prepared using

Adobe Photoshop (Adobe Creative Suite 5.5), addressing two main concerns: (1) the convenience to integrate the μarrays for on-chip measurements later (i.e. sufficient spaces for membrane sealing, refer to Section 3.2.3), and (2) the efficiency to develop the structures under ambient conditions and in a non-clean room setting (i.e. a photomask with sufficiently 'large' dimensions of μarrays was employed as we observed plenty defects, particularly around the edges of μarrays, when μarrays were smaller in sizes e.g. 50 nm x 50 nm).

Lastly, the substrates were coated using electron beam evaporator with either a 80 nm thickness gold film for transmission measurements or a 200 nm thick of gold or silver film for SERS mappings.

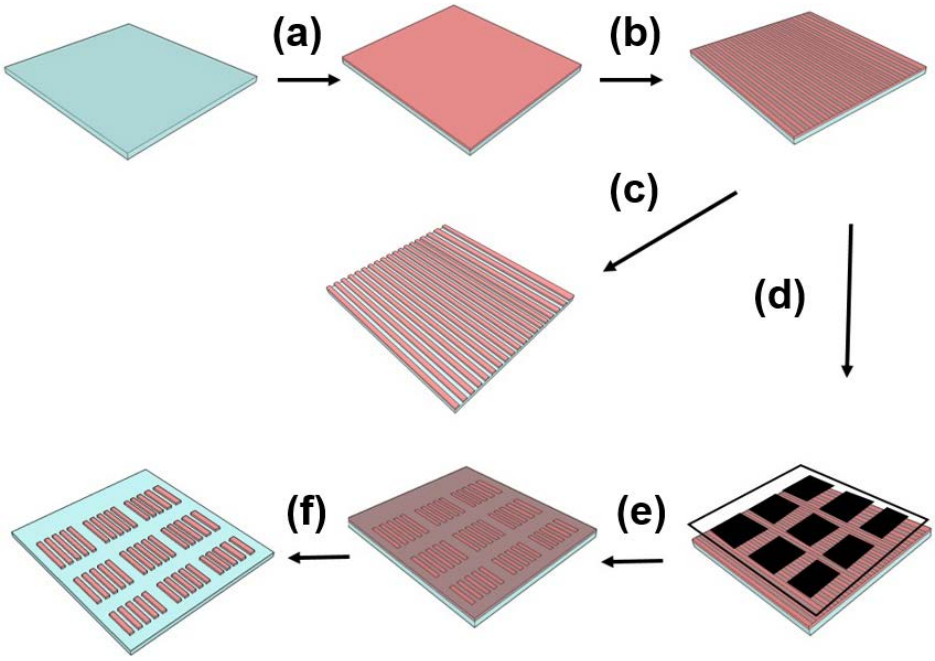

Figure 3.1 Schematic demonstration for SERS substrates fabrication: **(a)** Spin-coating: alcohol-washed glass slide is spin-coated with positive photoresist. **(b)** Laser interference lithography (LIL): the photoresist substrate is exposed to the laser through the interference lithography setup. **(c)** Large area substrate development: the substrate is developed in alkaline developer. **(d and e)** Laser photolithography (LPL): the substrate is direct-exposed to the laser through photomask. **(f)** μarrays development: the μarrays substrate is developed as in (c).

3.2.3 Substrate characterizations

The surface morphology of the substrates was characterized using SEM and AFM. Zero-order white light transmission spectra through the large area substrate (coated with 80 nm thickness of gold) were taken using a miniatured spectrometer (*model:* USB 2000, Ocean Optics, Inc). The polarization states of the incident beam were manipulated using linear polarizer films (i.e. perpendicular and parallel polarization to the main axis of the nanogratings).

The zero-order transmission characterization of μarrays were done using an in-house optical setup where a 1 mW laser beam (635 nm, model: LPS-635-FC from Thorlabs) first passed through a collimator, then a glass polarizer and a half-wave plate, as illustrated in Figure 3.2. The beam was then expanded by entering a duo-lens system (focal lengths of the lenses : f_2 / f_1 = 500 mm / 16.5 mm) to ensure that the entire gold μarrays substrate was illuminated. The beam transmitted through the substrate was de-magnified and focused by another duo-lens system (focal lengths of the lenses : f_4 / f_3 = 50 mm / 150 mm) before detecting by a CCD camera (model: DCC 1545 M from Thorlabs).

Polarized SERS measurements (i.e. large area substrate coated with 200 nm thickness of silver) of 4-mercaptopyridine (10 μM in 1 % aqueous ethanol) was obtained with a Raman microscope (model: In via Renishaw, 632.8 nm excitation). The polarization state of the excitation laser was rotated by placing a half-wave plate in the incoming path of the laser.

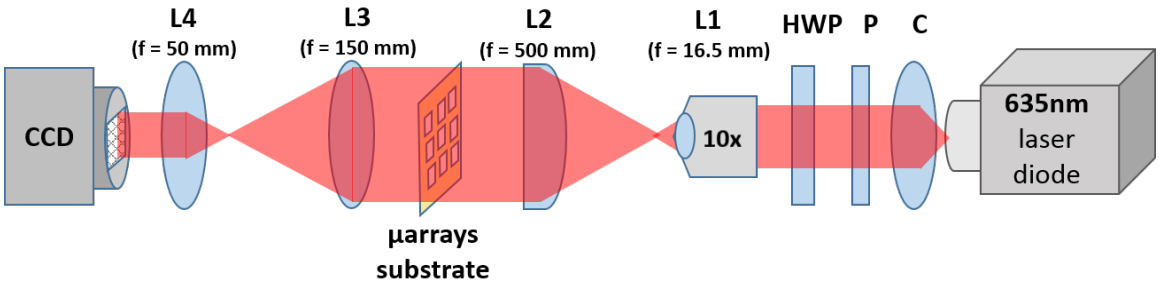

Figure 3.2 Schematic transmission measurement setup for μarrays substrate. (L = lens; f = focal length; HWP = half-wave plate; P = glass polarizer; and C = collimator)

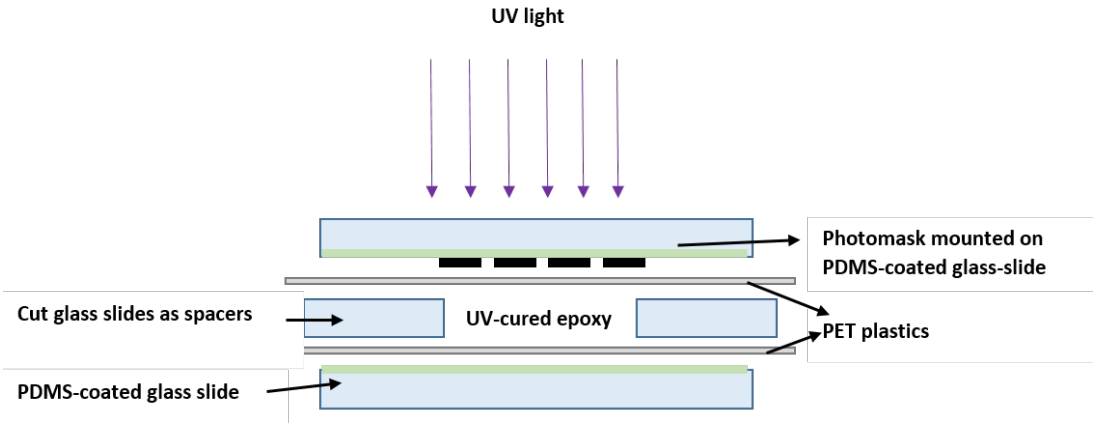

Figure 3.3 Perforated epoxy membrane fabrication scheme using deep-UV lithography.

3.2.4 On-chip SERS μarrays setup

Epoxy membranes with perforated channels were prepared, according to previous reported procedure by Zheng et al.[33] with some minor modifications. The membrane fabrication scheme can be found in Figure 3.3. Briefly, a small piece (~3 inch x 3 inch) of transparency polyethylene terephtalate (PET) plastic was adhered to a PDMS-coated glass slide. Another two 0.5 inch x 1 inch cut glass slides were arranged above the PET plastic, acting as a spacer and defining the thickness of the final membrane (see Figure 3.3). The epoxy was then drop-coated between the two spacers and another piece of PET plastic was gently laid on top of the epoxy, followed then by the Mylar-based photomask. The entire system was exposed to UV light (350 watts) for 50 seconds. The system was then disassembled and the membrane was developed using acetone, leading to microchannels. The membrane with perforated micro-channels was then aligned with the μarrays and sealed with glass cover slip, aided by a thin layer of grease to seal the whole device. Extreme caution was required to prevent contamination of the SERS substrate by the grease.

3.2.5 On-chip SERS measurements using μarrays

A series of 8-quinolinol aqueous solution (in <1 % methanol to improve solubility of the solids) in different concentrations, ranging from 0 to 60.0 ppm were introduced to the channels. SERS mapping of 20 x 20 μm^2 was then carried out on three arrays in each channel, using 785 nm laser (10 % power density, 0.5 s exposure time, 50x ultra long

objective lens). The area under the SERS band at 723 cm^{-1} was then normalized and plotted in calibration curve with increasing concentrations of 8-quinolinol.

3.3 Results and discussion

3.3.1 Fabrication and characterization of SERS substrates

Large area (overall substrate size of 1 $inch^2$) and μarrays (~ organized 900 μm^2 patches on 1 $inch^2$ substrate) nanogratings were fabricated by LIL. The surface morphological features of the nanograting structures on both large area and μarrays substrates were characterized using SEM and AFM. Figure 3.4(a) indicates that the resulting nanogratings were reasonably homogeneous and the periodicity of the structures (~ 450 nm) were uniform within the area of 1 $inch^2$. The μarray-to-μarray periodicity variation was examined through AFM and was found to be less than 5 %. The μarrays were arranged in six column containing either nine or fifteen nanogratings each (depending on the Mylar photomask design). Each of the μarray was an individual SERS sensing area. The white light diffraction picture of a gold-coated μarrays can be seen in Figure 3.4(b) and the inset shows the SEM image of the nanograting structures in one of the μarrays. Figure 3.4(c) presents a typical AFM image from the nanogratings.

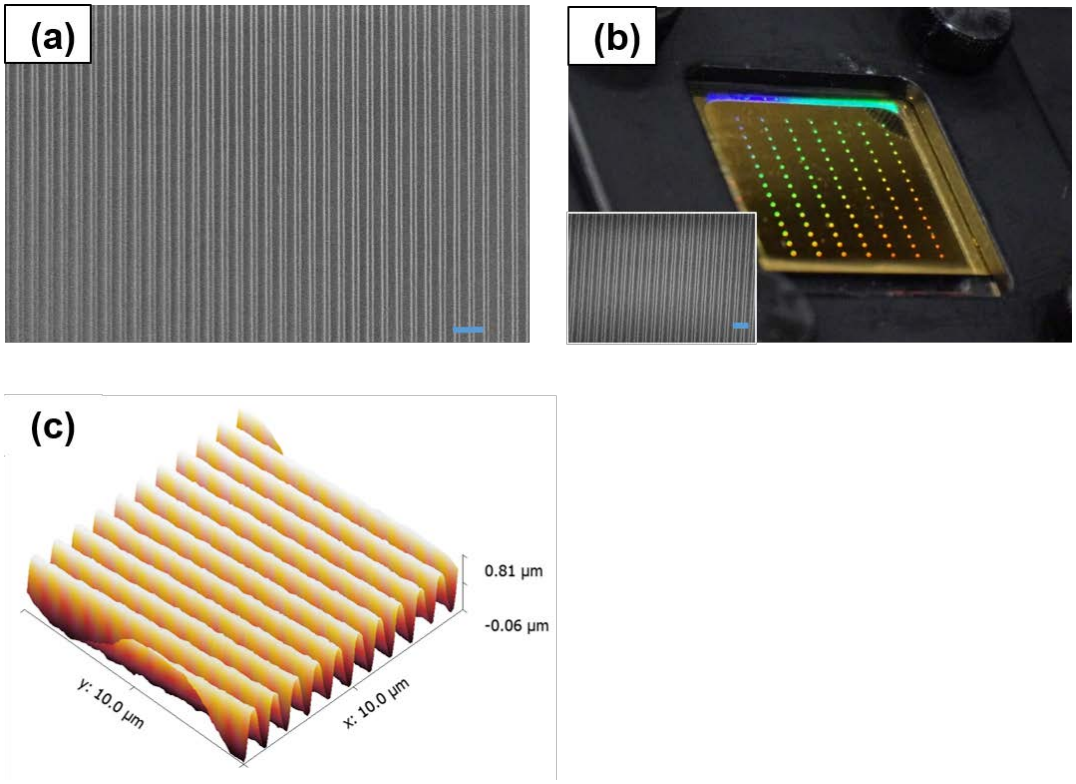

Figure 3.4 (a) SEM image of the large area nanograting substrate. **(b)** White light diffraction picture of the gold-coated µarrays. The inset is the SEM image of one of the µarrays. The blue scale bars are 1 µm. **(c)** An AFM image of a large area nanograting substrate.

3.3.2 Polarization-dependent optical transmission

Zero-order white light transmission through the large area metal-coated nanogratings substrates were measured. The plane-polarization direction (relative to the nanograting features) of the incident white light was manipulated using polarizer films to demonstrate the polarization dependency of the transmitted light. Typical white light transmission data for a gold nanograting (80 nm Au thickness) is shown in Figure 3.5(a). The TM-polarized (plane polarization perpendicular to the grating features) transmission spectrum demonstrates clear peaks and dips, which have been assigned to different scattering orders, including contribution from distinct interfaces (metal – glass and metal – air interfaces) [39]. The incidence of TM (or perpendicular-polarized light) on an one-dimensional gold nanogratings allows the excitation of surface plasmon (SP) resonance on the metal interfaces. This enables an increase in the transmitted field, a phenomenon related to the extraordinary optical transmission (EOT) [40]. The light transmission through noble metals (i.e. Au, Ag and Cu) nanostructures can then be tuned through their periodicity to allow maximum transmission within visible wavelength(s) [40]. In our case, the transmission maxima through Au nanogratings occur at 491 nm and 617 nm, respectivelly, as seen in Figure 3.5(a). The minimum observed in the TM-transmission spectrum (i.e. 528 nm), is the Wood's diffraction anomaly that happens when the diffracted waves from the nanogratings emerges tangentially to the main axis of the gratings' interface [41]. Ideally, the TE-polarized transmission spectrum from a plasmonic nanogratings should provide minimum response, as an smooth gold film which is not SP-active. Nonetheless, Figure 3.5(b) shows a fairly broad transmission band, also peaked at 535 nm, for the measurement taken using TE-polarization. Previously, the existence of similar broad transmission band from gold films has been assigned to bulk plasmon [42, 43] and interband electron transitions [43]. This type of transmission band was reported to become less significant for smoother Au films [42]. The observed transmission band in Figure 3.5(b) might then carry additional contributions from the presence of random roughness on the gold interface, which promotes optical transmission through the film.

In order to demonstrate the transmission characteristics of the gold μarrays and their potential to perform imaging-based biosensing, a laser diode with excitation wavelength at

635 nm (near to the SP resonance of the nanograting structure (see Figure 5(a)) was used to illuminate all elements simultaneously (experimental setup described in Figure 3.2). Since the excitation source delivered a single-wavelength, the amplitude variations of the transmission through the entire substrate were imaged at the CCD camera, as seen in Figure 3.5(b). The half-wave plate (HWP) in the setup (Figure 3.2) allowed us to rotate the polarization state of the laser to image the polarization dependency of the μarrays. Figure 3.5(b)(i) exhibits the transmission image of the nanograting μarrays at TM-polarization. The occurrence of enhanced transmission phenomenon on each of the μarrays can be viewed from the patches of bright spots in Figure 3.5(b)(i). When the polarization of the incident laser was the TE-mode, minimal amount of light passed through the arrays (see Figure 3.5(b)(ii)).

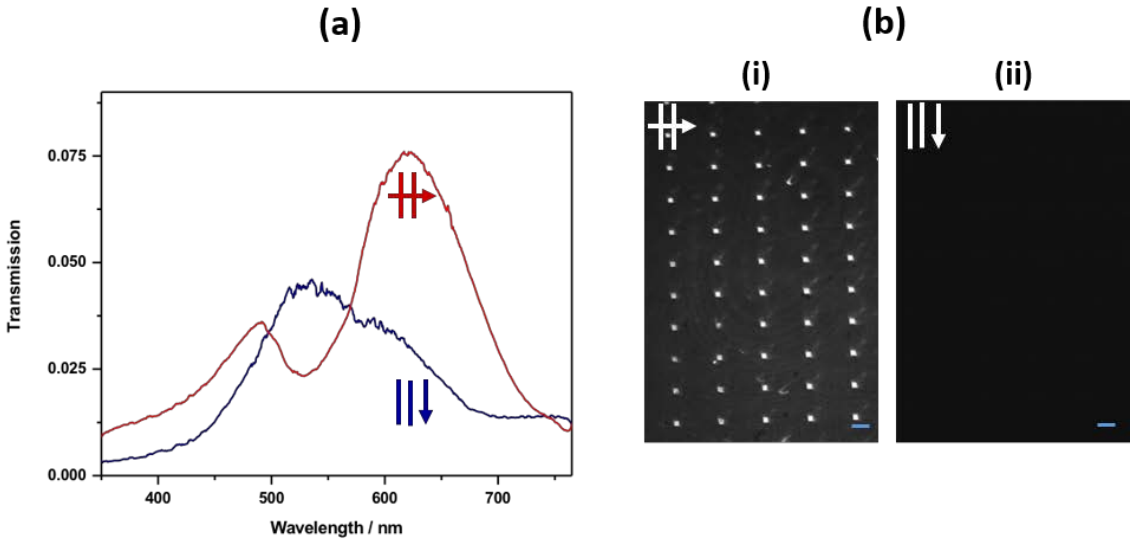

Figure 3.5 (a) The white light transmission spectra of the large area nanograting substrate evaporated with 80 nm of gold at (red) TM/perpendicular polarization and (blue) TE/parallel polarization. **(b)** The transmission image of gold μarrays at (i) TM-polarization and, (ii) TE-polarization, using 635 nm incident laser. The blue scale bars are 1 mm.

3.3.3 Polarization-dependent SERS

SERS measurements were first realized using 4-mercaptopyridine (4MPy) as probe molecules. Figure 3.6 shows an example of the results obtained for 4MPy adsorbed on a 200 nm silver-evaporated substrate. The SERS response was obtained under two different

laser incidence polarizations directions (perpendicular and parallel to the grating structure, as discussed above). A HWP was introduced into the incoming laser path of the Raman microscope to rotate the state of the incident laser polarization and ensure that the same area was probed throughout the experiment. Prior to the measurements, the nanogratings were incubated into 10.0 μM 4MPy solution for 20 minutes, and subsequently washed with copious amount of deionized water to remove any residual (non-adsorbed) molecules and dried under nitrogen. SERS measurements were taken using 633 nm laser line, 100x objective (NA = 0.90). The surface of the substrate was probed by SERS-mapping. The mapping area was 26 x 26 pixels (step size: 1 μm) and mappings were obtained for both perpendicular (Figure 3.6(a)) and parallel polarizations (Figure 3.6(b)) of the incident laser relative to the main axis of the grating structures. Figure 3.6(c) shows a typical average SERS spectrum from the mapped area (average over 675 spectra), with the two major SERS bands at 990 and 1080 cm^{-1} assigned to ring breathing and C-S bond vibration [44] of 4Mpy molecules. It is worth noting that the 2D-colormap images in Figure 3.6(a) and (b) were simulated using SERS intensity at 1080 cm^{-1} from each pixel in the mapped area on the substrate.

As observed in Figure 3.6(c), the average SERS spectrum of 4MPy obtained using TM- polarization was roughly five times stronger than the one obtained with TE polarization. This indicates that the nanogratings substrate presented a reasonable polarization anisotropy. SERS, as one of the plasmon-assisted spectroscopy, relies strongly on field enhancements at the interface of metal nanostructures. When the SP frequency of the metal nanostructures is in resonance with the incident laser, the SP excitation enables localized field at special regions on the metal surface, known as the SERS hot spots. Molecules at the hot spot region (i.e. adsorbates) experiences then enhanced excitation (and scattering) through this mechanism. For anisotropic structures, such as the metal-evaporated nanogratings studied here, SPs are only excited (generating “hot-spots”) when the incident laser is TM or perpendicular-polarized against the long axis of the grating, since the external electric field will interact with nano-confined free electrons on those conditions. This phenomenon is perfectly observed in Figure 3.6 (red). Some residual SERS intensity was observed (refer to Figure 3.6 (blue)) for TE-polarization. In fact, this observation is in

consonant with our earlier finding where a broad band spectrum was found in TE-mode transmission of gold nanogratings (see Figure 3.5(a)). The random roughness and fabrication defects on the silver nanogratings, lead to local field excitations (SERS 'hot-spots') that are not polarization dependent. Therefore, molecules adsorbed on random roughness and defects contributed to the SERS activity at TE-polarization.

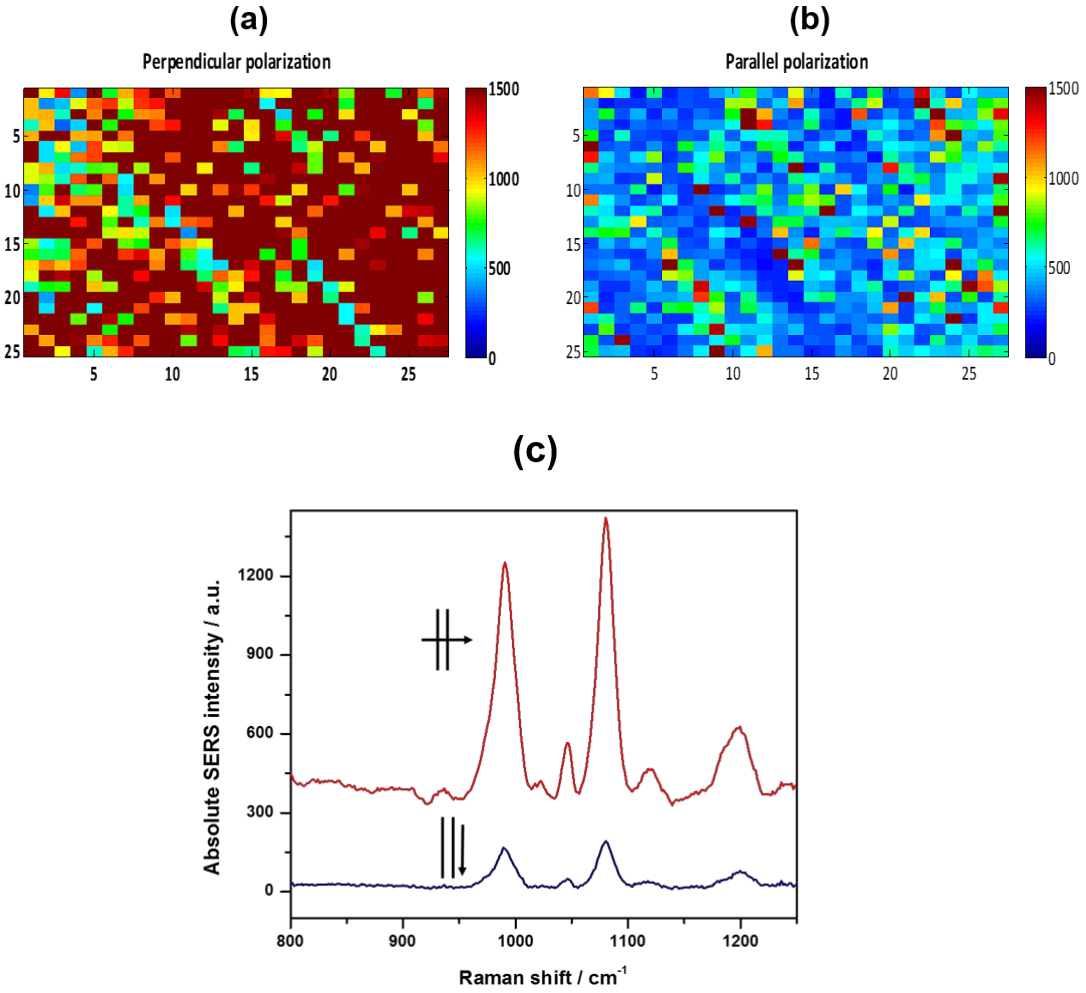

Figure 3.6 SERS mappings of 4MPy at **(a)** TM-polarization, and **(b)** TE-polarization. **(c)** The average SERS spectra of 4MPy (adsorbed from 10.0 μM solution) (red) TM/perpendicular polarization and (blue) TE/parallel polarization against the nanogratings main. Polarization directions are illustrated in the figure. Excitation: 633 nm. All the spectra generated from the mapping measurements were subject to baseline-correction before colormap simulation in (a) and (b), and spectra averaging in (c).

3.3.3 On-chip detection - SERS nanogratings μarrays

The μarrays of metallic nanogratings were utilized for SERS quantification of an environmental pollutant. Microfluidic channels were fabricated in an epoxy-based membrane to deliver different samples to the sensing surface of the μarrays (nanogratings). A sample of the perforated epoxy membrane containing micro-channels is shown in Figure 3.7(a,b). The design of the channels solely depended on the Mylar photomask used during the deep-UV lithography. The membrane consisting of microchannels aligned to the SERS active μarrays (see Figure 3.7(b)) isolated the substrate into a few isolated systems. This is useful to improve the detection throughput, especially when integrated with microfluidic facility, since a single SERS substrate is now able to handle a few samples (i.e. multiplexing applications). Additionally, instead of using the continuous nanostructure arrays, in this work we patterned the substrates into multiple μarrays (i.e. micro-patches) containing nanogratings for SERS environmental quantifications. We believed that the nanostructures patterning is helpful to improve the analytical perspective of the detections (i.e. the signals from a few μarrays can be averaged to improve the precision of the quantifications).

Different concentrations of aqueous 8-quinolinol solutions (varying from 0 – 60.0 ppm) were introduced into the microchannels. SERS mapping measurements were then carried out on an area of ~ 11 x 11 pixels (step size: 2 μm) in at least three μarrays in each column. The average spectra were then baseline corrected and the area under the Raman band at 723 cm^{-1}, which is one of the signature out-of-plane vibration modes [45] of 8-quinolinol, was used for the calibration plot shown in Figure 3.7(a). The experiments were realized using an ultra-long working distance 50 x lens (NA=0.55), to focus the laser (and collect scattered light) in each array through an optical window. This lens has a deeper focal volume and probed into the photoresist underneath the gold film, generating a spectral background in the region ~ 1100 – 1400 cm^{-1}. This background was absent in experiments that used objective lens with higher NA. Since the background was well-separated from the 723 cm^{-1} band, we were able to use it (~1100 cm^{-1} background band) as a constant intensity reference in the calibration plot, improving quantification. On the other hand, the lowest concentration attempted in this work was 1.18 ppm (i.e. limit of detection for the present methodology) and we can reliably detect the SERS signal of 8-quinolinol out from spectral

noise. The states-of-the-art for quinolones antibiotics (fluoroquinolones) detections in the aqueous samples is mostly associated with chromatographic techniques in tandem with mass spectrometry (MS). The limit of detections achieved were reported as low as sub-ppb (ug/L). However, these methods were subject to extensive sample pre-concentration (~ 100 – 1000 times) to improve the detections. It is worth mentioning that the present SERS detection of quinolones has not been subject to any pre-concentration and we believe that the LOD of the proposed detection can be brought lower with the pre-concentration step, as well as, the further optimization of SERS substrates.

Lastly, to demonstrate the potential application of polarization-dependent SERS substrates, polarization subtraction technique has been attempted to correct the background from the SERS substrate. In this case, SERS measurements of 8-quinolinol were recorded at the same spot under TM- and TE-polarized incident laser. As shown in Figure 3.8, the SERS response at TM-polarization ($S^{\perp}$) contains both contributions from analytes (i.e. 8-quinolinol) and the photoresist background; while under TE-polarization (S_{II}) that was previously corrected its artificial polarization effects from HWP [31], shows smaller contribution from the analyte (i.e. 8-quinolinol) signal due to the reduced SP excitation (refer to Section 1.4.2.2). To be specific, the observed signal at TE-polarization, $S_{II,observed}$, was compensated for the HWP's artificial polarization effects, σ, using Equation 3.1 [31]:

$$\sigma = \frac{I'_{\perp}}{I'_{II}} \qquad (3.1)$$

where $I'_{\perp}$ is the Raman intensity of silicon measured without HWP and I'_{II} is the intensity at the 45^{o} rotation with respect to the axis of HWP. In this case, a smooth silicon wafer (non-SP supported), was used to obtain the true artificial polarization effects from HWP. This resulted in the following expression for S_{II}:

$$S_{II} = \sigma\, S_{II,observed} \qquad (3.2)$$

The subtraction of S_{II} from $S^{\perp}$ then yielded $S_{analytical}$ (find Equation 3.3), which is the 8-quinolinol (i.e. the analyte) signal eliminated from those non-polarization dependent background, as seen in Figure 3.8.

$$S_{analytical} = S_{\perp} - S_{II} \qquad (3.3)$$

It is worth mentioning that prior to the background correction, all the spectra were baseline-corrected (Savitsky Golay filter at window size of 3 % of the total data points within the spectral region, Matlab 7.12.0) and smoothed (Savitsky Golay at 20 points window, OriginPro 8.5). In addition to that, from Figure 3.8, the spectral contributions of the background band at ~1100 cm^{-1} are seen to be relatively consistent in both TM- and TE-incidence polarization. This might indicate that the background could be attributed to the photoresist polymer, which was polarization-insensitive.

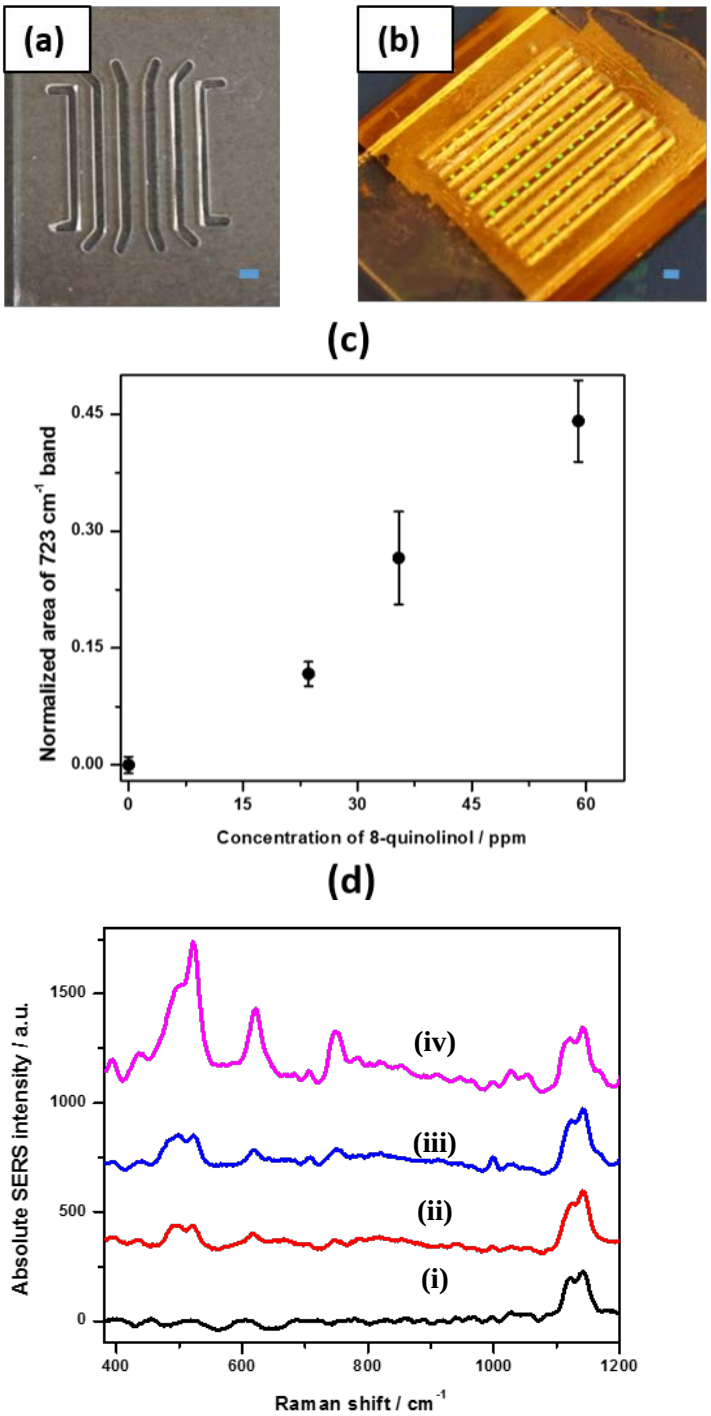

Figure 3.7 (a, b) Deep-UV lithography prepared epoxy membrane and the on-chip setup assembled to the SERS μarrays substrate. The blue scale bars are 2 mm. **(c)** Calibration curve plotted with average SERS intensity of normalized SERS band at 753 cm^{1} as a function of increasing concentration of 8-quinolinol. **(d)** 8-quinolinol SERS spectra at different concentrations: (i) 0 ppm, (ii) 23.2 ppm, (iii) 35.4 ppm and (iv) 59.0 ppm.

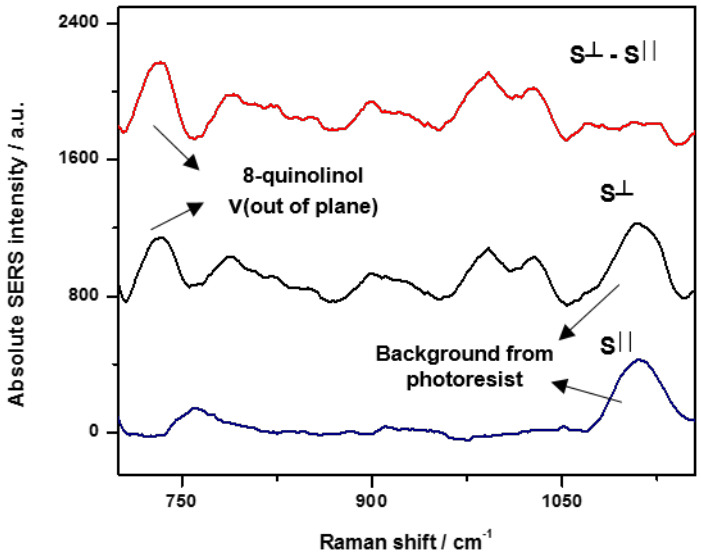

Figure 3.8 $S_{analytical}$ ($S_{\perp}$ - S_{II}) of 8-quinolinol is shown in red, obtained by eliminating S_{II} (blue) from $S_{\perp}$ (black). The spectra have been baseline-corrected and smoothed.

3.4 Conclusions

In conclusion, we have developed polarization-dependent large area and μarray nanogratings (array-to-array periodicity variation of <5 %) for SERS detection based on laser interference lithography (LIL). The proof-of-concept SERS simultaneous detection has been demonstrated through an integrated microfluidic system consisting of fabricated SERS μarrays. Deep-UV lithographic was used to prepare micro-perforated epoxy membranes to define the microchannels to isolate the metallic nano-patches into a few segregated fluidic systems. A widely applied antimicrobial in agricultural industry, 8-quinolinol, was chosen as the species of interest in this work. As a member of quinolone-based antibiotics, 8-quinolinol has emerged as one of the pharmaceutical contaminants in environment due to its persistent environmental fate. The successful detection of this molecule in different concentrations at ppm level using the SERS μarrays fluidic system illustrates the potential to develop the LIL substrate into an integrated lab-on-chip-based microfluidic environmental sensing system. The significant incidence-polarization dependency of the substrates might also be advantageous. Particularly, the polarization

dependence can be used as self-reference during real-time detection to tackle those non-polarization-sensitive spectral interferences.

Lastly, the proposed fabrication methodology using LIL, as compared to the state-of-the-art nanofabrication techniques (i.e. EBL and FIB) with greatest precision, stands out as a high-throughput fabrication technique with reasonable fabrication resolution (mainly relies on the wavelength of the laser incidence employed). The patterned area of the fabrication is scalable and a large-area fabrication can be achieved quickly, since the fabrication mechanism is primarily composed of the optical light interference (between the laser incidence and Lloyd's mirror's reflection) and the photon-absorption process (leading to either molecular decomposition, or complexation, depends on the types of photoresist used). Additionally, when compared to the other large area-based nanofabrications (e.g. NSL, AAO-template assisted lithography), LIL fabrication is distinctive in its long-range uniformity in the nanostructures patterning. This is important in analytical quantifications, since the degree of nanostructures' uniformity would directly impact to the SERS enhancement homogeneity of the substrates. The LIL fabrication process is also much less hazardous as there is no need to utilize those corrosive solvents (e.g. hydrofluoric acid or other strong etching solution) to develop the nanostructures. On the other hand, LIL process is readily coalesced with other optical-based lithographic techniques, for instance, UV-lithography, as demonstrated in the μarrays fabrication of this work. This is a great precedence of LIL process as it provides flexibility in nanofabrication to prepare a variety of nanostructures depending on the needs of the applications. The limitations of LIL process with respect to this work, however, lie mostly on the nature of this lithography process, where a photoresist is needed during the optical patterning. Generally, the existence of photoresists on the SERS substrates increases the background of the SERS signals, since most of the components in the photoresists are fluorescence-active or even SERS-active. This is particularly pronounced when a high focal volume objective lens is needed in the SERS acquisitions, as happened in this work (Section 3.3.3). Moreover, the employment of LIL process on those curvy- (e.g., flexible or soft support) or shiny (e.g., silicone wafer) is tricky as these structures might complicate the optical interference process that is required in LIL. In the following chapter (Chapter 4), the combination of template-stripping and LIL

demonstrates an alternative to improve the flexibility of LIL in patterning different surfaces of solid supports (i.e. optical fiber tips and glass slides).

3.5 References

[1] T. Vo-Dinh, SERS chemical sensors and biosensors: new tools for environmental and biological analysis, Sensors and Actuators B: Chemical, 29 (1995) 183-189.

[2] R.A. Alvarez-Puebla, J.D.S. dos Santos, R.F. Aroca, SERS detection of environmental pollutants in humic acid-gold nanoparticle composite materials, Analyst, 132 (2007) 1210-1214.

[3] R.A. Halvorson, P.J. Vikesland, Surface-enhanced Raman spectroscopy (SERS) for environmental analyses, Environmental Science & Technology, 44 (2010) 7749-7755.

[4] J.C.Y. Kah, Early diagnosis of oral cancer based on the surface plasmon resonance of gold nanoparticles, International Journal of Nanomedicine, 2 (2007) 785-798.

[5] M.Y. Sha, H. Xu, S.G. Penn, R. Cromer, SERS nanoparticles: a new optical detection modality for cancer diagnosis, (2007).

[6] R.A. Alvarez-Puebla, L.M. Liz-Marzán, SERS-based diagnosis and biodetection, Small, 6 (2010) 604-610.

[7] T.Y.-J. Han, C.A. Valdez, T.Y. Olson, S.H. Kim, J.H. Satcher Jr, Rapid detection and identification of energetic materials with surface enhanced raman spectrometry (SERS), Google Patents, 2015.

[8] T. Yang, X. Guo, H. Wang, S. Fu, H. Yang, Magnetically optimized SERS assay for rapid detection of trace drug-related biomarkers in saliva and fingerprints, Biosensors and Bioelectronics, 68 (2015) 350-357.

[9] A. Hakonen, T. Rindzevicius, M.S. Schmidt, P.O. Andersson, L. Juhlin, M. Svedendahl, A. Boisen, M. Käll, Detection of nerve gases using surface-enhanced Raman scattering substrates with high droplet adhesion, Nanoscale, 8 (2016) 1305-1308.

[10] K. Kneipp, Y. Wang, H. Kneipp, L.T. Perelman, I. Itzkan, R.R. Dasari, M.S. Feld, Single molecule detection using surface-enhanced Raman scattering (SERS), Physical Review Letters, 78 (1997) 1667-1670.

[11] K. Kneipp, H. Kneipp, H.G. Bohr, Single-molecule SERS spectroscopy, Surface-enhanced Raman scattering, Springer2006, pp. 261-277.

[12] J. Kneipp, H. Kneipp, K. Kneipp, SERS—a single-molecule and nanoscale tool for bioanalytics, Chemical Society Reviews, 37 (2008) 1052-1060.

[13] R.G. Freeman, K.C. Grabar, K.J. Allison, R.M. Bright, et al., Self-assembled metal colloid monolayers: An approach to SERS substrates, Science, 267 (1995) 1629.

[14] D. Philip, G. Aruldhas, SERS spectra of 2-Aminophenol in silver colloids, Journal of Solid State Chemistry, 116 (1995) 427-431.

[15] C.J. Addison, A.G. Brolo, Nanoparticle-containing structures as a substrate for surface-enhanced Raman scattering, Langmuir, 22 (2006) 8696-8702.

[16] M. Fan, A.G. Brolo, Silver nanoparticles self-assembly as SERS substrates with near single molecule detection limit, Physical Chemistry Chemical Physics, 11 (2009) 7381-7389.

[17] G.F.S. Andrade, M.K. Fan, A.G. Brolo, Multilayer silver nanoparticles-modified optical fiber tip for high performance SERS remote sensing, Biosensors and Bioelectronics, 25 (2010) 2270-2275.
[18] M.K. Fan, M. Thompson, M.L. Andrade, A.G. Brolo, Silver nanoparticles on a plastic platform for localized surface plasmon resonance biosensing, Analytical Chemistry, 82 (2010) 6350-6352.
[19] A.K. Sheridan, A.W. Clark, A. Glidle, J.M. Cooper, D.R.S. Cumming, Multiple plasmon resonances from gold nanostructures, Applied Physics Letters, 90 (2007).
[20] N.A. Abu Hatab, J.M. Oran, M.J. Sepaniak, Surface-enhanced Raman spectroscopy substrates created via electron beam lithography and nanotransfer printing, ACS Nano, 2 (2008) 377-385.
[21] G. Das, F. Mecarini, F. Gentile, F. De Angelis, H.G. Mohan Kumar, P. Candeloro, C. Liberale, G. Cuda, E. Di Fabrizio, Nano-patterned SERS substrate: Application for protein analysis vs. temperature, Biosensors and Bioelectronics, 24 (2009) 1693-1699.
[22] S. Cherukulappurath, T.W. Johnson, N.C. Lindquist, S.H. Oh, Template-stripped asymmetric metallic pyramids for tunable plasmonic nanofocusing, Nano Letters, 13 (2013) 5635-5641.
[23] X. Ke, B. Lu, J. Hao, J. Zhang, H. Qiao, Facile fabrication of SERS arrays through galvanic replacement of silver onto electrochemically deposited copper micropatterns, Chemphyschem, 13 (2012) 3786-3789.
[24] R. Gillibert, M. Sarkar, J.F. Bryche, R. Yasukuni, J. Moreau, M. Besbes, G. Barbillon, B. Bartenlian, M. Canva, M.L. de la Chapelle, Directional surface enhanced Raman scattering on gold nano-gratings, Nanotechnology, 27 (2016).
[25] H. Ahn, P. Thiyagarajan, L. Jia, S. Kim, J. Yoon, E.L. Thomas, J. Jang, An optimal substrate design for SERS: dual-scale diamond-shaped gold nano-structures fabricated via interference lithography, Nanoscale, 5 (2013) 1836-1842.
[26] T. Siegfried, M. Kind, A. Terfort, O.J. Martin, M. Zharnikov, N. Ballav, H. Sigg, Reusable plasmonic substrates fabricated by interference lithography: a platform for systematic sensing studies, Journal of Raman Spectroscopy, 44 (2013) 170-175.
[27] J.R. Anema, A.G. Brolo, P. Marthandam, R. Gordon, Enhanced Raman Scattering from Nanoholes in a Copper Film, Journal of Physical Chemistry C, 112 (2008) 17051-17055.
[28] Y. Lin, J. Liao, Y. Ju, C. Chang, A. Shiau, Focused ion beam-fabricated Au micro/nanostructures used as a surface enhanced Raman scattering-active substrate for trace detection of molecules and influenza virus, Nanotechnology, 22 (2011) 185308.
[29] K. Sivashanmugan, J. Liao, J. You, C. Wu, Focused-ion-beam-fabricated Au/Ag multilayered nanorod array as SERS-active substrate for virus strain detection, Sensors and Actuators B: Chemical, 181 (2013) 361-367.
[30] M. Fan, G.F. Andrade, A.G. Brolo, A review on the fabrication of substrates for surface enhanced Raman spectroscopy and their applications in analytical chemistry, Analytica Chimica Acta, 693 (2011) 7-25.
[31] J. Anema, A. Brolo, The Use of Polarization-dependent SERS from scratched gold films to selectively eliminate solution-phase interference, Plasmonics, 2 (2007) 157-162.
[32] F. Bahrami, M. Alam, J. Aitchison, M. Mojahedi, Dual polarization measurements in the hybrid plasmonic biosensors, Plasmonics, 8 (2013) 465-473.
[33] Y. Zheng, W. Dai, D. Ryan, H. Wu, Fabrication of freestanding, microperforated membranes and their applications in microfluidics, Biomicrofluidics, 4 (2010) 036504.

[34] M.R. Hoonejani, A. Pallaoro, G.B. Braun, M. Moskovits, C.D. Meinhart, Quantitative multiplexed simulated-cell identification by SERS in microfluidic devices, Nanoscale, 7 (2015) 16834-16840.
[35] A. Pallaoro, M.R. Hoonejani, G.B. Braun, C.D. Meinhart, M. Moskovits, Rapid identification by surface-enhanced Raman spectroscopy of cancer cells at low concentrations flowing in a microfluidic channel, ACS Nano, 9 (2015) 4328-4336.
[36] H.Z. Zhao, Y. Xu, C.Y. Wang, R. Wang, S.T. Xiang, L. Chen, Design and fabrication of a microfluidic SERS chip with integrated Ag film@nanoAu, RSC Advances, 6 (2016) 14105-14111.
[37] S. Lee, S. Joo, S. Park, S. Kim, H.C. Kim, T.D. Chung, SERS decoding of micro gold shells moving in microfluidic systems, Electrophoresis, 31 (2010) 1623-1629.
[38] Y. Deng, M.N. Idso, D.D. Galvan, Q. Yu, Optofluidic microsystem with quasi-3 dimensional gold plasmonic nanostructure arrays for online sensitive and reproducible SERS detection, Analytica Chimica Acta, 863 (2015) 41-48.
[39] Z. Sun, Y.S. Jung, H.K. Kim, Role of surface plasmons in the optical interaction in metallic gratings with narrow slits, Applied physics letters, 83 (2003) 3021-3023.
[40] T.W. Ebbesen, H.J. Lezec, H.F. Ghaemi, T. Thio, P.A. Wolff, Extraordinary optical transmission through sub-wavelength hole arrays, Nature, 391 (1998) 667-669.
[41] R.W. Wood, XXVII. Diffraction gratings with controlled groove form and abnormal distribution of intensity, Philosophical Magazine Series 6, 23 (1912) 310-317.
[42] Z.G. Pang, X.P. Zhang, T.R. Zhai, Hybrid metallic photonic crystals with higher-order coupling processes, Journal of Applied Physics, 110 (2011).
[43] A. Axelevitch, B. Apter, G. Golan, Simulation and experimental investigation of optical transparency in gold island films, Optics Express, 21 (2013) 4126-4138.
[44] J. Hu, B. Zhao, W. Xu, B. Li, Y. Fan, Surface-enhanced Raman spectroscopy study on the structure changes of 4-mercaptopyridine adsorbed on silver substrates and silver colloids, Spectrochimica Acta Part A: Molecular and Biomolecular Spectroscopy, 58 (2002) 2827-2834.
[45] J. Chowdhury, M. Ghosh, T.N. Misra, pH-dependent surface-enhanced Raman scattering of 8-hydroxy quinoline adsorbed on silver hydrosol, Journal of Colloid and Interface Science, 228 (2000) 372-378.

Chapter 4

Template Stripping Fabricated Plasmonic Nanogratings for Chemical Sensing

(This chapter is based on the paper recently accepted in Plasmonics.)

4.1 Introduction

The fabrication of nanostructures has been a vibrant research area in the last few years. A main drive for the wide interest in the field is the potential for applications of nanostructures in chemical sensing and detection [1-3]. In the specific case of metallic nanostructures, the chemical sensing mechanism is based on the excitation of surface plasmon (SP) modes at the interface between the metal and the medium containing the analyte of interest. Several types of metallic nanostructures, such as nanoparticles [4, 5], nanoholes [6, 7] , nanoslits [8], and nanogratings [9], are able to support SP-modes when the resonance conditions are satisfied. The developments of these "plasmonic" sensors have been centered in the desire of generating structures that optimize analytical figure-of-merits, such as sensitivity, resolution and limit-of-detection (LOD). Nonetheless, the possible commercial translation of those types of nanosensors also depends on the complexity of the fabrication process. In this regard, processing time, cost and ease for mass-production also become important evaluation parameters.

Plasmonic nanosensors have been fabricated by different techniques, ranging from chemical synthesis to nanolithography [10]. A variety of nanofabrication methods have been explored in recent decades, mainly due to the emergence of advanced lithography facilities in various research centers around the world. Among them, electron beam lithography (EBL) and focused-ion beam (FIB) milling are the two techniques that allow maximum control over the fabrication precision and resolution. Therefore, these techniques have been widely used to fabricate different types of nanostructures for prototypes and proof-of-concept experiments [11]. The limitations of these techniques; however, are related to their low throughput and their inability to quickly pattern larger areas. Interference lithography (IL) offers an alternative that provides large area patterning of periodic nanostructures with easy manipulation of the nanostructure geometric parameters, which is useful for sensor

optimization [12]. This maskless lithography technique normally utilizes the optical interference between two laser beams to produce a uniform periodic pattern that impress a photoresist [13]. The technology is relative time and cost-efficient and compatible with the common fabrication approaches currently used in microfabrication [14].

In this work, the IL technique was used to fabricate nanograting templates that were transferred to different glass surfaces. The template-stripping procedure has been reported [15] to yield metallic nanostructures capable of plasmonic-based chemical sensing. This strategy has not only leveraged the available nanofabrication methods, but it has greatly improved the fabrication throughput. Here we demonstrated the implementation of IL template-stripping procedure to transfer the nanogratings pattern to glass slides (1 $inch^2$) and optical fiber tips (OFTs) with small contact surface (~50 microns of core size). Plasmonic nanogratings structures (made of either Au or Ag) have been explored for chemical sensing [8, 16]. Typically, the transmission of white light through those one-dimensional nanostructures (with grooves and ridges) presents clear dips and peaks in the visible-NIR range. Another aspect of the one-dimensional nanostructures presented here is their dependence on the incident light polarization. This property has been explored to eliminate non-polarization dependent background interferences [17].

4.2 Experimental section

4.2.1 Chemicals and materials

Microposit SC 1827 positive photoresist, Microposit thinner type P, Microposit 351 developer, deionized water (produced through Barnstead Millipore system with resistivity of 18.2 MΩcm, 99.5% D-(+)-glucose (supplied by Sigma), epoxy resin adhesive (NOA 84 from Norland Products Inc.), Sylgard® 184 Silicone elastomer kit (elastomer and curing agent, supplied by Dow Corning Corporation), standard microscope slides (supplied from PEARL), optical fiber (AFS from Thorlabs with core and cladding size of 50 and125 microns)

4.2.2 Template preparation via IL

Microscope glass slides (1 in^2) and optical fiber tips (OFT – 50 μm core diameter) were used as support for the plasmonic structures. The glass slides were first sonicated in a water bath and then cleaned with copious amounts of acetone, methanol, ethanol, and isopropanol, respectively. After oven-drying (T ~120 ^oC) and cooling to room temperature, the glass slides were ready to be spin-coated with 1:1 Microposit SC 1827 positive photoresist diluted with Microposit thinner type P at 2000 rpm for 30 seconds. The substrates were then pre-baked in an oven at 120 ^oC for 10 minutes to remove the solvent from the photoresist layer. Next the glass substrate coated with the photoresist was then mounted on the interference lithography setup (Lloyd's interferometer) [18] and exposed to a 458nm laser (Coherent argon ion laser) once for 45 seconds (the energy density of the laser was 100 mJ/cm^2). After the laser exposure, the photoresist film was developed in 1:3 Microposit 351 developer diluted with deionized water (produced through Barnstead Millipore system, resistivity of 18.2 MΩ.cm) for 45 seconds under gentle motion parallel to the grating axis to generate a uniform 1-dimensional photoresist template. The photoresist templates were then evaporated with either gold or silver using electron beam and thermal evaporator (Angstrom Engineering Glove-box Evaporator, deposition rate of 1 Å/s). The film thicknesses were either 100 or 200 nm. Similar cleaning procedure was applied to a bare OFT (model AFS from Thorlabs, core diameter of 50 μm), which had been previously plane-cleaved and polished.

4.2.3 Template-stripping procedure

The stripping procedure is summarized in Figure 4.1. A silver (or gold) evaporated on the photoresist template was pressed against a glass slide coated with the epoxy adhesive (step (a) in Figure 4.1). The sandwiched system was then exposed to light from a 100 W incandescent lamp. The sandwiched system was left in a benchtop and illuminated overnight (~ 12 hours) at room temperature. When the epoxy was cured (i.e. epoxy is vulcanized/solidified completely), the patterned silver (or gold) was stripped from the original template (step b, in Figure 4.1). The stripped substrate was subject to a final rinsing with ~ 5% NaOH to remove any remaining photoresist from the metal surface. The surface morphology of the substrates was then characterized by scanning electron microscope

(SEM) and atomic force microscope (AFM) with operating conditions as follows: Mode: tapping, scan rate: 0.05 line per second, tip: silicon AFM probe (TAP190-G-50, supplied by Ted Pella, Inc.).

4.2.4 Surface plasmon resonance (SPR) refractive index sensing with template stripped (large area) substrates

The SPR measurements for the glass slides coated with metallic nanogratings were realized in transmission mode at normal incidence using an UV/Vis/NIR spectrometer (Perkin Elmer Lambda 1050). Small modifications were required on the sample and reference compartments to host a liquid cell with the patterned samples. The cell was fabricated from transparent poly dimethylsiloxane (PDMS), which allow liquid to be flown to a 400 μL sealed pocket in contact to the surface (sensing area 2 x 2 cm^2) of the metallic substrate. Briefly, the PDMS cell was prepared using Sylgard® 184 Silicone elastomer kit with elastomer and curing agent's ratio of 10:1 and cured in a oven at 90 ^oC for 45 minutes (resulting thickness at sensing area ~ 2 mm). Glucose solutions with different concentrations were prepared to test the SPR sensor response to different bulk refractive indexes.

4.2.5 Optical fiber experiments

The surface plasmon resonance-based refractive index measurements were also realized using a bifurcated optical fiber (model BIF400-VIS-NIR from Ocean Optics) and bare optical fiber (OF) adapter (model F-AM-SMA from Newport). One arm of the fiber was illuminated from a white light source (model LS-1 from Ocean Optics, optimized wavelength ranges 360 - 2000 nm, power output 6.5 watts), through a collimator. The second arm was connected to a spectrometer (model USB 2000 from Ocean Optics) through a SMA connector and the sensing tip was a gold nanograting structure prepared using the same IL-template stripping procedure described above was connected using the fiber adapter as mentioned earlier, also through a SMA connector.

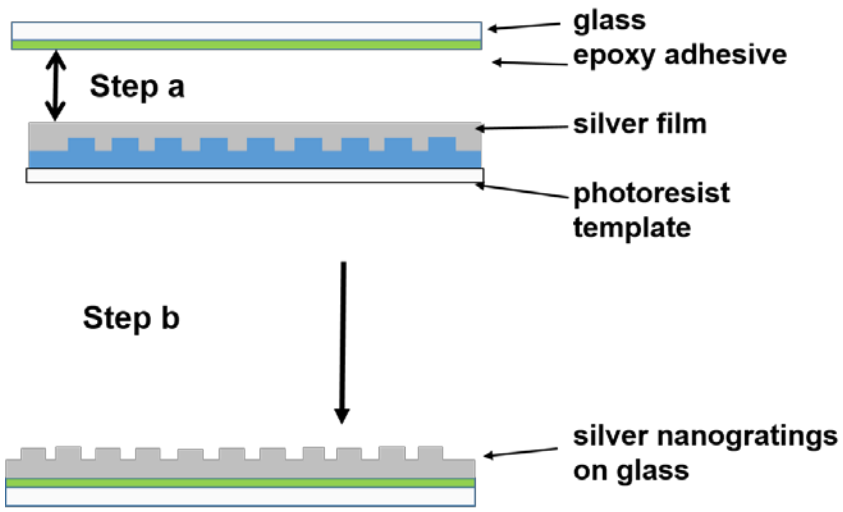

Figure 4.1 Template stripping procedure: Step a. Silver- or gold-evaporated photoresist template was pressed against a glass slide with the epoxy adhesive; Step b. When the epoxy cured, the patterned silver was stripped off from the original template. The substrate was then rinsed with dilute NaOH to remove the remaining photoresist from the metal.

4.3 Results and discussion

4.3.1 Substrate characterizations

The IL - template stripping procedure, illustrated in Figure 4.1, yielded one-dimensional grating nanostructures with a final patterned area of 1 inch^2. Figure 4.2(a) shows the SEM image of the patterned surfaces. The periodicity of the gratings was 450 nm and the height of the ridges was 75 nm. Small morphogical defects (roughness) can be noticed in Figure 4.2, which partly justified the variation of the optical sensitivity on refractive index (RI) variations (substrate-to-substrate sensitivity variation was less than 20% - see below). Additionally, the roughness of the substrate was examined before and after the template stripping procedure through atomic force microscopy (AFM). The AFM result, presented in Figure 4.2(b, c), shows that the overal roughness of the nanostructures was significantly reduced after the stripping procedure.

Zero-degree transmission spectrum through those large area patterned substrates led to clear peaks and dips at TM-polarization (linear polarization perpendicular to the direction of the grating lines), as shown in Figure 4.3(a)(i). The plasmonic response of nanoslit structures has been extensively studied by several research groups [8, 16]. Briefly, the

transmission bands through periodic nanoslit structures have been assigned to contributions from different surface modes on the plasmonic grating[16]. These include contributions from (i) localized SPR from the nanostructures and roughness, (ii) cavity modes (Fabri-Perot-type of effect), and (iii) coupling from the nearby nanograting features [16].The transmission through a 200-nm thickness silver nanogratings presented in Figure 4.3(a)(i) agrees well with the optical transmission properties reported on the previous findings[8]. The features (peaks and valleys) in the transmission spectrum in Figure 4.3(a)(ii) vanishes when the measurement was taken at TE (linear polarization parallel to the direction of the grating lines) polarization. The lack of features for TE excitation can be explained by the homogeinety of the electric field when the incidence polarization is parallel to the structures. The strong polarization-dependence observed in Figure 4.3(a) can potentially provide a control channel in chemical sensing experiments; for instance, to eliminate interferences from experimental variables that are polarization independent [17].

4.3.2 Surface plasmon resonance (SPR) band assignments

The SPR from an one-dimensional metallic nanogratings can be approximated through equation 1.9 (refer to section 1.4.2.2) [8, 16, 18]:

$$\lambda_{spr} = \frac{P}{m}\sqrt{\frac{\varepsilon_d \varepsilon_m}{\varepsilon_d + \varepsilon_m}} \;;\; m = 1 \qquad (1.9)$$

where λ_{spr} is the surface plasmon resonance wavelength, P is the periodicity of the nanogratings, m is the mode of the resonance, ε_d is the dielectric constant for the the dielectric side of the interface and ε_m is the dielectric constant for the metal side of the interface. The transmission spectrum from silver nanogratings in air was found to be significantly different as compared to that in water (refer to Figure 4.3(b)). The calculated (using Equation 1 for m=1) SPR mode of a silver nanogratings (λ_{spr}) is expected to shift from ~ 470 nm (dielectric properties of Ag obtained from ref. [19]) in air to about 585 nm in water. This resonance in water matches reasonably to the observed transmission features in Figure 4.3(a)(i) (also shown in Figure 4.3(b)(ii)). Another resonant mode in Figure 4.3(a)(i) should arise from the other interface between epoxy and silver. This resonance is

expected to occur at ~ 630 nm (considering n_{epoxy} = 1.46). This is again, comparable to the observed transmission features in Figure 4.3(a)(i).

The relative straightforward assignment obtained with equation 1.9 can be further confirmed experimentally by Figure 4.4. Figure 4.4 shows the dependence of the transmission features with changes in the refractive index of the aqueous dielectric in contact to the metallic grating. It is possible to observe in Figure 4.4 that the transmission wavelength red-shifts in response to the refractive index changes (refer to Figure 4.4) only for the transmission features ~ 550 nm. In contrast, the resonant features at ~ 630 nm were almost unaffected by the changes of refractive indexes in the solution, as seen in Figure 4.4. This can be explained by considering the buried metal-epoxy interface is not signficantly altered by the solution refractive index. On the other hand, the mode assigned to the water/analyte solution-silver nanogratings interface is expected to depend strongly on the optical properties of the aqueous solution.

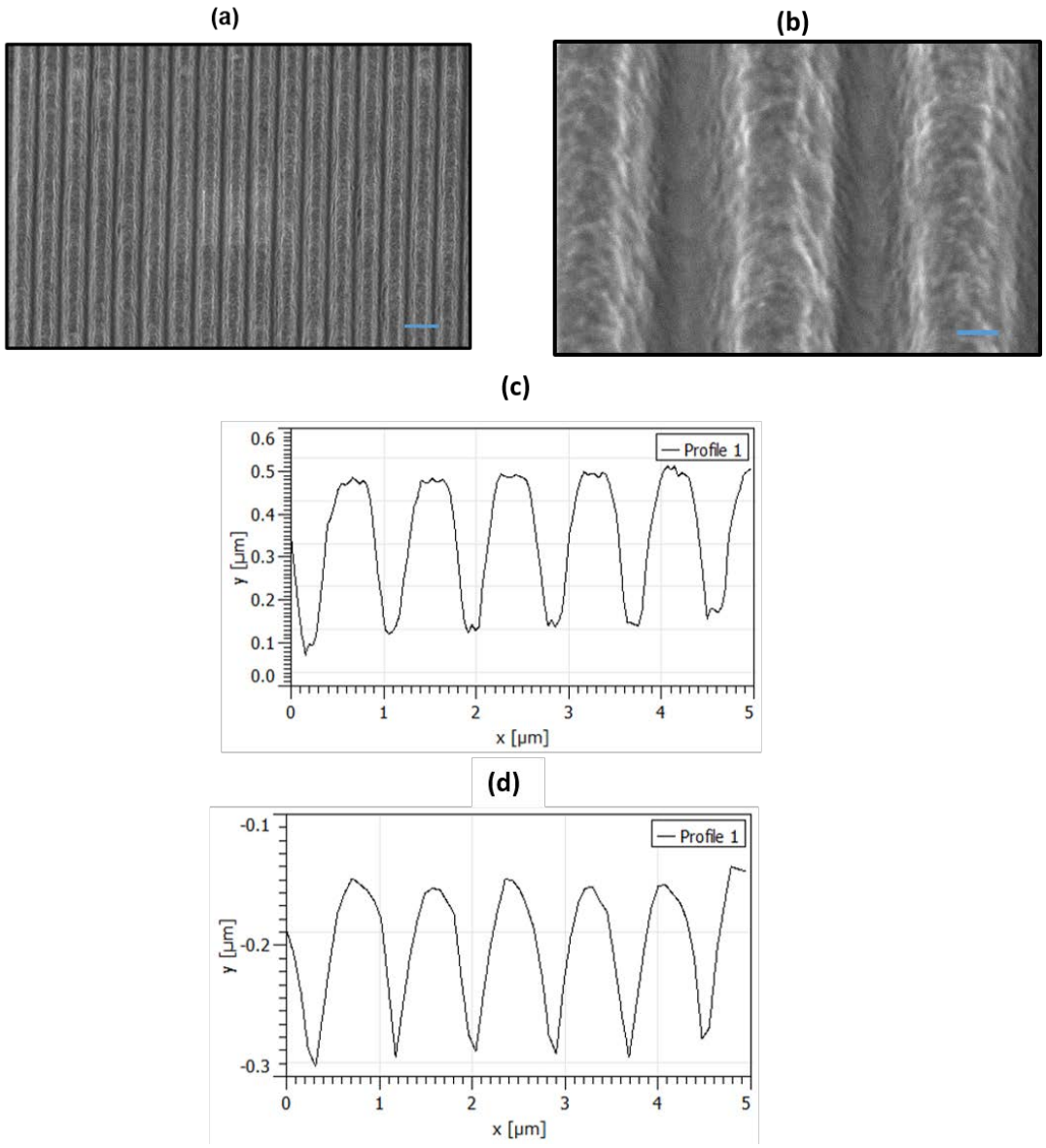

Figure 4.2 (a, b) Scanning electron micrograph of the template-stripped nanograting silver substrate. The blue scale bars in (a) represents 600 nm and (b) 50 nm. The topological (cross-section) measurements using AFM before **(c)** and after **(d)** template stripping procedure from 200 nm Ag nanogratings.

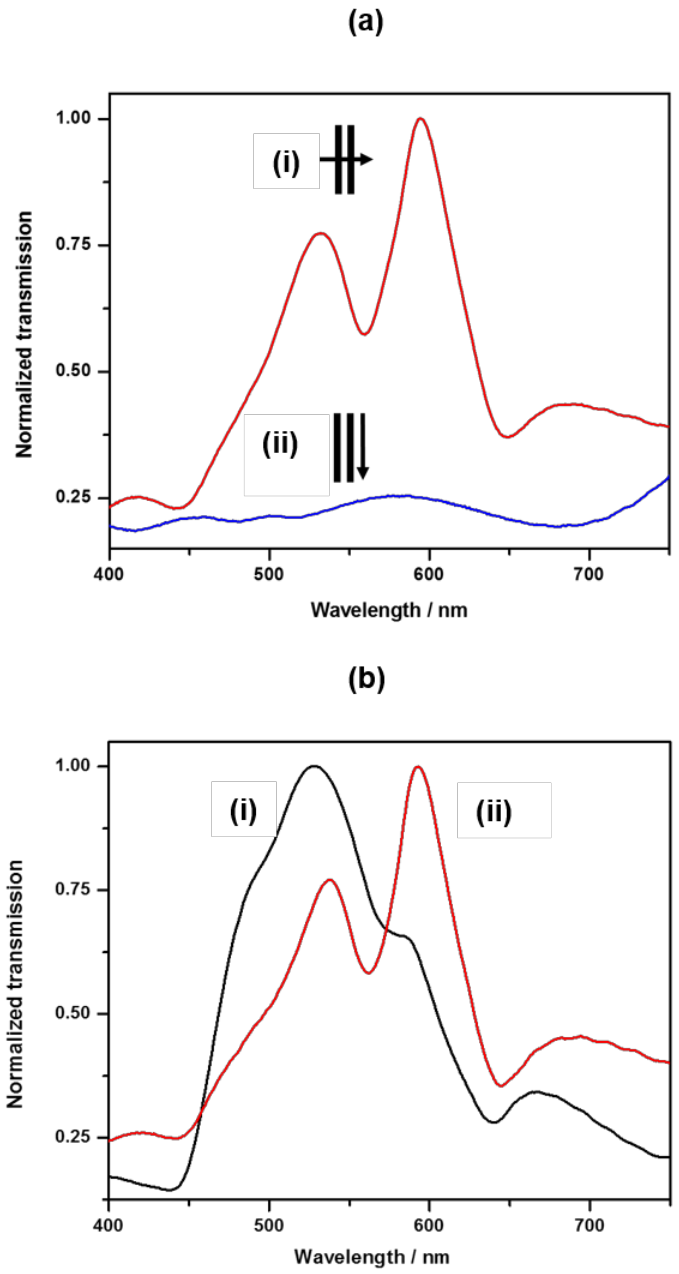

Figure 4.3 (a) Transmission spectra for the silver nanogratings under two different polarization states of incidence light (i, red) light polarization perpendicular to the structure orientation (TM-polarization); and (ii, blue) light polarization parallel polarization to the structure (TE-polarization). Both transmission spectra in (a) have been normalized to the transmission maximum of (a)(i). **(b)** Transmission spectra of silver nanogratings in (i, black) air and (ii, red) water. Both transmission spectra have been normalized to the respective transmission maxima.

4.3.3 Sensing measurements

The polarization dependence observed in Figure 4.3(a) was used to correct for polarization-independent background, such as, for instance, the effect of room temperature variations. The transmission spectra were then expressed using the following equation [17] (Equation 4.1):

$$T_{corrected} = \frac{I_{\perp} - I_{\parallel}}{I_{\perp} + I_{\parallel}} \qquad (4.1)$$

where $I_{\perp}$ is the transmission intensity at TM polarization and $I_{\parallel}$is the transmission intensity at TE polarization.

The transmission measurements for the sensing experiments were taken using an ordinary UV/Vis/NIR spectrometer. A thin PDMS cell was fabricated and used to exposed the nanograting substrates to aqueous solutions with different refractive indexes. The refractive index of glucose solutions of different concentrations ranged from 1.3354 to 1.3550, were read using refractometer after each transmission measurement. Normalized transmission spectra (according to equation 4.1) from different glucose solutions are presented in Figure 4.4. The SPR wavelength shifts with refractive index changes were then quantified using the integrated response (IR) method [20]. In this case, the whole visible spectrum, from 400 to 700 nm, were taken into account. Previously, our group and collaborators have employed this IR method to quantify nanohole SPR sensing and demonstrated an improvement of up to 90 % to the signal-to-noise ratio [24]. The IR equation is given below (Equation 4.2):

$$IR = \sqrt{\int_{\lambda_1}^{\lambda_2} \left| D(\lambda)^2 - \overline{D(\lambda)^2} \right| d\lambda} \qquad (4.2)$$

where $D(\lambda)$ is the difference in signal between a reference and a measured spectrum and $\overline{D(\lambda)}$ is the average of the difference in signal over the entire spectrum. In our particular case, the spectrum obtained from the aqueous solution with the lowest refractive index (n=1.3354) was used as reference.

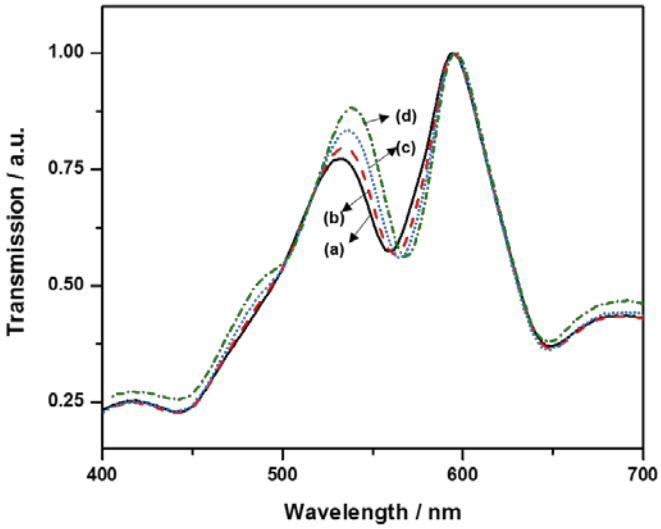

Figure 4.4 Transmission spectra for the silver nanogratings under perpendicular polarization states of incidence light in different refractive indexes solution **(a)** 1.3354, **(b)** 1.3401, **(c)** 1.3453, and **(d)** 1.3523. All transmission spectra were normalized to the respective transmission maxima.

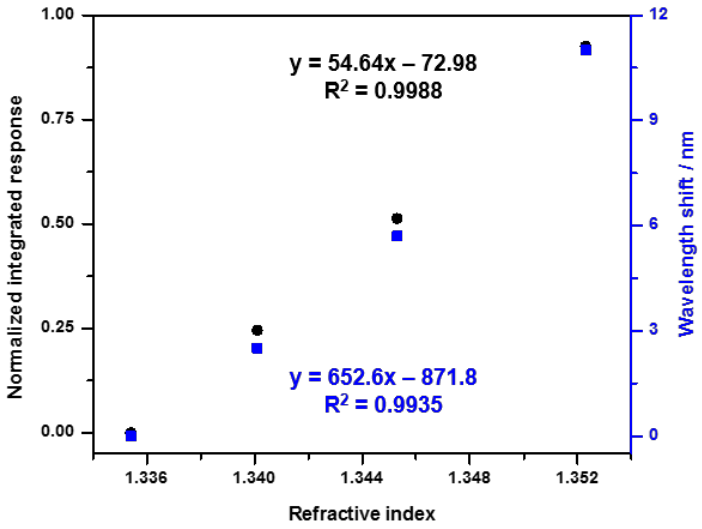

Figure 4.5 Normalized integrated response (y axis at left) and wavelength shift in the region between 545 – 560 nm (y-axis at right) plot as a function of the refractive index of the solution for 200-nm thick Ag nanogratings. The integrated response data were calculated from the normalized data of perpendicular-polarized transmissions to the respective parallel-polarized spectrum. (Refer to Appendix A for the IR plot with replicate measurements.)

The normalized IR response for 200-nm thick Ag nanogratings was plotted against the solution refractive index in Figure 4.5. The calibration sensitivity (discussed in section 1.3.1.1) the large area SPR substrates, calculated from the slope of Figure 4.5, were in the range between 50 to 160 IR/RIU, depending on the type of metal (Ag or Au), and on the thickness of the metal film. A summary of the experimental sensitivity values are shown in Figure 4.6. Typically in the literature, calibration sensitivity of plasmonic sensors are given in nm/RIU. Therefore, for sake of comparison, the calibration sensitivity was also recorded in the nm/RIU scale. In this case, the wavelength shifts of the SPR band (in the region between 545 – 560 nm, see Figure 4.4) were quantified. The shifts were measured at the full-width of half maximum (FWHM) of the SPR bands of the transmission maxima-normalized spectra. The first transmission spectrum in the series (i.e. in solution medium of the smallest refractive index) was used as reference and the wavelength shifts were read relative to that reference spectrum (i.e. a line was drawn at FWHM in the region of 545 – 560 nm and the respective wavelength shift was read based on the line). The wavelength shifts as a fuction of refractive index changes are also shown in Figure 4.5.The values of the calibration sensitivity (slope of the line in Figure 4.5) were between 500-600 nm/RIU (again depending of parameters, such as nature of the metal and film thickness, see Figure 4.6). This calibration sensitivity range is comparable to values that has been reported from other grating-based plasmonic substrates [6].

The structure reported here was prepared in a large area using a relative simple and inexpensive procedure. Another figure-of-merit to compare plasmonic sensor is the sensor resolution (refer to section 1.3.1.4), defined as the minimum refractive index change detectable by the device. The resolution was calculated from the calibration sensitivity values and the experimental variation measured by our detection system (either in wavelength or in IR), obtained from multiple measurements from the same sample [6]. Figure 4.6 shows the calibration sensitivity and resolution of nanogratings of different types of metal (silver or gold) and thickness of the metal film (100 or 200 nm) .The reproducibility of our fabrication procedure is represented in Figure 4.6 as an error bar in the sensitivity values, which were calculated from the average of three samples. The 100-nm thickness silver nanogratings demonstrated the sensor resolution (8.35×10^{-5} / RIU) in Figure 4.6. The

100 nm-transferred gold nanogratings exhibited the best sensing reproducibility of ~15%, which might be related to the chemically inert properties of gold metal. In order to further rationalize our findings in Figure 4.6, the substrates were examined by AFM (Figure 4.7(a-c)). It was observed that the 100-nm Ag nanograting presented more fractures (deformation) on the surface and consistantly showed more random roughness (refer to Figure 4.7(b)), as compared to 200-nm Ag nanogratings and 100-nm Au nanogratings (Figure 4.7 (a) and (c)). This might explain the larger variation shown (substrare-to-substrate reproducibility) observed in Figure 4.6 for the 100 nm Ag nanograting. On the other hand, the thinner Ag film should allow better transmission through the interaction between the plasmonic interfaces [21], which in turn improves the sensitivity of the system.

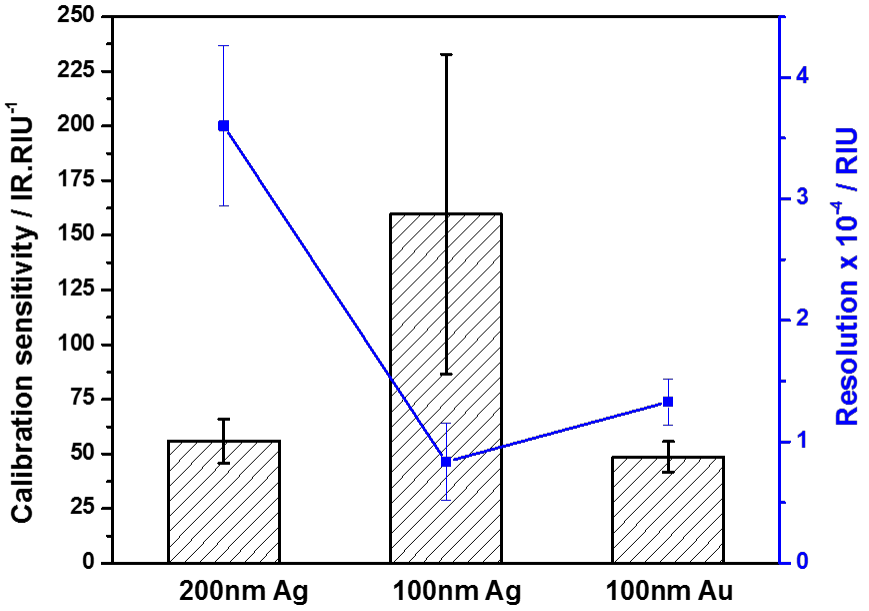

Figure 4.6 Comparison of the refractive index calibration sensitivity and resolution. (left). 200 nm Ag nanograting, (middle), 100 nm Ag nanograting, and (right) 100 nm Au nanograting.

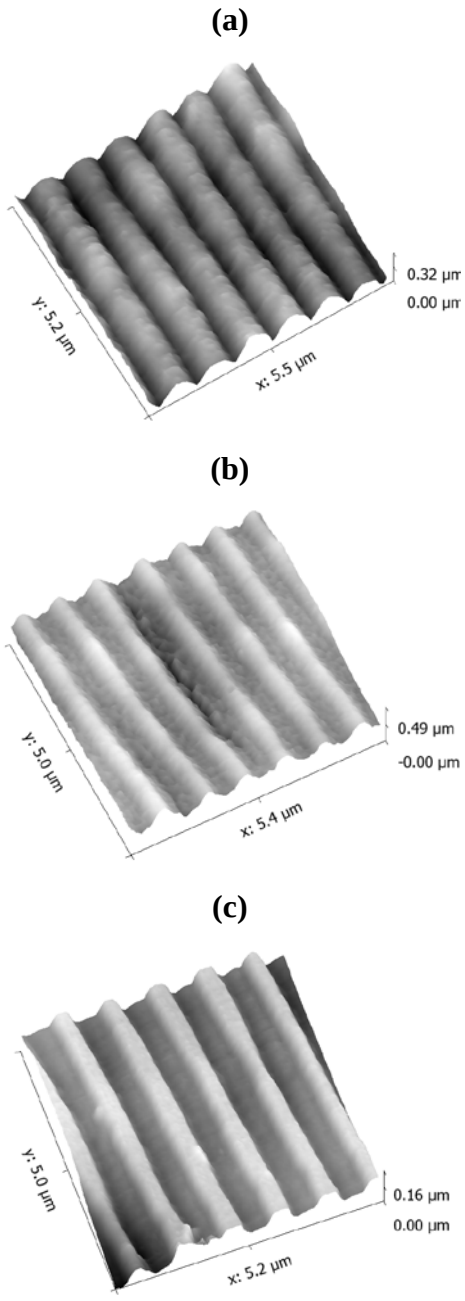

Figure 4.7 AFM characterization of the template-stripped nanogratings substrates of **(a)** 200 nm Ag, **(b)** 100 nm Ag, and **(c)** 100 nm Au.

4.3.4 Sensing with optical fiber tips

In order to demonstrate the potential of the stripping procedure to transfer pattern to different types of flat substrates, a plasmonic nanograting was fabricated on an optical fiber tip (OFT). There are several reports in the literature focused on the transfer of nanostructure to optical tips [22]. Yang et al. has reported an *in-situ*-IL fabrication on OFTs, but that requires a complex substrate-hosting setup to achieve the transfer [23]. Template-stripping procedure [24, 25] offers an easy and efficient solution to the setup complications of conventional lithography fabrication. In this case, the pattern from the IL template can be transferred onto optical fiber facet with the aid of an optical adhesive [25, 26] or some intermediate medias such as flexible polymeric structures [24]. Similarly, in this work, the IL-generated large area nanograting structures were template-stripped onto the fiber facet with the aid of epoxy adhesive. Specifically, the IL template was first deposited with 100 nm of gold film using electron beam evaporator. A drop of epoxy was added to the gold-nanostructured face of the IL substrate. The polished end of the OF, which had been held in a simple plastic holder to fix the fiber end at normal position, was brought to contact with the epoxy-gold nanogratings. The system was then allowed overnight exposure to 100 Watt white light source to ensure that the epoxy was cured completely. The photoresist template was then stripped from the fiber end, as demonstrated in Figure 4.8. Scanning electron micrographs of the resulting structures are presented in Figure 4.9(a, b). The plane-cut of the fiber core was achieved by connectorizing the OFT to a commercially available ceramic ferrule and polished extensively. The connectorized fiber tip was modified using the stripping template method. The patterned tip of the optical fiber was then used as a refractive index sensing element. In this case, the detection was done in reflection (backscattering) mode, using a birfurcated OF. As shown in Figure 4.8, one arm of the bifurcated fiber carried the white light while the other arm took the reflected signal to a miniaturized spectrometer. Either the patterned tip or a bare fiber tip can be connected to the system through an OF adapter purchased commercially. The measurements were done by immersing the fiber tip (either the patterned or the bare tips) into solutions with different refractive indexes. The solutions with different refractive indexes were placed in 5-mL disposable vials. A lab-lift (lab-jack) was used to control the immersion the fiber end of the optical setup into the analyte solutions (the solutions were approximately immersed to the

level at which bare fiber's jacket was removed prior to fiber tip plane-cleaving). The system was equilibrated for ~ 5 minutes before obtaining backscattered spectra using the spectrometer. The equilibation time was particularly important during solution changes. It allowed the system to settle and ensured a good degree of stability during the measurements. All measurements were done in a dark room to minimize background noise contributions.

The backscattered measurements carried information regarding the SPR mode excited on the metal nanograting tip. The SPR waves on the metal-solution interface were very sensitive to the refractive index changes (i.e. intensity changes and wavelength shifts). The recorded specta in the region from 400 – 850 nm were then smoothened, normalized and subjeted to the IR calculation, as shown in equation 4.2. An example of the wavelength shifts observed in response to the changes of refractive index from a nanograting patterned tip is shown in Figure 4.10(a)). The bare fiber's backscattered spectra remained unchanged for all the refractive indexes tested (Figure 4.10(b)). Figure 4.10(c) shows a comparison of the sensing performance of a Au nanograting patterned optical fiber tip to a bare optical fiber. The non-patterned (bare) fiber showed almost no response as compared to the patterned tip. In addition, since the measurements were taken with a bifurcated fiber setup, the results from Figure 4.10(c) illustrate the potential for application of this setup in an optrode geometry [27], which could be useful for in-line monitoring of chemical process, for instance. This relative simple and inexpensive procedure to modify the OFT with plasmonic nanostructures has also the potential to be utilized in other plasmonic sensing applications; i.e. surface-enhanced Raman spectroscopy.

It is worth to mention that the polarization-dependent characterictics of the nano-grating structures has not been utilized in the fiber setup reported here. The manipulation of the polarization effect, using a polarization mantaining fiber, for instance, is a potential future improvement that can be implemented for the application of this type of OFT-modified plasmonic device.

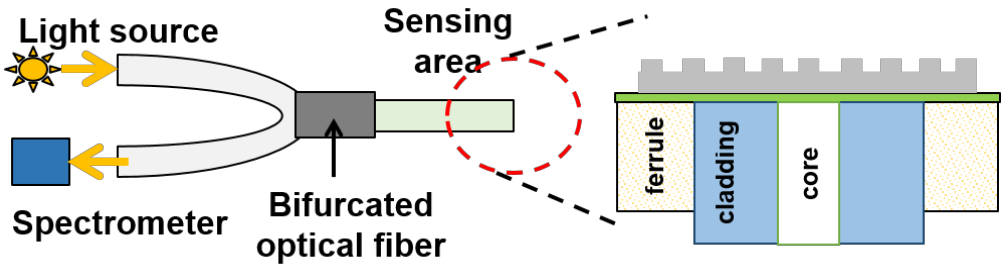

Figure 4.8 Portable assembly for the refractive index calibration measurement using bifurcated optical fiber; one arm of the fiber is illuminated with white light source (model: LS-1), the second arm is connected to ocean optic spectrometer (model: USB 2000) and the last arm is the sensing area with gold nanogratings where similar template stripping procedure is applied on plane-cleaved optical fiber tips.

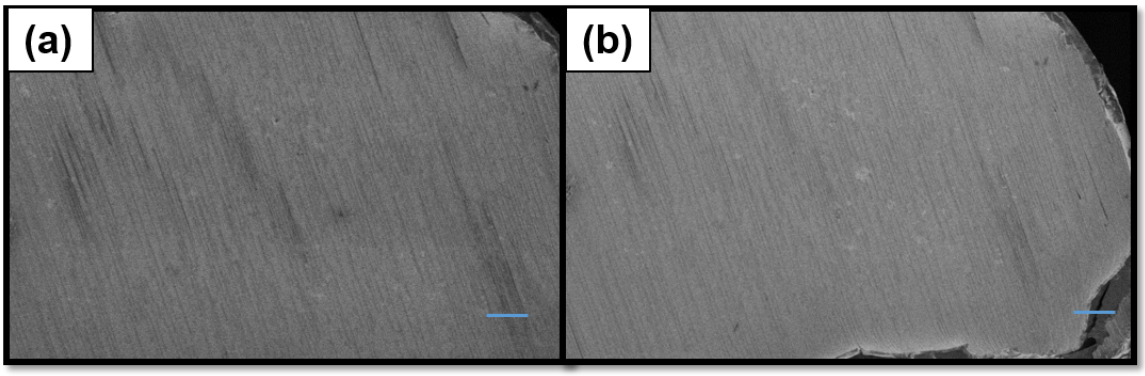

Figure 4.9 Scanning electron micrographs of (a) the nanogratings-patterned optical fiber tips, and (b) area with defects. The blue scale bars represent 20 μm.

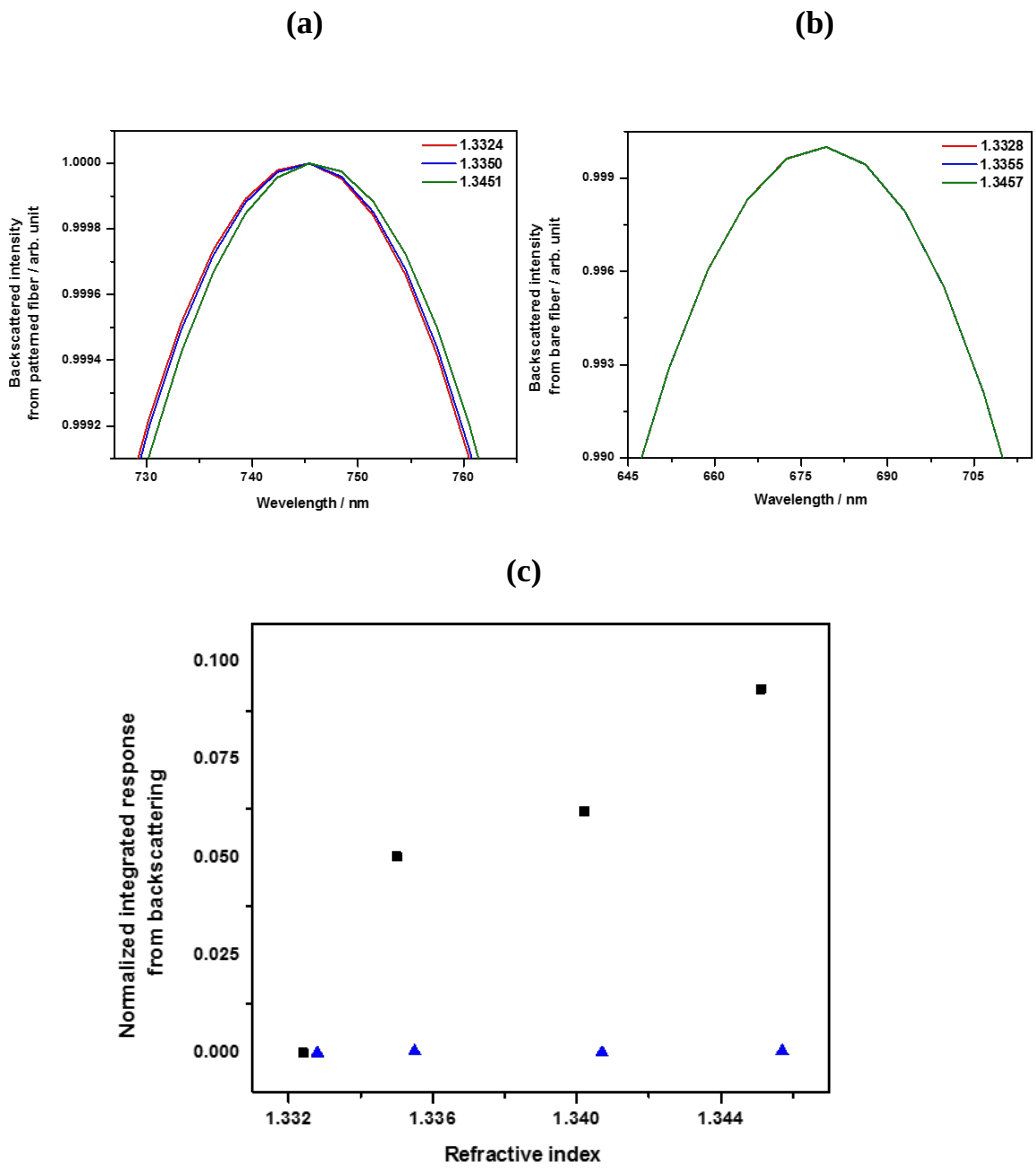

Figure 4.10 Smoothed, polynomial-fitted and normalized backscattered spectra from **(a)** nanogratings-patterned optical fiber, and **(b)** bare optical fiber. **(c)** Integrated response measured using the portable fiber assembly as a function of increasing refractive index of the solution (black square dots) tip-patterned optical fiber, and (blue triangle dots) bare optical fiber. The integrated response data were normalized to the respective maxima at the wavelength regions as shown in (a) and (b).

4.4 Conclusions

Summarizing, we succesfully utilized the IL-template stripping to prepare SPR substrates on both large area (1 inch^2) as well as on small surfaces (50 μm core-OPTs). These plasmonic substrates were used for bulk refractive index sensing. The successful integrations of the IL procedure have clearly demonstrated flexibility for the fabrication of good quality plasmonic substrates with different dimensions. The proposed methodology allows tailoring the fabrication for different applications. For instance, the realization of refractive index sensing using the optical fiber setup illustrated the potential of the procedure to prepare miniaturized (small area) plasmonic structures, suitable to accommodate remote sensing applications. Lastly, the substrates patterned with nanogratings demonstrated strong polarization dependency. This property has the potential to be used as an additional control in refractive index sensing applications. For instance, polarization controlled self-referencing can be implemented to eliminate non-polarization dependent interferences and backgrounds, such as stray illuminations and temperature variations, which can be very useful in improving the accuracy and precision in the analytical detections.

The proposed template-assisted fabrication methodology (combination of LIL and template-stripping), like mentioned earlier, has great flexibility to pattern the substrates in different surfaces, regardless of the sizes of contact areas. The LIL technique exploited in the preparation of template for this work, besides being high-throughput, has a relatively easy manipulation in the nanostructures design (e.g. nanopillars, nanoholes, nanorhombus or other more complicated three-dimensional structures when optical interferences are resulted from more than two beams) and periodicity (i.e. spacing between the nanostructures), with high reproducibility. This is definitely a bonus as compared to the other template-assisted lithography techniques (e.g., AAO-template, NSL-template etc.), since the simple and reproducible manipulation of nanostructure geometries/shapes is ultimately important in detection sensitivity optimization and mass production of the substrates. The significant drawback of the present LIL-template stripping procedure, however, is template-destructive, where re-use of the template is almost impossible. To solve this problem, the photoresist-based LIL-template might need to be transferred to an

intermediate (e.g. polymeric mold), which is more robust during the template-stripping procedure.

4.5 References

[1] M.I. Stockman, Nanoplasmonic sensing and detection, Science, 348 (2015) 287-288.
[2] L. Tong, H. Wei, S. Zhang, H. Xu, Recent advances in plasmonic sensors, Sensors, 14 (2014) 7959.
[3] A.G. Brolo, Plasmonics for future biosensors, Nature Photonics, 6 (2012) 709-713.
[4] M.K. Fan, M. Thompson, M.L. Andrade, A.G. Brolo, Silver nanoparticles on a plastic platform for localized surface plasmon resonance biosensing, Analytical Chemistry, 82 (2010) 6350-6352.
[5] M.J. Kwon, J. Lee, A.W. Wark, H.J. Lee, Nanoparticle-enhanced surface plasmon resonance detection of proteins at attomolar concentrations: Comparing different nanoparticle shapes and sizes, Analytical Chemistry, 84 (2012) 1702-1707.
[6] C. Valsecchi, A.G. Brolo, Periodic metallic nanostructures as plasmonic chemical sensors, Langmuir, 29 (2013) 5638-5649.
[7] J.P. Monteiro, L.B. Carneiro, M.M. Rahman, A.G. Brolo, M.J.L. Santos, J. Ferreira, E.M. Girotto, Effect of periodicity on the performance of surface plasmon resonance sensors based on subwavelength nanohole arrays, Sensors and Actuators B-Chemical, 178 (2013) 366-370.
[8] K.L. Lee, C.W. Lee, W.S. Wang, P.K. Wei, Sensitive biosensor array using surface plasmon resonance on metallic nanoslits, Journal of Biomedical Optics, 12 (2007).
[9] B. Xiao, S.K. Pradhan, K.C. Santiago, G.N. Rutherford, A.K. Pradhan, Enhanced optical transmission and Fano resonance through a nanostructured metal thin film, Scientific Reports, 5 (2015).
[10] M.E. Stewart, C.R. Anderton, L.B. Thompson, J. Maria, S.K. Gray, J.A. Rogers, R.G. Nuzzo, Nanostructured plasmonic sensors, Chemical Reviews, 108 (2008) 494-521.
[11] Y. Lin, J. Liao, Y. Ju, C. Chang, A. Shiau, Focused ion beam-fabricated Au micro/nanostructures used as a surface enhanced Raman scattering-active substrate for trace detection of molecules and influenza virus, Nanotechnology, 22 (2011) 185308.
[12] J. Zhang, X. Zhang, Sensitivity optimization for the index sensors based on waveguide metallic photonic crystals through angle-resolved tuning, Nanoscience Methods, 2 (2013) 16-22.
[13] Q. Xie, M.H. Hong, H.L. Tan, G.X. Chen, L.P. Shi, T.C. Chong, Fabrication of nanostructures with laser interference lithography, Journal of Alloys and Compounds, 449 (2008) 261-264.
[14] J.W. Menezes, J. Ferreira, M.J.L. Santos, L. Cescato, A.G. Brolo, Large-area fabrication of periodic arrays of nanoholes in metal films and their application in biosensing and plasmonic-enhanced photovoltaics, Advanced Functional Materials, 20 (2010) 3918-3924.
[15] S. Cherukulappurath, T.W. Johnson, N.C. Lindquist, S.H. Oh, Template-stripped asymmetric metallic pyramids for tunable plasmonic nanofocusing, Nano Letters, 13 (2013) 5635-5641.

[16] Z. Sun, Y.S. Jung, H.K. Kim, Role of surface plasmons in the optical interaction in metallic gratings with narrow slits, Applied physics letters, 83 (2003) 3021-3023.
[17] J. Anema, A. Brolo, The use of polarization-dependent SERS from scratched gold films to selectively eliminate solution-phase interference, Plasmonics, 2 (2007) 157-162.
[18] K.L. Lee, J.B. Huang, J.W. Chang, S.H. Wu, P.K. Wei, Ultrasensitive biosensors using enhanced Fano resonances in capped gold nanoslit arrays, Scientific Reports, 5 (2015).
[19] A.D. Rakić, A.B. Djurišić, J.M. Elazar, M.L. Majewski, Optical properties of metallic films for vertical-cavity optoelectronic devices, Appl. Opt., 37 (1998) 5271-5283.
[20] M. Das, D. Hohertz, R. Nirwan, A.G. Brolo, K.L. Kavanagh, R. Gordon, Improved performance of nanohole surface plasmon resonance sensors by the integrated response method, IEEE Photonics Journal, 3 (2011) 441-449.
[21] R. Gordon, A.G. Brolo, D. Sinton, K.L. Kavanagh, Resonant optical transmission through hole-arrays in metal films: physics and applications, Laser & Photonics Reviews, 4 (2010) 311-335.
[22] G.F.S. Andrade, A.G. Brolo, Nanoplasmonic structures in optical fibers, in: A. Dmitriev (Ed.), Nanoplasmonic Sensors, Springer New York (2012) 289-315
[23] X. Yang, N. Ileri, C.C. Larson, T.C. Carlson, J.A. Britten, A.S.P. Chang, C. Gu, T.C. Bond, Nanopillar array on a fiber facet for highly sensitive surface-enhanced Raman scattering, Opt. Express, 20 (2012) 24819-24826.
[24] E.J. Smythe, M.D. Dickey, G.M. Whitesides, F. Capasso, A technique to transfer metallic nanoscale patterns to small and non-planar surfaces, ACS Nano, 3 (2009) 59-65.
[25] G. Kostovski, U. Chinnasamy, S. Jayawardhana, P.R. Stoddart, A. Mitchell, Sub-15nm optical fiber nanoimprint lithography: A parallel, self-aligned and portable approach, Advanced Materials, 23 (2011) 531-535.
[26] J. Peipei, J. Hao, S. Jayshri, Y. Jun, Plasmonic nanohole array sensors fabricated by template transfer with improved optical performance, Nanotechnology, 24 (2013) 195501.
[27] G.F.S. Andrade, M.K. Fan, A.G. Brolo, Multilayer silver nanoparticles-modified optical fiber tip for high performance SERS remote sensing, Biosensors and Bioelectronics, 25 (2010) 2270-2275.

Chapter 5

Determination of Aqueous Antibiotic Contamination using SERS Nanogratings

(This chapter is based on a manuscript recently submitted to Analytica Chimica Acta. Dr. Carlos Diego Lima de Albuquerque contributed to the chemometrics data analysis in this work.)

5.1 Introduction

A variety of artificial organic compounds have been synthesized and developed to satisfy different societal needs (e.g. medical, agricultural and household applications) over the years. Consequently, organic contaminates can be found everywhere in the environment, even in very remote places [1-3]. One class of anthropogenic compounds is the antibiotics, which have been used for many decades as antibacterials to treat both humans and animals [4, 5]. Quinolone-based antibiotics have garnered much attention since the 1960s [6, 7]. They are widely applied in the agriculture industry to prevent infectious diseases and promote the growth of poultry and livestock [8-10]. The widespread application of quinolones led to their accumulation in the environment. These compounds are never absorbed entirely by humans or animals and most of the antibiotics are excreted either in their intact form or as their metabolites [10, 11].

There are many possible pathways for quinolones (and other antibiotics) to enter into the environment: runoff or infiltration of animal sewage (i.e. urines or feces) [12, 13]; wastewater from treatment plants [14, 15]; leakage from landfills [16, 17]; and many others. Farming sewage generally does not go through wastewater treatment systems [13, 18] before discharging into the environment. This increases the likelihood of surface water contamination due to the residues of antibiotics, including quinolones and their metabolites, from the agricultural waste.

The environmental fate of quinolone antibiotics is not completely understood. Several studies [19, 20] have proposed that the residues of antibiotics and their metabolites in the aquatic environment, even at a very low concentration (parts per billion (ppb) level

[21]), have a potential to become a threat to the ecosystem. They promote the breeding of drug-resistant microorganisms, which can be pathogenic and dangerous for both humans and animals. The presence of these emerging pollutants might also contaminate plants and animals as they uptake water [20]. As the demands for potable water increases, the reuse of water will be necessary [22, 23]. The issue of surface water contamination has then motivated analytical chemists towards the development of sensitive and reliable sensors to monitor traces of antibiotics and metabolites in drinking water sources.

Enrofloxacin (ENRO), a fluoroquinolone (FQs) approved as a veterinary antibiotic in poultry and bovine industries, is proven to be biologically effective for a broad-spectrum of microbial and bacterial prevention [10, 11]. ENRO, as other antibiotics, is never taken in fully by animals but excreted unchanged or in its primary active metabolite, ciprofloxacin (CIPRO). The states-of-the-art for FQ analysis from water samples is associated with chromatographic techniques in tandem with mass spectrometry (MS) [24-26] for compound identification. The current detection method presents a reasonable low limit of detection (1 – 10 ppb) [27, 28]; however, the method requires sophisticated instruments and well-trained personnel. In addition to that, the analysis requires extensive sample pre-treatment/ pre-concentration, which is a time-consuming step in the process.

Surface enhanced Raman scattering (SERS) is a large increase in the Raman cross-section (enhancement factor as high as 10^9 – fold [29, 30] as compared to the normal Raman) observed from molecules adsorbed in certain metal nanostructures (SERS substrates). SERS offers high sensitive detection allied to vibrational fingerprint information of the adsorbed molecules. SERS has been widely used for the detection of pharmaceuticals (or their metabolites), including anorexic drugs and analogues [31], nicotine [32], and FQs in spiked samples (chicken or fish [33, 34], urine [35, 36], blood [37]). Most of the SERS work in the area has utilized random metal nanostructures, such as colloidal metal nanoparticles [31-38], dendritic metal nanostructures [39] and electrochemically roughened metal film [40]. Those random SERS substrates are known for their simplicity in terms of fabrication and by their high SERS enhancement efficiency. On the other hand, these random SERS platform suffers from issues related to spatial uniformity and SERS intensity reproducibility. These limitations can be addressed by using fabricated nanometric metallic

patterns in solid supports as SERS substrates. Interference lithography (IL) [41-43] is a fabrication method that is quick, cost-effective, and yield a relative uniform periodic pattern that supports SERS. Compared to other advanced nanofabrication approaches, such as electron beam lithography (EBL) [44, 45] and focused-ion beam milling (FIB) [46-48], IL allows the patterning of a large area (2" x 2", for instance). SERS substrates generated through IL-chip technology have the potential to be miniaturized as portable or handheld devices [49, 50] for remote environmental detection [51].

The main goal of this work is then to explore the possibility of pharmaceutical and metabolite multiplexing detection using a uniform SERS platform fabricated using IL. As a proof of concept, the common FQ parent-and-metabolite pair, ENRO and CIPRO, was targeted for multiplexing detection. We also assessed the applicability of the isotope-edited internal calibration method [52-54] to deal with the complex matrix effects commonly found in environmental samples.

5.2 Experimental section

5.2.1 Chemicals and materials

Fisherfinest premium plain microscope slides (3" x 1" x 1 mm, supplied by Fisher Scientific); Microposit SC 1827 positive photoresist, Microposit thinner type P, Microposit 351 developer, deionized water (produced through Barnstead Millipore system with resistivity of 18.2 MΩcm), hydrochloric acid (37%, ACS reagent grade, supplied by VWR International), enrofloxacin and ciprofloxacin solid (both supplied by Sigma-Aldrich), isotope edited ciprofloxacin (2, 3, carboxyl-^{13}C, 99%-quinoline-^{15}N, 98%, 100 μg/mL in methanol; provided by AXYS Analytical Services).

5.2.2 Template preparation via IL

Microscope glass slides were cut from 3" x 1" standard size to 1 inch^2 and were used as the support. The glass slides were first sonicated in a water bath and then cleaned with copious amounts of organic solvents (acetone, methanol, ethanol and isopropanol). After oven-drying (T ~120 ^{o}C) and cooling to room temperature, the glass slides were ready to be spin-coated with 1:1 positive photoresist diluted with thinner at 2000 rpms for 30 seconds, as

illustrated in Figure 5.1. The substrates were then pre-baked in an oven at 120 ^{o}C for 10 minutes to remove the solvent from the photoresist layer. Next, the glass substrate coated with the photoresist was then mounted on the interference lithography setup and exposed to a 458 nm laser once for 45 seconds (the laser power was 250 mW) [41, 50, 51]. After the laser exposure, the photoresist film was developed in 1:3 Microposit 351 developer diluted with deionized water for 45 seconds under gentle motion parallel to the grating axis to generate a uniform 1-dimensional photoresist template. The fabrication steps involving the photoresist were all realized under yellow light, and aluminum foil was used to protect the samples when room transfer was necessary. The photoresist templates were then coated with a 250 nm silver film (Angstrom Engineering glove-box evaporator, deposition rate of 1Å/s).

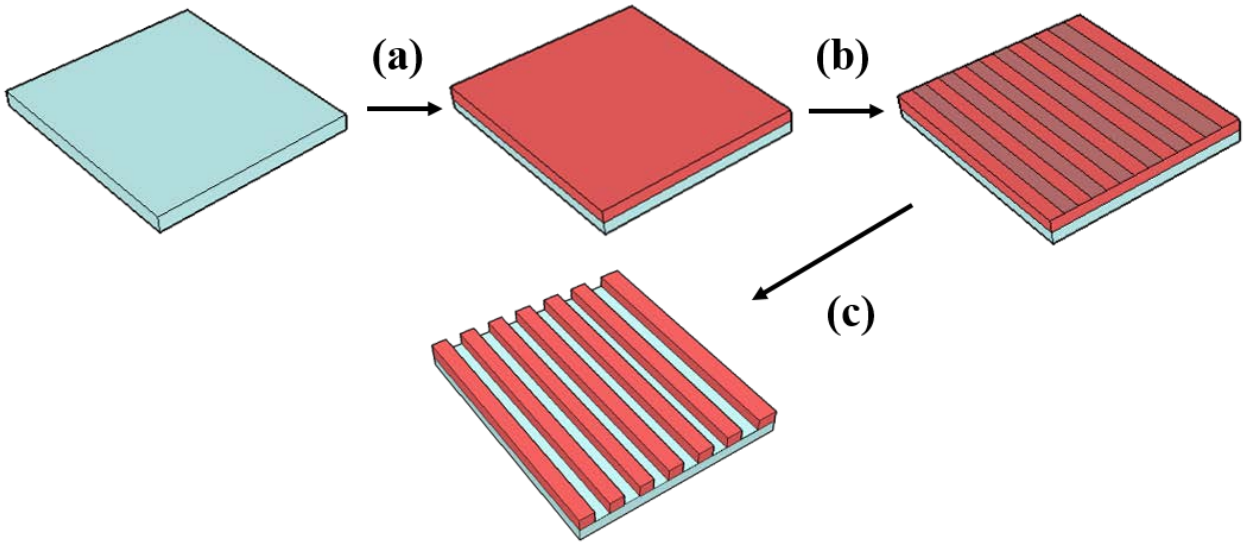

Figure 5.1. Nanogratings fabrication through interference lithography (IL): **(a)** spin-coating of photoresist onto the glass support; **(b)** laser IL process to pattern the photoresist substrate, and **(c)** wet-development of the photoresist substrate to wash away the exposed part.

5.2.3 Single and bi-analyte SERS detections

The silver-coated SERS nanograting substrates were drop-coated with 20 μL of one of the following standard solutions: (i) aqueous solution containing only enrofloxacin (ENRO), (ii) aqueous solution containing only ciprofloxacin (CIPRO), or (iii) aqueous solution

containing a mixture of ENRO and CIPRO. The concentration range explored was from 0 to 150 ppm and all the solutions were prepared in 0.01 M of hydrochloric acid to improve solubility of the analytes. The droplets were gently dried under nitrogen. In order to accounts for the effect of spatial variation due to drying, SERS spatial mappings were obtained for each droplet. Three areas of ~ 400 μm^2 were mapped for each droplet. The SERS maps were obtained using a Raman microscope (Renishaw inVia system) equipped with 785 nm excitation (laser power of 31.6 mW, 2 seconds acquisition, single accumulation). The spectra were obtained under 100X objective (NA = 0.90).

5.2.4 SERS detection with isotope-edited internal standard

A series of bi-analyte standard aqueous solutions containing both ENRO and CIPRO were spiked with 1 ppm isotope-edited CIPRO (as internal standard). Similar to section 5.2.3, 20 μL of each standard solution (solution coverage area approximately 7 mm^2, estimated from a round spot with radius length ~ 1.5 mm) was drop-casted onto the SERS nanograting substrates and dried under the gentle blow of nitrogen gas. SERS mappings (~ 1200 μm^2) was obtained in the same conditions as described in 5.2.3.

5.2.5 Data analysis

As discussed in Chapter 1 (Section 1.6), chemometric methods, including principal component analysis (PCA) [55, 56] and multivariate curve resolution (MCR) [57, 58], were applied to process the SERS mapping datasets. Routines developed in house were run in Matlab (version 7.12.0) to implement the analysis [59]. Briefly, all the raw datasets were unfolded in a 2D matrix (concentration and spectral profiles). Next, the data was pre-processed for baseline correction (asymmetric least squares (ALS) algorithm [60]; $\lambda = 10^4$ and $p = 0.01$*)* and smoothing (Savitzky-Golay algorithm [61]; window of 15 data points and polynomial degree of 1). Prior to MCR, PCA was employed to determine the number of factors using the mean-centered datasets. The non-negative matrix factorization (NMF) models of MCR were then developed using the non-mean centered datasets to evaluate the spectral profiles, and the optimization was repeated until the pure response profiles of each species were recovered. The recovered spectral profiles were in turn used to estimate the concentration profiles of each species in the mixture. A score, as the estimated

concentration, was obtained from NMF for each species in the dataset. The ‘calibration pseudo-curve’ was plotted as the function of scores (from the series of datasets) and correlated to the actual concentrations of analytes.

5.3. Results and discussion

5.3.1 SERS substrate characterization – surface morphology and reproducibility

The IL fabrication process [41, 50, 51] of large area nanograting substrates is illustrated in Figure 5.1. The final patterned area was ~1 inch^2 and silver film thickness was 250 nm. The surface morphology of the fabricated substrates was characterized by using scanning electron microscopy (SEM) (Figure 5.2). The nanogratings structure fabricated is morphologically reproducible with periodicity ~ 450 nm and grating width ~ 200 nm (periodicity variation ~ 0.3 %, assessed through atomic force microscopy). The IL template fabrication has been found to be relatively simple, cost and time-effective. The entire process of fabrication, starting from photoresist spin-coating to template solvent development, took less than 15 minutes in total for one nanograting substrate. The fabrication time could be even shorter if mass-produced. The homogeneity of SERS performance within a substrate was estimated by the standard errors obtained from MCR analysis for a single analyte mapping dataset (~ 900 μm^2). The spatial variation in SERS intensity within a single mapped area was found to be less than 10%. In addition, the SERS reproducibility between different substrates was evaluated through the mapping measurements (~ 600 μm^2 each) on three substrates previously drop-casted with Nile Blue A (10 μM) solution. The substrate was rinsed with copious of deionized water after 20 minutes of incubation and dried with nitrogen gas. The variation of SERS intensity was ~ 20 % between the substrates.

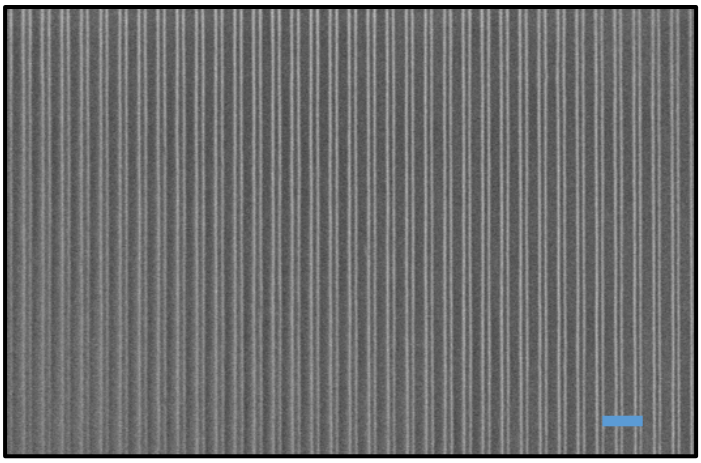

Figure 5.2 SEM morphology of the IL nano-gratings. Scare bar shows 1 µm.

5.3.2 Raman and SERS spectra of ENRO and CIPRO

Figure 5.3 presents the normal Raman and SERS spectra of ENRO and CIPRO. The molecular structure from these species are shown in scheme 5.1. The normal Raman spectra are from solid ENRO and CIPRO samples deposited on a glass slide and probed with the 100x objective. The SERS spectra are from aqueous samples dried in the nanograting substrate, as described in the experimental section (section 5.2.3). As expected, the SERS spectra in Figure 5.3(c) and 5.3(d) generally presents broader vibrational features when compared to the bands of the normal Raman spectra of the solids (Figures 5.3(a) and 5.3(b)). The interaction of adsorbates with metallic surfaces lead to shifts in the vibrational energy and the broadening of vibrational levels [62, 63]. Moreover, the relative intensities of the adsorbed species also change (relative to the solid) due to the surface selection rules [64-66]. Some characteristic SERS bands were found in both ENRO and CIPRO, including features at 747 cm^{-1} (methylene rocking), 1391 cm^{-1} (O-C-O stretching), 1461 cm^{-1} (benzene ring vibration), 1594 cm^{-1} (benzene ring stretching/breathing) and 1627 cm^{-1} (C=O stretching). The SERS band at 1627 cm^{-1}, assigned to the carboxyl stretching (in both species) was significantly stronger than observed in the previous reported SERS spectra for ENRO and/or CIPRO [33, 39] This might be related to the high degree of carboxyl group protonation [67, 68] in both ENRO and CIPRO solutions, as they were prepared in acidic medium to promote dissolution of the solids. Although both CIPRO and ENRO present strong similarities in their molecular structure (see scheme 1), it is still possible to find

strong variations in their vibrational signatures presented in Figure 5.3. For instance, the SERS spectra for ENRO (Figure 5.3(d)) and CIPRO (Figure 5.3(c)) present unique features in the spectral region below 900 cm^{-1}, including the SERS band at 850 cm^{-1} which is only present in the SERS spectrum of ENRO (Figure 5.3(d)). Although it would be possible to concentrate on that particular band (and others, for instance in the 1400 cm^{-1} - region, for instance) to determine the relative presence of each species in a mixture, a more representative quantification was obtained using chemometrics (this will be discussed further in section 5.3.3). In that case, the entire SERS spectral window (from 350 to 1650 cm^{-1}) was taken into consideration to interpret the SERS spectra of CIPRO and ENRO mixtures.

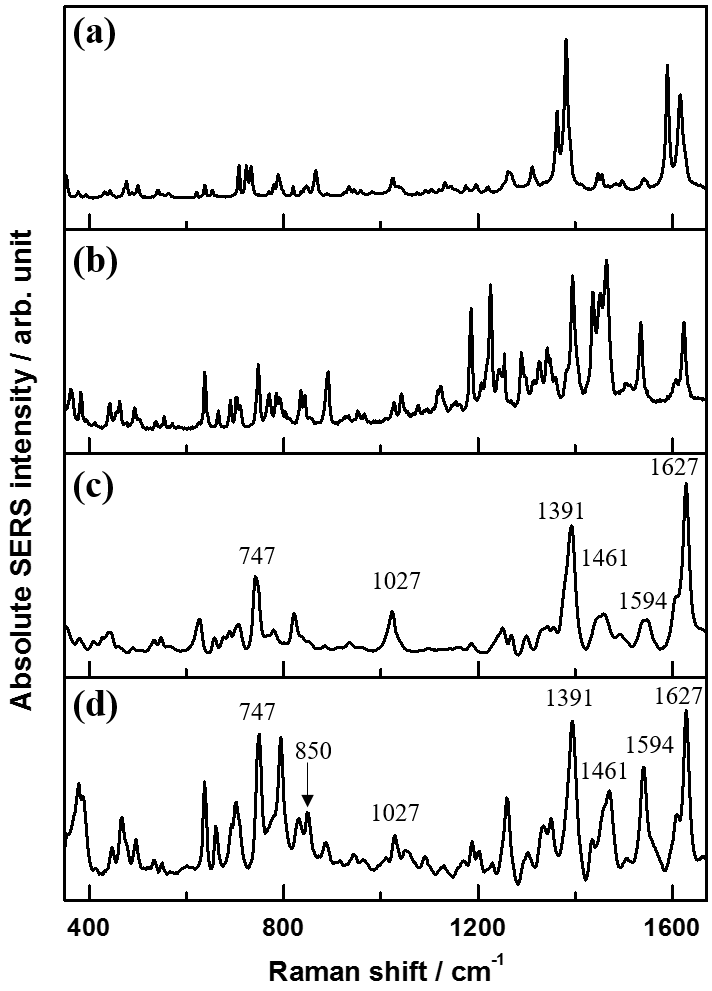

Figure 5.3 Normal Raman spectra using 785 nm laser excitation of **(a)** CIPRO solid and **(b)** ENRO solid. SERS spectra using 785 nm laser excitation of **(c)** 12.0 ppm aqueous CIPRO solution and **(d)** 60.0 ppm ENRO aqueous solution. The solutions measured in (c) and (d) were let dried on the nanograting substrates prior to the SERS analysis.

(a)

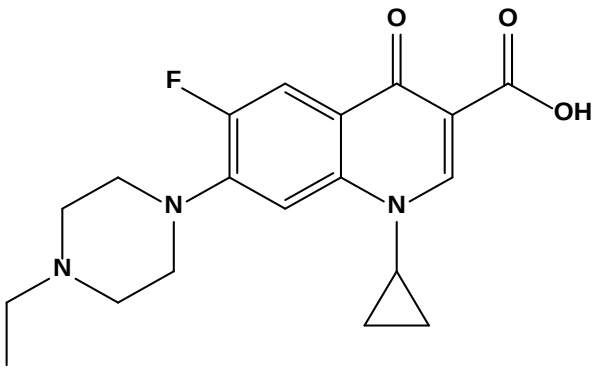

(b)

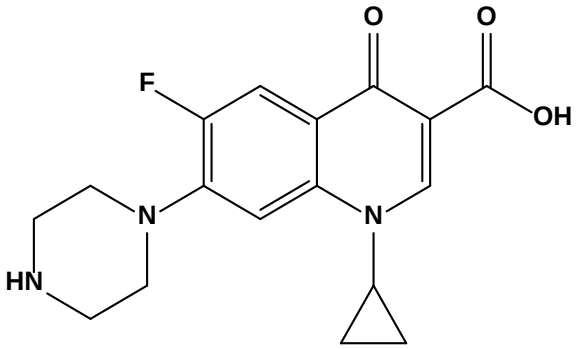

(c)

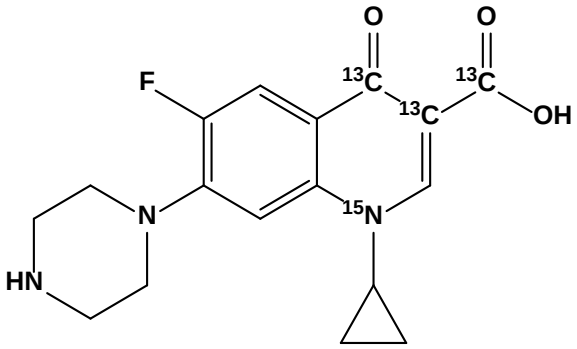

Scheme 5.1 Molecular structures of **(a)** enrofloxacin (ENRO), **(b)** ciprofloxacin(CIPRO), and **(c)** isotope-edited ciprofloxacin (iso-CIPRO).

5.3.3 Individual and bi-mixture FQs detection

The goal of this work is to quantify a mixture of antibiotic and its metabolite in aqueous solution using SERS from nanogratings. ENRO and CIPRO, the parent-and-metabolite FQ antibiotics pair used in our proof of concept measurements, are relatively similar in their molecular structures (see scheme 5.1), resulting in several overlap in their SERS spectral features (Figure 5.3). The structural similarity provides a challenge for the quantifications of these species from mixtures. As discussed in section 5.3.2, it is possible to find a few non-overlapping regions in their vibrational fingerprinting, but a restrict analysis of those regions might limit the possibility of quantification. Alternatively, chemometric methods were used to take advantage of the whole spectral range. All SERS mapped datasets were analyzed through non-negative matrix factorization with alternating least square algorithm (NMF-ALS); a class of algorithms under the multivariate curve resolution (MCR) [69] methods. Basically, this unsupervised learning chemometric technique resolves the complicated spectral information of the mixture into loadings (simulated pure spectra for each individual analyte) and scores (simulated concentration profiles of the analytes). This technique was previously applied to in SERS environmental contaminants detection (i.e. malathion in fruit peels [59], antibiotics detection in tertiary mixtures [70]) and was proven to be effective to recover both the spectral and concentration information of the species of interest, without being affected by sample matrix interferences.

Although the final goal was to detect FQs using our IL fabricated silver nano-gratings, preliminary experiments concentrated on the quantification of individual components (CIPRO and ENRO) in aqueous sample. Figure 5.4 shows representative SERS spectra of CIPRO adsorbed from different concentrations in the nanograting substrate. A series of CIPRO standard solutions within a concentration range between 1 ppm and 120 ppm were deposited (20 µL) on the nanogratings. SERS mappings were obtained for each concentrations and the results analyzed by NMF-ALS. The generated scores (pseudo-concentration profiles) were plotted against the actual CIPRO concentration and presented in Figure 5.4(b). A linear relationship (R^2 = 0.983) was found for the entire measured calibration range, from 1 to 120 ppm, of individual CIPRO. This reasonable linear fit was obtained within less than 10 % of relative standard deviation (RSD) in spatial variation for

each SERS map. This data spreading was reflected in the error bars of the calibration curve (Figure 5.4(b)). The % RSD was assessed through the ratio of the NMF-ALS processed standard errors (pixels to pixel variation in the mapped datasets) and the average scores from the replicates of mapped measurements. It is also notable that each of the data point in the calibration curve in Figure 5.4(b) was obtained from the average of three SERS mappings of 400 μm^2 for each concentration (~ 1200 spectra). The limit of detection (LOD), defined as the smallest concentration of analytes that produces reasonable characteristic SERS spectrum of the species (refer to Chapter 1 Section 1.3.1.2), was found to be ~ 1 ppm (specifically, the smallest concentration attempted experimentally was 1.65 ppm). As the concentration decreased further, the spatial variation becomes stronger and the error in the determination was overwhelming. This is an interesting characteristics of SERS, since the enhancement occurs from very localized regions, strong spatial variations are expected for low surface coverages of the analyte molecules. In other words, the large spatial variation for low concentration (i.e. low molecules coverage in a definite mapped area), can be viewed by the low probability to find the molecules in that area, as compared to those of higher concentrations. The quantification in those conditions are challenging and we are developing a method to deal with this issue that will be presented in future works.

As seen in section 1.5.2, the performance of most analytical applications in SERS, including pharmaceutical detection, were evaluated through the LOD or limit of quantification (LOQ). The LOD achieved in this work (~ 1 ppm) is higher than those reported for SERS antibiotic detections [33-37, 39], which were ranging from tenths [33, 39] to a few hundreds of part per billions (ppb) [34, 36]. All the previous work on the quantification of antibiotics by SERS used random metallic nanostructures, that are known to be less reproducible and reliable, but sensitive (i.e. SERS-enhancing). This is mainly due to: (1) the existence of excessive nanometric roughness (hot-spots) on the random nanostructured substrates; (2) the surface modification previously done to prepare the random metallic substrates (e.g., Ag or Au NPs immobilized substrates), might attract the analyte molecules to the hot-spots. By using a periodic SERS substrate that can be mass fabricated using a relative simple method, the giant SERS efficiency (observed in random substrates) was traded off by spatial uniformity and sample to sample reproducibility.

Environmental methods for the analysis of water generally employs pre-concentration steps using solid phase extraction [71]. Although the nanogratings described here could potentially substitute some of the advanced instrumentation employed in the state-of-the-art water analysis, the pre-concentration step will be required to achieve competitive sensitive levels. This comes from a compromise between a reasonable enhancement factor and the reproducibility of the surface achieved using these nanogratings as platforms for SERS.

SERS quantification of bianalyte mixtures of aqueous solution containing ENRO and CIPRO was demonstrated. A set of muti-analytes standard solutions with varying concentrations of ENRO, but constant CIPRO concentration were employed. The SERS spectra of some of the mixtures are presented in Figure 5.5(a). The SERS bands at 850 cm^{-1} noticeable increases in intensity it with the ENRO concentration, as illustrated in the enlarged view of that portion of the spectra in Figure 5.5(b). The pseudo-concentration information (scores) were retrieved a NMF-ALS data analysis of the spectra in Figure 5.6 and the results are plotted in Figure 5.6(a). The ENRO scores from the mixtures yielded a linear relationship with the concentration (R^2 = 0.981, as shown in Figure 5.6(a)). Figures 5.6(b) and 5.6(c) compared the recovered pseudo spectra (loadings) from the NMF-ALS analysis to the experimental SERS data. The ‘pseudo’ spectra for both analytes were observed to match well to the actual SERS spectra of the individual analytes (Figures 5.6(b) and 5.6(c)). This is a strong indication of the successful implementation of the NMF-ALS analysis for bi-analyte mixtures of FQs by SERS.

The standard errors for each data point in Figure 5.6(a) (averaged from all mappings in a particular concentration, ~ 1200 spectra altogether) were slightly higher (ranging from 0.51 – 4.1 % relative to the average scores) as compared to the individual CIPRO quantification shown in Figure 5.5(b) (magnitude of 0.37- 3.9 % relative to the average scores). This suggests that the spatial reproducibility of the mappings was marginally poorer for the mixture than for the case of individual analytes. The higher error can be attributed to the processing of mixed spectra from two almost identical molecules is challenging and it is expected to carry more uncertainty in the concentration information (scores).

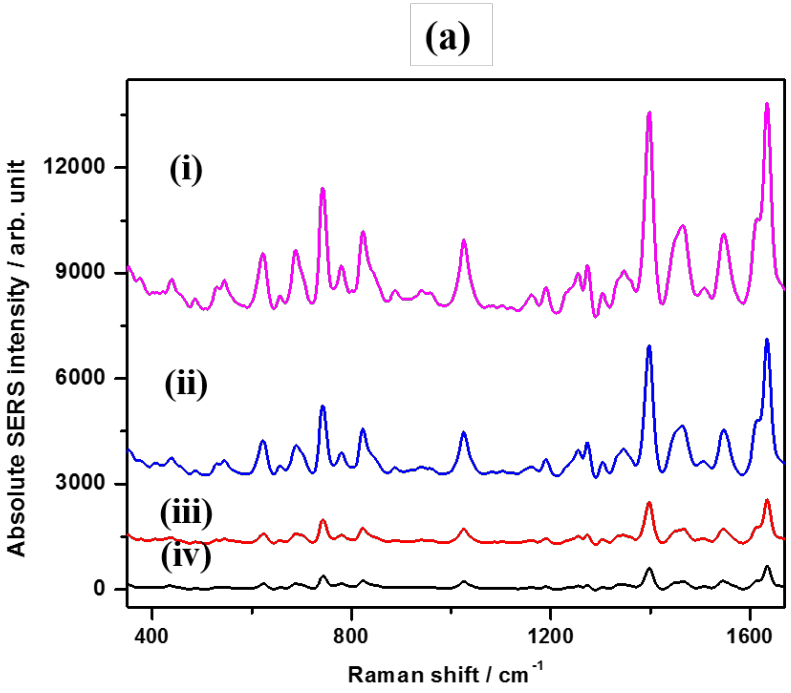
(a)
Absolute SERS intensity / arb. unit
12000
9000
6000
3000
0
(i)
(ii)
(iii)
(iv)
400
800
1200
1600
Raman shift / cm-1

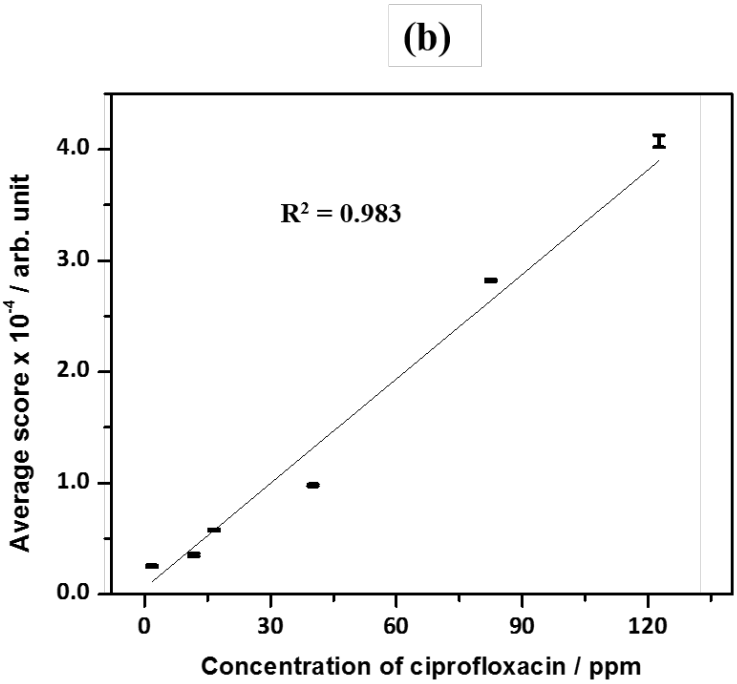
(b)
Average score x 10-4 / arb. unit
4.0
3.0
2.0
1.0
0.0
R2 = 0.983
0
30
60
90
120
Concentration of ciprofloxacin / ppm

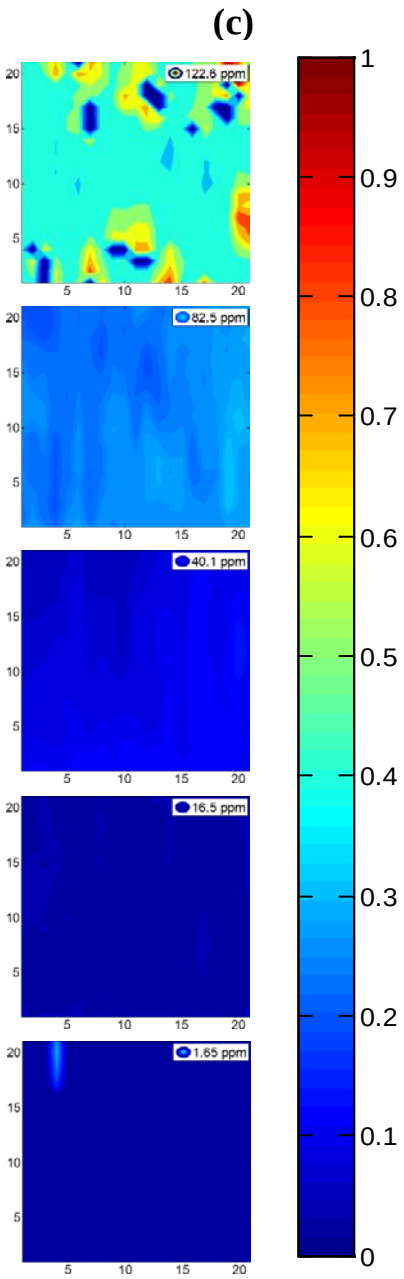

Figure 5.4 (a) SERS measurements using LIL- generated large area silver nanograting structures as substrates dried in 20 μL of different concentrations of CIPRO solutions: (i) 123 ppm; (ii) 82.5 ppm; (iii) 40.1 ppm; and (iv) 16.5 ppm. **(b)** Average score from MCR as a function of increasing concentration of ciprofloxacin. The error bars in the calibration plot were the standard errors from NMF-ALS processing of the mapped datasets (pixels to pixel variation in the mapped datasets). **(c)** The colormaps of different concentrations of CIPRO on the substrates (simulated from the respective scores on each pixel of the mapped areas).

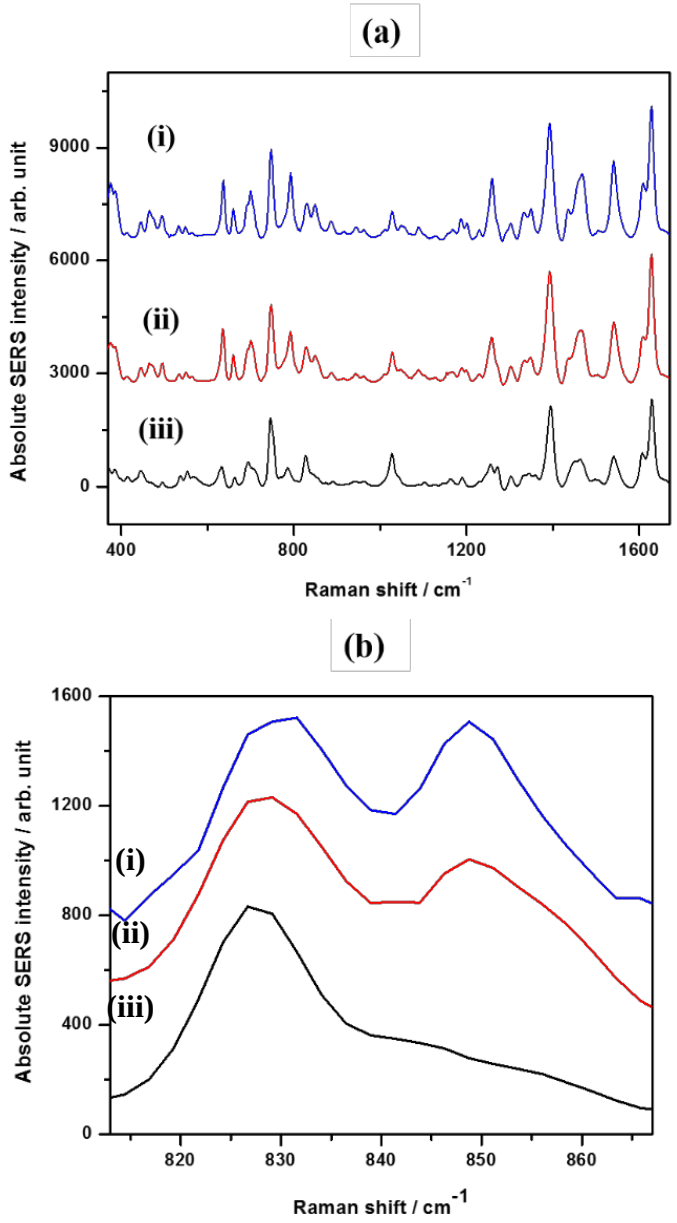

Figure 5.5 (a) SERS spectra of mixtures of ENRO and CIPRO with constant concentration of CIPRO (16.5 ppm), while the concentrations of ENRO are as follows: (i) 93.0 ppm; (ii) 46.5 ppm; and (iii) 1.86 ppm. (b) Enlarged mixture spectra at 840 cm^{-1} -region to demonstrate the individual SERS band increment with ENRO concentration.

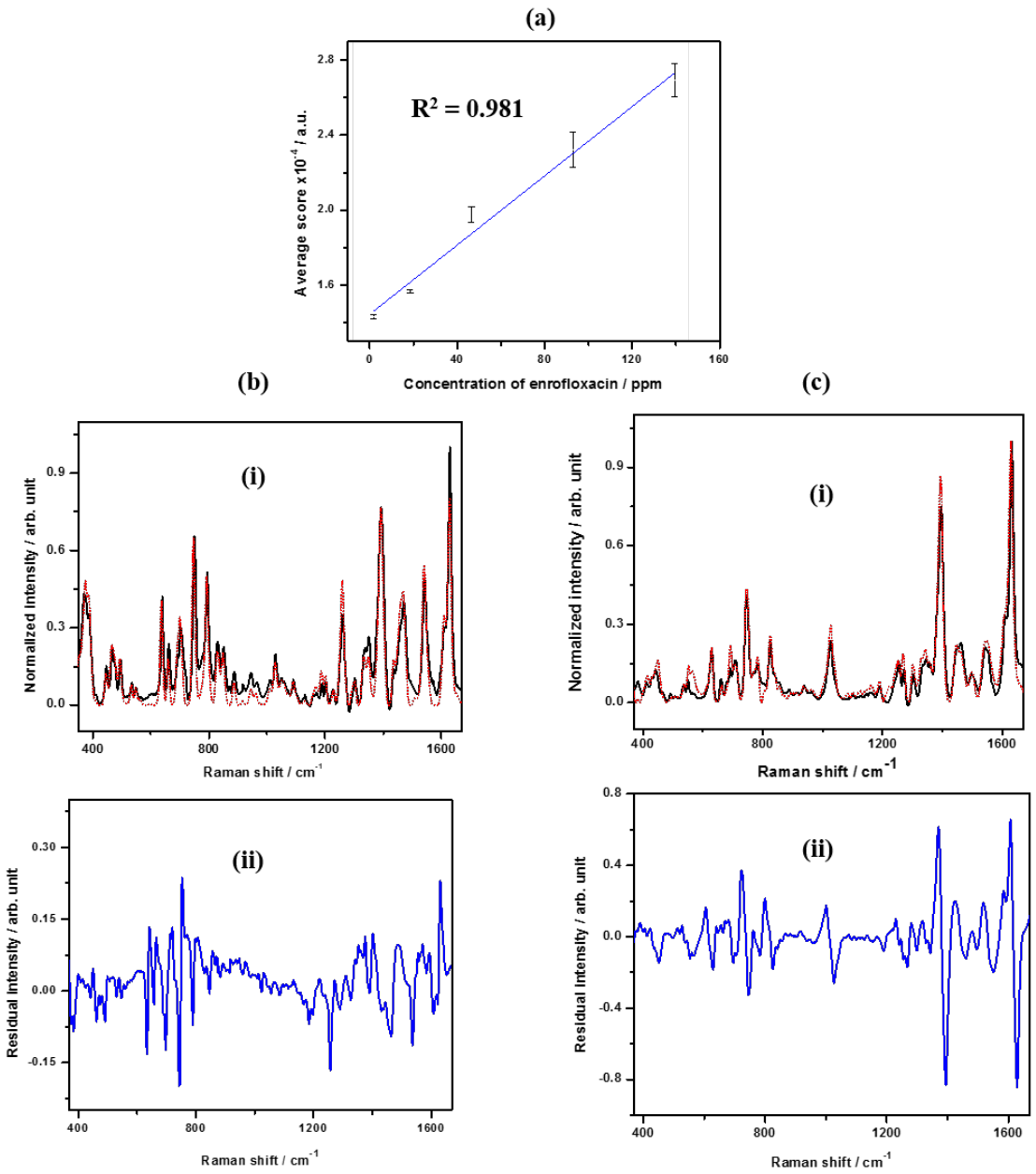

Figure 5.6 (a) Average score from MCR as a function of increasing concentration of ENRO while constant in the concentration of CIPRO. The error bars in the calibration plot were the standard errors from NMF-ALS processing of the mapped datasets (pixels to pixel variation in the mapped datasets). Comparison of the actual SERS spectra (solid, black) and MCR-resolved spectral profile of analyte (dotted, red) for (b) (i, ii) ENRO and (c) (i, ii) CIPRO. All the spectra in (b)(i) and (c)(i) were normalized to the maxima of the respective spectra. The plots in (b)(ii) and (c)(ii) correspond to the residuals from the comparison of the actual SERS and MCR-resolved spectra from (b)(i) and (c)(i).

5.3.4 SERS spectra of CIPRO and isotope-edited CIPRO

The SERS spectra of CIPRO and isotope-edited CIPRO (iso-CIPRO) are shown in Figure 5.7. The molecular structures of these compounds are presented in scheme 1. The iso-CIPRO was purchased pre-dissolved in methanol; therefore, the C-O stretching band from methanol at 1055 cm^{-1} is observed in Figure 5.7 (the highlighted region in the green spectrum). CIPRO, which was originally purchased in solid form, was dissolved in 0.01 M HCl and does not present any spectral feature in the 1055 cm^{-1}-region. Since the iso-CIPRO was carbon-13 edited at 2, 3 and in the carboxy position (see scheme 1), several vibrational bands red-shifted relative to their original position in regular CIPRO. For instance, the carboxy (O-C-O) stretching shifted from 1391 cm^{-1} in CIPRO to 1350 cm^{-1} in iso-CIPRO, while the carbonyl (C=O) mode moved from 1627 cm^{-1} to 1600 cm^{-1} due to the presence of heavier carbon-13 in iso-CIPRO. Other signature SERS band of CIPRO, such as the feature at 1027 cm^{-1} attributed by C-H rocking, was also shown to shift to lower Raman frequency (998 cm^{-1}) in iso-CIPRO, due to the collective effect of the existence of three C-13 and one N-15 on the iso-CIPRO molecules.

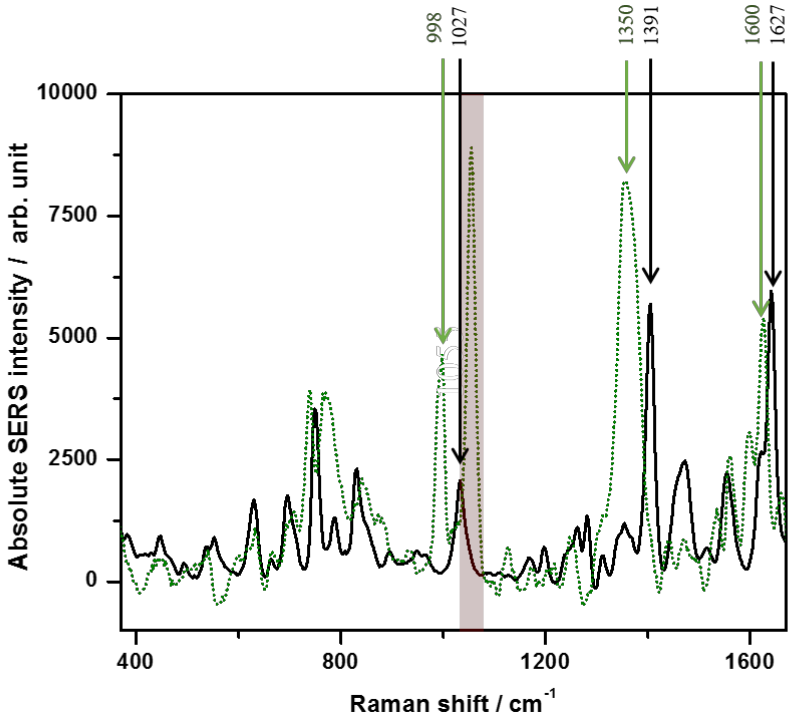

Figure 5.7 SERS spectra using 785 nm laser line of (green, dotted) 100 ppm isotope-edited ciprofloxacin in methanol and (black, solid) 123 ppm ciprofloxacin solution. The highlighted region indicated the methanol (solvent) band.

5.3.5 Isotope-edited internal standard calibration of ENRO and CIPRO

Finally, simultaneous quantification of both ENRO and CIPRO was attempted using an internal standard. In this case, an isotopic analogue of CIPRO (iso-CIPRO; molecular structure presented in scheme 1) was used as internal standard. Isotopic-edited internal calibration approach has been reported in SERS [52-54, 72] to improve the quantifications of single species of the analytes with the aid of its respective isotopologue [52-54, 72]. The technique aims at correcting for typical experimental variations observed in SERS, such as substrate inhomogeneity, the competition between different analytes for the substrate, as well as unknown matrixes effects as expected from complex environmental samples.

A series of tertiary aqueous mixture solutions containing ENRO, CIPRO and iso-CIPRO were prepared. Specifically, the ENRO and CIPRO concentrations were adjusted to be complementary within the concentration range (the concentration ratios of ENRO:CIPRO were 99.8 ppm:5.14 ppm, 74.9 ppm:10.3 ppm, 49.9 ppm:20.6 ppm, 25.0 ppm:41.1 ppm, 12.5 ppm:61.7 ppm, and 6.24 ppm:82.2 ppm respectively), in order to ease the chemometric recognition of the analytes. The iso-CIPRO, the internal standard, was spiked at a constant concentration (1.00 ppm) in each of the standard mixtures. SERS maps (~ 1200 spectra) were taken from each standard mixture deposited in the nanograting substrate. The results were analyzed through NMF-ALS, as discussed in sections 5.3.3.

The internal calibration curves for both ENRO and CIPRO were obtained using the normalized scores, and the results are presented in Figure 5.8. Figure 5.8(a) shows that the scores for ENRO was found to increase with its concentrations, which is expected. However, the scores in the lower concentration range showed little concentration dependence, suggesting an increase in the LOQ. The CIPRO results in Figure 5.8(b) shows a lack of linear correlation between the scores and the concentrations. The chemometric methodology used here could not resolve the mixtures of a two very identical molecules (CIPRO and iso-CIPRO), which cause the errors in the retrieved concentration profiles. This was confirmed when three MCR-recovered spectra for all three species were compared to their experimental SERS spectra. The loading (pseudo spectra) for the iso-CIPRO did not adequately match its experimental SERS spectrum, as seen in Figure 5.9.

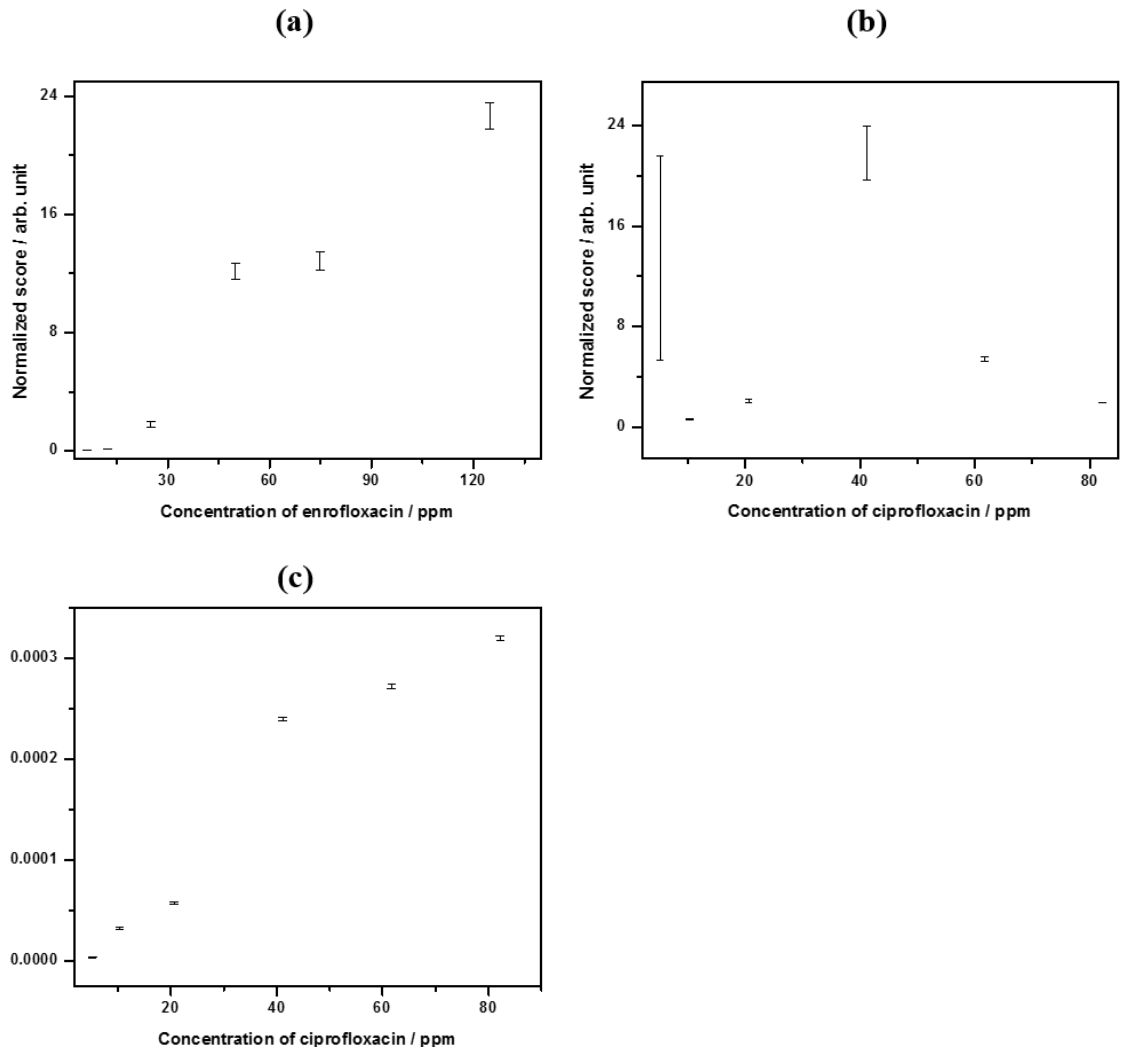

Figure 5.8 Isotoped-edited internal calibrations for (a) ENRO and (b) CIPRO. (c) The sum of score of CIPRO and iso-CIPRO plot against the concentration of CIPRO.

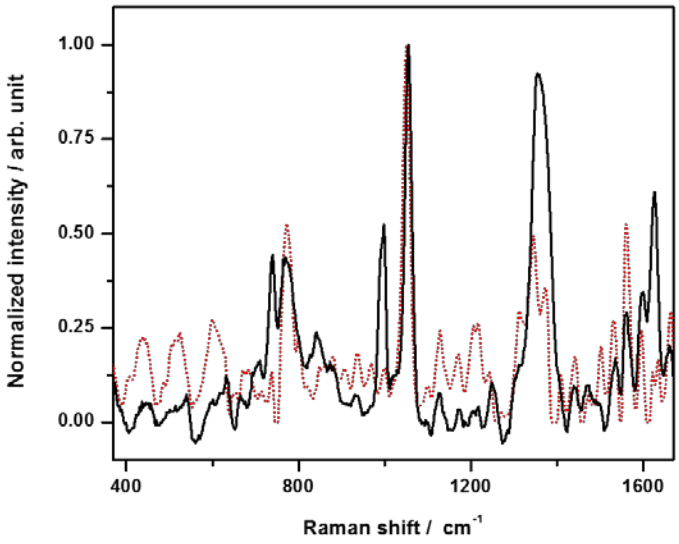

Figure 5.9 Comparison of the actual SERS spectra (solid, black) and MCR-resolved spectral profile of analyte (dotted, red) for iso-CIPRO.

In addition to that, the sum of the scores from CIPRO and iso-CIPRO were obtained and plotted against the total concentration of CIPRO and iso-CIPRO in the mixture (the concentrations of iso-CIPRO in each solution was the constant). The results in Figure 5.8(c) shows an acceptable linear plot, suggesting that the algorithm failed to differentiate between CIPRO and its isotope-edited analogue. Another aspect that might have contributed to the problem encountered in Figure 5.8 is that the concentration of iso-CIPRO (internal standard) was too low (close to the LOD of the substrate and the analyte's signals can be buried in noise), and maybe too small relative to the concentrations of the analytes. The spectra normalization would not only amplify the signal but also the noise. This effect might partly account for the inefficiency of the MCR data analysis for our tertiary mixture system.

5.4 Conclusions

We have successfully employed the IL fabricated nanogratings in SERS detection of the antibiotics residues (i.e. ENRO and CIPRO), as proof-of-concept of SERS applications in environmental detection. The quantifications, which aided by NMF-ALS has proven to be successful in recovering the concentration and spectral profiles of the analytes, up to bi-mixtures. Ongoing effort is still required to optimize the ENRO and CIPRO quantifications

in tertiary mixtures or other more complex mixtures (i.e. real environmental samples). Notwithstanding, the SERS substrates (i.e. silver nanogratings) fabricated through the LIL technology has high potential to apply into the environmental monitoring due to their uniformity. This type of substrate can potentially be integrated in portable handheld devices or compact bench-top readers. These would be useful for on-site monitoring and detection of emerging contaminants.

5.5 References

[1] G.L. Daly, F. Wania, Organic Contaminants in mountains, Environmental Science & Technology, 39 (2005) 385-398.
[2] H. Hirai, H. Takada, Y. Ogata, R. Yamashita, K. Mizukawa, M. Saha, C. Kwan, C. Moore, H. Gray, D. Laursen, E.R. Zettler, J.W. Farrington, C.M. Reddy, E.E. Peacock, M.W. Ward, Organic micropollutants in marine plastics debris from the open ocean and remote and urban beaches, Marine Pollution Bulletin, 62 (2011) 1683-1692.
[3] E. Meyer, E.A. Eskew, L. Chibwe, J. Schrlau, S.L. Massey Simonich, B.D. Todd, Organic contaminants in western pond turtles in remote habitat in California, Chemosphere, 154 (2016) 326-334.
[4] E.J. Bigwood, L. Merre, The discovery of antibiotics in general and penicillin in particular, Journal of the American Medical Association, 128 (1945) 461-462.
[5] A. Penesyan, M. Gillings, I.T. Paulsen, Antibiotic discovery: Combatting bacterial resistance in cells and in biofilm communities, Molecules, 20 (2015) 5286-5298.
[6] D. Kaminsky, R.I. Meltzer, Quinoline antibacterial agents. Oxolinic acid and related compounds, Journal of Medicinal Chemistry, 11 (1968) 160-163.
[7] J.F. Ryley, W. Peters, The antimalarial activity of some quinolone esters, Annals of tropical medicine and parasitology, 64 (1970) 209-&.
[8] S. Schwarz, E. Chaslus-Dancla, Use of antimicrobials in veterinary medicine and mechanisms of resistance, Veterinary Research, 32 (2001) 201-225.
[9] F.M. Aarestrup, Veterinary drug usage and antimicrobial resistance in bacteria of animal origin, Basic & Clinical Pharmacology & Toxicology, 96 (2005) 271-281.
[10] M. Martinez, P. McDermott, R. Walker, Pharmacology of the fluoroquinolones: A perspective for the use in domestic animals, Vet. J., 172 (2006) 10-28.
[11] J.A. O'Donnell, S.P. Gelone, Fluoroquinolones, infectious disease clinics of North America, 14 (2000) 489-513.
[12] Y. Luo, L. Xu, M. Rysz, Y. Wang, H. Zhang, P.J.J. Alvarez, Occurrence and transport of tetracycline, sulfonamide, quinolone, and macrolide antibiotics in the Haihe River Basin, China, Environmental Science & Technology, 45 (2011) 1827-1833.
[13] N. Kemper, Veterinary antibiotics in the aquatic and terrestrial environment, Ecological Indicators, 8 (2008) 1-13.
[14] X.-S. Miao, F. Bishay, M. Chen, C.D. Metcalfe, Occurrence of Antimicrobials in the Final Effluents of Wastewater Treatment Plants in Canada, Environmental Science & Technology, 38 (2004) 3533-3541.

[15] A.J. Watkinson, E.J. Murby, D.W. Kolpin, S.D. Costanzo, The occurrence of antibiotics in an urban watershed: From wastewater to drinking water, Science of The Total Environment, 407 (2009) 2711-2723.
[16] R.J. Slack, J.R. Gronow, N. Voulvoulis, Household hazardous waste in municipal landfills: contaminants in leachate, Science of The Total Environment, 337 (2005) 119-137.
[17] K.K. Barnes, D.W. Kolpin, E.T. Furlong, S.D. Zaugg, M.T. Meyer, L.B. Barber, A national reconnaissance of pharmaceuticals and other organic wastewater contaminants in the United States - I) Groundwater, Science of The Total Environment, 402 (2008) 192-200.
[18] A. Nikolaou, S. Meric, D. Fatta, Occurrence patterns of pharmaceuticals in water and wastewater environments, Analytical and Bioanalytical Chemistry, 387 (2007) 1225-1234.
[19] F. Baquero, J. Martínez, R. Cantón, Antibiotics and antibiotic resistance in water environments, Current Opinion in Biotechnology, 19 (2008) 260-265.
[20] K. Kümmerer, Antibiotics in the aquatic environment – A review – Part I, Chemosphere, 75 (2009) 417-434.
[21] Code of Federal Regulation, Title 21 (Food and Drugs), 6 Part 556.
[22] P. Hong, N. Al-Jassim, M. Ansari, R. Mackie, Environmental and public health implications of water reuse: Antibiotics, antibiotic resistant bacteria, and antibiotic resistance genes, Antibiotics, 2 (2013) 367.
[23] B. Jiménez-Cisneros, Wastewater reuse to increase soil productivity, Water Science and Technology, 32 (1995) 173-180.
[24] M.J. Focazio, D.W. Kolpin, K.K. Barnes, E.T. Furlong, M.T. Meyer, S.D. Zaugg, L.B. Barber, M.E. Thurman, A national reconnaissance for pharmaceuticals and other organic wastewater contaminants in the United States - II) Untreated drinking water sources, Science of The Total Environment, 402 (2008) 201-216.
[25] J. Gibs, H.A. Heckathorn, M.T. Meyer, F.R. Klapinski, M. Alebus, R.L. Lippincott, Occurrence and partitioning of antibiotic compounds found in the water column and bottom sediments from a stream receiving two wastewater treatment plant effluents in Northern New Jersey, 2008, Science of The Total Environment, 458–460 (2013) 107-116.
[26] A. Iglesias, C. Nebot, B.I. Vázquez, J.M. Miranda, C.M.F. Abuín, A. Cepeda, Detection of veterinary drug residues in surface waters collected nearby farming areas in Galicia, North of Spain, Environmental Science and Pollution Research, 21 (2014) 2367-2377.
[27] F. Cañada-Cañada, A. Espinosa-Mansilla, A. Muñoz de la Peña, Separation of fifteen quinolones by high performance liquid chromatography: Application to pharmaceuticals and ofloxacin determination in urine, Journal of Separation Science, 30 (2007) 1242-1249.
[28] N. Dorival-García, A. Zafra-Gómez, S. Cantarero, A. Navalón, J.L. Vílchez, Simultaneous determination of 13 quinolone antibiotic derivatives in wastewater samples using solid-phase extraction and ultra performance liquid chromatography–tandem mass spectrometry, Microchemical Journal, 106 (2013) 323-333.
[29] W.R. Somerville, B. Auguie, E.C. Le Ru, Distribution of the SERS enhancement factor on the surface of metallic nano-particles, Nanotechnology (IEEE-NANO), 2012 12th IEEE Conference on, IEEE (2012) 1-4.

[30] E.C. Le Ru, P.G. Etchegoin, Quantifying SERS enhancements, MRS Bulletin, 38 (2013) 631-640.
[31] H. Mao, M. Qi, Y. Zhou, X. Huang, L. Zhang, Y. Jin, Y. Peng, S. Du, Discrimination of sibutramine and its analogues based on surface-enhanced Raman spectroscopy and chemometrics: toward the rapid detection of synthetic anorexic drugs in natural slimming products, RSC Advances, 5 (2015) 5886-5894.
[32] O. Alharbi, Y. Xu, R. Goodacre, Simultaneous multiplexed quantification of nicotine and its metabolites using surface enhanced Raman scattering, Analyst, 139 (2014) 4820-4827.
[33] Y. Xu, Y. Du, Q. Li, X. Wang, Y. Pan, H. Zhang, T. Wu, H. Hu, Ultrasensitive detection of enrofloxacin in chicken muscles by surface-enhanced Raman spectroscopy using amino-modified glycidyl methacrylate-ethylene dimethacrylate (GMA-EDMA) Powdered porous material, Food Analytical Methods, 7 (2014) 1219-1228.
[34] Y. Zhang, Y. Huang, F. Zhai, R. Du, Y. Liu, K. Lai, Analyses of enrofloxacin, furazolidone and malachite green in fish products with surface-enhanced Raman spectroscopy, Food Chemistry, 135 (2012) 845-850.
[35] I.J. Hidi, M. Jahn, M.W. Pletz, K. Weber, D. Cialla-May, J. Popp, Toward levofloxacin monitoring in human urine samples by employing the LoC-SERS technique, The Journal of Physical Chemistry C, (2016).
[36] M. Mamián-López, R. Poppi, Quantification of moxifloxacin in urine using surface-enhanced Raman spectroscopy (SERS) and multivariate curve resolution on a nanostructured gold surface, Analytical & Bioanalytical Chemistry, 405 (2013) 7671-7677.
[37] S. Liu, J. Huang, Z. Chen, N. Chen, F. Pang, T. Wang, L. Hu, Raman spectroscopy measurement of levofloxacin lactate in blood using an optical fiber nano-probe, Journal of Raman Spectroscopy, 46 (2015) 197-201.
[38] L. Yang, X. Qin, X. Jiang, M. Gong, D. Yin, Y. Zhang, B. Zhao, SERS investigation of ciprofloxacin drug molecules on TiO_2 nanoparticles, Physical Chemistry Chemical Physics, 17 (2015) 17809-17815.
[39] L. He, M. Lin, H. Li, N.-J. Kim, Surface-enhanced Raman spectroscopy coupled with dendritic silver nanosubstrate for detection of restricted antibiotics, Journal of Raman Spectroscopy, 41 (2010) 739-744.
[40] S.L. Clauson, J.M. Sylvia, T.A. Arcury, P. Summers, K.M. Spencer, Detection of pesticides and metabolites using surface-enhanced Raman spectroscopy (SERS): Acephate, Applied Spectroscopy, 69 (2015) 785-793.
[41] J.W. Menezes, J. Ferreira, M.J.L. Santos, L. Cescato, A.G. Brolo, Large-area fabrication of periodic arrays of nanoholes in metal films and their application in biosensing and plasmonic-enhanced photovoltaics, Advanced Functional Materials, 20 (2010) 3918-3924.
[42] A. Arriola, A. Rodriguez, N. Perez, T. Tavera, M.J. Withford, A. Fuerbach, S.M. Olaizola, Fabrication of high quality sub-micron Au gratings over large areas with pulsed laser interference lithography for SPR sensors, Optical Materials Express, 2 (2012) 1571-1579.
[43] P. Mandal, A. Nandi, S.A. Ramakrishna, Propagating surface plasmon resonances in two-dimensional patterned gold-grating templates and surface enhanced Raman scattering, Journal of Applied Physics, 112 (2012) 044314-1 - 044314-12.

[44] N.A. Abu Hatab, J.M. Oran, M.J. Sepaniak, Surface-enhanced Raman spectroscopy substrates created via electron beam lithography and nanotransfer printing, ACS Nano, 2 (2008) 377-385.
[45] G. Das, F. Mecarini, F. Gentile, F. De Angelis, H.G. Mohan Kumar, P. Candeloro, C. Liberale, G. Cuda, E. Di Fabrizio, Nano-patterned SERS substrate: Application for protein analysis vs. temperature, Biosensors and Bioelectronics, 24 (2009) 1693-1699.
[46] J.R. Anema, A.G. Brolo, P. Marthandam, R. Gordon, Enhanced Raman Scattering from nanoholes in a copper film, Journal of Physical Chemistry C, 112 (2008) 17051-17055.
[47] Y. Lin, J. Liao, Y. Ju, C. Chang, A. Shiau, Focused ion beam-fabricated Au micro/nanostructures used as a surface enhanced Raman scattering-active substrate for trace detection of molecules and influenza virus, Nanotechnology, 22 (2011) 185308.
[48] K. Sivashanmugan, J. Liao, J. You, C. Wu, Focused-ion-beam-fabricated Au/Ag multilayered nanorod array as SERS-active substrate for virus strain detection, Sensors and Actuators B: Chemical, 181 (2013) 361-367.
[49] J.A. Huang, Y.L. Zhang, H. Ding, H.B. Sun, SERS-enabled lab-on-a-chip systems, Advanced Optical Materials, 3 (2015) 618-633.
[50] K.Y. Hong, J.W. Menezes, A.G. Brolo, Template Stripping Fabricated Plasmonic Nanogratings for Chemical Sensing, Plasmonics, (2017) 1-7
[51] K.Y. Hong, A.G. Brolo , Polarization-dependent surface-enhanced Raman scattering (SERS) from microarrays, Analytica Chimica Acta, (*under revision)* (2016).
[52] R. Stosch, A. Henrion, D. Schiel, B. Güttler, Surface-enhanced Raman scattering based approach for quantitative determination of creatinine in human serum, Analytical Chemistry, 77 (2005) 7386-7392.
[53] D. Zhang, Y. Xie, S.K. Deb, V.J. Davison, D. Ben-Amotz, Isotope edited internal standard method for quantitative surface-enhanced Raman spectroscopy, Analytical Chemistry, 77 (2005) 3563-3569.
[54] A. März, K.R. Ackermann, D. Malsch, T. Bocklitz, T. Henkel, J. Popp, Towards a quantitative SERS approach – online monitoring of analytes in a microfluidic system with isotope-edited internal standards, Journal of Biophotonics, 2 (2009) 232-242.
[55] S. Wold, K. Esbensen, P. Geladi, Principal component analysis, chemometrics and intelligent laboratory systems, 2 (1987) 37-52.
[56] R.R. Meglen, Examining large databases: A chemometric approach using principal component analysis, Marine Chemistry, 39 (1992) 217-237.
[57] J.R. Schoonover, R. Marx, S.L. Zhang, Multivariate curve resolution in the analysis of vibrational spectroscopy data files, Applied Spectroscopy, 57 (2003) 154A-170A.
[58] A. de Juan, J. Jaumot, R. Tauler, Multivariate curve resolution (MCR) - Solving the mixture analysis problem, Analytical Methods, 6 (2014) 4964-4976.
[59] C.D.L. Albuquerque, R.J. Poppi, Detection of malathion in food peels by surface-enhanced Raman imaging spectroscopy and multivariate curve resolution, Analytica Chimica Acta, 879 (2015) 24-33.
[60] P.H.C. Eilers, Parametric time warping, Analytical Chemistry, 76 (2004) 404-411.
[61] A. Savitzky, M.J.E. Golay, Smoothing and differentiation of data by simplified least squares procedures, Analytical Chemistry, 36 (1964) 1627-1639.
[62] T. Yano, P. Verma, Y. Saito, T. Ichimura, S. Kawata, Pressure-assisted tip-enhanced Raman imaging at a resolution of a few nanometres, Nature Photonics, 3 (2009) 473-477.

[63] T. Ichimura, H. Watanabe, Y. Morita, P. Verma, S. Kawata, Y. Inouye, Temporal fluctuation of tip-enhanced Raman spectra of adenine molecules, The Journal of Physical Chemistry C, 111 (2007) 9460-9464.
[64] M. Moskovits, Surface selection rules, The Journal of Chemical Physics, 77 (1982) 4408-4416.
[65] M. Moskovits, J.S. Suh, Surface selection rules for surface-enhanced Raman spectroscopy: calculations and application to the surface-enhanced Raman spectrum of phthalazine on silver, The Journal of Physical Chemistry, 88 (1984) 5526-5530.
[66] E.C. Le Ru, S.A. Meyer, C. Artur, P.G. Etchegoin, J. Grand, P. Lang, F. Maurel, Experimental demonstration of surface selection rules for SERS on flat metallic surfaces, Chemical Communications, 47 (2011) 3903-3905.
[67] S. Kim, S. Joo, Adsorption of 2,2′-biquinoline and 8-hydroxyquinoline on gold and silver nanoparticle surfaces, Vibrational Spectroscopy, 39 (2005) 74-80.
[68] U. Neugebauer, A. Szeghalmi, M. Schmitt, W. Kiefer, J. Popp, U. Holzgrabe, Vibrational spectroscopic characterization of fluoroquinolones, Spectrochimica Acta Part A: Molecular and Biomolecular Spectroscopy, 61 (2005) 1505-1517.
[69] R. Tauler, InCINC '94 Selected papers from the First International Chemometrics Internet Conference - Multivariate curve resolution applied to second order data, Chemometrics and Intelligent Laboratory Systems, 30 (1995) 133-146.
[70] M.B. Mamián-López, R.J. Poppi, Standard addition method applied to the urinary quantification of nicotine in the presence of cotinine and anabasine using surface enhanced Raman spectroscopy and multivariate curve resolution, Analytica Chimica Acta, 760 (2013) 53-59.
[71] E.M. Golet, A.C. Alder, A. Hartmann, T.A. Ternes, W. Giger, Trace determination of fluoroquinolone antibacterial agents in urban wastewater by solid-phase extraction and liquid chromatography with fluorescence detection, Analytical Chemistry, 73 (2001) 3632-3638.
[72] P. Yin, L. Jiang, X. Lang, L. Guo, S. Yang, Quantitative analysis of mononucleotides by isotopic labeling surface-enhanced Raman scattering spectroscopy, Biosensors and Bioelectronics, 26 (2011) 4828-4831.

Chapter 6

Conclusions, Future Directions and Outlook

6.1 Conclusions

In this work, LIL-generated nanogratings have been utilized as the core technology for the fabrication of plasmonic substrates for chemical sensing. LIL technique is high-throughput, cost-effective and versatile. LIL can be combined with other state-of-the-art nanofabrication (e.g., photolithography) to prepare substrates with interesting features (e.g., μarrays).

In Chapter 3, a versatile fabrication using LIL technique was demonstrated. Large area and μarrays of nanogratings were successfully prepared. The geometrical variation between μarrays was less than 5 %. The gold evaporated-μarrays have been exploited in the on-chip detection of 8-quinolinol, a pharmaceutical contaminant that is widely found in the aqueous media of ecosystem (rivers, lakes). The working concentration of the on-chip sensor was in the order of ppm-level. In addition to that, the substrate's background (in-borne from photoresist components used in LIL process) was eliminated from the signal of interest by manipulating the polarization anisotropy nature of the one-dimensional substrates.

While in the following chapter (Chapter 4), the LIL generated template was used as the blue-print in a flexible template-stripping procedure. The nanogratings-containing pattern was transferred to the planar solid support in different dimensions: large (~1 $inch^2$) and small (core size of optical fiber ~50 μm^2) contact areas. Both substrates were shown to be effective bulk refractive index sensors with the large area substrates showed the detection resolution between 10^{-4} to 10^{-5} RIU, which is still two to three orders of magnitude away from the state-of-the-art SPR commercial system (i.e. BIACORE as discussed in Chapter 1 Section 1.3). The tip-patterned optical fibers have been integrated with miniaturized light source and detector. This demonstrates the great potentials of the setup to be incorporated into the handheld or other portable compact systems for the remote sensing applications.

Parallel to the on-chip SERS environmental sensing in Chapter 2, the Ag-evaporated large area nanogratings have been applied for SERS detection of the mixtures of antibiotic and its metabolite (i.e. ENRO and CIPRO), as proof-of-concept SERS applications in environmental detection. The chemometric assisted quantifications (NMF-ALS) have proven to be successful in recovering the concentration and spectral profiles of the analytes, up to bi-mixtures of the parent antibiotic and the respective metabolite. Ongoing effort is still required to optimize the ENRO and CIPRO quantifications in tertiary mixtures or other more complex mixtures (i.e. real environmental samples).

6.2 Future directions

As part of the modern chip technology, LIL has great prospective in the development of miniaturized plasmonic-based sensors. In SERS-based sensing, the uniformity of the nanostructures fabricated is useful and contrast to the inhomogeneity issues found from random SERS substrates. In previous SERS work on antibiotics detection reported in the literature, it was noticed that larger molecules (i.e. ENRO and CIPRO) were not anchored effectively to the substrates, which caused the detection under fluidic system to be practically impossible. One possible improvement is through the surface-functionalization on the substrate's interface so that to the analytes molecules can be attracted to the metal nanostructures. On the other hand, the sensitivity of SERS pharmaceutical detection can be further boosted through: (1) better surface plasmon coupling by matching the laser line to the substrates' SPR by optimizing the periodicity of the nanostructures, (2) optimizing the chemometric data analysis, (attempt other chemometrics alternatives or further optimize the current NMF-ALS algorithm), and (3) go back to random SERS substrates instead, but improve the precision of the quantifications by better sampling during measurements or to use the isotopic – edited internal calibration strategy. As for the SPR-based detection, it might be interesting to look at the refractive-index sensing from the μarrays. In this case, the microfluidic platform should be relatively easy to be integrated to an EOT system, which can be useful for biosensing applications (i.e. based on antigen-antibody detection).

6.3 Outlook

The fabrication of plasmonic nanostructures has progressed extensively in the recent decades and there are still growing research interest in the field each year, as clearly seen in Figure 1.1. It is well-known that the enormous electric field enhancement from the SP resonance phenomenon has great potentials to be exploited in a variety of applications, including plasmonic-based chemical or biochemical sensing. As mentioned in Chapter 1 Section 1.3, there have been reported plasmonic-based technology (both instruments and substrates) commercialized in the market, this scientific field (i.e. plasmonics) nonetheless, is foreseen to continue to expand and develop, alongside with other branches of science. With the better understanding in the field and advent of the nanofabrication technology, the plasmonic substrates (both solution- and lithography-based substrates) would be greatly optimized in terms of their sensitivity and reproducibility. In view of this, the real analytical detections using plasmonic-based sensing would be possible, with much better device setup and design as compared to those currently available systems (chromatographic or mass spectrometric-associated systems). This lies on the fact that the plasmonic effect is solely an optical phenomenon and this allows the plasmonic devices to be miniaturized (e.g., using the available optical fiber technology) into compact (or even handheld or portable) systems, without trading off the respective detection sensitivity. In short, it definitely will be a bright future for plasmonic sensors.

Appendix A

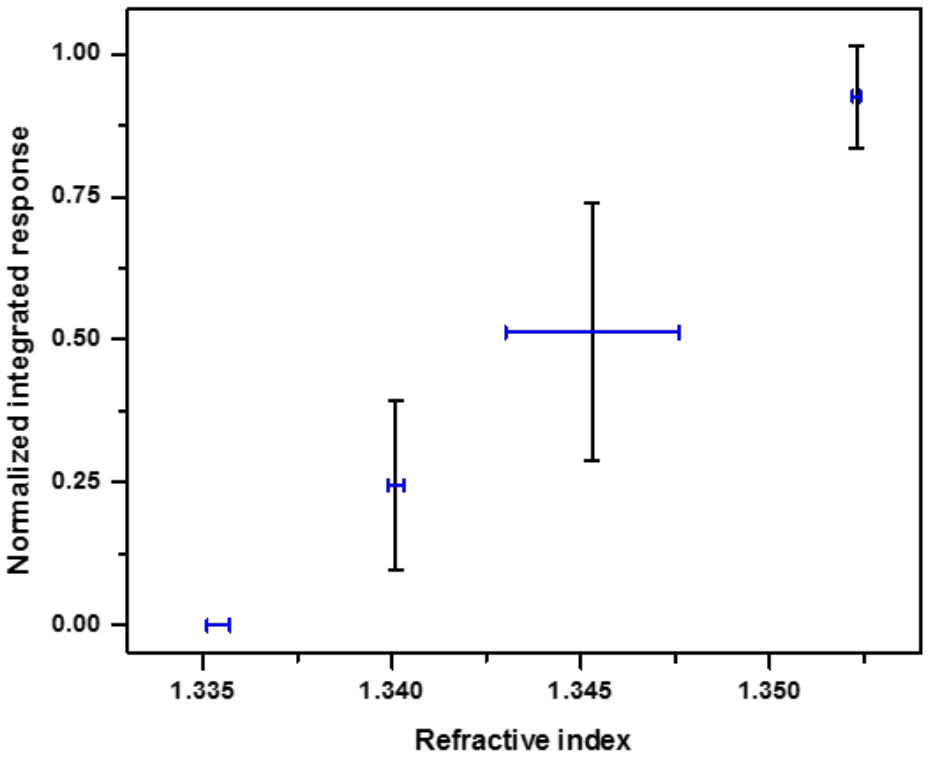

Figure A1 Normalized integrated response plot as a function of the refractive index of the solution for 200-nm thick Ag nanogratings.